

<b>REPORT DOCUMENTATION PAGE</b>			Form Approved OMB NO. 0704-0188	
Public Reporting burden for this collection of information is estimated to average 1 hour per response, including the time for reviewing instructions, searching existing data sources, gathering and maintaining the data needed, and completing and reviewing the collection of information. Send comment regarding this burden estimates or any other aspect of this collection of information, including suggestions for reducing this burden, to Washington Headquarters Services, Directorate for Information Operations and Reports, 1215 Jefferson Davis Highway, Suite 1204, Arlington, VA 22202-4302, and to the Office of Management and Budget, Paperwork Reduction Project (0704-0188,) Washington, DC 20503.				
1. AGENCY USE ONLY (Leave Blank)		2. REPORT DATE 30 January 2004		3. REPORT TYPE AND DATES COVERED FINAL: 01 May 2003 – 31 October 2003
4. TITLE AND SUBTITLE Urban Propagation Modeling for Wireless Systems			5. FUNDING NUMBERS DAAD19-03-1-0069	
6. AUTHOR(S) William Mark Smith and Donald C. Cox				
7. PERFORMING ORGANIZATION NAME(S) AND ADDRESS(ES) Department of Electrical Engineering Stanford University, Stanford, California 94305-9515			8. PERFORMING ORGANIZATION REPORT NUMBER	
9. SPONSORING / MONITORING AGENCY NAME(S) AND ADDRESS(ES) U. S. Army Research Office P.O. Box 12211 Research Triangle Park, NC 27709-2211			10. SPONSORING / MONITORING AGENCY REPORT NUMBER  45140.1-C1-11	
11. SUPPLEMENTARY NOTES The views, opinions and/or findings contained in this report are those of the author(s) and should not be construed as an official Department of the Army position, policy or decision, unless so designated by other documentation.				
12 a. DISTRIBUTION / AVAILABILITY STATEMENT  Approved for public release; distribution unlimited.			12 b. DISTRIBUTION CODE	
13. ABSTRACT (Maximum 200 words) Measurements taken in the San Francisco financial district provide new descriptions of propagation effects and extend existing propagation models to quantify the repeatability of signal variation assumed by new resource allocation techniques. The financial district is a flat portion of the city comprising a grid-like pattern of streets surrounded by buildings up to 160 m tall and is like many areas that are now experiencing network congestion. Changes of 15–25 dB in signal strength are known to occur in the vicinity of intersections and along orthogonal streets. Previously not studied, the signal strength's rate of change determines how quickly the system must respond to loss of signal quality. The sudden change in signal level at street corners requires an averaging window of less than 5 wavelengths to determine the local average power. A new partitioning technique incorporates the layout of streets to reduce the prediction error of existing path loss models by up to 6 dB. Using a new model, repeatability of large- and small-scale signal variations is quantified over a 15-month period.				
14. SUBJECT TERMS propagation, measurements, repeatability, corner effect, velocity estimation, large-scale variation, small-scale variation			15. NUMBER OF PAGES 235	
			16. PRICE CODE	
17. SECURITY CLASSIFICATION OR REPORT UNCLASSIFIED	18. SECURITY CLASSIFICATION ON THIS PAGE UNCLASSIFIED	19. SECURITY CLASSIFICATION OF ABSTRACT UNCLASSIFIED	20. LIMITATION OF ABSTRACT UL	

NSN 7540-01-280-5500

Standard Form 298 (Rev.2-89)  
Prescribed by ANSI Std. Z39-18  
298-102

Enclosure 1

# URBAN PROPAGATION MODELING FOR WIRELESS SYSTEMS

A REPORT SUBMITTED TO THE ARMY RESEARCH OFFICE  
IN FULFILLMENT OF SHORT TERM INNOVATIVE RESEARCH (STIR) GRANT  
DAAD19-03-1-0069

William Mark Smith  
Donald C. Cox  
January 2004

# Contents

<b>Abstract</b>	<b>1</b>
<b>List of Publications</b>	<b>3</b>
<b>List of Personnel</b>	<b>4</b>
<b>Report of Inventions</b>	<b>5</b>
<b>1 Introduction</b>	<b>6</b>
1.1 Motivation . . . . .	6
1.2 Report Outline . . . . .	7
<b>2 Background on Propagation Models</b>	<b>10</b>
2.1 A Historical Perspective . . . . .	10
2.1.1 Free-Space Propagation . . . . .	12
2.1.2 Point-to-Point Communications . . . . .	14
2.1.3 Two-Ray Model . . . . .	15
2.2 Theoretical Models for Complex Environments . . . . .	18
2.2.1 Multi-Ray Models . . . . .	18
2.2.2 Waveguide Models . . . . .	21
2.3 Statistical Models . . . . .	22
2.3.1 Statistical Properties . . . . .	22
2.3.2 Empirical Path-Loss Models . . . . .	27
2.4 Further Reading . . . . .	29

<b>3</b>	<b>Experiment Configuration</b>	<b>31</b>
3.1	Experiment Objectives . . . . .	31
3.2	Signal Strength Measurement . . . . .	34
3.3	Data Reduction Methods . . . . .	39
3.3.1	Corner Identification . . . . .	39
3.3.2	Distance Axis Linearization . . . . .	41
3.3.3	Aligning Multiple Runs for Comparison . . . . .	42
3.4	Summary . . . . .	44
<b>4</b>	<b>The Corner Effect</b>	<b>45</b>
4.1	Previous Work . . . . .	47
4.2	Local Average Received Signal Power . . . . .	48
4.2.1	Sampling and Averaging the Received Signal Power . . . . .	48
4.2.2	Adjusting to Transients . . . . .	50
4.3	Analysis of Measurements . . . . .	54
4.4	Measurement Results . . . . .	71
4.5	Summary . . . . .	72
<b>5</b>	<b>Cell Partitioning for Improved Statistical Propagation Modeling</b>	<b>73</b>
5.1	Objectives . . . . .	73
5.2	Related Work . . . . .	74
5.3	Observations . . . . .	76
5.4	Summary . . . . .	97
<b>6</b>	<b>Repeatability of Large-Scale Signal Variations</b>	<b>98</b>
6.1	Motivation . . . . .	98
6.2	The Repeatability Model . . . . .	102
6.3	Simulation for Comparison . . . . .	104
6.4	Comparing Data Sets . . . . .	107
6.5	Summary . . . . .	141



<b>7</b>	<b>Conclusion</b>	<b>142</b>
7.1	Report Summary . . . . .	142
7.2	Contributions . . . . .	144
7.3	Future Work . . . . .	146
<b>A</b>	<b>Experiment Details</b>	<b>147</b>
A.1	Hardware Design and Configuration . . . . .	147
A.1.1	Distance Measurement . . . . .	147
A.1.2	Base Station Identification . . . . .	150
A.1.3	Power Supplies . . . . .	155
A.2	Software Design and Configuration . . . . .	156
A.2.1	Device Drivers . . . . .	156
A.2.2	Software Tools . . . . .	159
A.3	Transmitter Location . . . . .	161
A.4	Summary of Measurements . . . . .	163
A.4.1	Large-Scale Properties . . . . .	165
A.4.2	Small-Scale Properties . . . . .	173
<b>B</b>	<b>Simulation Examples</b>	<b>180</b>
<b>C</b>	<b>Mobile-User Velocity Estimation in Multipath Environments</b>	<b>189</b>
C.1	Motivation . . . . .	189
C.2	The General Problem of Velocity Estimation . . . . .	191
C.3	Time Methods . . . . .	193
C.3.1	Estimation Based on Envelope Variations . . . . .	193
C.3.2	Estimation Based on Level Crossing . . . . .	196
C.3.3	Methods Almost Independent of Small-Scale Fading . . . . .	202
C.3.4	Speed Estimation Using Wavelets . . . . .	203
C.4	Phase and Frequency Methods . . . . .	205
C.4.1	Estimation of the Doppler Shift Using the Phase Drift in DPSK Signals . . . . .	205
C.4.2	Parametric Estimation of the Doppler Shift . . . . .	208
C.4.3	Best Basis Method . . . . .	210

C.5	Indirect Methods . . . . .	211
C.5.1	Cell Dwell Time . . . . .	211
C.5.2	Velocity Estimation Using Diversity . . . . .	212
C.5.3	Other Methods . . . . .	214
C.6	Closed-Loop Doppler Estimate for Velocity Estimation . . . . .	216
C.7	Summary . . . . .	222

<b>Bibliography</b>	<b>226</b>
---------------------	------------

## List of Tables

4.1	Intersections Exhibiting the Corner Effect . . . . .	71
5.1	Summary of Measurements . . . . .	80
6.1	Summary of Same-Lane Repeatability Simulations . . . . .	110
6.2	Summary of Adjacent-Lane Repeatability Simulations . . . . .	114
A.1	Equipment List . . . . .	149
A.2	Transmit Antenna Location and Orientation . . . . .	163
B.1	Simulation Parameters . . . . .	181
C.1	Frame Rate Restrictions . . . . .	222

# List of Figures

1.1	The San Francisco Financial District . . . . .	7
2.1	The Two-Ray Model . . . . .	15
2.2	Propagation Characteristics of the Two-Ray Model . . . . .	17
2.3	Absorbing Half-Plane . . . . .	19
2.4	Normalized Envelope Autocorrelation of an Ideal, Isotropic Scattering Channel . .	23
2.5	Normalized Power Spectral Density of an Ideal, Isotropic Scattering Channel . . .	24
2.6	Typical Sample of a Correlated Rayleigh Process . . . . .	25
3.1	Measurement Hardware Overview . . . . .	33
3.2	Vehicle Configuration . . . . .	33
3.3	Spectrum Analyzer Block Diagram . . . . .	35
3.4	Spectrum Analyzer Calibration Setup . . . . .	36
3.5	Spectrum Analyzer Calibration Curve . . . . .	36
3.6	Spectrum Analyzer Resolution Bandwidth Filter Response . . . . .	37
3.7	Example of Baseband Filtering . . . . .	38
3.8	Digital Filter Response . . . . .	38
3.9	Adjusting for Boresight Offset . . . . .	40
3.10	Finding the Corner Location . . . . .	41
3.11	Example of a Stopped Vehicle . . . . .	43
3.12	Alignment for Multiple Measurement Runs . . . . .	44
4.1	Transition Regions for Montgomery at California . . . . .	51
4.2	Piecewise Linear Fit for Montgomery at California . . . . .	52
4.3	Piecewise Linear Fit for Montgomery at Pine . . . . .	53

4.4	Locations of Intersections with Significant Corner Effect . . . . .	55
4.5	Piecewise Linear Segments for Multiple Measurements on Clay at Battery . . . . .	57
4.6	Piecewise Linear Segments for Multiple Measurements on Sacramento at Battery . . . . .	59
4.7	Piecewise Linear Segments for Multiple Measurements on California at Battery . . . . .	60
4.8	Piecewise Linear Segments for Multiple Measurements on Sansome at Pine . . . . .	61
4.9	Piecewise Linear Segments for Multiple Measurements on Montgomery at California . . . . .	62
4.10	Piecewise Linear Segments for Multiple Measurements on Montgomery at Pine . . . . .	65
4.11	Piecewise Linear Segments for Multiple Measurements on Montgomery at Bush . . . . .	66
4.12	Piecewise Linear Segments for Multiple Measurements on Montgomery at Sutter . . . . .	67
4.13	Rate and Extent Relationships . . . . .	69
5.1	Measurement Area . . . . .	77
5.2	Drive Along Montgomery Street . . . . .	78
5.3	Distance-Dependent Trend . . . . .	81
5.4	Path Loss Along Battery Street . . . . .	82
5.5	Path Loss Along Pine Street . . . . .	83
5.6	Path Loss Along Sansome Street . . . . .	84
5.7	Path Loss Along California Street . . . . .	85
5.8	Path Loss Along Sacramento Street . . . . .	86
5.9	Path-Loss Trend . . . . .	87
5.10	Distance-Dependent Trend Offset for Intersecting Streets . . . . .	88
5.11	Distance Trend Offsets . . . . .	93
5.12	Partitioned Fit . . . . .	94
5.13	CDF of Estimation Error . . . . .	95
6.1	Two Drives Down Sansome Street . . . . .	100
6.2	Measurement Area . . . . .	101
6.3	Overview of Comparison of Simulation and Measurements . . . . .	105
6.4	Small-Scale Fading Simulation . . . . .	106
6.5	Cross-Correlation for Different Weights . . . . .	107
6.6	Signal Strength Comparisons for the Left Lane of Battery Street . . . . .	111
6.7	Signal Strength Comparisons for Sansome Street . . . . .	115

6.8	Signal Strength Comparisons for the Center Lane of Battery Street . . . . .	118
6.9	Signal Strength Comparisons for the Left Lane of California Street . . . . .	122
6.10	Signal Strength Comparisons for the Right Lane of California Street . . . . .	125
6.11	Signal Strength Comparisons for Clay Street . . . . .	127
6.12	Signal Strength Comparisons for Sacramento Street . . . . .	129
6.13	Signal Strength Comparisons for the Left Lane of Pine Street . . . . .	131
6.14	Signal Strength Comparisons for the Right Lane of Pine Street . . . . .	133
6.15	Signal Strength Comparisons for the Left and Center Lanes of Battery Street . . . .	135
6.16	Signal Strength Comparisons for the Center and Right Lanes of Battery Street . . .	136
6.17	Signal Strength Comparisons for the Left and Right Lanes of Battery Street . . . .	137
6.18	Signal Strength Comparisons for the Left and Right Lanes of California Street . . .	138
6.19	Signal Strength Comparisons for the Left and Right Lanes of Pine Street . . . . .	140
A.1	Synchronization Overview . . . . .	148
A.2	Anti-Lock Braking System (ABS) Sensor . . . . .	148
A.3	AMPS Base Station Transceiver . . . . .	152
A.4	VCO Tuning Characteristics . . . . .	153
A.5	VCO Circuit . . . . .	153
A.6	Frequency Reference Circuit . . . . .	154
A.7	Modified Base Station Transceiver . . . . .	154
A.8	Power Supply Grounding Scheme . . . . .	155
A.9	A/D Control Flow . . . . .	157
A.10	Video Camera Timing Frame Format . . . . .	158
A.11	Sound Card Interrupt Service Routine . . . . .	159
A.12	TIA/EIA-136 Control Channel Format . . . . .	160
A.13	Base Station Decoder . . . . .	160
A.14	Video Alignment Tool . . . . .	162
A.15	Heights of Buildings in the Vicinity of the Transmitter . . . . .	164
A.16	Large-Scale Signal Distributions . . . . .	167
A.17	Large-Scale Autocorrelations . . . . .	170
A.18	Small-Scale Signal Distributions . . . . .	174

A.19	Small-Scale Autocorrelations . . . . .	177
B.1	Composite Signal Strength . . . . .	182
B.2	Small-Scale Fading Envelope Distribution . . . . .	183
B.3	Autocovariance of the Small-Scale Fading Envelope . . . . .	183
B.4	Large-Scale Fading Distribution . . . . .	184
B.5	Autocorrelation of the Large-Scale Fading Power . . . . .	184
B.6	Simulated Repeatability Overlay Comparisons . . . . .	185
B.7	Simulated Comparison Curves . . . . .	187
C.1	Squared Bessel Function and Approximation . . . . .	195
C.2	Angle-of-Arrival Distributions Relative to User Motion . . . . .	197
C.3	Overview of Mobile Terminal Frequency Tracking . . . . .	217
C.4	Mobile Unit Doppler Computation . . . . .	218
C.5	Base Station Doppler Computation . . . . .	218
C.6	Frequency Synthesis . . . . .	220

# Abstract

Network congestion in wireless systems is particularly problematic in urban areas where the concentration of users is high. System operators seek to extend the capacity of their systems while leveraging existing infrastructure by allocating resources more efficiently. Incorporating knowledge of the propagation environment into the resource allocation problem can aid this effort.

Measurements taken in the San Francisco financial district provide new descriptions of propagation effects and extend existing propagation models to quantify the repeatability of signal variation assumed by new resource allocation techniques. The financial district is a flat portion of the city comprising a grid-like pattern of streets surrounded by buildings up to 160 m tall and is like many areas that are now experiencing network congestion. Measurements of the signal strength of active cellular base stations are taken along the streets with an instrumented automobile.

Changes of 15–25 dB in signal strength are known to occur in the vicinity of intersections and along orthogonal streets. Previously not studied, the signal strength's rate of change determines how quickly the system must respond to loss of signal quality. The sudden change in signal level at street corners requires an averaging window of less than 5 wavelengths to determine the local average power. Using an adaptive averaging window, changes as rapid as 19.7 dB/m are observed with signal change extent around 5–13 dB. For more gradual changes an empirical relationship exists between the rate and the extent.

A new partitioning technique incorporates the layout of streets to reduce the prediction error of existing path loss models by up to 6 dB. Using a new model, repeatability of large- and small-scale signal variations is quantified over a 15-month period. For measurements made on the same night, the large-scale signal variations are shown to be repeatable, and small-scale signal variations have normalized envelope cross-correlation values of up to 0.6. After 15 months, small-scale signal variations are uncorrelated from one run to the next, and large-scale signal variations differ by up



to a 4 dB standard deviation between measurement runs. Measurements in adjacent lanes have uncorrelated small-scale variation and differences in the large-scale variation are 4–5 dB.

# List of Publications

## Conference Proceedings

1. W. M. Smith and D. C. Cox, "Urban Cell Partitioning for Improved Statistical Propagation Modeling," *IEEE Antennas and Propagation Society International Symposium*, June 2003.
2. W. M. Smith and D. C. Cox, "Repeatability of Large-Scale Signal Variations in Urban Environments," *IEEE Vehicular Technology Conference*, Oct. 2003.

## Submitted Manuscripts

1. W. M. Smith and D. C. Cox, "Rate and Extent of Signal Change at Street Corners in Urban Environments," submitted to *IEEE Antennas and Propagation Society International Symposium*, June 2004.
2. W. M. Smith and D. C. Cox, "A Closed-Loop Doppler Measurement for Velocity Estimation in Wireless Systems," submitted to *IEEE Antennas and Propagation Society International Symposium*, June 2004.

## List of Personnel

Donald C. Cox

William Mark Smith

Academic Advisor

Ph.D. expected Winter 2004

## **Report of Inventions**

No inventions to report.

# Chapter 1

## Introduction

Wireless systems have experienced explosive growth in the number of subscribers in recent years. In fact, for the past several years, U. S. cellular service providers have sustained exponential growth. As the number of subscribers continues to grow, additional base stations are being installed to service the new demand. Nevertheless, network congestion remains a difficult issue and is particularly problematic in urban areas where the concentration of users is high. Since adding new base stations is an expensive endeavor, a variety of proposed resource allocation techniques [52, 58, 63, 101] enable service providers to extend the capacity of their systems while leveraging the investment in their existing infrastructure. In this report, we study propagation characteristics in ways that are useful for improved resource allocation methods.

### 1.1 Motivation

Academically, urban environments are interesting to study because of the complexity they present for the radio wave propagation. The many surfaces of buildings and objects in the streets produce reflections, diffraction, and shadowing of the signal, guiding it as it propagates from transmitter to receiver. An example of this type of environment is shown in Fig. 1.1.

Urban environments are also of practical interest because these areas attract great concentrations of users. In fact, the popularity of wireless services in these areas is leading to network congestion. Since adding additional base stations to extend capacity is an expensive endeavor, system operators seek ways to extend the capacities of their existing systems.

One way to extend capacity is through improved resource allocation methods. A resource is



Figure 1.1: The San Francisco Financial District. This region of the city is characterized as a dense urban environment, having tall buildings situated on a grid-like pattern of streets. The buildings cause reflections, diffraction, and scattering, guiding the radio wave propagation along the streets.

any shared commodity that the system provides to users on demand. Examples of such resources are frequency, timeslots, transmitted power, and modulation level/bandwidth. For example, in systems that spend less time performing unnecessary handoffs in regions where two base stations serve equally well, an improved handoff algorithm can use information from the propagation characteristics in the area to better refine the handoff location point [58, 63, 101].

Propagation models are important in this regard since they predict the received signal strength. Although other parameters may be used in resource allocation decisions, the received signal strength is the fundamental parameter by which these decisions are made. We study propagation models since they yield predictions of signal strength. The signal strength is the primary parameter by which resource allocation decisions are made in cellular systems.

## 1.2 Report Outline

In Chapter 2 we survey approaches to modeling propagation in a variety of environments. We begin with simple models and gradually work our way up to more complex urban environments.

We discuss deterministic and statistical approaches to modeling these environments. The statistical models discussed in Chapter 2 provide the framework for the development of topics in later chapters.

Since much of the work presented in this report is based on measurements, we spend some time in Chapter 3 discussing the experimental setup and procedures. The San Francisco financial district is chosen as the measurement area for several reasons. First of all, it is consistent with areas that now experience network congestion in many cities. Even though San Francisco is hilly, the financial district, with its tall buildings and grid-like pattern of streets, occupies flat terrain, making it similar in characteristics to other cities classified as dense urban environments. Since the area fits a general classification of environment type, the results in this report are more broadly applicable as well.

In Chapter 4, we study the corner effect, a well-known phenomenon in urban environments. This phenomenon describes the abrupt change in signal strength experienced by a mobile user while turning a corner or going through an intersection. This signal strength change is important since it may drive a resource allocation event, *e.g.*, a handoff or a change in modulation level or transmit power. The rate at which the signal changes determines how quickly the system must respond.

The average received signal strength is the parameter on which these resource allocation decisions are based. Because the characteristics of the small-scale fading must be reduced to estimate the large-scale fading characteristics, averaging windows of  $20\text{--}40\lambda$  are typically used [7, 47]. A constant averaging window of this size works well in places where the local average does not change much, but it is not appropriate near street corners where the signal changes abruptly. We introduce a method in which the averaging window is adjusted at corners to estimate the local average received signal strength. Using this method, we introduce a new characterization of the rate and extent of signal changes at street corners.

In Chapter 5, we introduce a new partitioning method that reduces prediction errors of statistical propagation models by up to 6 dB in urban environments. There are generally two approaches to modeling propagation in urban environments. The more deterministic approaches, *e.g.*, ray-tracing, are more computationally intensive and rely on detailed dimensions and dielectric specifications of the objects in the propagation environment. Statistical models, on the other hand, are much simpler and generally ignore the detailed, deterministic features of the environments. Our

approach augments the statistical models by including rudimentary information about the street layout, increasing the model's complexity only slightly, to achieve significant reduction of the model's prediction error.

In Chapter 6, we study the repeatability of signal strength measurements in urban areas. A majority of the environment in Fig. 1.1 does not move. Buildings keep their same relative positions, so one expects their impact on the radio wave propagation to remain unchanged over time. At the street level, however, there are in fact many objects, such as cars and people, that change position over time and affect the propagation. We challenge the previously held assumption that the large-scale fading is repeatable between measurements while the small-scale fading is not repeatable. We quantify the repeatability and find that there is a continuum of the degree of repeatability in the signal measurements. We use the San Francisco measurements, relying on the fidelity of our location estimate, to verify our repeatability model. We characterize this model in terms of both time and position between repeated measurements.

The appendices include background and additional information not central to the theme of this report. Appendix A describes additional details about the experimental setup. While Chapter 3 contains the information necessary to understand how the data reduction was done, this appendix provides the detailed description of the hardware that makes the previously mentioned data analysis possible. Also included in this appendix are summaries of the statistical properties of the measurements taken in the financial district.

Appendix B serves as a complement to Chapter 6. Examples of simulation output are presented so that qualitative comparisons between simulated and measured data may be made over a range of simulation parameters.

Mobile-user velocity estimation is presented in Appendix C. Radio wave propagation is a spatial phenomenon. Algorithms that exploit propagation characteristics must process the measurements as a function of position. Since communication systems are time-based, an accurate velocity estimate mapping the time-domain to the space-domain makes the utilization of these algorithms possible.

Our discussion in Appendix C gives an overview of the mobile-user velocity estimation problem along with a survey of recent approaches to solving it from the technical literature. We introduce a new method, based on existing communication standards, to estimate the Doppler spectrum based on a round-trip measurement in a mobile, multipath environment.



## Chapter 2

# Background on Propagation Models

One of the things that makes radio propagation so difficult to analyze in urban environments is the fact that the propagation environment is filled with objects that are beyond the engineer’s precise knowledge and control, and have properties that are sufficiently complex to make a complete description unreasonable over large areas of a city. It is therefore the engineer’s job to determine what general principles may be applied.

This chapter presents an overview of various propagation models used in assessing performance of wireless communications systems. Our discussion begins with the early studies that predicted the existence of electromagnetic waves. After waves were successfully transmitted and received with sufficient fidelity, then studies of propagation could be performed. We begin with simple models, accounting for no obstructions. We work our way up to increasingly complex models that account for more and more obstructions. Although this chapter presents only an overview of various techniques, we spend the most time on the statistical models that are relevant to discussion throughout the remainder of this report.

## 2.1 A Historical Perspective

The field of wireless communication was born in 1865 with the publication of a paper [55] by James Maxwell regarding the dynamic nature of electromagnetics.<sup>1</sup> Maxwell’s now famous inclusion of a term for displacement current was the key to the coupling of electric and magnetic fields,

---

<sup>1</sup>Many other fields of study that rely on Maxwell’s equations were also “born” at this time, but we focus on wireless communication here.

predicting electromagnetic wave propagation. At the time, however, there was no experimental evidence suggesting the inclusion of such a term [1], and Maxwell instead relied on his keen sense of intuition [46] regarding the continuity of mathematics and physics.

The acceptance of Maxwell's model within the scientific community was difficult initially since there was no underlying physical explanation for the displacement current term [1]. Furthermore, the experimental evidence was difficult to produce since no one knew how to generate electromagnetic waves, much less receive them. It was not until 23 years later in 1888 that Hertz was able to verify experimentally the propagation of electromagnetic waves and confirm that the propagation was at the speed of light as predicted by Maxwell.

Hertz's breakthrough was significant not only for the validation of Maxwell's equations, but for the experimental setup itself. By applying his knowledge acquired from previous studies of electrical resonance, Hertz was able to tune his transmitter and receiver close enough in frequency that the wave generated at the transmitter would be detected by the receiver. Also, the frequency was high enough that it would propagate from one end of his lab and back [1].

The early days of radio were consumed by efforts to improve the performance of the rudimentary devices that were used for transmission and detection. About another decade of device improvements followed before commercial interests in radio were feasible. Aitken [1, 2] gives a technical and historical background on these developments, and Lee provides an entertaining summary of these activities in his book [46, Ch. 1].

The study of electromagnetic waves matured along with commercial developments. With advances in wireless telegraphy, radio, and television, antenna design improved, making the study of wave propagation and reflection possible. We pick up our technical development of radio propagation models in the 1940s with the free-space propagation equation of Friis [29]. Although ground reflections were studied prior to Friis's work, we use the Friis model as a starting point for the two-path model as well as multipath propagation models that have been studied more recently.

The remainder of this chapter focuses on impairments of the propagation environment that must be handled by the wireless engineer. We start with models that have few or no reflectors. We eventually work our way up to more complex environments with many surfaces causing reflections and shadowing. Both theoretical and empirical models are summarized in this chapter.

### 2.1.1 Free-Space Propagation

Friis [29] derived a compact representation of the relationship between transmitted and received signal power in a wireless communication link. The Friis equation—sometimes called the free-space, or link equation—accounts for the free-space path loss and the effects of the antennas on each end of the communication link. The Friis equation is widely used today to characterize point-to-point communications links, and a modified form of the equation describes the returned signal in radar applications.

The derivation in [29] is outlined in this section since it gives some intuition for the propagation mechanisms. The Friis equation itself provides a starting point for discussing multi-ray models that are introduced later in this chapter.

We begin with a hypothetical isotropic radiator with transmit power  $P_t'$ . This power radiates uniformly in all directions away from this idealized point source. Since the power radiating through a sphere centered on the source is always  $P_t'$ , the power per unit area at a given point on a sphere of radius  $d$  is

$$p = P_t' / 4\pi d^2. \quad (2.1)$$

At the receiver, the antenna captures a portion of the energy radiating in this expanding sphere. The received power describes the effective surface area of the sphere that the antenna is able to capture:

$$P_r = pA_{\text{eff}}. \quad (2.2)$$

The effective area of the receive antenna in terms of the transmitted and received power is

$$A_r = P_r / p = P_r 4\pi d^2 / P_t'. \quad (2.3)$$

Rewriting in terms of the transmitted and received power yields

$$\frac{P_r}{P_t'} = \frac{A_r}{4\pi d^2}. \quad (2.4)$$

In reality, the transmitting antenna is not an ideal isotropic radiator. Instead, using the effective capture area of the transmit antenna, the transmit power  $P_t$  can be related to the transmit power of

an isotropic radiator  $P'_t$  through a ratio of the capture areas:

$$P_t = \frac{A_t}{A_{\text{iso}}} P'_t. \quad (2.5)$$

The effective area for an isotropic antenna is given as [84]:

$$A_{\text{iso}} = \frac{\lambda^2}{4\pi}. \quad (2.6)$$

Substituting (2.5) and (2.6) into (2.4) yields

$$\begin{aligned} \frac{P_r}{P_t} &= \frac{A_r A_t}{4\pi d^2 A_{\text{iso}}} \\ &= \frac{A_r A_t}{(\lambda d)^2}. \end{aligned} \quad (2.7)$$

Friis preferred to characterize antennas by their effective areas [29]; however, today it is common practice to refer to antennas by their gains relative to an ideal isotropic radiator. The antenna gain is related to its effective area by [84]

$$A = \frac{\lambda^2 g}{4\pi}. \quad (2.8)$$

Substituting (2.8) for each antenna into (2.7) yields

$$\begin{aligned} \frac{P_r}{P_t} &= \left( \frac{\lambda^2 g_r}{4\pi} \right) \left( \frac{\lambda^2 g_t}{4\pi} \right) \frac{1}{(\lambda d)^2} \\ &= g_r g_t \left( \frac{\lambda}{4\pi d} \right)^2. \end{aligned} \quad (2.9)$$

This equation relates the received power to transmit power, antenna gains, and the distance,  $d$ , between transmitter and receiver. The  $1/d^2$  distance dependence is known as the free-space path loss and results from the expanding of the wavefront as it emanates from the source with no obstructions.

### 2.1.2 Point-to-Point Communications

For long-range line-of-sight (LOS) wireless communications links, terrain clearance and atmospheric effects are the primary considerations when designing a link for reliability. Fresnel zones identify when an obstruction blocks the primary propagation path in such a way that the received signal is the result of diffraction around the object. Fresnel zones are ellipsoidal regions with foci at the transmitter and receiver. Each zone is identified by a surface that indicates path lengths that are integer multiples of  $\lambda/2$  longer than the direct path from transmitter to receiver. The radius of the  $n$ -th Fresnel zone at a distance  $d_1$  from the end of the path is given by [9]:

$$F_n = \sqrt{n\lambda d_1(d - d_1)/d} \quad (2.10)$$

where  $d$  is the length of the path.

Rappaport [75] suggests a rule of thumb that 55% of the first Fresnel zone should be kept clear of obstacles. Because of diurnal temperature changes, the resulting changes in the refractivity of the atmosphere alters the effective Fresnel zone clearance. The changes in the refractivity are equivalent to analyzing the link in which the radius of the earth has been expanded by a factor of [9]

$$K = 1/(1 + N'/157) \quad (2.11)$$

where  $N'$  is the refractivity gradient.<sup>2</sup> The fading due to these refractive irregularities is thus called “earth-bulge fading.” The rule of thumb identified in [9] suggests using antenna heights that keep the daytime Fresnel zone clear of obstructions, while the nighttime earth-bulge fading is characterized by a statistical model.

Barnett [8] developed a statistical model for multipath fading based on measurements from a 28.5-mile relay in Ohio and extrapolated for other links in the Bell System having an average path length of 26 miles and an average antenna height of 250 ft [92]. The formula is given as [8]

$$\text{prob}\{p/p_0 < L^2\} = c(f/4)d^3L^210^{-5} \quad (2.12)$$

where  $f$  is the frequency given in GHz,  $d$  is the path length in miles,  $c$  is a climate and terrain factor, and  $L^2$  is the fade level, expressed in linear power units, relative to the level received in

---

<sup>2</sup>The units of  $N'$  are  $N$ -units (changes in parts per million of the refractivity index) per km.

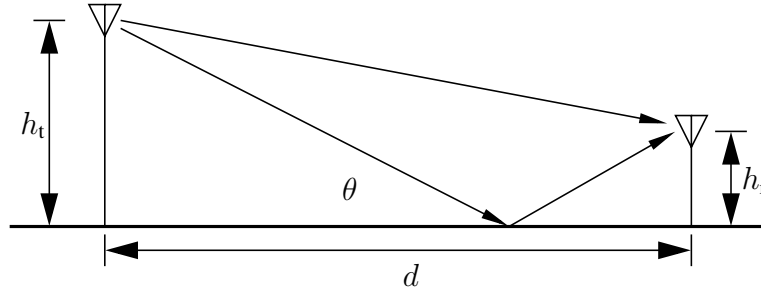


Figure 2.1: The Two-Ray Model. This model includes a reflection from the ground in addition to the direct path.

the absence of fading. The value of  $c$  varies according to location. Values of  $c > 6$  are used for smooth terrain in southern U.S. coastal areas, and values of  $c < 0.2$  are used in rough terrain in dry climates.

Another concern is the absorption caused by the atmosphere on long LOS propagation paths. Absorption primarily affects frequencies above 3 GHz and depends on path length and frequency of the signal. Bell Laboratories [9] give an absorption graph for a range of microwave frequencies. Even under cloudburst conditions (100 mm/hr), there is less than 0.05 dB/km absorption reported for frequencies less than 3 GHz, indicating that absorption is negligible for typical cell sizes at the most common cellular frequencies (800, 900, and 1900 MHz).

### 2.1.3 Two-Ray Model

In many cases, there is more than one propagation path from transmitter to receiver. This section outlines a straightforward extension to the Friis model (2.9) as summarized in [39, Ch. 2]. This extension includes the effects of the earth in the propagation by considering the ground reflection as shown in Fig. 2.1.

Propagation over a plane can be represented by [39]

$$P_r = P_t \left[ \frac{\lambda}{4\pi d} \right]^2 g_t g_r \left| 1 + R e^{j\Delta} + (1 - R) A e^{j\Delta} + \dots \right|^2. \quad (2.13)$$

The first two terms inside  $|\cdot|^2$  represent the direct and reflected paths. Other terms represent secondary effects of ground currents that may be neglected if the antenna is more than a few

wavelengths above the ground [39]. The phase difference between the two paths is  $\Delta$ , and the reflection coefficient  $R$  is given as

$$R = \frac{\sin \theta - z}{\sin \theta + z} \quad (2.14)$$

where

$$z = \begin{cases} \frac{\sqrt{\epsilon_0 - \cos^2 \theta}}{\epsilon_0} & \text{vertical polarization} \\ \sqrt{\epsilon_0 - \cos^2 \theta} & \text{horizontal polarization,} \end{cases} \quad (2.15)$$

$\epsilon_0$  is the normalized dielectric constant of the ground, and  $\theta$  is the incidence angle of the ground-reflected wave. If the transmitter and receiver are separated by large enough distance, the incidence angle is grazing and the reflection coefficient becomes  $R \approx -1$ . If these conditions are met, equation (2.13) then simplifies to [39]

$$P_r = 4P_t \left[ \frac{\lambda}{4\pi d} \right]^2 g_t g_r \sin^2 \left( \frac{2\pi h_t h_r}{\lambda d} \right). \quad (2.16)$$

Using the small angle approximation for the sine term, (2.16) simplifies to

$$P_r = P_t g_t g_r \left[ \frac{h_t h_r}{d^2} \right]^2. \quad (2.17)$$

An example of the propagation characteristics exhibited by the two-ray model of (2.16) is shown in Fig. 2.2. Close to the transmitter, the phases of the two propagation components add either constructively or destructively. The nulls correspond to locations in which the two paths are out of phase. The local maxima occur at locations in which the phases add constructively. Since the components add coherently, the local maxima are 6 dB above what the free-space model predicts. When the transmitter and receiver are far enough apart, the first Fresnel zone touches the ground, indicating that the direct and reflected path differ by half a wavelength. Taking the phase shift of the ground reflection into account, the two components add in phase. If the transmitter and receiver are separated beyond this point, the small angle approximation in (2.16) becomes valid and the signal strength falls off at 40 dB/decade as predicted by (2.17).

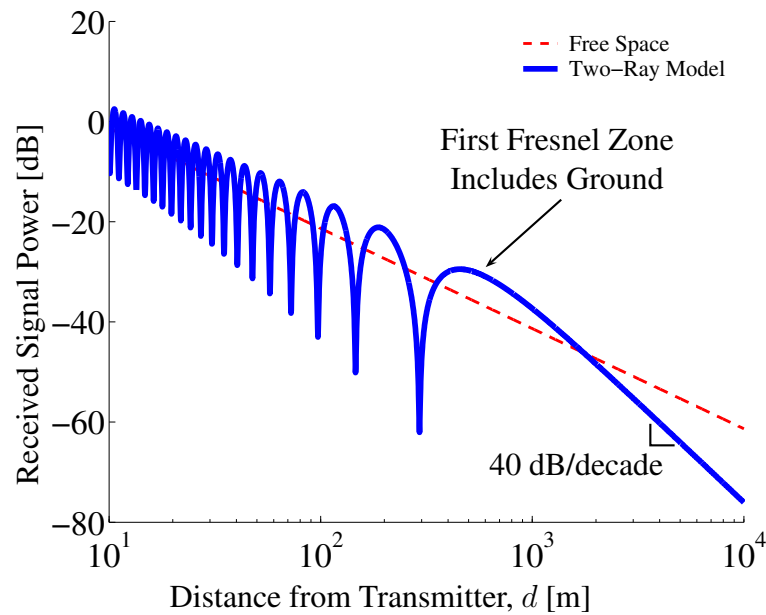


Figure 2.2: Propagation Characteristics of the Two-Ray Model. As the receiver moves further away from the transmitter, changing phase combinations of the two paths produce signal fluctuations around the free-space path loss characteristics, *i.e.*,  $d^{-2}$ , until the first Fresnel zone touches the ground, after which the signal strength is limited by diffraction and decays as  $d^{-4}$ .



## 2.2 Theoretical Models for Complex Environments

### 2.2.1 Multi-Ray Models

In urban environments with many buildings to act as reflectors and shadowing objects, the two-ray model is clearly not sufficient. In fact, it has become quite popular in recent years to use multiple rays to characterize the propagation in urban environments [3, 11, 20, 21, 23–26, 40, 42, 43, 49, 56, 64, 74, 77, 78, 80, 83, 86, 89, 94, 102]. Each time a ray is modeled with a reflection, however, there is some error associated with the model's prediction due to inaccurate representation of material properties or dimensions of objects in the environment. For rays that are modeled by multiple reflections, these errors tend to accumulate, making the model's predictions less accurate farther away from the transmitter.

Over small areas ray models provide reasonable agreement with measurements. One such study that agrees well with measurements was conducted by Rustako, *et. al.* [80]. The study includes comparisons of the two-ray model mentioned in Section 2.1.3 with measurements. Urban and suburban measurements made in New York and New Jersey are compared with a six-ray model.

The six-ray model characterizes propagation along a straight street that forms a so-called “dielectric canyon.” The six rays are modeled as a direct path, a ground reflection, single reflections from buildings on either side of the street, and paths that include both building and ground reflections. The dielectric properties listed in [39] for average ground are used for the buildings and the ground. This model uses a modified form of the two-path model in Section 2.1.3:

$$\begin{aligned}
 P_r &= K \left| \frac{G_d}{r} + \sum_{i=1}^{N-1} \frac{G_{ri} R_i e^{j\Delta\phi_i}}{r_i} \right|^2 \\
 &\approx \frac{K}{r^2} \left| G_d + \sum_{i=1}^{N-1} G_{ri} R_i e^{j\Delta\phi_i} \right|^2
 \end{aligned} \tag{2.18}$$

where  $K$  is a proportionality constant that includes the transmit power,  $G_d$  and  $G_{ri}$  are the gains of the direct and reflected paths taking antenna patterns into account,  $\Delta\phi_i$  is the phase difference of each reflected path relative to the direct path,  $R_i$  is the reflection coefficient for the  $i$ -th path as given in (2.14), and  $r$  and  $r_i$  are the path lengths of the direct and reflected rays.

Many ray-tracing models also consider diffraction effects around corners and over the tops of

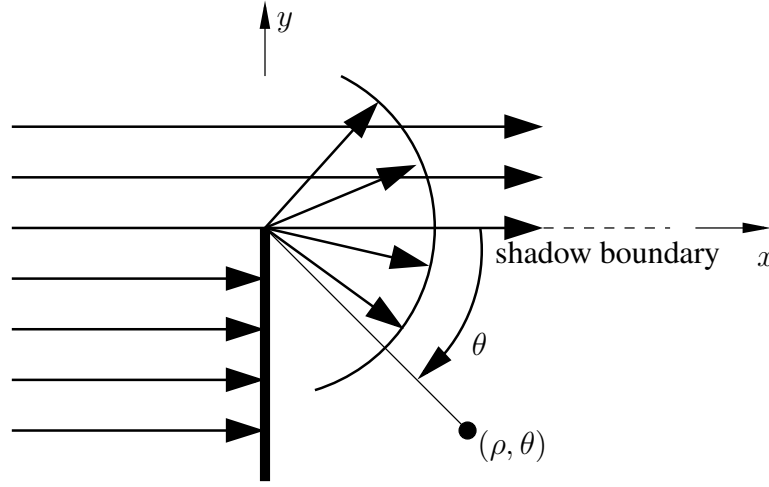


Figure 2.3: Absorbing Half-Plane. Diffraction effects of a plane wave incident on an absorbing half-plane are analyzed using the Huygens-Fresnel method for sources over the half-plane.

buildings. Bertoni has been involved in many ray-tracing studies [11, 49, 64, 68, 94]; his book provides the fundamental background needed to include diffraction in ray-tracing models [12, Ch. 5].

The diffraction of a plane wave over an absorbing half-plane illustrates the underlying principles of diffraction and is a common starting point for discussion of the subject [12, 39]. We use the notation and follow the derivation of Bertoni [12] in this section.

A 2-D cross-sectional diagram of an absorbing half-plane is shown in Fig. 2.3. The absorbing half-plane is of infinite extent along the  $z$ -axis, which extends out of the page. The line corresponding to  $(x, y) = (0, 0)$  is the edge of the absorbing half-plane.

The Huygens-Fresnel principle is used to compute the field strength at any point to the right of the half-plane ( $x > 0$ ) by summing the contributions of point sources in the wave front above the half-plane ( $x = 0, y > 0$ ).

After some approximations to make a closed-form solution possible for the integration in the previous step, the geometrical theory of diffraction (GTD) result is obtained in the following form:

$$\left. \begin{array}{l} E(x, y, 0) \\ H(x, y, 0) \end{array} \right\} = A_0 e^{-jkx} U(y) + A_0 e^{-j\pi/4} \frac{e^{-jk\rho}}{\sqrt{\rho}} D(\theta) \quad (2.19)$$

where  $A_0$  is the electric or magnetic field strength—electric or magnetic—at the origin,  $U(y)$  is a unit step function, and  $D(\theta)$  is the diffraction coefficient given by

$$D(\theta) = -\frac{1}{\sqrt{2\pi k}} \frac{1 + \cos \theta}{2 \sin \theta}. \quad (2.20)$$

The interpretation of (2.19) is as follows: The first term is from the incident wave and is only valid above the shadow boundary ( $y > 0$ ); hence, the step function,  $U(y)$ . The second term in (2.19) represents a cylindrical wave emanating from a theoretical line source situated along the edge of the half-plane.

Because of the discontinuous nature of the step function, the solution in (2.19) is not valid near the shadow boundary. A better approximation for the integration distance used to derive (2.19) is used to get the uniform diffraction theory (UTD) result that is more accurate near the shadow boundary. The UTD result takes the same form as (2.19) and is

$$\left. \begin{array}{l} E(x, y, 0) \\ H(x, y, 0) \end{array} \right\} = A_0 e^{-jkx} U(y) + A_0 e^{-j\pi/4} \frac{e^{-jk\rho}}{\sqrt{\rho}} D_T(\theta) \quad (2.21)$$

where

$$D_T(\theta) = D(\theta)F(\theta) \quad (2.22)$$

and  $F(\theta)$  is a correction factor to the previous diffraction coefficient,  $D(\theta)$ , and is given by an expression that includes Fresnel integrals.

The preceding analysis provides the building blocks for ray-tracing. Using analytical methods similar to those above, values for reflected and diffracted waves are computed for plane waves with oblique incidence on dielectric wedges. To build a ray-tracing model, the engineer must determine what rays to launch, and for each ray that comes into contact with a corner, the subsequent reflected and diffracted waves are computed. Each subsequent ray has its reflected and diffracted components derived in the same manner until arriving at the receiver.

### 2.2.2 Waveguide Models

Although ray models are the predominant methods for studying the deterministic effects of propagation in complex environments, waveguide models are becoming increasingly popular in describing the propagation mechanisms in tunnels [18], streets [44, 69, 71], and hallways [69, 70]. Porrat and Cox [69, 71] take waveguide theory used to describe the behavior of light in fiber-optic cables with rough walls and extend it to RF propagation in streets.

Since the widths of streets are much greater than the carrier wavelength, streets act as multimoded waveguides. The buildings that line the edge of the street and the street surface act as the walls of the waveguide. Assuming the dielectric loss tangent is small compared to the dielectric constant, and the imaginary part of normalized wave vector in the lateral direction is small, approximations can be made regarding the number of significant modes that exist in the waveguide. Additionally, the roughness of the edges of the waveguide cause coupling between these significant modes (both TE and TM) as the signal travels down the street [69, 71]. A statistical description of the building surfaces is used to extend the perturbed waveguide model to streets. The resulting coefficients describe the coupling of the modes:

$$\frac{\partial A_m}{\partial z} = \sum_{n=1}^N c_{mn} A_n. \quad (2.23)$$

In (2.23),  $A_m$  is the phasor representation, *i.e.*, magnitude and phase, of the TE or TM mode indexed by  $m$ ;  $c_{mn}$  is the coupling from mode  $n$  to mode  $m$ . Based on the perturbed waveguide theory, the expression for  $c_{mn}$  accounts for the street width, the dielectric properties of the buildings, and the rough building surfaces. The full expression is given by Porrat and Cox [69, 71]. Assuming Gaussian autocorrelations for the roughness of the building surfaces, the coupled mode equation (2.23) is transformed into a coupled power equation of the form [69, 71]

$$\frac{\partial \bar{P}(z)}{\partial z} = \Gamma \bar{P}(z). \quad (2.24)$$

In (2.24), the column vector  $\bar{P}(z)$  identifies the power contained in each mode at a particular distance  $z$  along the street. The matrix  $\Gamma$  contains the power coupling coefficients that describe the behavior of the modes based on the street dimensions and the statistical description of the building

surfaces.

Equation (2.24) can be solved using the eigenvalue decomposition:

$$\overline{P}(z) = Q\Lambda^z Q^T \overline{P}_0 \quad (2.25)$$

where  $Q$  is the eigenvector matrix,  $\Lambda$  is the diagonal eigenvalue matrix, and  $\overline{P}_0$  is the initial distribution of power in the modes. Since the matrix  $\Gamma$  is real and symmetric, the eigenvector matrix does not need to be inverted.

The powers of the modes add incoherently to give the power at a given position  $z$  along the street by

$$p(z) = \mathbf{1}^T \overline{P}(z) \quad (2.26)$$

where  $\mathbf{1}$  is a column vector of ones.

## 2.3 Statistical Models

Electromagnetic propagation in complex environments is site-specific. The ray and waveguide theoretical models explain the first-order effects of the signal propagation in a given environment. Since the signal is not fully characterized by these first-order effects, statistical models may be used to augment the small-scale behavior. In cases where the precise geometries and material properties are not known for a particular environment, statistical models may be applied based on general classifications of the environment, such as rural, suburban, urban, etc.

### 2.3.1 Statistical Properties

The propagation of high-frequency signals from transmitter to receiver in a mobile, multi-path environment is characterized by three properties: (1) small-scale fading, indicated by large, rapid fluctuations in the received signal strength over distances less than a wavelength, (2) large-scale variation over distance on the order of sizes of buildings, hills, trees, and other large objects in the environment, and (3) a distance-dependent trend. The small-scale fading is caused by the constructive and destructive interference of multipath components from reflections and scattering arriving at the receiver with different phases at the receiver. The large-scale fading is generally attributed

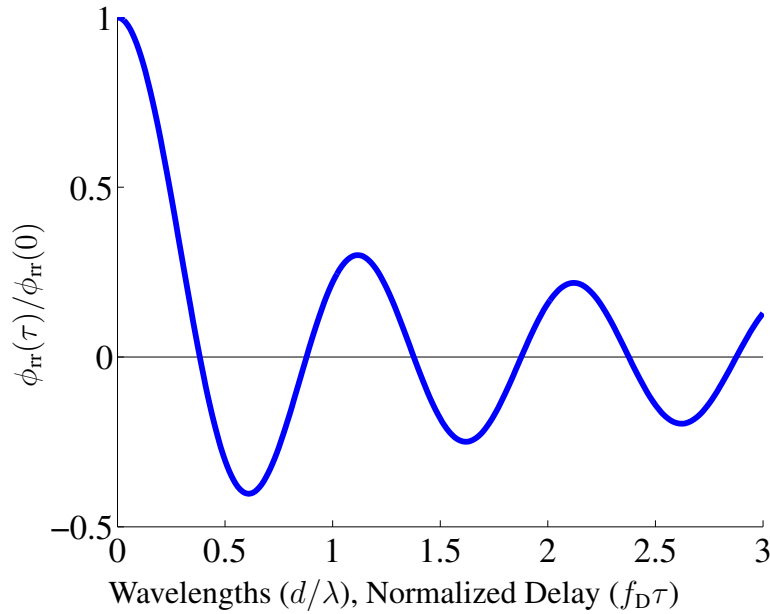


Figure 2.4: Normalized Envelope Autocorrelation of an Ideal, Isotropic Scattering Channel. The null locations in the autocorrelation function using the 2-D isotropic scattering model depend on the wavelength of the carrier. When a constant velocity is assumed, the null locations are inversely proportional to the maximum Doppler frequency.

to shadowing by large objects, such as buildings and hills, in the propagation environment.

### Small-Scale Fading

Clarke's model<sup>3</sup> is a theoretical model that describes the behavior of the small-scale fading in a mobile, multipath environment. In this model, the arriving multipath components arrive in and are confined to the horizontal plane. Furthermore, the power of these arriving components is assumed to be uniformly distributed over arrival angles  $[0, 2\pi]$  in the horizontal plane.

Following the derivation and notation used in [87], the received signal can be represented in quadrature form as

$$x(t) = r_I(t) \cos 2\pi f_c t - r_Q(t) \sin 2\pi f_c t \quad (2.27)$$

---

<sup>3</sup>sometimes called the Jakes model or the Rayleigh model in the technical literature

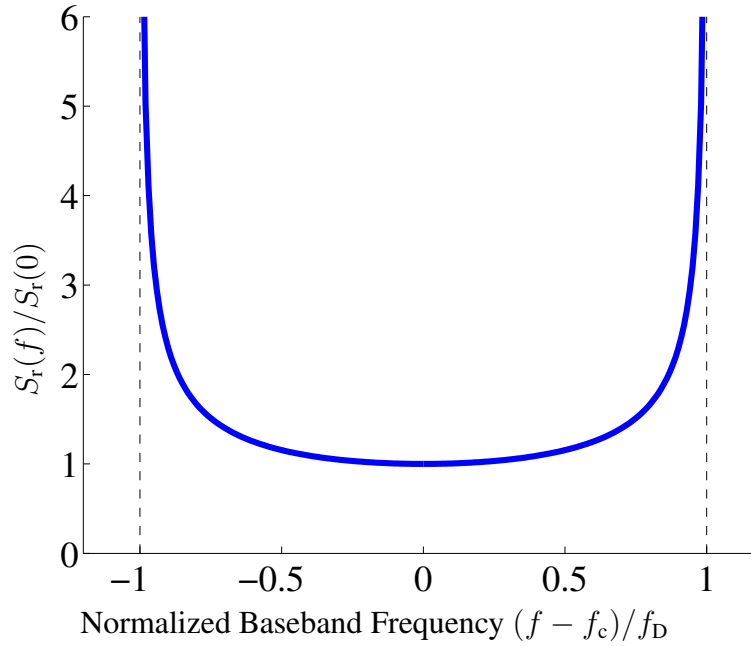


Figure 2.5: Normalized Power Spectral Density of an Ideal, Isotropic Scattering Channel. This temporal frequency spectrum assumes the mobile user is traveling at a constant speed.

with a complex baseband representation of

$$r(t) = r_I(t) + jr_Q(t). \quad (2.28)$$

The autocorrelation of this baseband received signal is

$$\phi_{rr}(t) = \frac{1}{2}E[r^*(t)r(t + \tau)] = \phi_{r_I r_I}(\tau) + j\phi_{r_I r_Q}(\tau). \quad (2.29)$$

To further simplify the analysis, the arriving components are assumed to have an initial phase uniformly distributed over  $[0, 2\pi]$ . It then follows that the net received in-phase and quadrature components are uncorrelated ( $\phi_{r_I r_Q}(\tau) = 0$ ). Since there are many multipath components, the in-phase and quadrature components are assumed to be Gaussian random processes. With these additional assumptions, the autocorrelation of the baseband received signal becomes [87]

$$\phi_{rr}(\tau) = \phi_{r_I r_I}(\tau) = \phi_{r_Q r_Q}(\tau) = \sigma^2 J_0(2\pi f_D \tau) \quad (2.30)$$

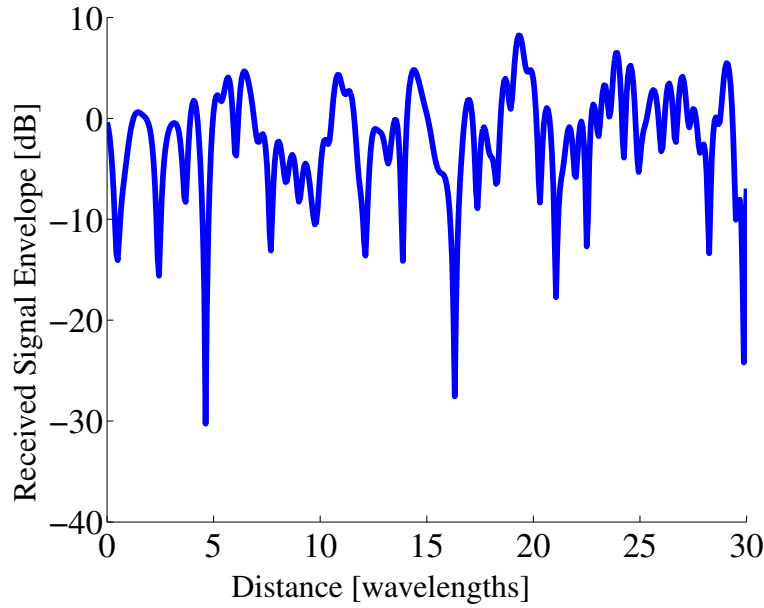


Figure 2.6: Typical Sample of a Correlated Rayleigh Process. The average null spacing is proportional to the carrier wavelength.

where the in-phase and quadrature components each have power  $\sigma^2$ . The autocorrelation relationship in (2.30) is shown in Fig. 2.4, and a sample of the process is shown in Fig. 2.6. The Fourier transform of (2.30) yields the power spectral density [87]

$$S_r(f) = \begin{cases} \frac{G\sigma^2}{\pi f_D} \frac{1}{\sqrt{1 - \left(\frac{f-f_c}{f_D}\right)^2}}, & |f - f_c| \leq f_D \\ 0, & \text{otherwise} \end{cases} \quad (2.31)$$

where  $G$  is the gain of an omnidirectional antenna at the receiver. This power spectral density is shown in Fig. 2.5. Also implicit in the preceding derivation is the fact that we are considering narrowband signals, *i.e.*, the bit period is significantly less than the delay spread, such that the effects of the delay spread are averaged out in the receiver during each symbol period.

The Clarke model is an ideal scattering model. An extension to the Clarke model includes a LOS path, *i.e.*, the “specular” component, to the receiver in addition to uniform scattering. This extended model is sometimes used to model propagation within a single street where a LOS component exists in addition to reflections and scattering by objects in the street. The inclusion of the specular component produces a Ricean-distributed signal envelope.



### Large-Scale Fading

The Clarke model describes the scattering characteristics within the vicinity of several wavelengths on either side of a particular receiving location. The statistics of the small-scale signal variations of the channel are assumed to be stationary over this distance so that a useful average power can be attained. As the mobile user travels over a greater distance, however, the local average of the received power will change as well.

These large-scale variations result from both the propagation loss from the transmitter and the shadowing caused by large objects such as buildings and hills in the propagation environment. This large-scale, or slow, fading causes the local average of the small-scale fading to change over large distances. Over small distances, however, the statistics of the small-scale fading are considered to be stationary.

The received signal power at a given position,  $\mathbf{x}$ , may be represented empirically as

$$P(\mathbf{x}) = D(\mathbf{x})L(\mathbf{x})Y(\mathbf{x}) \quad (2.32)$$

where  $D(\mathbf{x})$  is a distance-dependent trend,  $L(\mathbf{x})$  is the large-scale variation, and  $Y(\mathbf{x})$  is the small-scale variation. To estimate the distance-dependent trend,  $D(\mathbf{x})$ , and the large-scale fading,  $L(\mathbf{x})$ , the effects of the small-scale fading term,  $Y(\mathbf{x})$ , must be reduced through spatial averaging of the received signal. The correlation length of  $Y(\mathbf{x})$  is a frequency-dependent value, and at cellular frequencies, this correlation length is much shorter than the correlation lengths observed for  $L(\mathbf{x})$ , making the empirical separation of these two fading effects possible.

Theoretical studies by Lee [47] and Austin and Stüber [7] suggest that an averaging interval of  $20\text{--}40\lambda$  should be used to average out most of the small-scale fading while preserving the characteristics of the large-scale fading. Over a large area, many spatially averaged samples, when expressed in decibels, are fit to the following formula to estimate the distance-dependent trend:

$$\hat{D}_{\text{dB}}(\mathbf{x}) = K_0 - 10 n \log_{10}(|\mathbf{x}|). \quad (2.33)$$

In (2.33), the origin is situated at the transmitter, and  $K_0$  is a calibration constant that accounts for the transmitter power, the transmitter and receiver antenna gains, and an initial, empirically determined path-loss value.

The estimate of the large-scale variation is taken by subtracting the distance-dependent trend from the local spatial averages:

$$\hat{L}_{\text{dB}}(\mathbf{x}) = 10 \log_{10}(\langle P(\mathbf{x}) \rangle_W) - \hat{D}(x). \quad (2.34)$$

The averaging operation  $\langle \cdot \rangle_W$  denotes a spatial average of the power  $P(\mathbf{x})$  over an averaging window  $W$ , centered on  $\mathbf{x}$ . Averaging windows of  $20\lambda$  to  $40\lambda$  are used to average out the small-scale variations [7, 47].<sup>4</sup> Based on experimental evidence, the distribution of  $L(\mathbf{x})$  in many cases can be modeled by a log-normal process [14, 31, 39]. Gudmundson [31] characterizes the correlation properties of the large-scale variation in both urban and suburban areas in an unnamed, large European city. Although the correlation model is not valid in all circumstances, it is the only one available, and it is widely used. The autocorrelation function of  $L(\mathbf{x})$ , taken in decibels, is given as

$$R_L(\delta) = \sigma^2 \varepsilon_D^{|\delta|/D} \quad (2.35)$$

where  $\varepsilon_D$  represents the correlation value between two points separated by a distance  $D$ . Taking the correlation length to be the separation distance at which the normalized autocorrelation function reaches a value of 0.5, Gudmundson reports correlation lengths of around 400 m for suburban environment and around 5 m for urban environments.

### 2.3.2 Empirical Path-Loss Models

#### Okumura Model

Okumura, *et. al.*, made extensive measurements in the Tokyo area and present the results in an empirical path loss model [66]. The results characterize the propagation effects over a number of variables: frequency, antenna height at both transmitter and receiver, and terrain parameters. The results are summarized in a simple path loss equation:

$$E_{\text{mu}} = E_{\text{fs}}(d) - A_{\text{mu}}(f, d) + H_{\text{tu}}(h_{\text{te}}, d) + H_{\text{ru}}(h_{\text{re}}, f) \quad (2.36)$$

---

<sup>4</sup>See Appendix A for examples of estimating the large-scale signal variation from measurement data.

where each term is given in decibels, and the terms  $E_{\text{mu}}$  and  $E_{\text{fs}}$  are taken relative to the same reference value. Each term on the right-hand side of the equation corresponds to parametric plots of the data given in [66] taken over some number of variables.  $E_{\text{mu}}$  represents the predicted median field strength for an urban area over quasi-smooth terrain.  $E_{\text{fs}}$  is the free-space path loss at distance  $d$  from the transmitter.  $A_{\text{mu}}$  is the median attenuation relative to free space when the transmitter and receiver antenna heights are 200 m and 3 m, respectively.  $H_{\text{tu}}$  and  $H_{\text{ru}}$  are the transmit and receive antenna height gain factors relative to the standard antenna heights used for  $A_{\text{mu}}$ . Additional correction terms are given in [66] for the type of area (open, suburban, etc.) and for the street orientation. Path loss can vary by as much as 5 or 10 dB for streets with different orientation relative to the transmitter. The actual variation depends on the frequency and the distance from the transmitter.

Okumura's model characterizes measurements over a finite range of parameters. These are as follows: frequencies between 150 and 2000 MHz, base station effective antenna heights from 30 to 1000 m, and distances from 1 to 100 km. Although Okumura's curves were derived from data up to 2 GHz, extrapolation up to 3 GHz is not uncommon [75].

### Hata Model

When using Okumura's model, an engineer finds a value for each term in (2.36) from the plots in [66] based on the parameters, such as frequency, antenna heights, and terrain type, for the communication link. Unfortunately, this method does not lend itself well to computer analysis. For this reason, Hata [34] established parametric equations that fit the curves reported by Okumura. Using Hata's model, an engineer need only to plug the parameters into the empirically derived formulas.

Hata's formula is as follows [34]:

$$L_p(\text{dB}) = 69.55 + 26.16 \log_{10} f_c - 13.82 \log_{10} h_b - a(h_m) + (44.9 - 6.55 \log_{10} h_b) \log_{10} R. \quad (2.37)$$

In (2.37), the ranges of the parameters are more limited. The frequency ( $f_c$ ) is limited to 150–1500 MHz, the base station antenna height ( $h_b$ ) is limited to 30–200 m, and the distance ( $R$ ) is limited to 1–20 km. The term  $a(h_m)$  is a correction factor for the mobile station antenna height if

it is different from the baseline height of 1.5 m.

### **COST-231 Extensions**

Committee 231 of the European Cooperation in the Field of Scientific and Technical Research (EURO-COST) extends the Hata model for specific frequencies of interest (900 and 1800 MHz). A formula similar to (2.37) is given in [19] after analyzing the 1.5–2 GHz of Okumura's curves. This model, dubbed the COST-Hata model, is applicable for only cases in which the antenna heights are above the rooftops of the surrounding buildings.

The COST committee also suggests a combination of work done by Walfisch [94] and Ikegami [38] to come up with a model called COST-Walfisch-Ikegami, or COST-WI, characterizing urban environments. This model combines more detailed characteristics of the environment to estimate path loss prediction. In particular, the heights of buildings, the widths of roads, the building spacing, and the road orientation relative to the transmitter are taken into account. All of the parameters are characteristic of the entire coverage area, so the resulting model is statistical in nature. The model is based on measurements made in Stockholm, and the parameters are restricted to the following ranges: frequencies of 800–2000 MHz, base station antenna heights of 4–50 m, mobile station antenna heights of 1–3 m, and distances of 0.02–5 km.

## **2.4 Further Reading**

This chapter is intended to give the reader an overview of the challenges in modeling various aspects of electromagnetic propagation in complex environments. Since each section in this chapter covers only a brief summary of each topic, the reader is referred to the following sources for more detailed discussions: The texts by Jakes [39], Rappaport [75], and Stüber [87] are overviews that cover many topics in wireless communications. Jakes is usually the starting point for fundamentals of wireless communication, including propagation modeling. Many research topics in propagation modeling are extensions of topics covered in Jakes. Rappaport provides summaries of several propagation techniques, with pointers to sources in the literature for further study. Stüber focuses on the performance of digital modulation schemes in mobile wireless environments, with an emphasis on mathematical analysis. The 1991 report by the COST-231 Committee [19], in addition

to providing the Hata and Walfisch-Ikegami extensions, provides a rather complete survey of approaches to propagation modeling in urban environments. Bertoni [12] explores theoretical models specifically for communication in environments with buildings and/or trees. His book provides an overview of the ray and diffraction theories used in ray-tracing in complex environments.

In addition to the previous texts on mobile wireless communication, the following electromagnetics and communications texts provide fundamental background information: Ramo, *et. al.* [73], covers radiation and reflection as derived from the basic principles of Maxwell's equations. A handbook by Bell Laboratories [9] gives a systems engineering approach for designing reliable point-to-point microwave links for telecommunications. Pozar [72] focuses primarily on microwave systems and circuit design. His book has an overview chapter on antenna design and radiation as they pertain to microwave systems.

## **Chapter 3**

# **Experiment Configuration**

### **3.1 Experiment Objectives**

The objective of this work is to study radio wave propagation in built-up urban environments. Specifically of interest are the corner effect and repeatability of the signal propagation. The corner effect describes the rate and extent of the change in signal power as a mobile receiver turns a corner in an urban area. The repeatability study characterizes the similarities in the signal strengths as a mobile receiver repeats measurements at given locations within a street. Together, these studies constrain how well the receiver location must be estimated relative to the city structure. Our method of collecting signal strength measurements with an accurate position estimate is part of what makes this work unique. This chapter outlines the design and configuration of the experiment and how it meets the research objectives.

Urban areas are of commercial interest because of the large number of users that need wireless services there. For the experimentalist, unfortunately, the activities that take place in cities also make it especially difficult to design a well-controlled experiment. Access to buildings and resources required for transmitting test signals can be especially difficult. For this reason, the equipment needed for this experiment is designed to be self-contained; the measurement apparatus is completely contained in a vehicle that can be driven through the city. By focusing only on the receiving end, we rely on existing transmitters to generate the signals we measure.

Control channel signals from active cellular base stations are transmitted continuously at constant power levels, providing beacons that can be characterized throughout the coverage area.

AT&T Wireless has provided base station locations, center frequencies, and antenna height and orientation for cell sites in the San Francisco financial district, an area classified as a dense, urban environment.

The AT&T base stations operate in the 800 MHz band and follow the EIA/TIA-136 standard [91], also known as North American Digital Cellular. As required by the Federal Communications Commission (FCC), cellular operators in this frequency band must maintain backward compatibility with the Advanced Mobile Phone System (AMPS), the original analog cellular standard used in the U.S. To comply with this FCC mandate, EIA/TIA-136 specifies two sets of control channels: one for digital traffic channels and one for analog traffic channels. The Forward Analog Control Channel (FOCC<sup>1</sup>) is the downlink control channel for handsets using analog traffic channels. The FOCC is digitally modulated using frequency-shift keying (FSK).

The base station control channels bear modulating signals that are used to convey system information and instructions to mobile handsets in the coverage area. We choose to monitor the FOCC since the control channels are reassigned to different base stations much less often than the digital control channels in AT&T's network. Since we are interested in the signal variation imposed by the multipath environment itself, independent of any modulating signal, the modulation of FOCC is removed prior to making signal strength measurements.

The functional diagram for the equipment used in this experiment is shown in Fig. 3.1, and the vehicle configuration is shown in Fig. 3.2. A spectrum analyzer operating in zero-span mode is used as a tunable filter. The center frequency is tuned to the control channel and the resolution bandwidth is set to 10 kHz, which is narrower than the channel bandwidth of 30 kHz to remove the data modulation. The output of the spectrum analyzer is sampled and stored on a laptop computer. Additional baseband filtering is performed to remove any residual modulation components. To verify that the same base station is being monitored throughout the coverage area, the received signal is split off (before the spectrum analyzer) to an FM receiver, which is used to decode and verify the base station's system identification (SID) and digital color code (DCC).

The spectrum analyzer is connected to a roof-mounted antenna and is placed inside a 1992 Chevrolet Cavalier to move through the coverage area. The antenna is a quarter-wave magnetic mount antenna with a gain pattern that is approximately omnidirectional. Since the antenna sits on

---

<sup>1</sup>Logically, it would seem that the proper abbreviation would be FACC, but the standard consistently uses FOCC for this channel. This 'o' comes from the second letter in the word 'forward' which follows the convention used for the Reverse Analog Control Channel, RECC.

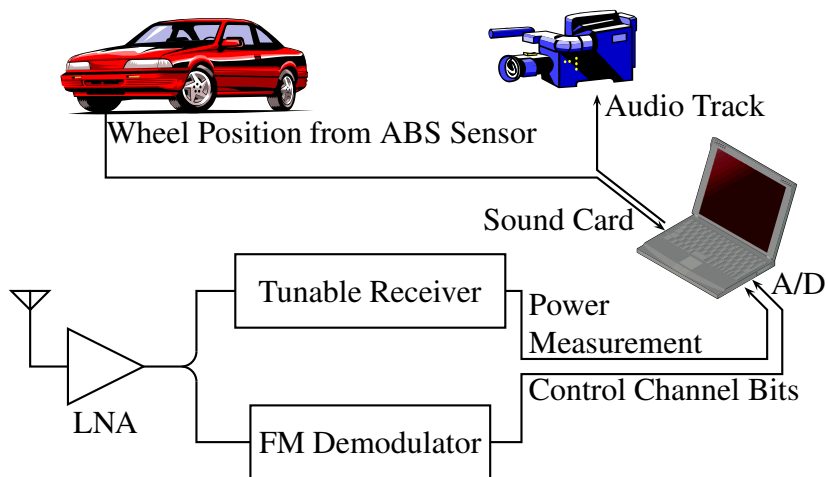


Figure 3.1: Measurement Hardware Overview. The laptop synchronizes the recording of individual data streams for offline data reduction.

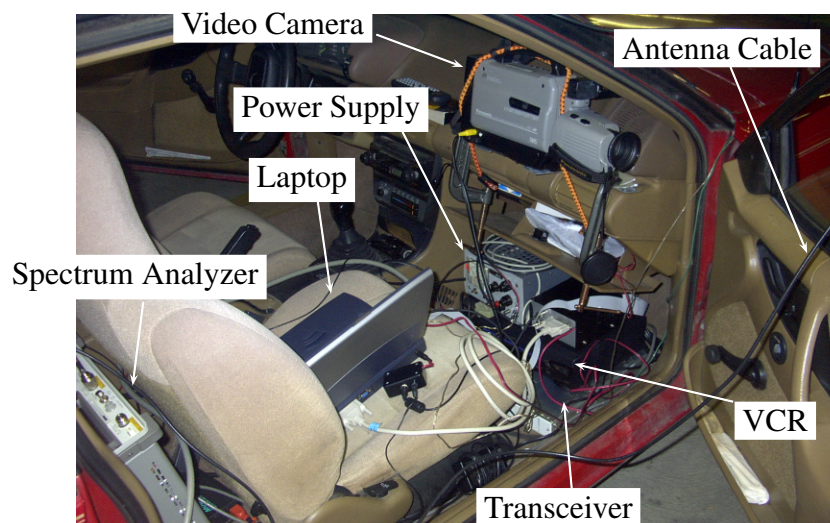


Figure 3.2: Vehicle Configuration. This figure shows the placement of the measurement equipment inside the vehicle.



an irregular ground plane, however, the pattern is not perfectly uniform. Due to the random nature of the arriving multipath components, the precise antenna pattern is not considered in this work.

The laptop computer also stores samples of the car's anti-lock braking system (ABS) sensor. This sensor generates a pulse approximately every 4 cm of travel, providing a drive path distance measurement. The pulse distance is calibrated over drive paths of known distances in parking lots around the Packard Electrical Engineering building at Stanford University. The distance measurement, however, does not give any indication of the vehicle's location relative to buildings and street corners in the coverage area. For this reason, a video camera is mounted perpendicular to the direction of travel and indicates the receiver's location relative to buildings along the drive route. Using the video record of each drive down a street, multiple runs are compared by aligning the locations of the buildings along the route for each measurement run. Using the video transcript provides a systematic way of aligning two signal traces without having to adjust the relative distance offsets by manually aligning features in the two signal traces. The video camera and the samples from the spectrum analyzer and the ABS sensor are synchronized to the laptop's system clock, providing a method to match signal strength to receiver location during offline processing of the data. Because of possible signal delays in the video processing equipment, a flashing LED is used to calibrate the video delay.

## 3.2 Signal Strength Measurement

The spectrum analyzer is used to make the fundamental signal strength measurement for this experiment. To understand how the measurement is taken, a brief overview of the operation of the spectrum analyzer as a receiver is useful.

A simplified block diagram of the spectrum analyzer is shown in Fig. 3.3. The spectrum analyzer uses the heterodyning principle of downconverting the frequency of a signal before taking its measurement. The spectrum analyzer used in this experiment is the HP 8595E, which performs at least two frequency conversions. Fig. 3.3 represents the last frequency-conversion stage.

The input filter to this stage rejects the image frequencies inherent to the heterodyning process. The scan generator provides the control voltage that sweeps the oscillator over a frequency range such that the desired measurement band will at different times be converted to baseband. Following the mixing process is a logarithmic amplifier that provides sensitivity over a very broad dynamic

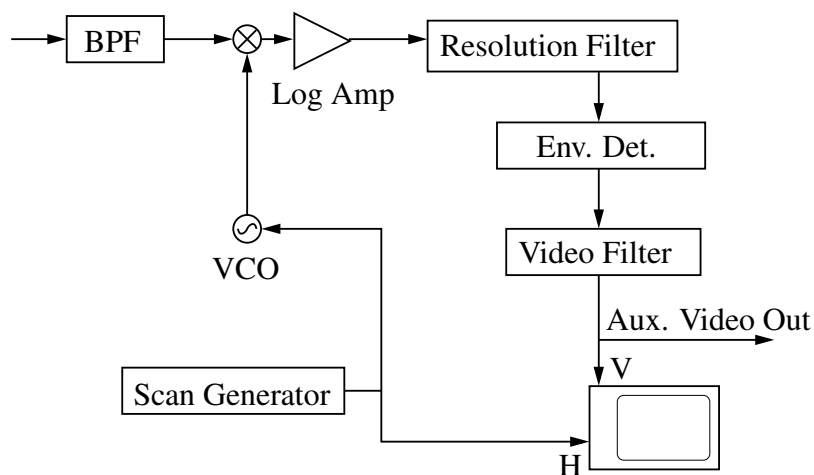


Figure 3.3: Spectrum Analyzer Block Diagram. The spectrum analyzer uses the heterodyning principle to convert the measured signal to baseband. Filtering and envelope detection yield a voltage representing the signal strength. Used together with the control voltage on the oscillator, the detected signal gives power versus frequency on the display.

range of power levels. The resolution filter captures only the frequencies of interest before passing them on to the envelope detector, which determines the received signal power level. Finally, a video filter is available to clean up any noisy signals for easier viewing on the scope display. Older spectrum analyzers use the oscillator control voltage to control the horizontal deflection of a cathode ray tube (CRT) while the signal strength controls the vertical deflection, giving a signal strength versus frequency trace on the display. Modern machines, however, digitize the horizontal and vertical signals and display the results digitally.

When operating in zero-span mode, the scan generator holds a constant control voltage on the voltage-controlled oscillator (VCO), locking it to a single frequency. In this sense, the spectrum analyzer acts as a tunable filter since only a single frequency is downconverted. The resolution filter is then used to select the bandwidth of the channel monitored.

The video filter has the same minimum cutoff frequency as the resolution filter in the HP 8595E. As a result, at the 10 kHz cutoff frequency, the video filter passes the same signals that the resolution filter does. The auxiliary video output then gives a direct reading of the signal strength as indicated at the output of the envelope detector. This voltage level representing the signal strength is available on the auxiliary video output port of the HP 8595E and is sampled by the A/D converter card in the laptop to provide continuous monitoring of the signal strength.

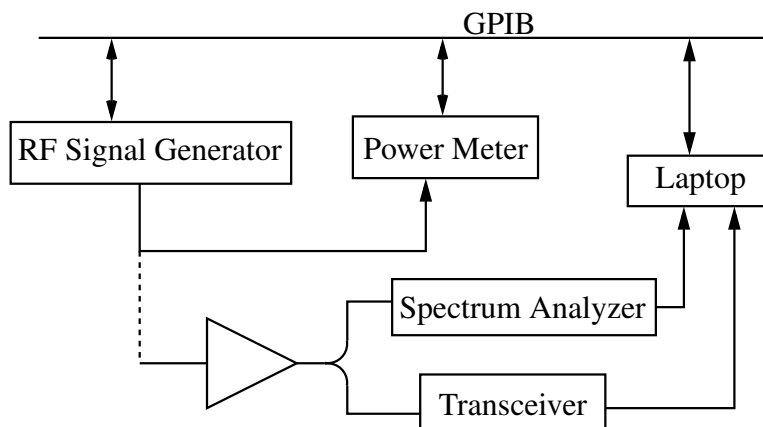


Figure 3.4: Spectrum Analyzer Calibration Setup. The RF signal generator is calibrated against a power meter. The signal generator is re-cabled to the input of the LNA so that the entire receiver chain is calibrated.

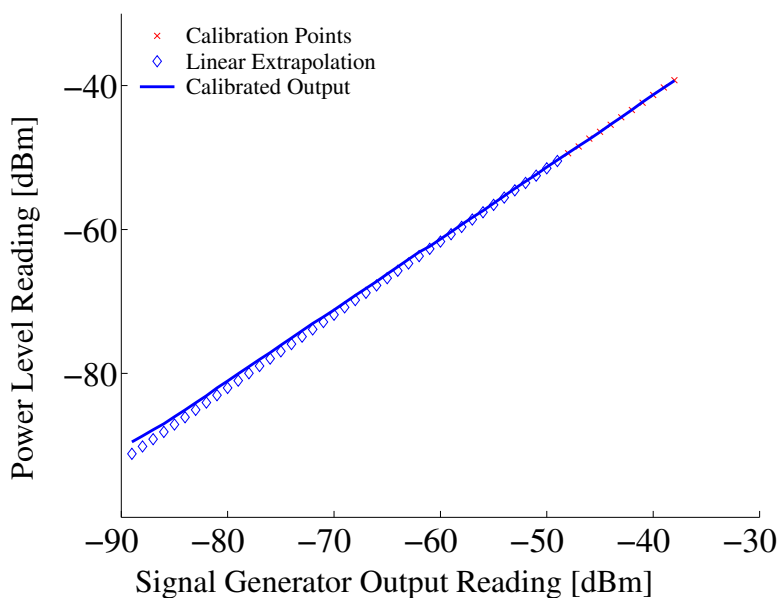


Figure 3.5: Spectrum Analyzer Calibration Curve. Since the power meter has a limited dynamic range due to its bandwidth, this curve shows that the extrapolation of calibration curve is valid to within 1 dB over the dynamic range of the spectrum analyzer.

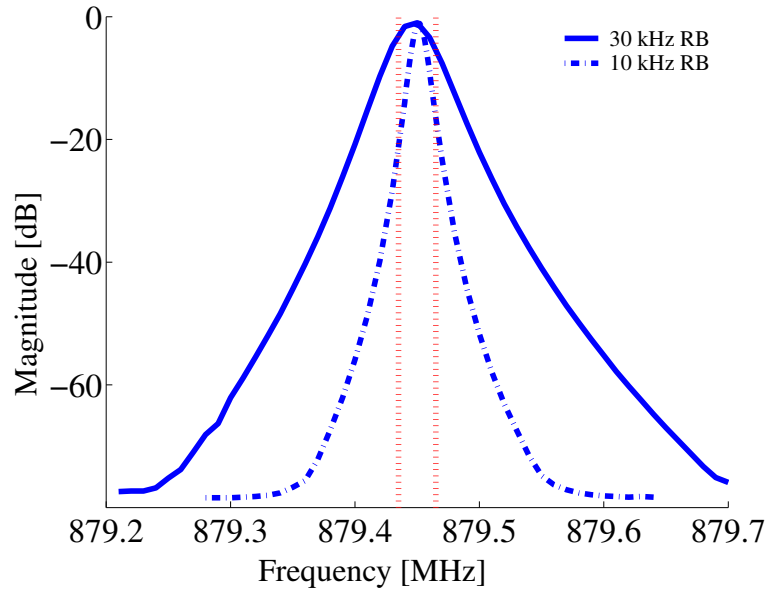


Figure 3.6: Spectrum Analyzer Resolution Bandwidth Filter Response. The 10 kHz filter acts as a better channel selection filter for the control channel, which has a bandwidth indicated by the vertical lines on this plot.

The voltage level is calibrated as shown in Fig. 3.4.<sup>2</sup> The signal strength is calibrated at the input to the preamplifier. The calibrated signal measurements therefore represent the power received at the antenna. The calibration procedure uses an RF signal generator as well as a power meter. The laptop controls the calibration sequence through the General Purpose Instrumentation Bus (GPIB), also known as the HP Instrumentation Bus. Initially, the power output of the RF signal generator is calibrated against the power meter. The power meter has a 400 MHz bandwidth and can only be reliably used down to -50 dBm. The RF signal generator can step all the way down to -90 dBm. The calibration is performed against the power meter for only the linear section above -50 dBm. The power meter is disconnected and the signal generator is then connected to the input of the preamplifier. The signal generator subsequently steps through the entire range. In Fig. 3.5, one can see that the linear extrapolation from the power meter calibration remains within 1 dB of the measured output for the entire 50 dB dynamic range.

Using the spectrum analyzer as a receiver, the resolution filter acts as the channel selection filter. The smallest bandwidth that the HP 8595E can use for the resolution filter is 10 kHz. The

<sup>2</sup>It should be noted that for the 2002 measurement campaign, the base station transceiver was not used, but the rest of the spectrum analyzer calibration remains the same.

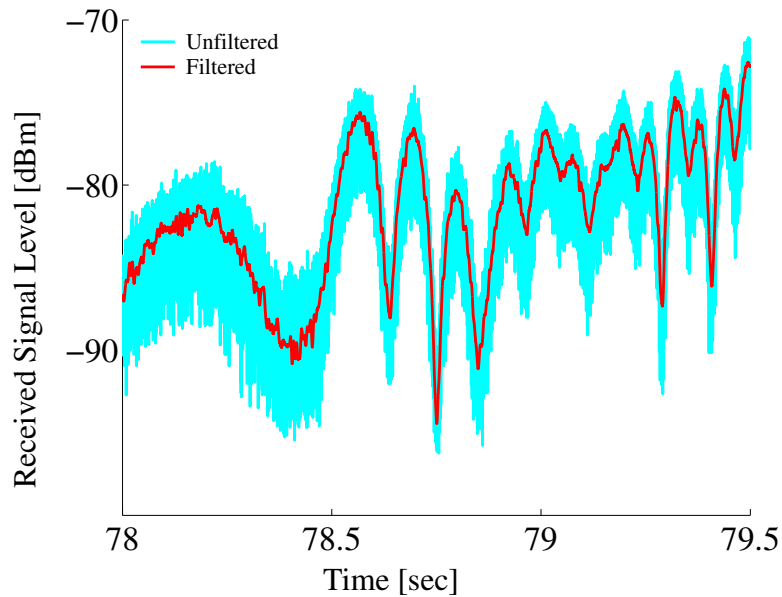


Figure 3.7: Example of Baseband Filtering. The 10 kHz channel selection filter does not completely remove the modulation from the signal as indicated by the unfiltered version of the signal in this plot.

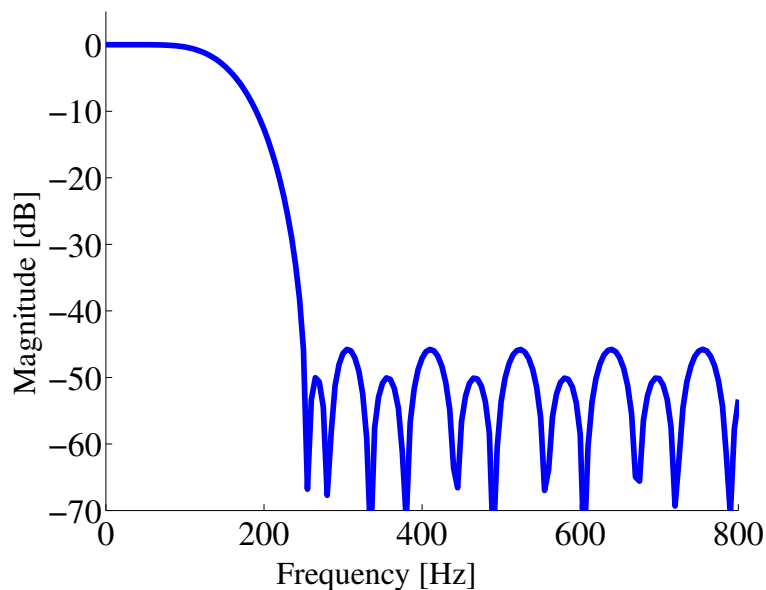


Figure 3.8: Digital Filter Response. This figure shows the frequency response of the baseband digital filter. The cutoff frequency is just wide enough to pass the highest-frequency Doppler components, but it is low enough to remove the residual modulation on the received signal.

filter response is shown in Fig. 3.6. The 10 kHz bandwidth is adequate for channel selection, but it does not remove the data modulation completely from the carrier. The residual modulation is seen in the thick trace of the unfiltered signal in Fig. 3.7. Additional baseband filtering is performed to remove the residual modulation components. Since the raw data is stored on the laptop computer, the filtering of the baseband signal is performed offline.

The frequency response of the baseband filter is shown in Fig. 3.8. The passband of the filter is 100 Hz, and the rejection band is everything above 250 Hz. The 100 Hz cutoff frequency is chosen to allow the time variations from the entire Doppler spectrum to pass through the filter. The maximum Doppler shift is given by  $f_m = \frac{v}{c}f_c$  where  $v$  is the vehicle speed,  $c$  is the speed of light, and  $f_c$  is the carrier frequency of the signal. For the downlink frequency of 880 MHz, a Doppler frequency of 100 Hz corresponds to a maximum speed of 76 miles per hour (122 km/hr), which is certainly faster than one can drive through the financial district. The result of the baseband filtering is seen in the dark trace in Fig. 3.7.

### 3.3 Data Reduction Methods

All of the measurements that are collected are time-based. The study of radio wave propagation, however, requires the use of signal strength versus position within the environment. This section outlines the steps necessary to put the measurements in a distance-based format that can be used to compare measurements made in multiple runs down a street.

#### 3.3.1 Corner Identification

The alignment of the camera used in this setup is not precise. Although it is close, the boresight of the camera does not line up exactly perpendicular to the direction of travel. In order to tell when the corner of a building has passed a particular point relative to the receiver, the perpendicular direction must be identified within the video display. A customized video processing tool designed for this project is used to annotate features in the video transcript.

The perpendicular direction is identified by marking items within the video display that are in fact perpendicular to the direction of travel using the video processing tool. These markings are lines entered manually that most often follow the curb or the painted markings in a side street.

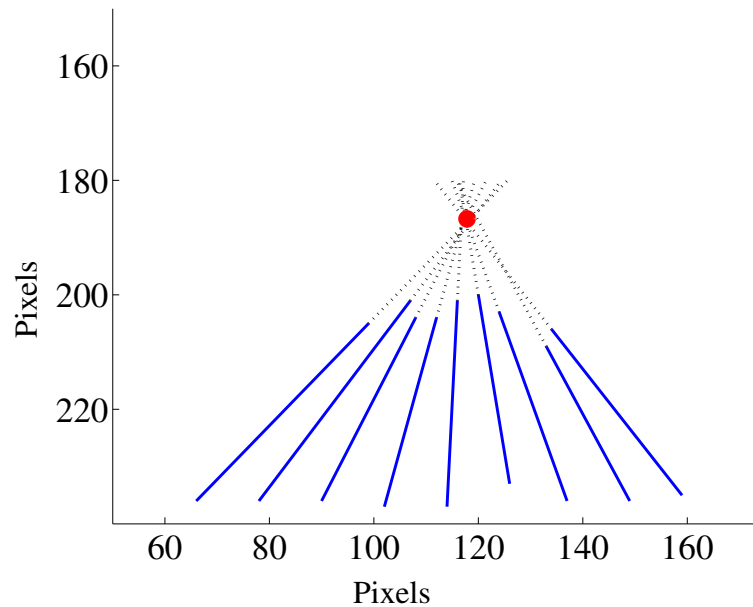


Figure 3.9: Adjusting for Boresight Offset. Over a sequence of video frames, extensions of line segments, marking a tracked object perpendicular to the camera motion, converge to a point on the horizon.

Over a sequence of frames, these lines converge to a single point as shown in Fig. 3.9. This point is taken to be the perpendicular direction in the horizontal plane of travel.

Again using the video processing tool, the edge of a building is used to mark the corner. The marked building edges rise up vertically and are perpendicular to the ground. A sequence of these markings is shown in Fig. 3.10. Since the camera is not perfectly aligned, the markings are not perfectly vertical on the display. Furthermore, the markers are noisy estimates of the building position since the image is sometimes blurry. The horizontal trajectory must therefore be estimated as being perpendicular, on average, to all the lines and must run through the center of gravity of all the markers.

Since the actual distance traveled between each video frame is available from the ABS sensor, the corner markers are adjusted, in the least-squares sense, to points along the trajectory that are proportional to the distance traveled in each frame. This adjustment compensates for inaccuracies in marking the corner by hand. The horizontal convergence point is then projected onto the estimated trajectory to identify where the corner lies along the path. The resulting distance is linearly interpolated using the corrected markers between which it falls.

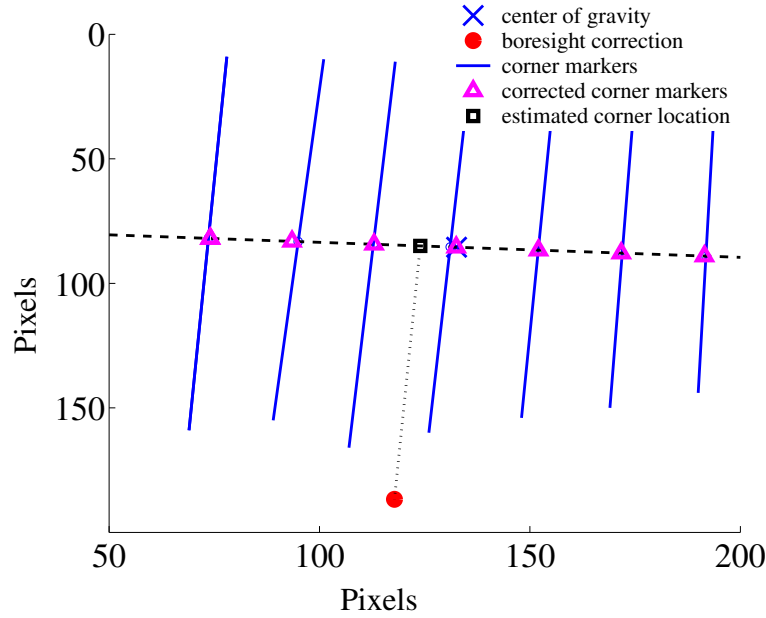


Figure 3.10: Finding the Corner Location. The corner of a building is tracked over a sequence of video frames. Corrections are made for the camera orientation and estimation errors in the corner markers to derive the position of the corner relative to the motion of the camera.

### 3.3.2 Distance Axis Linearization

During the post-processing phase, a distance value is assigned to each measurement sample using the common system time reference to interpolate each sample between distance pulses from the ABS sensor. This distance measurement, however, cannot be used for analysis since the distance between measurement points depends on vehicle speed. In fact, in places where the vehicle is slowed or stopped, there are many more points than in places where the vehicle is moving faster. This unequal spacing gives an unfair weighting to the measurements where the vehicle either slowed down or stopped. To correct for unequal weighting, the distance axis is linearized.

The objective of the linearization procedure is to correct the distance axis without losing any of the small-scale fading information. To meet this objective, the step size of each distance sample is made as small as possible. The entire distance axis is broken up into segments 1/20th the size of a single distance pulse from the ABS sensor. This distance turns out to be approximately 2 mm. All data points falling within each such segment are averaged together to form a single point. Since the signal strength measurements are taken at 10 kHz, this segment size limits the vehicle speed to



approximately 45 miles per hour (72 km/hr) without skipping segments.

An example of a resulting distance axis linearization is seen in Fig. 3.11. The plot shows the same set of measurements. In Fig. 3.11(a), the vehicle comes to a stop at around 52 seconds and remains stopped until about 76 seconds. After the distance axis is linearized (Fig. 3.11(b)), one can see that the samples where the vehicle is stopped have been collapsed into a single point while the variations occurring where the vehicle is moving are stretched accordingly.

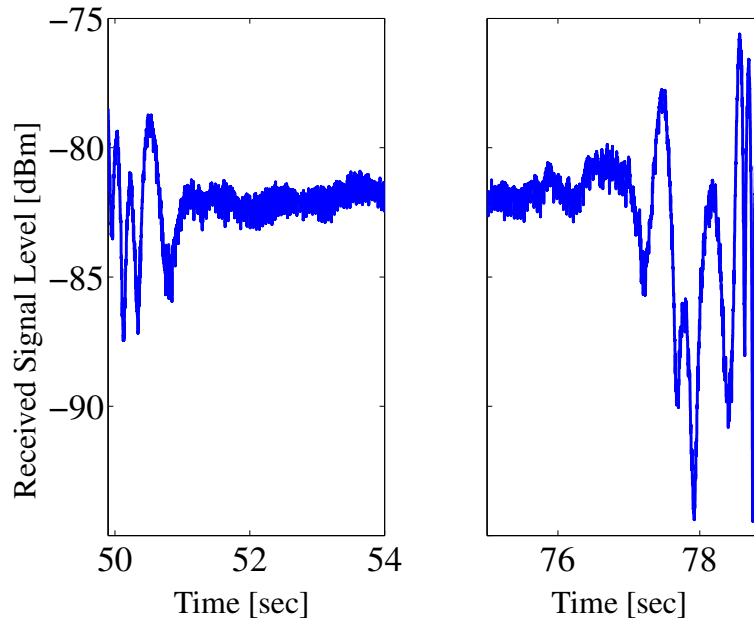
### 3.3.3 Aligning Multiple Runs for Comparison

Another important part of the work in this report is comparing one measurement run against another in the same street. Aligning a single corner on two separate runs is not sufficient since small deviations in the vehicle's path cause distance errors to accumulate as one moves away from the aligned corner. Furthermore, traffic or people in the streets may obscure one specific corner on a particular run. The alignment procedure must take into account these factors in order to make a meaningful comparison.

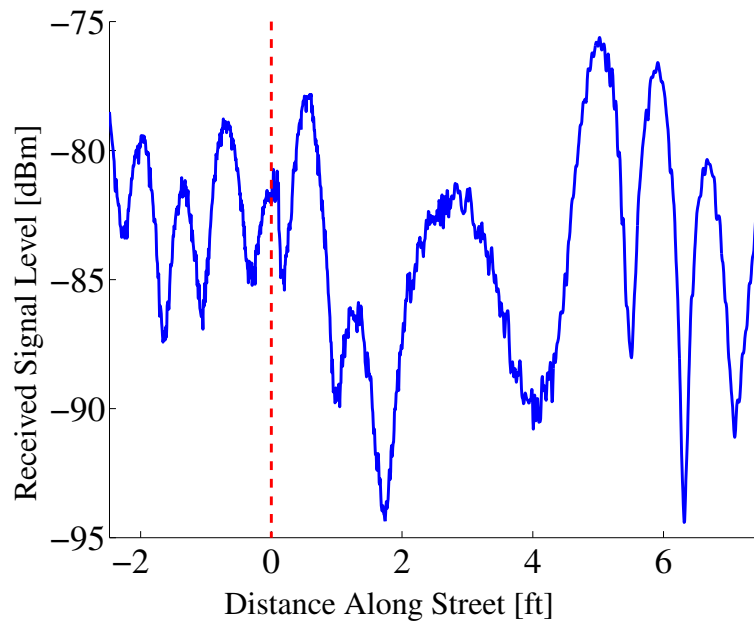
The first step in the alignment procedure is to jointly estimate the distances between all marked corners. After the corners are aligned, the locations of all the intervening samples are interpolated so that the endpoints match. For example, Fig. 3.12 shows two separate runs in which one of the runs is missing location information for one of the corners. The aligned distances between the corners are taken as the least-squares solution to the following matrix equation:

$$\begin{bmatrix} 1 & 0 & 0 \\ 0 & 1 & 0 \\ 0 & 0 & 1 \\ 1 & 1 & 0 \\ 0 & 0 & 1 \end{bmatrix} \begin{bmatrix} w_1 \\ w_2 \\ w_3 \end{bmatrix} = \begin{bmatrix} m_1 \\ m_2 \\ m_3 \\ m_4 \\ m_5 \end{bmatrix}. \quad (3.1)$$

The first marker is then defined to be the origin of the distance axis. Then, for each run, the location of each sample is interpolated so that the endpoints match the least-squares solution. In this example, on run number two the sample locations between marker 1 and marker 3 are interpolated so that the third marker occurs at  $w_1 + w_2$ , as shown in the fourth row of the matrix in (3.1).



(a)



(b)

Figure 3.11: Example of a Stopped Vehicle. This figure demonstrates how the distance axis of the raw data is linearized. Both subfigures show the same measurement on (a) a time scale and (b) a distance scale. The vertical line in (b) shows the location where the vehicle stopped, indicated by the time span in (a) in which the signal strength does not fluctuate.

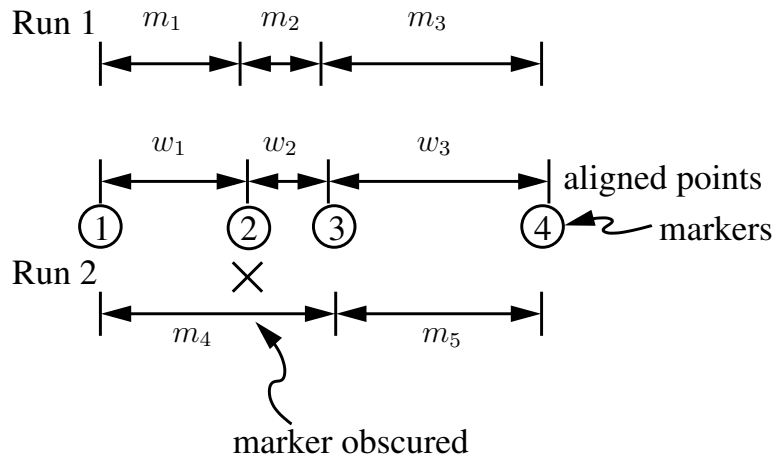


Figure 3.12: Alignment for Multiple Measurement Runs. This figure illustrates how the distances for two measurement runs are aligned. The values  $w_1, w_2, w_3$  represent the true distances between the markers, and the values  $m_1, \dots, m_5$  represent the measured distances between markers on the two measurement runs. The least squares solution to (3.1) is used to find  $m_1, \dots, m_5$ .

### 3.4 Summary

To meet the experiment's objectives, the measurement hardware is designed to be mobile and self-contained. Placing the measurement equipment in a car and driving it through the measurement area meet these requirements. Through the use of a video camera and a modified base station transceiver, the measurements are processed offline to give signal strength versus position within a street and relative to building corners. Further details regarding the hardware and software configuration for the experiment are found in Appendix A. The equipment and data reduction methods outlined in this chapter set the stage for the analysis performed throughout the remainder of this report.

## Chapter 4

### The Corner Effect

Propagation in a multipath environment is characterized by large, rapid fluctuations in the received signal strength. Several techniques have been introduced to mitigate the effects of these large fluctuations in signal strength. Coding and interleaving the bits that are transmitted in a data frame can alleviate some of the problems encountered by bursty bit errors that occur during a deep signal fade. Diversity techniques use different observations of the same signal and combine the results to obtain a composite signal that is of better quality than any of the constituent signals. The different observation may take place in space, time, or frequency.

These mitigation techniques inherently depend on the stationarity of the received signal. Interleaving works because only portions of a data frame may be in error. The technique depends on the fact that the signal is likely to experience a deep fade for only a short time. After a mobile user turns a corner in a dense urban area, however, the signal may not increase significantly after the initial fade. This phenomenon has come to be known as the “corner effect.” Not only does the corner effect impact the effectiveness of fading mitigation techniques, but there are deeper system issues involved as well. Since much of the control of mobile wireless systems is conditioned on the signal quality of each link, the rate of change in the signal quality determines how rapidly the system must respond before the link quality deteriorates and the call is dropped.

The signal quality of each communication link is the primary parameter by which the system adjusts its resources. Typically, the signal-to-interference-and-noise ratio (SINR) is a signal quality measure used by the system to make resource allocation decisions. Sudden changes to the communication link’s signal quality, *i.e.*, sudden changes in either the desired signal or an interfering signal, therefore have a direct impact on overall system performance.

For example, a call with poor signal quality may be handed over to a neighboring base station that can provide a better link. If the signal quality is below an acceptable threshold and communication can no longer be maintained on the link, this handover is imperative. By allowing a user to remain on a channel with unacceptable quality, the system keeps the resource from other users for whom the link quality may be acceptable. An upper bound on the time that the signal quality may remain below this acceptable threshold is usually established to prevent these calls from draining all the system's resources. If the system is unable to hand the call over to a neighboring base station in the acceptable amount of the time, then the call must be dropped. Service providers are particularly interested in the corner effect since the sudden drop in signal quality at street corners can lead to dropped calls, which are a primary cause for customer dissatisfaction.

In addition to handover and forced call termination (dropping), signal quality is used as a basis for other system policies as well. Call admission policies require that a link must achieve a minimum signal quality before a requested call may be serviced by the system [52]. Furthermore, next-generation systems propose using signal quality histories to assist in making more informed, and therefore more efficient, resource allocation decisions. For example, pattern recognition techniques have been proposed by Wong [101] and Narasimhan [63] to improve handoff performance. Under these proposals, patterns in the large-scale signal variation are used to determine a mobile user's location relative to a resource allocation event, in this case, a handoff. The pattern classifiers proposed in [101] and [63] require spatial distances of up to 30 or 40 wavelengths to converge to a pattern match. Because of this long convergence time, abrupt changes in the signal strength may necessitate a handoff decision before the pattern classifier converges.

Two important characteristics of the corner effect are the *rate* and *extent* of the signal change at the corner. Keeping in mind that propagation characteristics are a spatial phenomenon, the *rate* describes the amount the signal strength changes over a specified distance. The *extent* of the signal change at a corner is the difference between the received signal strength just before and just after turning a corner. The extent of the signal strength change has been extensively studied. Because many previous studies were primarily interested in determining cell coverage areas, the rate of signal strength change at street corners has been largely overlooked.

## 4.1 Previous Work

Urban cell sites are usually categorized into two types: *macrocells* and *microcells*. When cellular systems were first implemented, service providers wanted to achieve the widest possible coverage area. As a result, many of the first cell towers deployed in urban areas were on top of tall buildings. As the subscriber base increased, however, system capacity became more of a concern. To handle the influx of new users, new cell sites were designed for smaller and smaller coverage areas. To distinguish between the two cases, the term *macrocell* commonly refers to cells in which the antennas are above rooftops of the surrounding buildings, while the term *microcell* typically refers to cell sites in which the antennas are much closer to street level and certainly below the rooftops of surrounding buildings.

Due to the increased interest in smaller cell sizes, many measurements have been made to characterize urban microcells. Many microcell studies conducted at 800 and 900 MHz document signal level changes of 15–25 dB after turning corners in urban areas [24,25,42,51,93,96]. At 2 and 6 GHz, corner attenuation values of 10–40 dB are reported [26,57]. Even in a typical macrocell, changes in signal level of 10 dB are noted [14]. While these studies all suggest that the corner effect is typical in urban areas, none of them analyze the *rate* of the signal change at the corners. One reason the rate is not discussed is that the large-scale variations are typically analyzed after the small-scale fading has been averaged out. The fixed-length averaging windows are usually long enough to mask the rate of change at the corners. Also, the accurate distance measurement needed is often not available in typical experiments.

Researchers conducting simulation studies using ray-tracing models [11,20,21,24,26,33,38,40,42,64,80,90] and waveguide models [44,69–71] seek to understand the mechanisms by which the signals propagate through streets and around buildings. The aim of these simulations is to predict the first-order propagation effects, and the results of these simulations are typically averaged to make a comparison to the local average received power obtained by measurements. The impact of averaging the local received signal power, as discussed in this chapter, therefore has application to both measurements and to simulation results. The purpose of this chapter is to identify and to describe those features of the corner effect that are important to system design.

## 4.2 Local Average Received Signal Power

The idea of a local average received signal power is based on the ability to separate the large- and small-scale variations in the received signal when certain conditions are met. The correlation length of the large-scale variation (also called slow fading) is typically related to the dimensions of buildings or other large objects in the propagation environment. The correlation length of the small-scale (or fast) fading, on the other hand, depends on the wavelength of the carrier signal [39, Ch. 1]. At cellular frequencies, the correlation distance of the small-scale fading is much shorter than that of the large-scale fading. Because of this difference in magnitudes of the correlation lengths, the large-scale fading is estimated by averaging out the small-scale fading. By keeping the averaging interval much shorter than the correlation length of the large-scale fading process, the value of the large-scale fading process remains approximately constant and is the average value of the small-scale fading process in that interval. This analysis holds as long as there are no abrupt changes in the average received signal level. At street corners in urban areas, however, there are indeed abrupt changes in the signal strength, and a different averaging strategy must be adopted.

### 4.2.1 Sampling and Averaging the Received Signal Power

Since signal strength varies as a function of position, spatial averaging is used to estimate the large-scale fading. The local average received power is obtained as

$$P_{\text{ave}}(x) = \langle P(x) \rangle_W = \int_{-\infty}^{\infty} a_W(\xi - x) P(\xi) d\xi \quad (4.1)$$

where  $W$  is the length of the averaging interval,  $P(x)$  is the received power at position  $x$ , and  $a_W(x)$  is the averaging kernel. The averaging function  $a_W(x)$  is centered about the origin and has the constraint

$$\int_{-\infty}^{\infty} a_W(x) dx = 1. \quad (4.2)$$

The averaging function may weight the current signal strength value more heavily than others, as is the case of the triangle function used by Goldsmith [30]. A rectangular averaging function is the

most commonly used averaging function [7, 47]:

$$a_W(x) = \begin{cases} 1/W & -W/2 \leq x \leq W/2 \\ 0 & \text{otherwise.} \end{cases} \quad (4.3)$$

This function is used throughout the remainder of this report.

The choice of the averaging interval  $W$  is also very important. If  $W$  is too small, then not enough of the small-scale fading is averaged out. If  $W$  is too large, however, the variations in the large-scale fading will be averaged out as well. To determine an appropriate averaging interval, it is useful to consider ideal propagation models to characterize the accuracy of different averaging methods.

Lee [47] considers a multipath environment in which signals following several independent paths give rise to a Rayleigh-distributed signal envelope. He solves for a confidence interval using the Rayleigh distribution to find that at least 36 independent samples are required to have an estimate that is within 1 dB of the true value with a 90% confidence level. The autocorrelation of the received signal determines how far apart the samples must be to be considered independent. Because independent samples are assumed, a minimum sampling distance is established based on the decorrelation distance of the small-scale fading process using both theory ( $0.5\lambda$ ) and measurements ( $0.8\lambda$ ) [47]. The basic conclusion from Lee's analysis is that the averaging window should be between  $20$  and  $40\lambda$ .

Austin and Stüber [7] follow Lee's analysis to determine what changes in averaging strategy, if any, must be made if the underlying scattering model is changed. To determine the proper averaging window for the received signal power in a Ricean fading environment, they compute the variance of averages of a Ricean distributed random variable when the averaging interval is changed. They find that not only does the variance of the estimate depend on the length of the averaging window, but it also depends on the angle of arrival and the Rice factor  $K$  of the line of sight (LOS) component.<sup>1</sup> It is determined in [7] that the variance is significantly reduced in most cases when the averaging window is  $20\lambda$  or greater. Taking averages over intervals longer than this in most cases yields diminishing returns.

The effect of the inter-sample spacing also is evaluated in [7]. By observing the variance of

---

<sup>1</sup>The Rice factor  $K$  is the ratio of received power from the specular (LOS) component to the received power of the scattered components, *i.e.*,  $K = s^2/2\sigma^2$ . See Chapter 2 for more details.



the estimates as the sampling interval of the Ricean process is varied, a jump in the variance of the estimate is noted at sample spacings of  $\lambda/2$  and at other distances where there are nulls in the autocovariance function of the square of the envelope. For this reason, Austin and Stüber recommend inter-sample spacing of less than  $0.5\lambda$ .

Parsons [67, Ch. 8] also analyzes signals with Rayleigh-distributed envelopes. In his analysis, however, he uses the averaged received signal *power*, rather the *envelope*, as done in [47]. The analysis also includes results for both linear and logarithmic averaging. The linear average requires 57 independent samples, while the logarithmic average requires 85 independent samples for the standard deviation of the estimator error to be less than 1 dB. Erceg, *et. al.*, use this analysis for measurement data in [24]. Although the theory suggests a minimum averaging window of  $22\lambda$ , Erceg, *et. al.*, indicate that  $66\lambda$  is a more appropriate averaging window for their data. This discrepancy may be due to differences in angle-of-arrival distributions, which are not known.

These spatial averaging windows must be translated to a time window for signal processing that is done in the time domain. The window length must be adjusted according to the speed of the mobile user. This constraint is recognized in [7, 37, 60, 61, 63].

Key contributions in this research area are made by Narasimhan [60, 61, 63]. In [60], the averaging window is determined from the expected spacing of the nulls in the received signal envelope generated by a 2-D isotropic scattering model. The nulls are detected through wavelet analysis, and the averaging window is adjusted based on the null detection rate, which is known for ideal isotropic scattering. The wavelet method in [60] depends on *a priori* knowledge of the scattering environment. This restriction is circumvented in [61] when best-basis methods of statistical analysis are used on the received signal. In [63], the best-basis method is applied to the corner detection problem, which is difficult since the sudden loss of signal strength at a corner may initially be indistinguishable from a deep null caused by the small-scale fading.

### 4.2.2 Adjusting to Transients

The responsiveness of the averaging filter to changes in the local power is limited by the width of the averaging window. Longer windows lead to filters that are slower to respond to abrupt changes in signal strength. This slow response is the desired behavior when the filter is responding to the fluctuations of the small-scale fading. The abrupt change in signal strength at a corner is sometimes

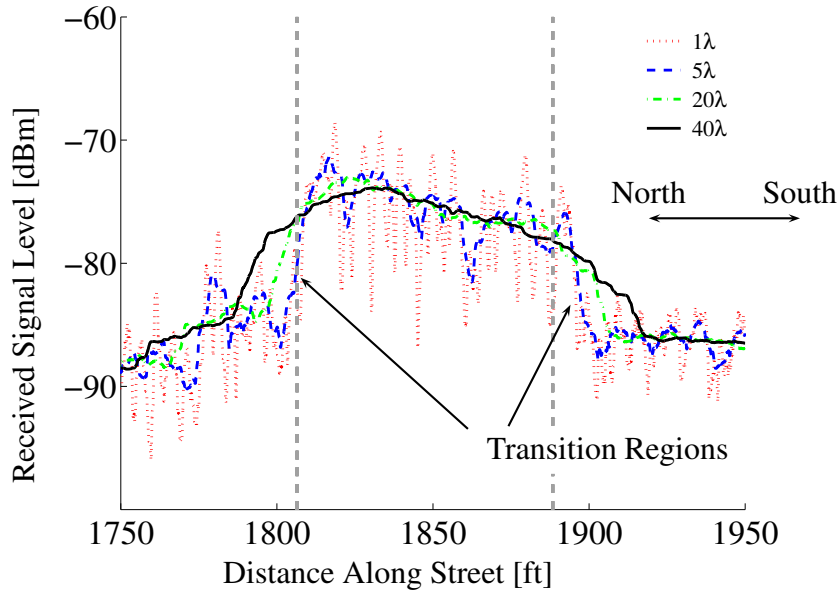


Figure 4.1: Transition Regions for Montgomery at California. The averages using longer spatial windows agree in the low-rate areas, but the results for shorter windows agree in the high-rate areas.

very similar to the sudden signal drop in a multipath fade. The difference, however, is that a signal that is in a deep fade will return to a stronger value after a short distance. This does not happen for signal changes at street corners.

This effect is seen in the corner transition regions at the edges of the street intersection depicted in Fig. 4.1. This figure is an overlay plot of the same signal strength profile averaged with sliding window averages having different window lengths.

In the regions where the local average changes slowly, *i.e.*, the flatter, low-rate regions, the results of the longer window averages converge to the same trend. In the regions near the edges of the intersection where the signal strength abruptly changes, however, the shorter window averages converge to a steeper, higher-rate trend. This disparity strongly suggests that near the edges of intersections, a shorter window should be used for averaging. In other regions, however, a longer window should be used.

A piecewise linear fit of the local average received power is shown in Fig. 4.2. Each segment is fit to the signal average with the window that is most appropriate for a particular region. The

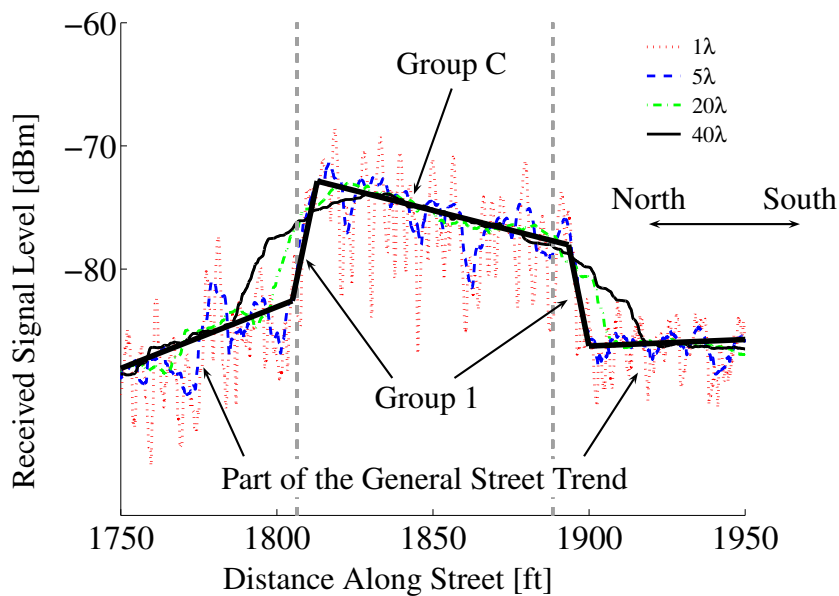


Figure 4.2: Piecewise Linear Fit for Montgomery at California. The local average power is determined by fitting linear segments to sliding window averages using shorter windows in the transition regions and longer windows in the center of the intersection and along the general street trend. Group 1 segments identify the first transition at the edge of the intersection. Group C identifies segments that are located in the center of the intersection.

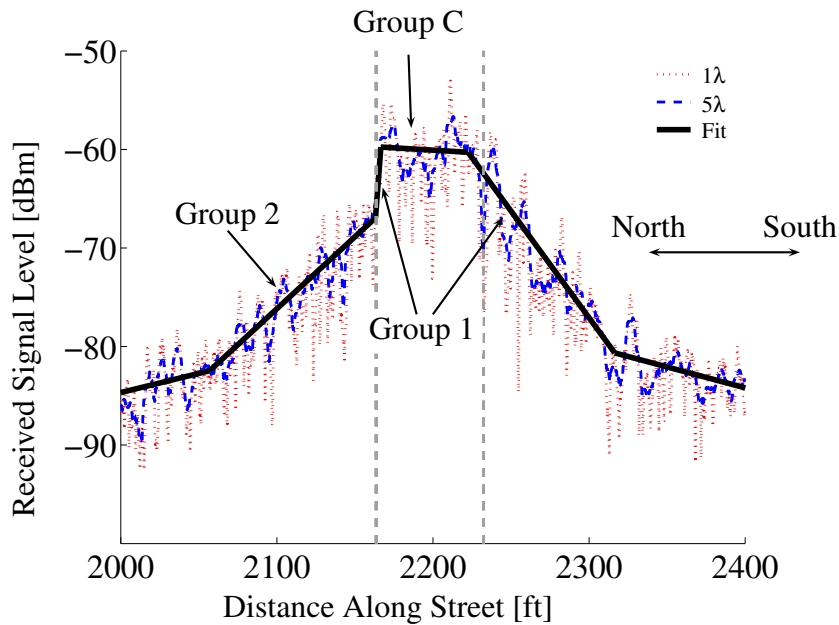


Figure 4.3: Piecewise Linear Fit for Montgomery at Pine. The north side of the intersection sees an abrupt change in signal strength at 2165 ft followed by a more gradual trend. The second trend is placed in Group 2 to differentiate it from segments that are adjacent to the intersection. The south side of the intersection, however, has only a gradual trend, classified as Group 1 since it is adjacent to the intersection.

determination of the slope in the transition region is somewhat subjective. The slope in the transition region is chosen where there is an obvious shift in the signal strength, not just where there is a signal fade.

In Fig. 4.3 for instance, on the north side of the intersection there is a sudden change in the signal strength of 8 dB near the edge of the intersection at 2165 ft. On the south side of the intersection, however, there is a similar abrupt change in signal strength of 12 dB at 2232 ft. In this case, however, the sudden dip in signal strength is but a single variation within a much slower trend, marked by the Group 1 segment, so it is not singled out as a corner transition.

The line segments are joined together to describe the local average received power through the intersection. The vertices in the joined pattern define the rate and extent of the change in received signal strength in each region.

### 4.3 Analysis of Measurements

In this section we look at many measurements of street intersections that exhibit the corner effect throughout the San Francisco financial district. Intersections are considered to exhibit the corner effect if the peak in signal strength through the intersection is significantly greater than the standard deviation of the large-scale fading throughout the remainder of the street. This condition is required so that transitions due to the corner effect may be distinguished from the signal variations due to large-scale fading. The intersections that meet this requirement are shown in the map in Fig. 4.4.

Figures 4.5 through 4.12 present multiple measurements of each intersection indicated in Fig. 4.4. Each intersection is summarized by piecewise linear segments similar to those in Figs. 4.2 and 4.3 using the method described in Section 4.2.2. Most of the signal profiles are adjusted so that the peak of the intersection is 0 dB, giving an indication of the corner attenuation on each side of the intersection. Figures 4.9 and 4.11, however, are adjusted so that the center of the intersection is at 0 dB since there is such a large variation in rates of signal change across the intersection in these two cases.

The intersections that most clearly exhibit the corner effect are the intersections with streets that cross the main radial streets from the transmitter (Battery and Pine). Along Montgomery Street, in addition to the primary radial streets from the transmitter, there are several cross streets (Bush, California, and Sutter) that have strong enough signals for the strength in the intersections to rise above the large-scale fading. A street's perpendicular distance ( $D_p$ ) to the transmitter will determine whether it is the inlet to or the outlet from the intersection. The inlet street is the street that has the shorter distance  $D_p$  to the transmitter and is the street from which the signal enters the intersection. The signal flows from the intersection to the outlet street, which has a larger distance  $D_p$  to the transmitter. This general rule helps explain why the corner effect is usually exhibited along cross streets to the main radial streets from the transmitter. For these intersections, there is a large difference in the distance  $D_p$  for each of the streets. This also explains why the corner effect is not as strong in the interior of the cell where the intersections are close to a  $45^\circ$  line extending from the transmitter.

Several intersections along Montgomery Street exhibit the corner effect. The transmitter is lined up most closely with Battery Street and is not located exactly at the intersection with Pine

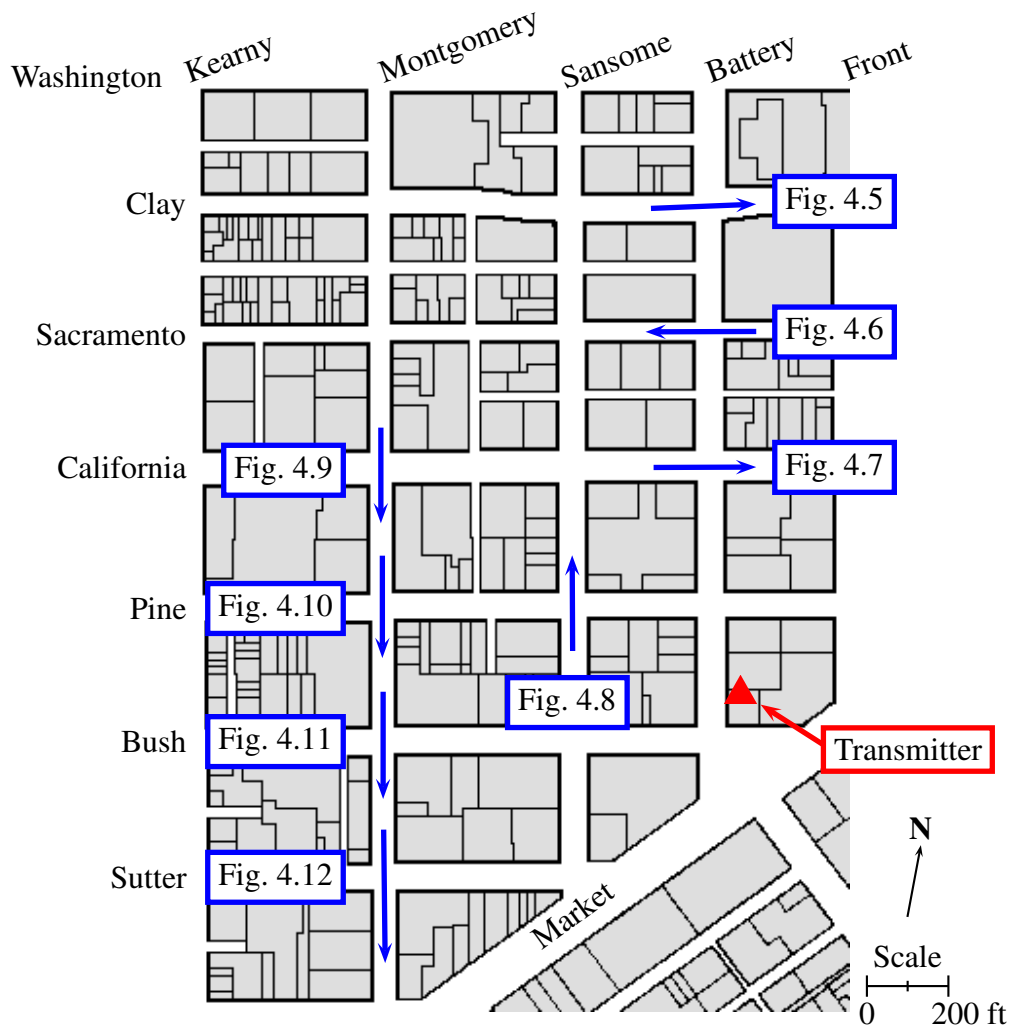


Figure 4.4: Locations of Intersections with Significant Corner Effect. Not all intersections exhibit the corner effect. The phenomenon is primarily observed in the cross streets that cut through a radial street from the transmitter.

Street. The signal from Battery Street is strong enough to feed over into the cross streets (California, Bush, and Sutter<sup>2</sup>).

---

<sup>2</sup>Sutter does not intersect Battery Street, but the signal apparently feeds Sutter through the plaza near Market Street.

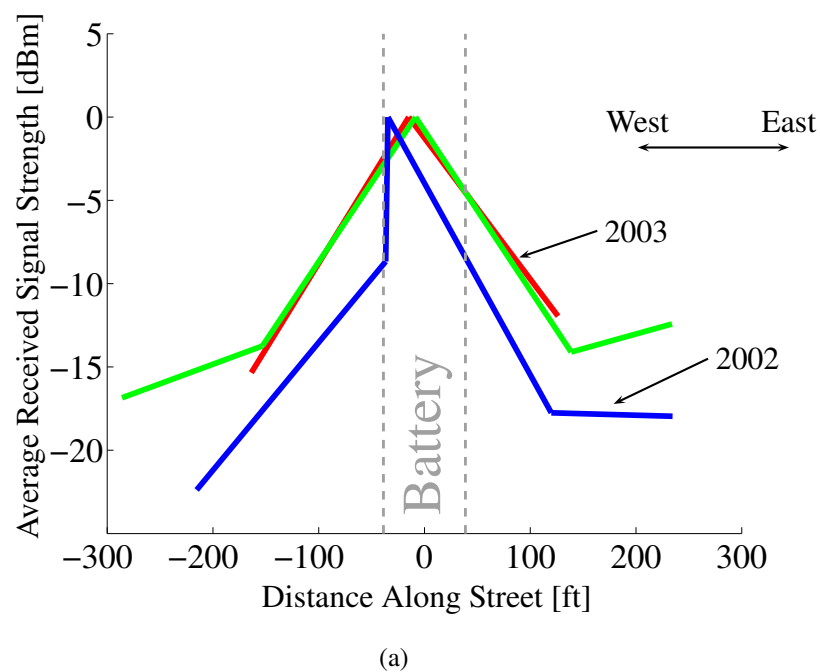
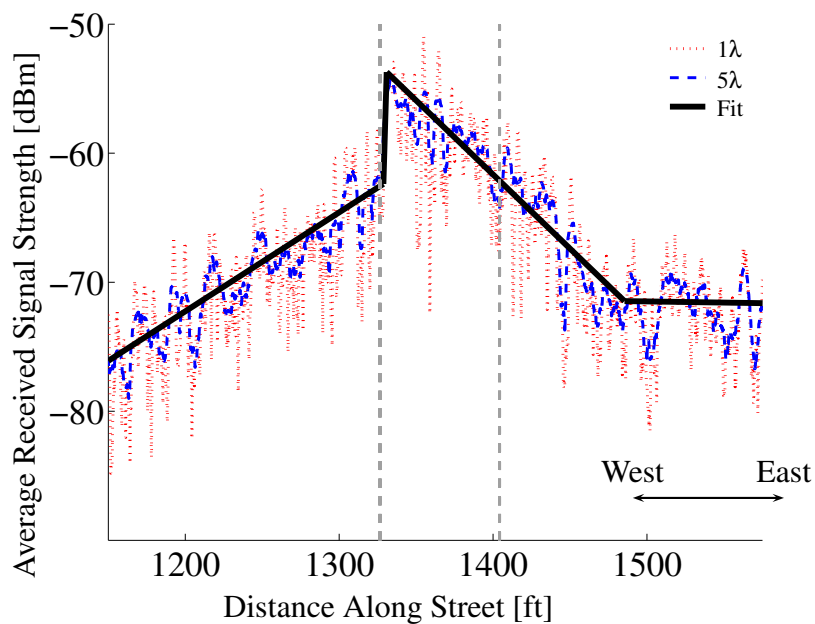
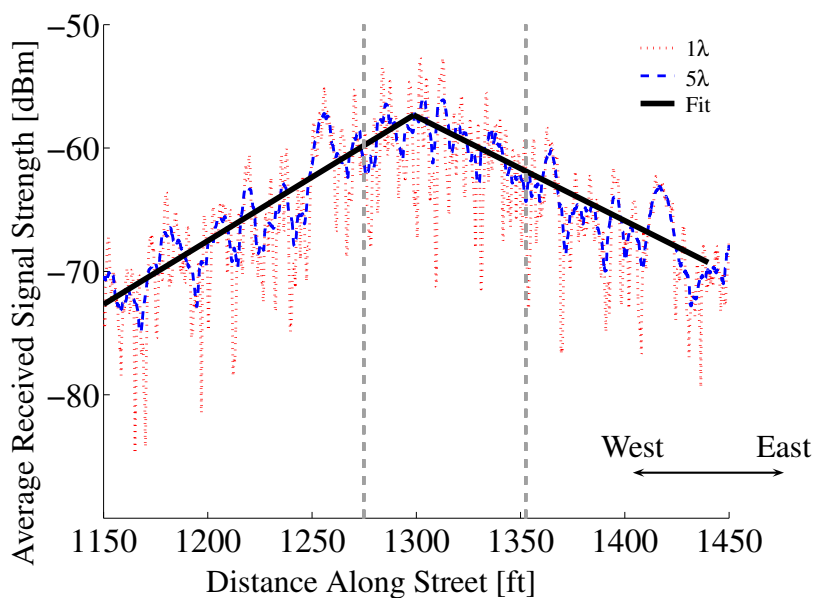


Figure 4.5: Piecewise Linear Segments for Multiple Measurements on Clay at Battery. The path-loss profile summaries are given in (a). (b) and (c) show details of the line fitting for the 2002 and 2003 measurements, respectively. Building construction, underway in 2002 on the northwest corner of the intersection, may account for the discrepancy between the 2002 and 2003 measurements.





(b) 2002



(c) 2003

Figure 4.5: Piecewise Linear Segments for Multiple Measurements on Clay at Battery (*continued*).

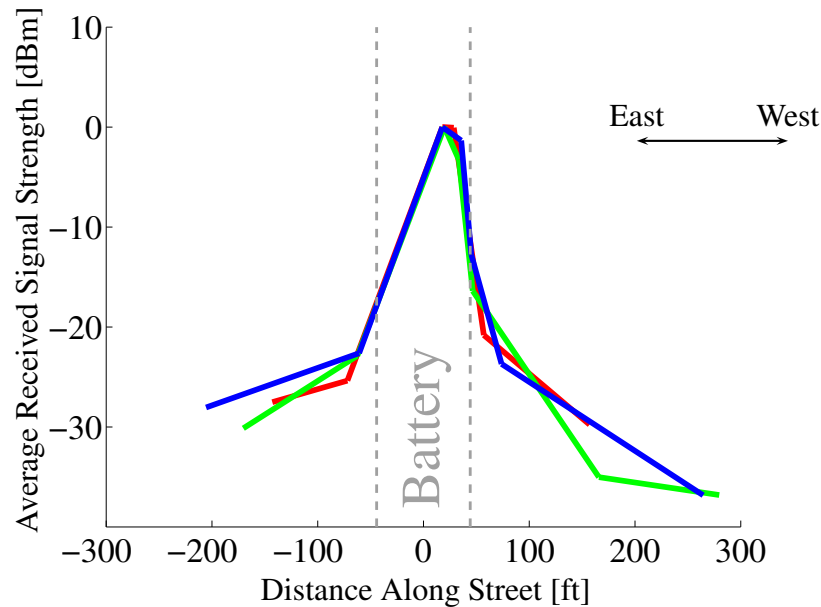
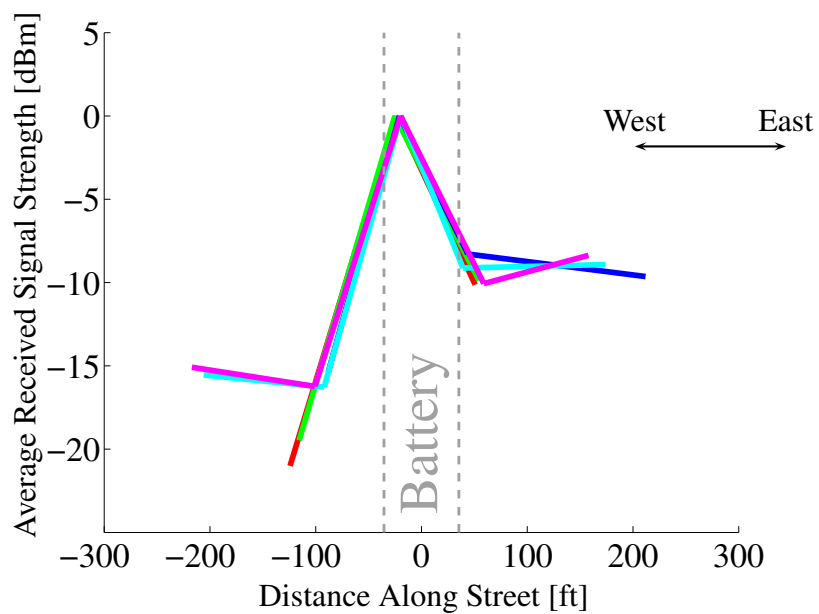


Figure 4.6: Piecewise Linear Segments for Multiple Measurements on Sacramento at Battery. Although the overall rate and extent agree for many runs, there are some variations in the exact signal pattern on the right-hand side of the intersection.

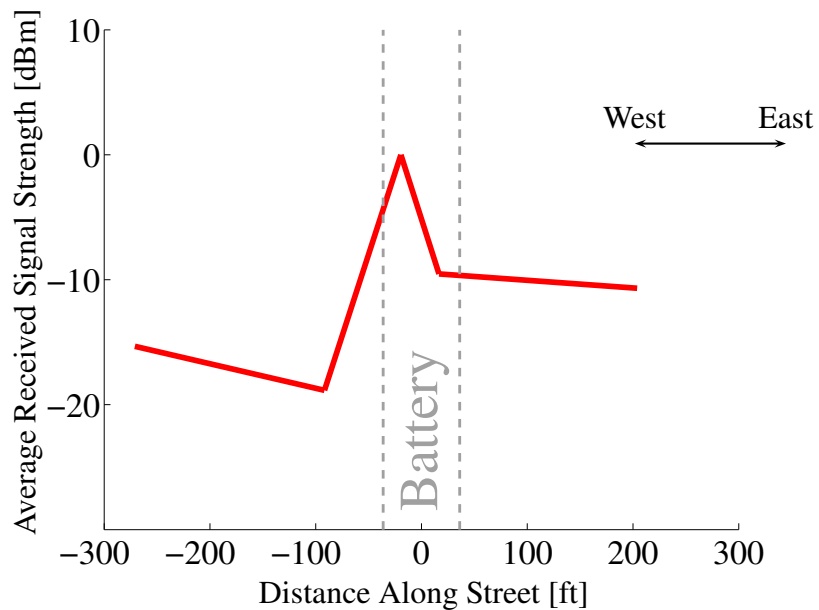
For the intersections that cross Battery Street (Figs. 4.5 through 4.7) the signal profile comes to a point within the intersection and gradually rolls off at the edges. The intersections that have a flat portion within the intersection are accompanied by steeper rollofs at the edges.

Considering the intersections with Pine Street, the flat portion is wider and the rolloff at the edges is steeper at Montgomery than at Sansome. The other intersections along Montgomery also have flat segments in the intersections and steep rollofs at the edges.

These behaviors are qualitatively consistent with overmoded waveguide descriptions of the signal propagation. It is that the energy tends to concentrate in lower-order modes as the signal propagates down a street [69, 71]. At intersections, the higher-order modes in the original street are more likely to couple into lower-order modes in the cross street and *vice versa* [71]. Using an optical ray theory analogy, the lower-order modes correspond to rays that propagate nearly straight down the street. Higher-order modes correspond to rays that bounce back and forth much more between the buildings that line the streets. A concentration of energy in the lower-order modes would be expected to produce less coupling into the side streets and should therefore exhibit a sharper rolloff in signal strength at corners. A mixture of higher-order modes should produce more



(a) Left Lane



(b) Right Lane

Figure 4.7: Piecewise Linear Segments for Multiple Measurements on California at Battery. This intersection exhibits only transitions with no leveling off in the middle of the intersection. Both (a) left and (b) right lanes have very similar signal strength profiles.

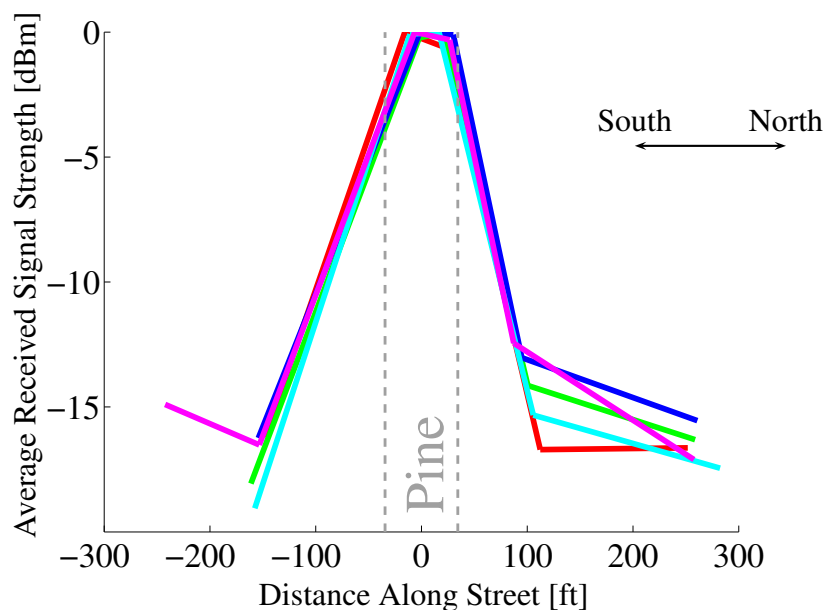


Figure 4.8: Piecewise Linear Segments for Multiple Measurements on Sansome at Pine. Over many different measurement runs, the linear segments agree very well at this intersection.

coupling into the side streets and therefore exhibit a more gradual rolloff in signal strength.

The transmitter is located at 22 Battery Street at an elevation of 178 ft. The antenna is mounted on the north face of a medium-sized building in the area and is below the rooftops of the surrounding tall buildings. Since the side streets are flanked by buildings that are taller than the elevation of the transmitter, the signal energy is likely to propagate around the corners of the tall buildings rather than over the top of them.<sup>3</sup> Because Battery is aligned primarily with the transmitter, there is a large mixture of modes that propagate down the street. For the intersections along Battery Street (Figs. 4.5 through 4.7), this rich mixture of modes contributes to the gradual rolloff at the street corners and to the pointed peak in the signal strength within the intersection.<sup>4</sup>

Because the transmitter is located in the middle of the block, the signal must turn at least one corner before reaching any of the other intersections studied in this chapter. Where Sansome crosses Pine (Fig. 4.8), the signal profile has a narrow flat region within the intersection and a more

<sup>3</sup>See Appendix A for more details regarding the transmit antenna elevation and building heights in the vicinity.

<sup>4</sup>Since the building at the southwest corner of the intersection of California and Battery is somewhat shorter than the elevation of the antenna, diffraction over the top of this building is an alternate explanation for the gradual rolloff in signal strength on the west side of the intersection.

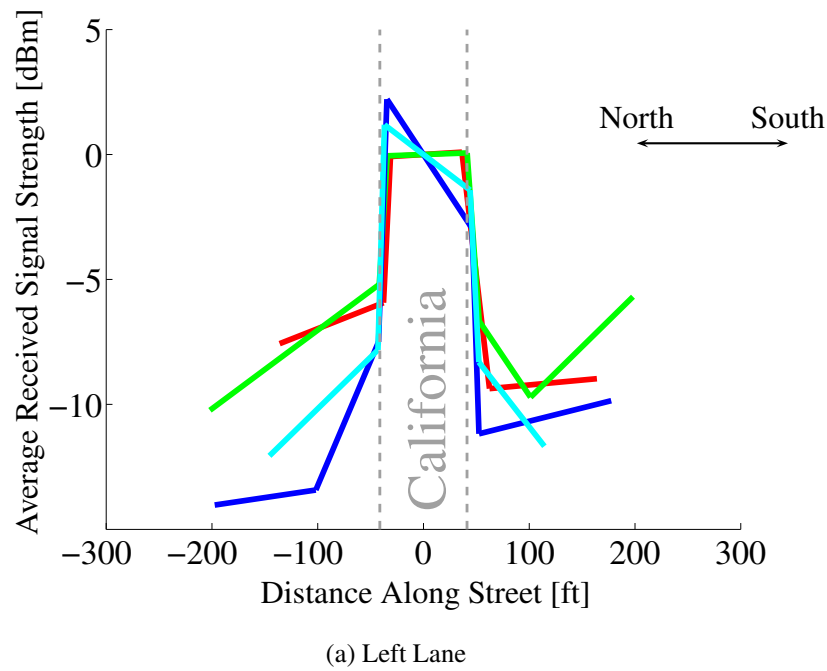
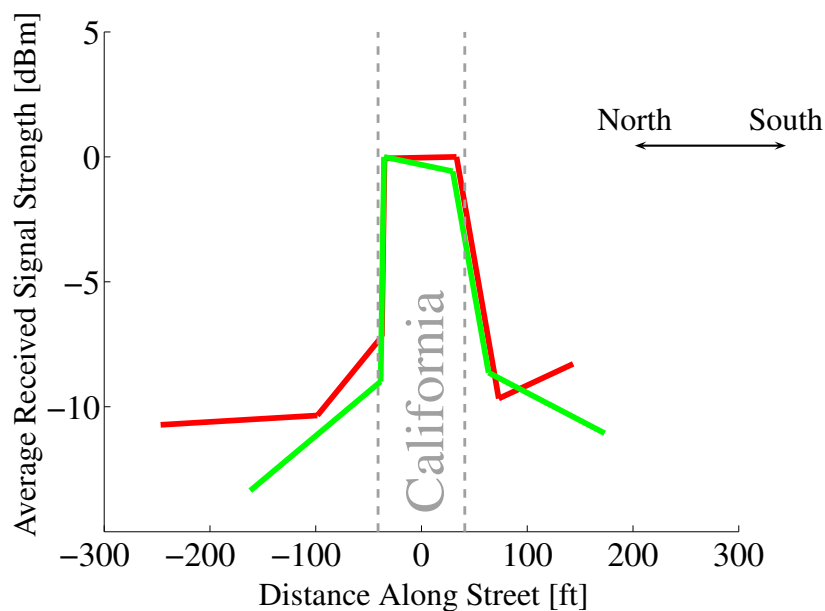
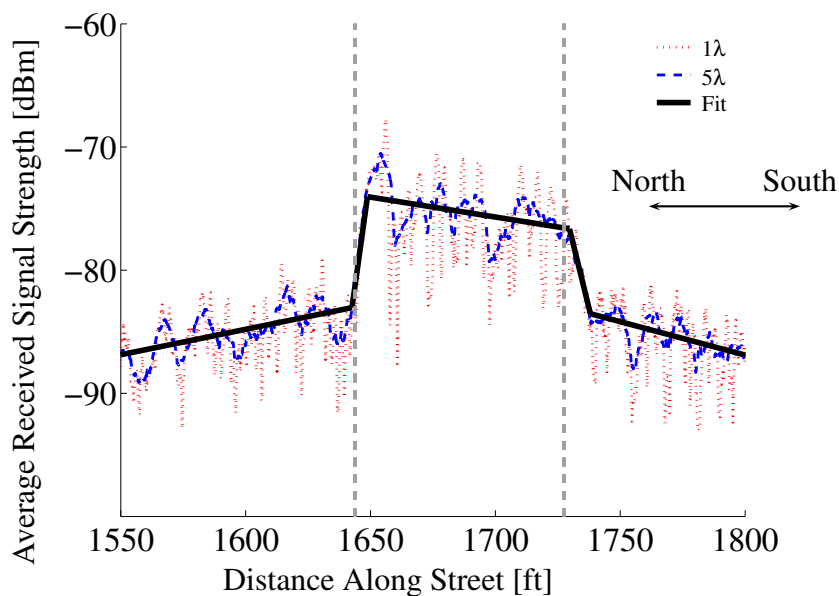


Figure 4.9: Piecewise Linear Segments for Multiple Measurements on Montgomery at California. This intersection is characterized by many different slopes across the intersection for the left lane measurements (a). The profiles in (a) left and (b) right lanes that agree were taken on the same day. The two steepest slopes are from the 2002 measurements, and the profile with the steepest slope in (a) corresponds to Fig. 4.1. (c) and (d) detail two more profiles from (a) that have different slopes across the intersection.

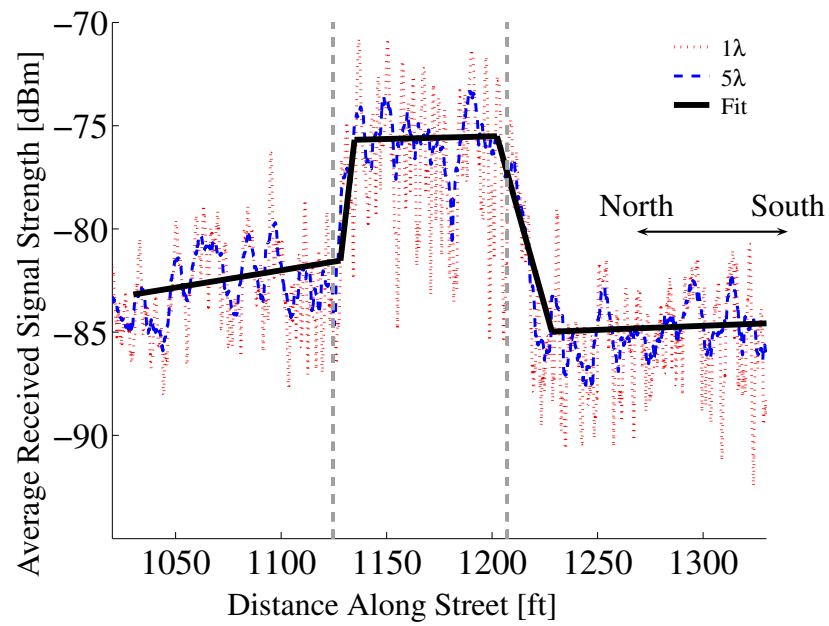


(b) Right Lane



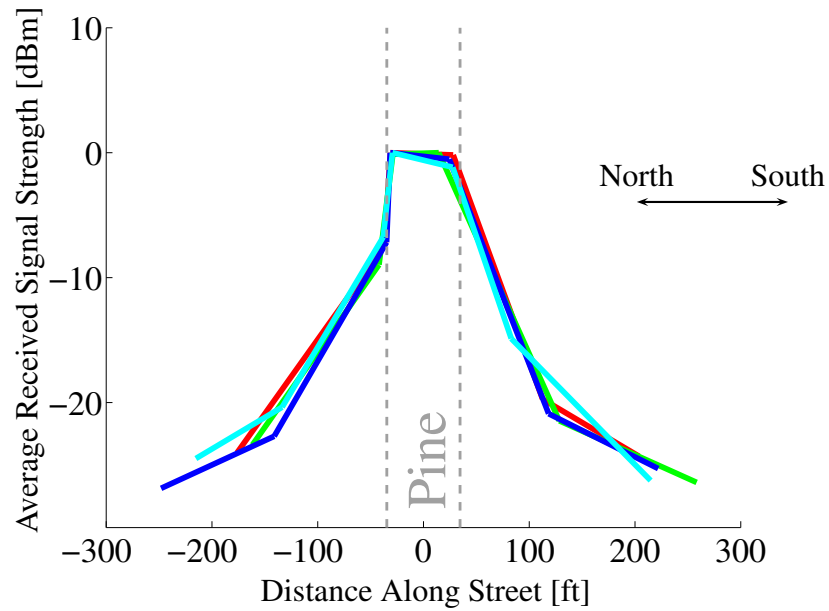
(c) Left Lane, 2002

Figure 4.9: Piecewise Linear Segments for Multiple Measurements on Montgomery at California (*continued*).

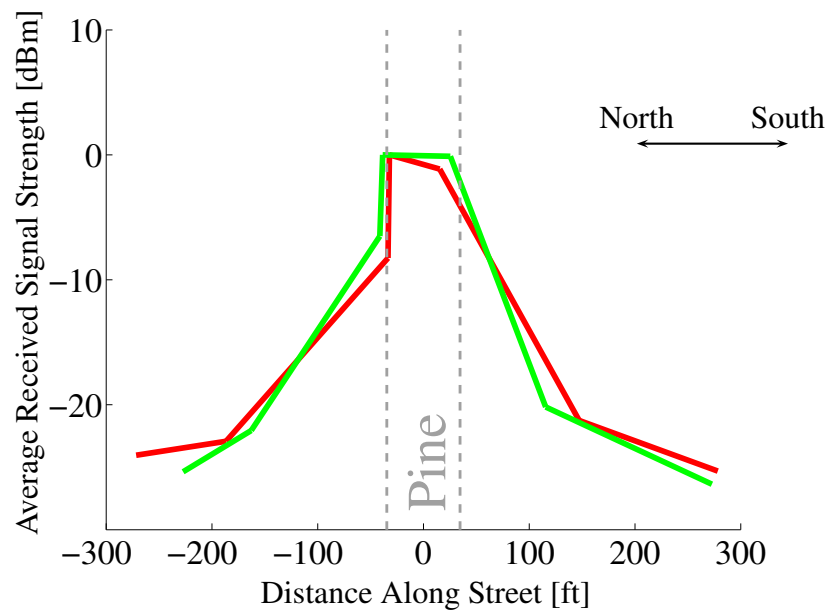


(d) Left Lane, 2003

Figure 4.9: Piecewise Linear Segments for Multiple Measurements on Montgomery at California (*continued*).



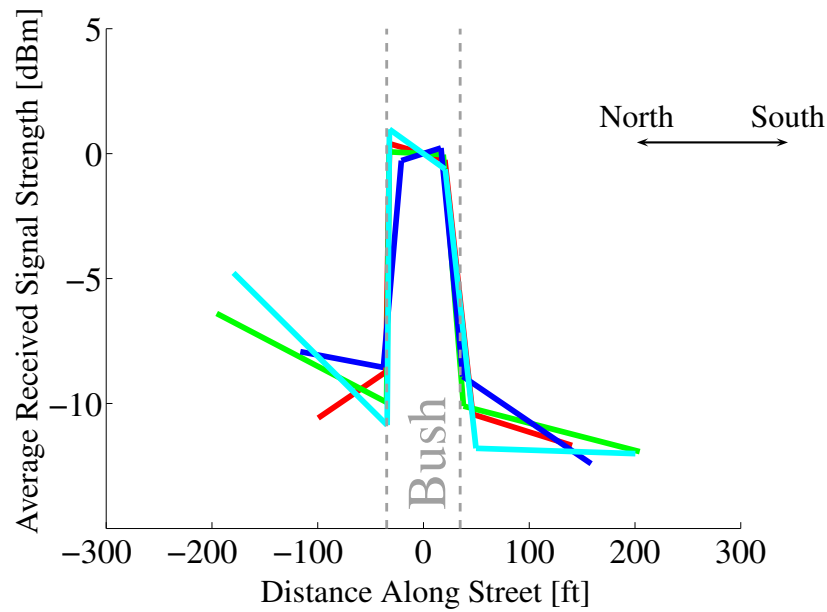
(a) Left Lane



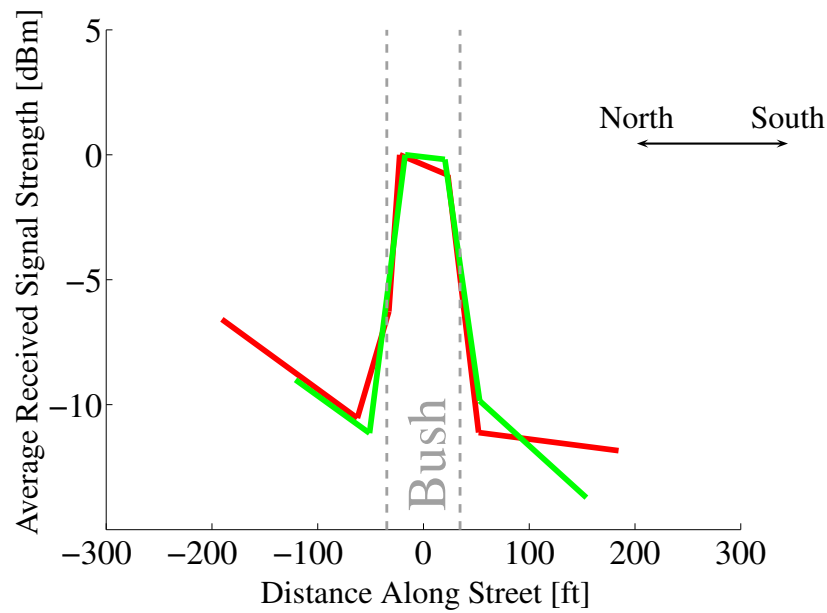
(b) Right Lane

Figure 4.10: Piecewise Linear Segments for Multiple Measurements on Montgomery at Pine. The two-segment characterization of this intersection is repeatable for many measurements.



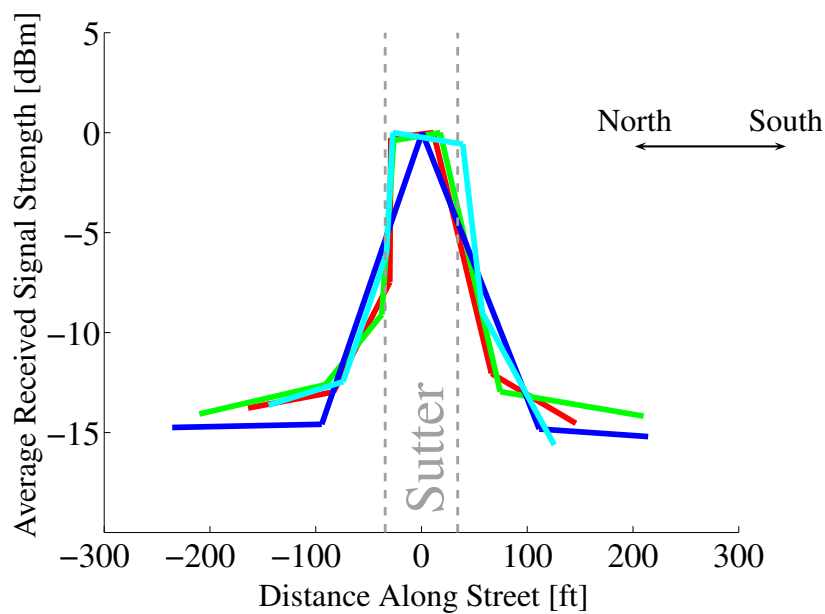


(a) Left Lane

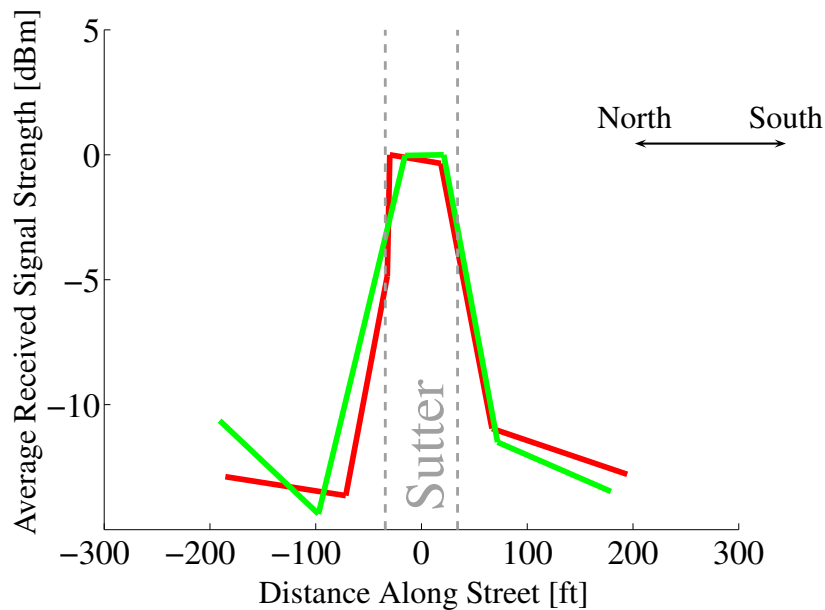


(b) Right Lane

Figure 4.11: Piecewise Linear Segments for Multiple Measurements on Montgomery at Bush. With a few dB signal variation across the intersection and very sharp dropoffs on either side, this intersection has very similar signal characteristics as those of Montgomery at California (Fig. 4.9).



(a) Left Lane



(b) Right Lane

Figure 4.12: Piecewise Linear Segments for Multiple Measurements on Montgomery at Sutter. Although the signal change extent is the same for many measurements, the rates show some variation.

gradual rolloff at the edges than does the intersection with Montgomery (Fig. 4.10). The intersection with Sansome, being closer to the transmitter, apparently sees a richer mixture of modes, leading to a more gradual signal profile. At Montgomery, on the other hand, the modes have concentrated into lower-order modes after having traveled further down Pine Street, making the transition at the corner much sharper. Similar arguments can be made for lower-order modes causing a sharp rolloff for the Montgomery intersections with California (Fig. 4.9), Bush (Fig. 4.11), and Sutter (Fig. 4.12).

In order to make a composite description of the corner effect throughout the coverage area, several common characteristics in the signal profiles are noted. At the edges of the intersections, there is naturally a decrease in signal power. In some intersections, this change is gradual (Figs. 4.5 through 4.7). In some cases, however, there is a very abrupt change in signal strength (Figs. 4.9 through 4.12). Sometimes the corner effect is described by two piecewise linear segments (Figs. 4.6, 4.5, 4.10–4.12).

The choice to include additional segments in the analysis of the intersection depends on whether or not the segment is part of the corner transition or is part of the larger street trend. For example, in Fig. 4.2, there is only one segment on either side of the intersection that can clearly be attributed to the presence of a street intersection. In Fig. 4.3, however, one side of the intersection clearly has two segments that are attributed to the presence of the intersection before the signal falls down to the general street trend.

Another interesting characteristic of the intersection profiles is the signal strength in the middle of the intersection. In most cases, the average signal strength remains relatively constant through the intersection. Sometimes there is no level section in the middle and only the transition on either side of the intersection. In a couple of cases, the trend through the middle of the intersection varies greatly from one measurement to the next (Figs. 4.9(a) and 4.11(a)).

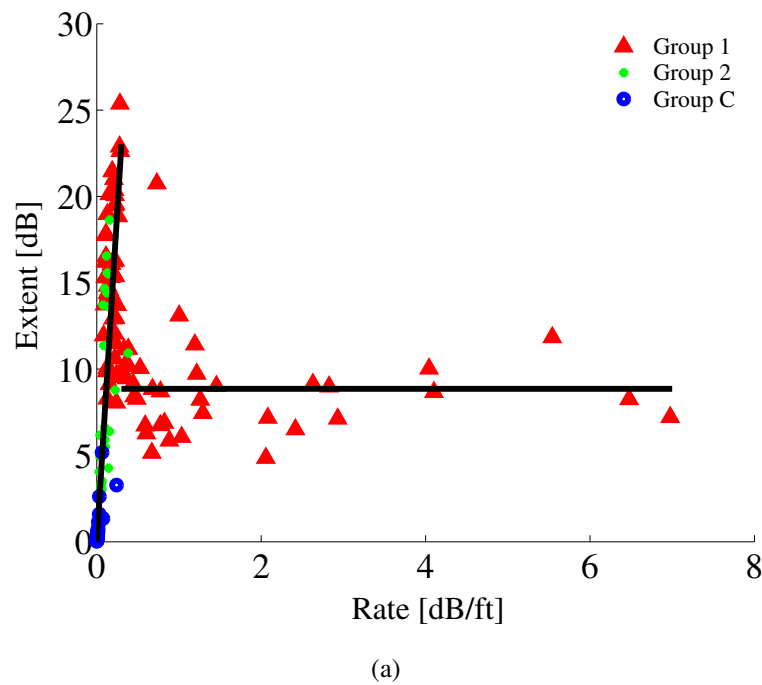
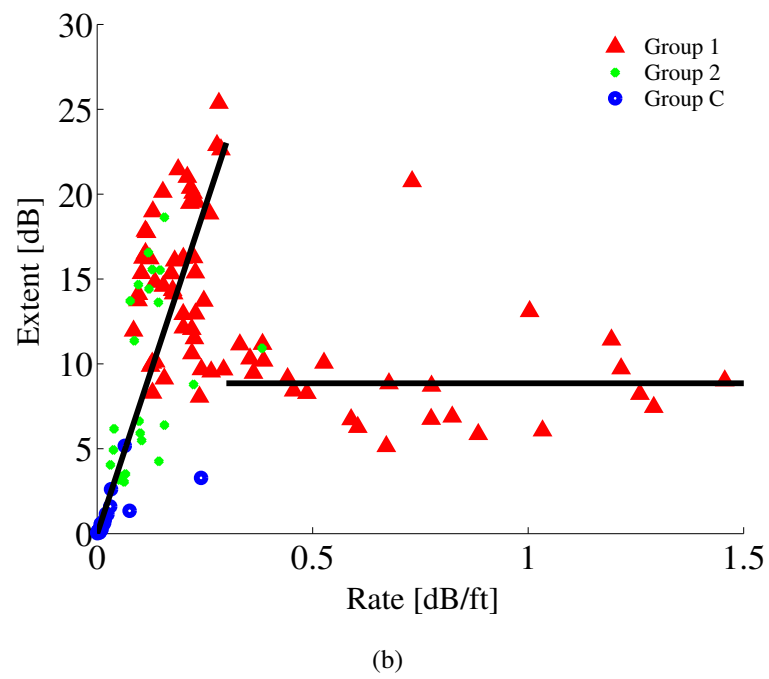


Figure 4.13: Rate and Extent Relationships. The scatter plot for the entire area is shown in (a), while (b) zooms in on the rate axis to show the details of the empirical relationship for low-rate segments. Each segment for the analyzed intersections is grouped by its type and characterized here by its rate and extent. The horizontal line represents the average rate for segments with slopes greater than 0.3 dB/ft. The low-rate segments are characterized by a linear relationship with slope of 77 ft.

Figure 4.13: Rate and Extent Relationships (*continued*).

Intersection	Reference	Group		
		1	2	C
Clay at Battery	Fig. 4.5	✓	~	
Sacramento at Battery	Fig. 4.6	✓	✓	✓
California at Battery	Fig. 4.7	✓		
Sansome at Pine	Fig. 4.8	✓		✓
Montgomery at California	Fig. 4.9	✓	~	✓
Montgomery at Pine	Fig. 4.10	✓	~	✓
Montgomery at Bush	Fig. 4.11	✓		✓
Montgomery at Sutter	Fig. 4.12	✓	~	~

Table 4.1: Intersections Exhibiting the Corner Effect. The intersections listed in this table are those exhibiting the corner effect as described in Section 4.2.2. For each row, the first street listed is the street in which the measurements are taken, and the second street is the cross street. The group representation is tallied as follows: Groups present in every profile for a given intersection are marked by ✓. Groups missing from every profile are left blank, and groups present in some, but not all, profiles are marked by ~.

## 4.4 Measurement Results

The piecewise linear segments fall into three groups. The first group is the primary slope that is closest to the edge of the intersection. At least two segments for each intersection, one for the leading edge and one for the trailing edge, are included in Group 1. The second group is for the second segment in a transition that has two segments before returning to an overall street trend. Not all intersections have a segment in Group 2. Finally, Group C, for center, consists of the relatively flat segments that sometimes occur in the middle of an intersection.

The specified intersections, listed in Table 4.1, are analyzed using the criteria established in Section 4.3. The segments are grouped according to their positions in the signal trace (Group 1, Group 2, Group C). The relationship between rate and extent for each segment is shown in Fig. 4.13(a) with a close-up view for the low-rate points in Fig. 4.13(b). The following observations are made:

- Most of the steep transition regions occur on Montgomery Street. This is postulated by the concentration of low-order modes as described in Section 4.3.
- A steep slope, greater than 0.3 dB/ft, is typically 5–13 dB in extent. A lower slope is much more common for segments with a large signal change extent and for Group 2 segments.

- The extent of the change in the average signal strength across the plateau region of the signal strength profile for an intersection is typically 2.5 dB or less.
- For low-rate transitions, the relationship to the extent is

$$\text{extent} = m \times \text{rate} \quad (4.4)$$

with  $m = 77$  ft.

The signal change extent is approximately 5 dB more than the distance trend offset between the primary and cross streets as described in Chapter 6. The distance trends in each street are subject to large-scale fading. The extent of the signal change observed in this chapter essentially captures some of the additional signal variation about the distance trends for each street.

## 4.5 Summary

The traditional study of large-scale and small-scale fading in urban environments is done using fixed-length averaging windows to smooth out the small-scale fading. A fixed-length averaging window, however, can lead to mischaracterization of the rate of signal strength change at street corners. The rate of the signal strength change is an important parameter for systems that must react to sudden changes in received signal strength. Additionally, rate of change is important for system modelers that use simulation techniques to predict the local average received power in and around street intersections.

Analysis of data from intersections that exhibit the corner effect in the San Francisco financial district yields their empirical properties. For low rates of change of the average signal strength, *i.e.*, less than 0.3 dB/ft, the rate and extent appear to be related. For higher rates of change, the extent of the change is around  $8.9 \pm 4.5$  dB.

## Chapter 5

# Cell Partitioning for Improved Statistical Propagation Modeling

### 5.1 Objectives

Signal quality plays an important role in how resources are allocated in wireless systems. For instance, channels with higher signal quality can achieve higher data rates and can be assigned higher modulation levels, freeing bandwidth resources for other users. When the spatial variation of signal quality is taken into account, the geographical distribution of resources is then determined.

In cellular systems, path loss characteristics are used to determine the coverage area for a particular base station. Not only is path loss an important measure, but its statistical variation is as well. This is particularly true at the cell boundaries. The statistical variation of the path loss, taken in conjunction with its distance-dependent trend for two co-channel cells, is very important in evaluating interference. These quantities also determine the “softness” of the cell boundaries. On the edge of cells in which the path loss variation is large, the soft handoff region, *i.e.*, the region where either or both base stations may be used, is wider than for cells in which the variation is smaller.

Urban areas contain obstacles to radio wave propagation, which shape the coverage area of a wireless system. In this respect, urban environments present significant challenges to wireless system designers since radiated signals reflect off of buildings, cars, and other objects consisting of diverse materials and having very complex surfaces. Out of necessity, details of this environment are obscured in models so that a reasonably compact representation may be used to design and



evaluate new systems.

The continuum of models ranges from statistical models, which take into account only broad classifications of the propagation environment, *i.e.*, dense urban, suburban, etc., to ray-tracing methods, which require detailed knowledge of objects between transmitter and receiver. Taking the standard deviation of the prediction error as a measure of model accuracy, one would expect the standard deviation to become smaller as more information about the environment is folded into the model, making it more accurate.

In this chapter, we discuss a modification to traditional statistical models that significantly improves the estimation error with a minimal increase in complexity. The street orientation relative to transmitter and receiver is seen to have an impact on the analysis. Empirical relationships discussed in this chapter are used to draw qualitative comparisons to other research in which much lower antenna heights are used.

## 5.2 Related Work

With the development of cellular telephone technology, propagation studies in urban environments are increasingly of technical interest to aid system designers. Two quantities of interest are path loss and delay spread. Delay spread studies are important for establishing receiver requirements, namely, constraints on equalizer lengths. Path loss studies are used to compute cell coverage areas and outage probabilities. Our interest in this chapter is in cell coverage, so we focus on path loss here.

In the early days of cellular telephony, coverage areas were very large, and consequently, early studies used very high antennas, covering wide areas. For example, Okumura, *et. al.* [66], report extensive measurements over wide areas in the Tokyo region. Similarly, for work prior to the deployment of the Advanced Mobile Phone System (AMPS) in the U. S., Black and Reudink [14] report on measurements in the Philadelphia area. Their experiment uses a transmitter at 500 ft above street level, and the measurements extend out to five miles from the transmitter location. Even though the antenna is well above the surrounding rooftops, radial streets, *i.e.*, streets extending directly from the transmitter, still experience signal levels that are approximately 10 dB higher than in the cross streets.

With the proliferation of cellular subscribers, there has been increasing pressure to reduce the

cell sizes so that more customers can be added. As a result, many “micro-cell” studies have been performed with the transmitter well below the rooftops, *e.g.*, at street lamp level. One such study was performed by Whittaker [96] in the streets of downtown Ottawa. This study was conducted at 910 MHz using a transmitter with antenna height of 8.5 m and a receive antenna at 3.65 m, both of which were well below the tops of the surrounding buildings. In this study, distinct peaks in signal strength are observed at cross streets that are aligned with the transmitter.

Mahbobi [54] conducted studies of the cell coverage area shape when the transmitter was located at various locations in downtown Manhattan. When the transmitting antenna is located 20 ft above the ground but still below the roofline, the coverage area is elongated and extends narrowly along the streets most closely aligned with the transmitter. When the transmitter is located on the roof of a building, however, the coverage area takes a more regular shape.

Erceg, *et. al.* [25], report on propagation studies conducted in New York City at 1956 MHz using transmit antenna heights of 6.6 m and 3.3 m and a receive antenna height of 1.5 m. All of the antennas are below the rooftops in the measurement area and are typically 30 m in height. The measurements are compared with the results of a ray-tracing model. The changes in the path-loss exponent and the corner attenuation are characterized against the distance the street or corner is from the transmitter location. Both parameters, path-loss exponent and corner attenuation, are found to increase with distance from the transmitter.

Another milestone in the study of urban microcells was the determination of the cell coverage shape. Goldsmith and Greenstein [30] use empirical studies of propagation in Manhattan at 894 MHz to describe the cell shape. In this case, the signal strength transition from radial to cross streets is fit to a polynomial expression. This polynomial expression is then used to derive contours of constant average attenuation throughout the cell coverage area. The result is a concave diamond shape centered on the transmitter. Others such as Feuerstein, *et. al.* [28], and Maciel and Bertoni [53] make similar observations. Maciel and Bertoni see a similar qualitative cell shape when performing ray-tracing simulations for signals at 900 MHz with uniform building structures on a regular street grid. Feuerstein, *et. al.*, note that at 1900 MHz in San Francisco, the signal levels in side streets are weaker. They then suggest that the cell consists of segments down the radial streets and a much smaller circle that is centered on the transmitter for the side streets.

Similarly, Erceg, *et. al.* [26], use ray-tracing analysis for comparison to measurements taken in Boston at 900 MHz, 2 GHz, and 6 GHz. In the course of the analysis, contours of constant

average signal level are derived using the ray tracing analysis. The contours are very similar to the empirically derived contours of Goldsmith and Greenstein.

Several microcell studies identify the differences in path-loss properties for streets based on their orientation relative to the transmitter. Börjeson, *et. al.* [15, 16], and Berg, *et. al.* [10], perform empirical studies that give both path loss and fading parameters for individual streets. These studies and others [25, 26] characterize individual streets based on distance from an intersection, not distance from the transmitter. Results from adjacent streets, therefore, are not readily summarized in a single model.

With the exception of the rooftop measurements of Mahbobi [54], all of the urban microcell studies were conducted with the transmitter much closer to street level than to the tops of buildings. The characteristics observed then are of the propagation effects as the signal goes around the corners rather than over the tops of buildings. In fact, Erceg explicitly states that this is one of the constraints on the ray-tracing analysis performed in [26]. In our experiments, however, a much higher antenna is used. Since it is still below the rooftops of the surrounding buildings, however, many of the propagation properties will reflect the observations made in other microcell studies.

### 5.3 Observations

The measurements used for the analysis in this chapter come from two measurement campaigns conducted in the San Francisco financial district using the equipment and methods described in Chapter 3. The coverage area is as shown in Fig. 5.1. The base station at 22 Battery Street serves as the beacon from which the measurements are made. The antennas for this sector are mounted on the north face of the building with an antenna height of 178 ft, which is lower than the rooftops of the surrounding tall buildings.

As with other measurements made in urban areas, there are several locations in which distinct peaks in the signal level occurred at street intersections. Fig. 5.2 shows an example of this phenomenon. This figure shows the raw data from signal measurements made during a southbound drive on Montgomery Street. The thick lines on the trace are from the rapid fluctuations due to the multipath arrival of the signal. The peaks correspond to cross streets in which the signal level is higher. Since these peaks occur at known locations, this information should be incorporated into the statistical model in order to reduce the path-loss prediction error.

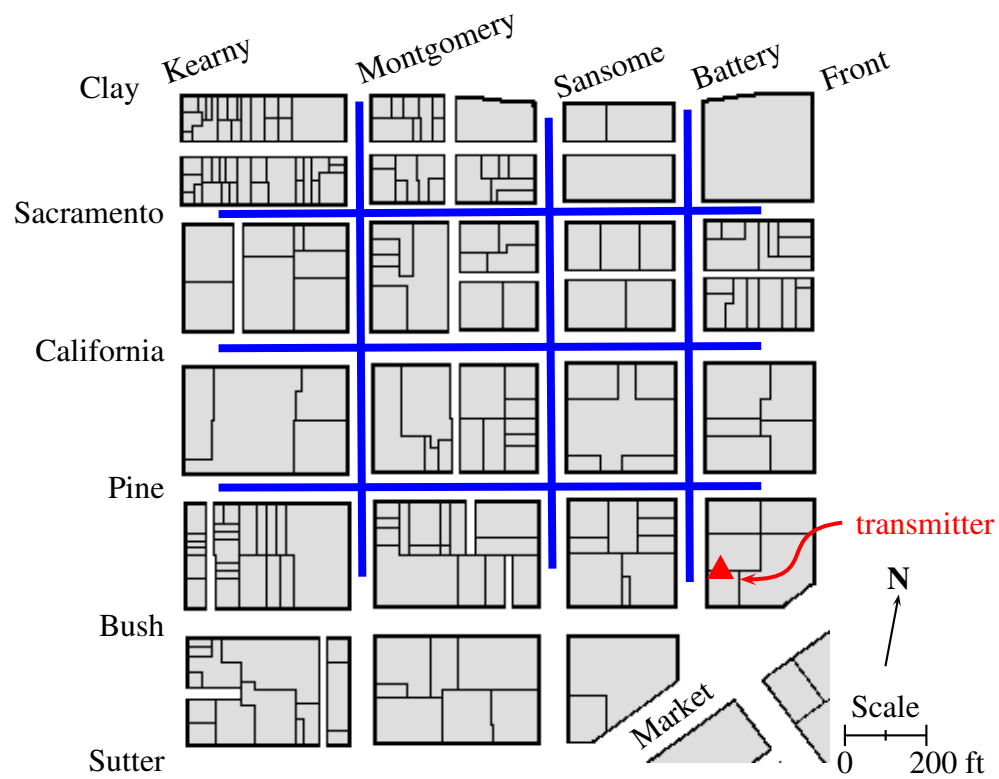


Figure 5.1: Measurement Area. The center of the financial district is chosen for this study since it is the area most representative of dense, urban environments.

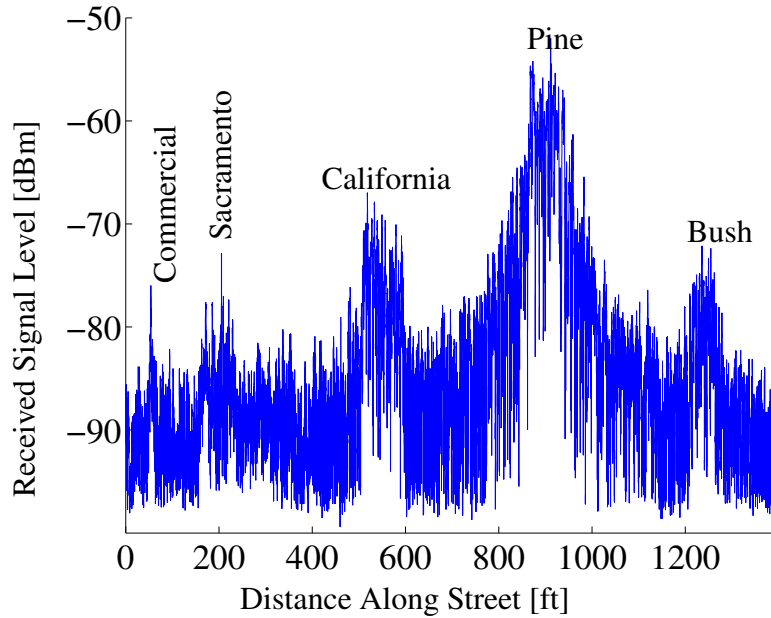


Figure 5.2: Drive Along Montgomery Street. The signal variations caused by buildings are identified in this figure as the peaks in signal strength that occurs at cross-street intersections along Montgomery Street.

The rapid fluctuations of the small-scale variation are reduced by averaging the signal power over intervals of 10 wavelengths. These local averages are taken from overlapping sets every 5 wavelengths along the drive path. Fig. 5.3 shows these local averages versus the radial distance to the transmitter. Using the traditional method of statistical analysis as described in [39], the data are fit to the following path-loss formula using least squares:

$$P(d) = K_0 - 10 n \log_{10} d \quad (5.1)$$

where  $K_0$  is a constant that accounts for transmitter and receiver antenna gains and any attenuation incurred by turning a corner between transmitter and receiver,  $n$  is the path-loss exponent, and  $d$  is the radial distance to the transmitter. The path-loss exponent ( $n$ ) and the standard deviation ( $\sigma$ ) of the prediction error are consistent with other results for dense urban environments [75, Ch. 3]. For comparison, Black and Reudink [14] observe slightly lower values for  $\sigma$  (7–8 dB) in Philadelphia at 836 MHz using a much higher antenna (500 ft) that is above the rooftops of the surrounding buildings. This observation suggests that the environment itself may have more of an influence on

this value than does the transmitting antenna height.

Looking at Fig. 5.3, one can see that the signal level falls off more rapidly for streets that are further away from the transmitter. To further analyze the data, we take the street orientation into account. The radial streets are those that extend directly out from the transmitter, *i.e.*, Battery and Pine, and the cross streets are all others, *i.e.*, Sansome, California, Montgomery, and Sacramento. In this case, Pine Street is close enough to the transmitter for it to function as a radial street. For the path-loss calculations in Fig. 5.3, data points from peaks in intersections with radial streets are removed from the cross street and included in the calculation for the radial street. Data points in the narrow transition region between a radial street and a cross street are excluded from the calculation altogether (see Chapter 4).

The distance-dependent path-loss trends for each street are shown in Figs. 5.4 through 5.8. Figure 5.9 summarizes the path-loss exponent  $n$  for each street based on the street's distance from the transmitter. The distance metric for the trend in Fig. 5.9 is the length of a perpendicular line drawn from the transmitter to the street in question. A path-loss trend similar to that in Fig. 5.9 is observed by Erceg, *et. al.* [25], for microcell measurements at 2 GHz using transmitting antenna heights of 6.6 m and 3.3 m. Montgomery Street is not included in Fig. 5.9 since the street lies in a narrow range of radial distance and therefore doesn't give a reliable value for  $n$ .

Since the corner transition regions are not included in the curve fitting of the side streets, the distance-dependent trends on the cross streets do not match the radial street trends in the common intersections. Figure 5.10 illustrates the offsets of the path-loss trends for perpendicular streets. The distance axis is referenced to the common intersection shared by both streets. We define the offset between the distance-dependent trends as the corner attenuation. The corner attenuation is characterized in Fig. 5.11 based on the distance of the intersection from the transmitter.<sup>1</sup>

Based on the path-loss trend, the absence of additional streets between Pine and California and between Battery and Sansome explains the apparent "gap" between the Pine and Sansome data in Fig. 5.3. The values of  $\sigma$  for the individual streets range from 2.7 dB to 4.4 dB. Because the data for individual streets overlap and because of the city-block-induced "gap," there is a natural partitioning between radial and cross streets.

The partitioning procedure is summarized as follows:

---

<sup>1</sup>It should be noted that for Battery Street (see Fig. 5.10(a)) the measurements deviate significantly from the trend close to the transmitter. This is attributed to antenna pattern effects since Battery Street runs beneath the transmitter antenna.

	2002 Measurements			2003 Measurements		
	radial	cross streets	total set	radial	cross streets	total set
$n$	1.7	6.4	5.0	1.2	5.8	4.6
$\sigma$ [dB]	4.3	5.1	10.3	4.6	4.6	10.8

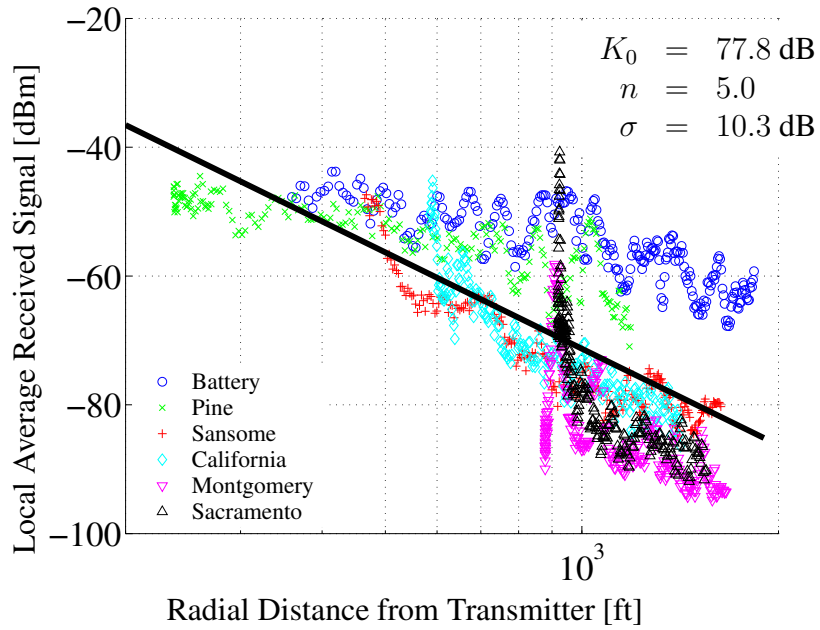
Table 5.1: Summary of Measurements. Street partitioning reduces the prediction error by up to 6 dB. This result is consistent for both measurement campaigns.

1. Divide the streets in the coverage area into radial and cross-street sets.
2. For the cross-street set, remove the intersections that overlap with the radial set and place the corresponding data points into the radial set.
3. Perform the distance fit for each set according to (5.1).

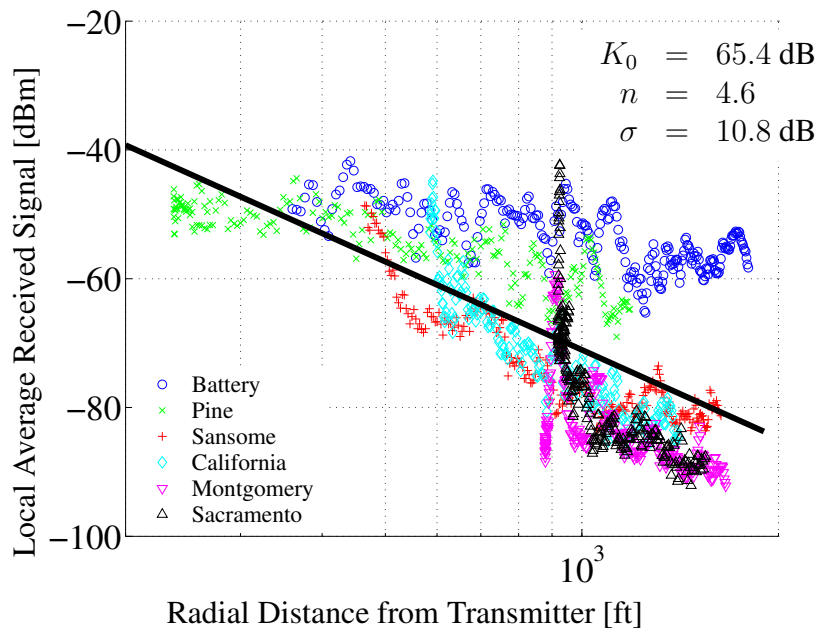
Similar to the individual street calculations, the street intersections between the radial and cross-street sets are removed from the cross-street sets and added to the radial sets for the calculation with the transition regions removed. The path-loss trends for the partitioned sets are shown in Fig. 5.12. The estimation error of each set is calculated by subtracting out the distance trends. This error fits a lognormal distribution for each set. The cumulative distribution functions<sup>2</sup> (CDFs) for the radial and cross streets are shown in Fig. 5.13. The same analysis is performed on measurements from each campaign and is summarized in Table 5.1.

---

<sup>2</sup>Note that the vertical scale is “warped” so that a straight line represents a normal distribution (Gaussian), and the slope of the line represents the standard deviation,  $\sigma$ .



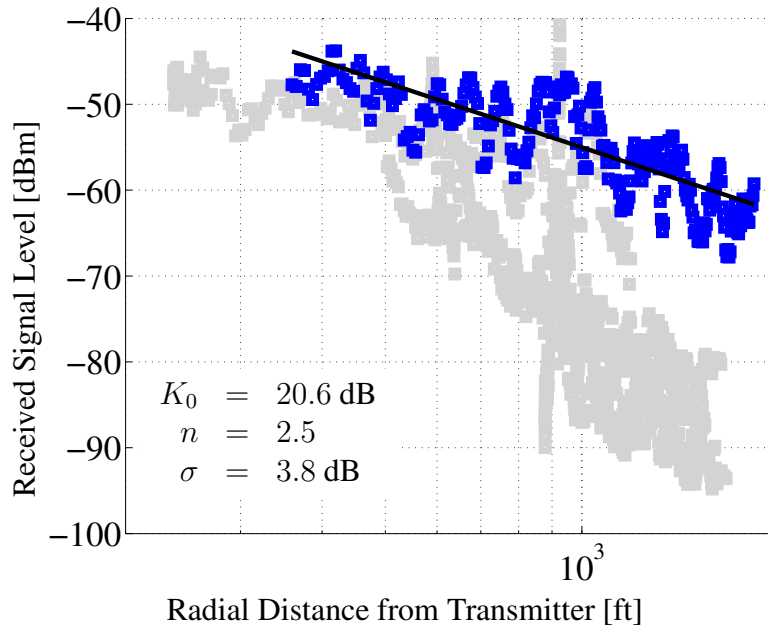
(a) 2002 Measurements



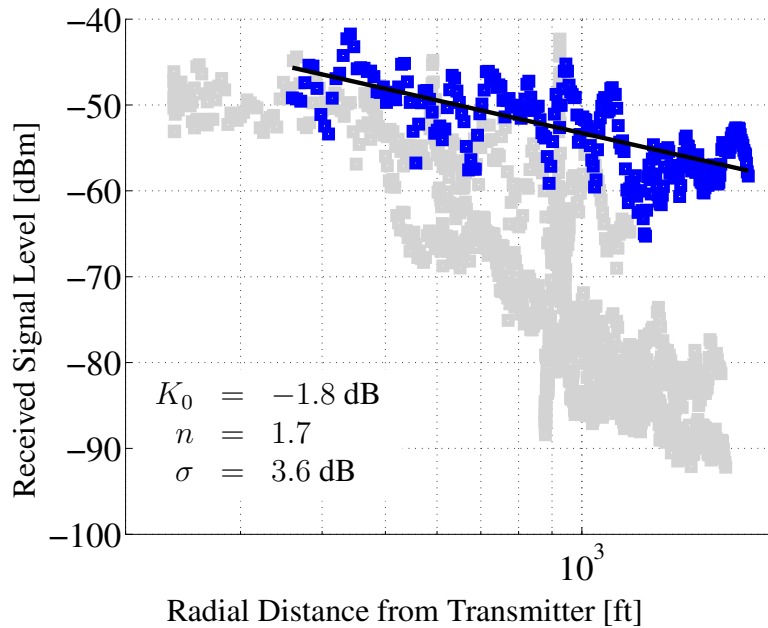
(b) 2003 Measurements

Figure 5.3: Distance-Dependent Trend. By treating the measurement area as a homogeneous group, a single distance-dependent trend is found.



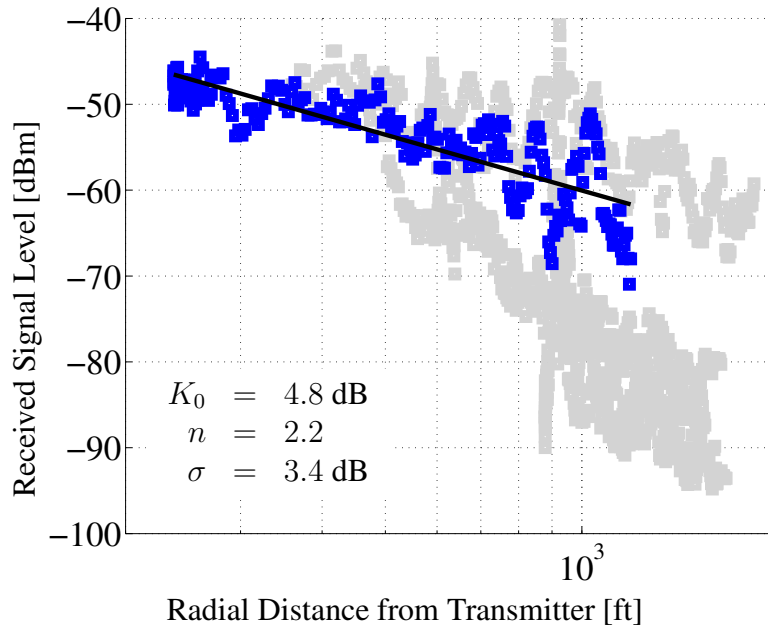


(a) 2002 Measurements

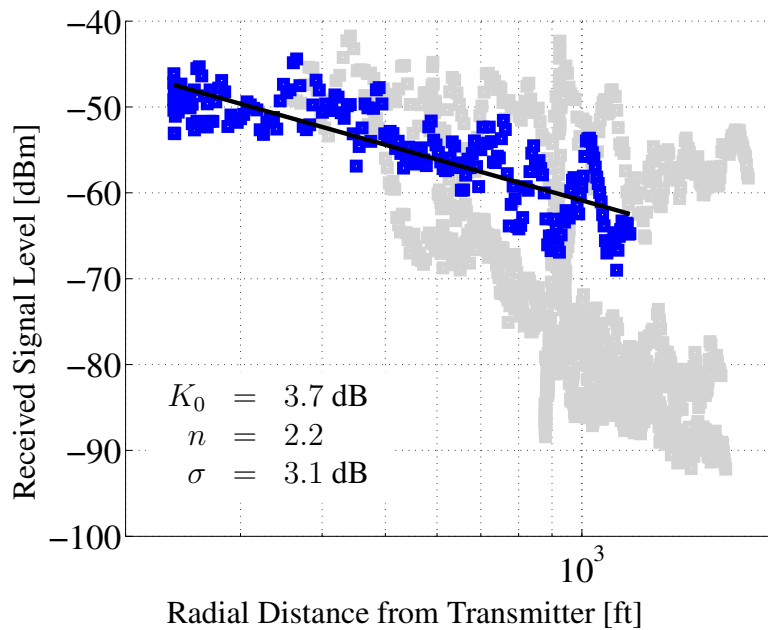


(b) 2003 Measurements

Figure 5.4: Path Loss Along Battery Street. Battery, the street most closely aligned with the transmitting antenna, has the shallowest path-loss curve of any street in the measurement area.

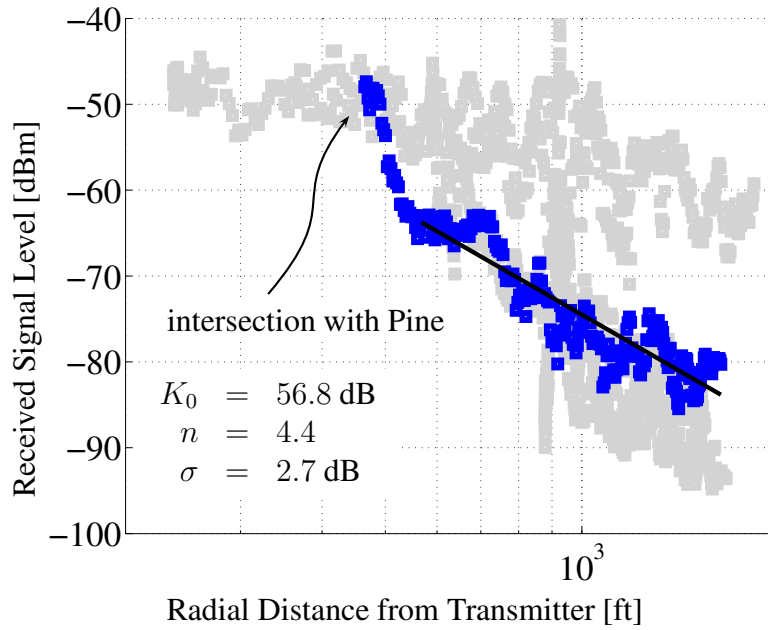


(a) 2002 Measurements

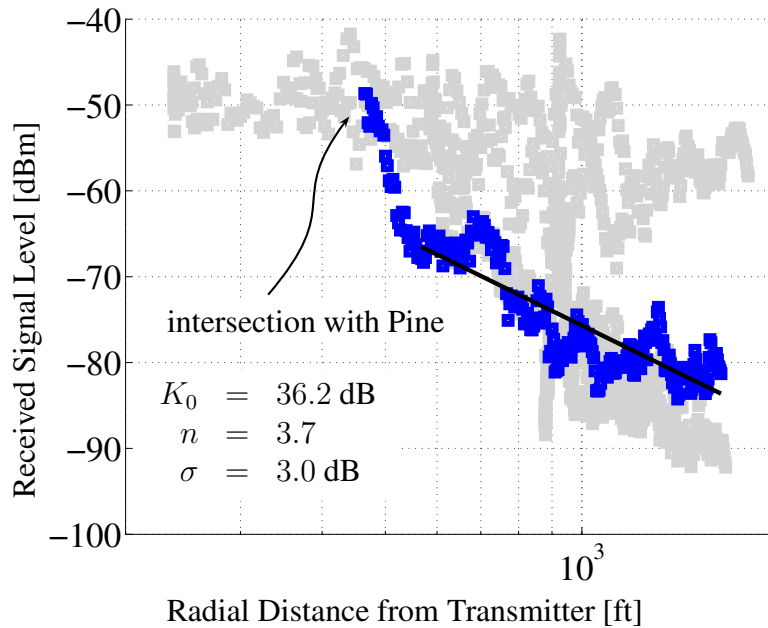


(b) 2003 Measurements

Figure 5.5: Path Loss Along Pine Street. Similar to those on Battery, the Pine Street measurements have an average path-loss curve that is close to that of free space, *i.e.*,  $n = 2$ .

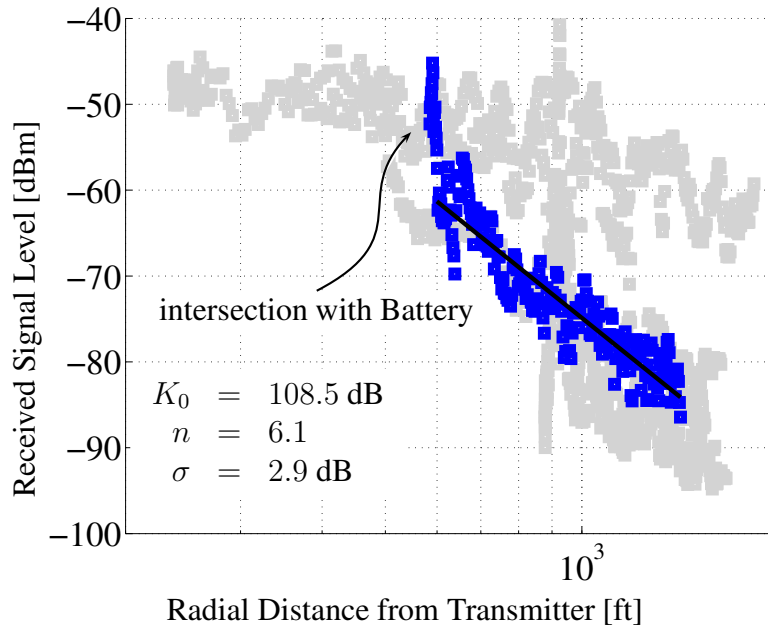


(a) 2002 Measurements

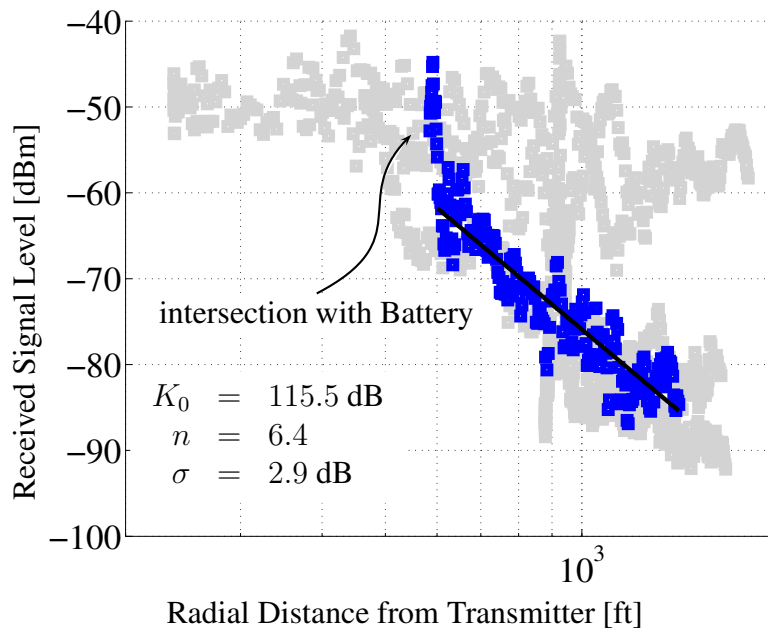


(b) 2003 Measurements

Figure 5.6: Path Loss Along Sansome Street. On Sansome Street, we see that for the street itself there is a path-loss trend that is separate from the transition at the intersection with Pine Street.

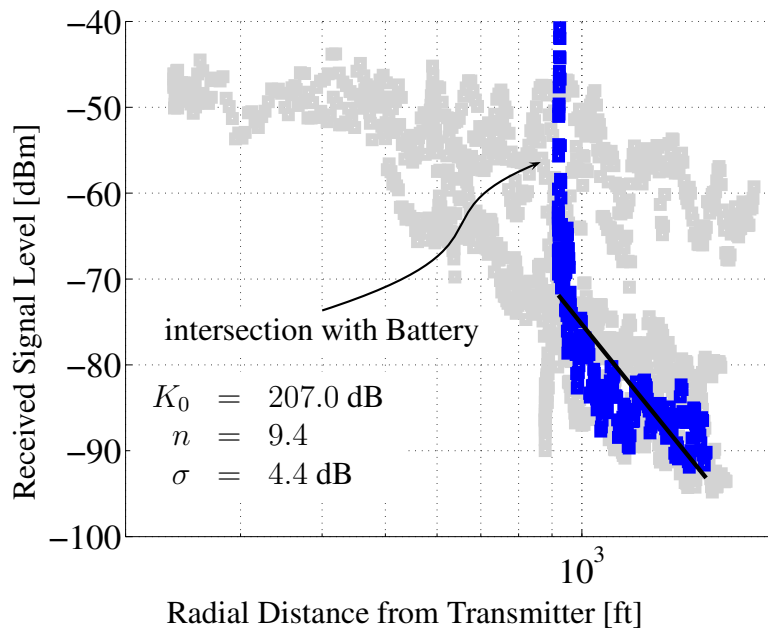


(a) 2002 Measurements

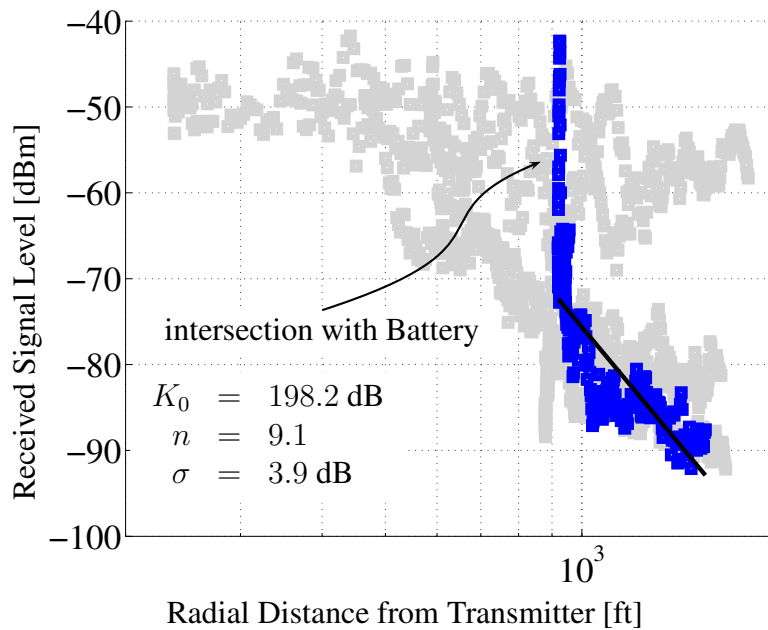


(b) 2003 Measurements

Figure 5.7: Path Loss Along California Street. Similar to Sansome Street, California has a distance-dependent trend along the street that is different from the transition at the intersection with Battery Street.

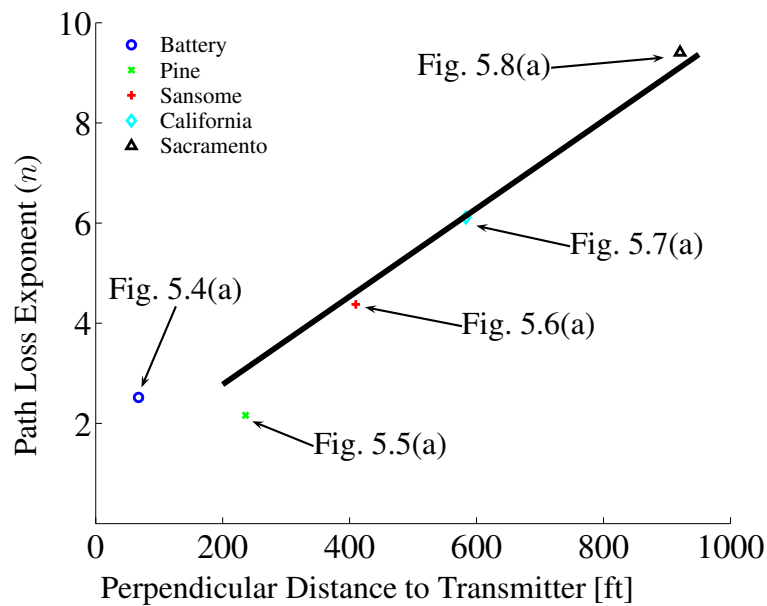


(a) 2002 Measurements

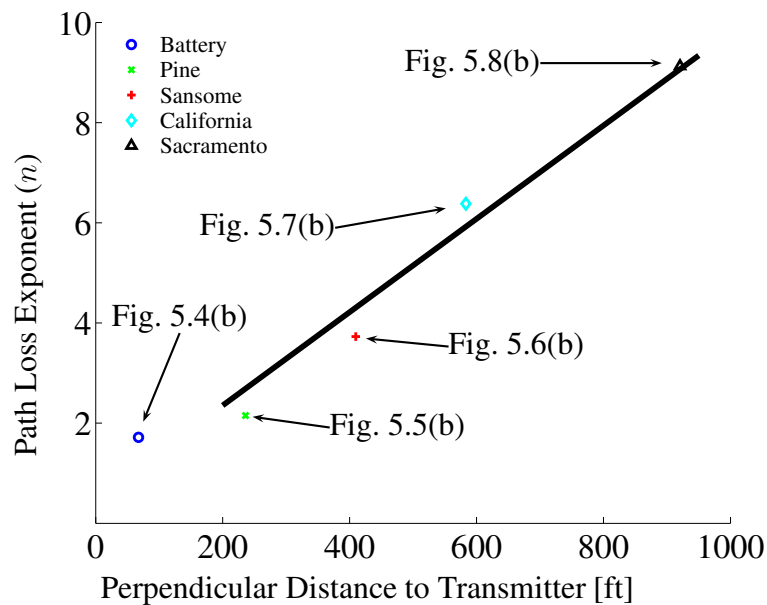


(b) 2003 Measurements

Figure 5.8: Path Loss Along Sacramento Street. Viewing Figs. 5.4 through 5.8 in turn, one can see that the distance-dependent trend becomes steeper and shifts down for streets that are farther away from the transmitter.

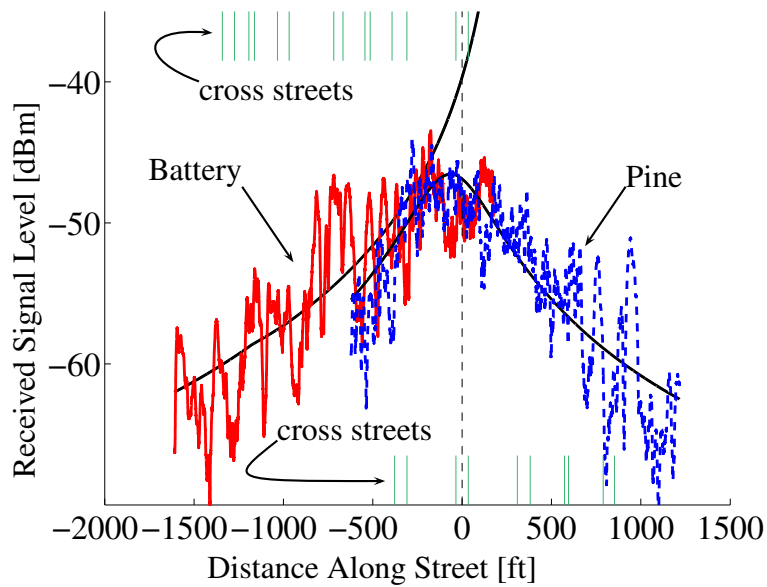


(a) 2002 Measurements



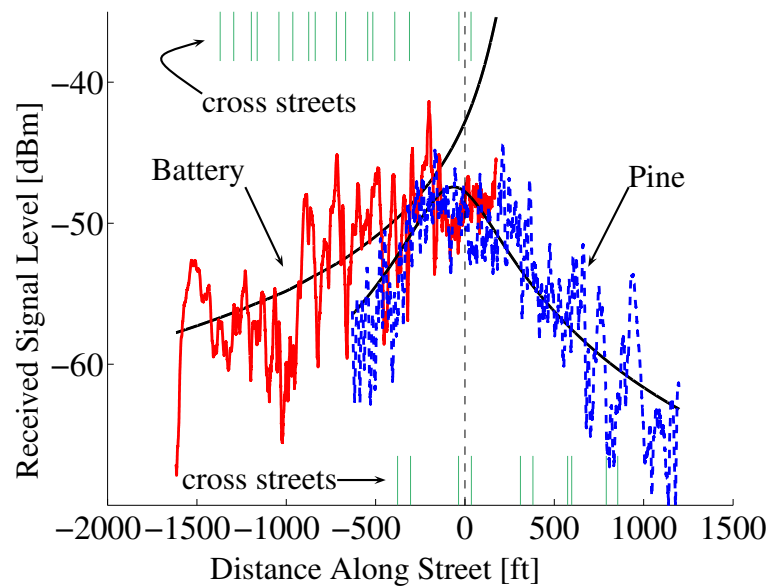
(b) 2003 Measurements

Figure 5.9: Path-Loss Trend. Summarizing the results in Figs. 5.4 through 5.8, we observe steeper path-loss characteristics, *i.e.*, higher values of  $n$ , for streets that are farther away from the transmitter.



(a) Battery &amp; Pine, 2002

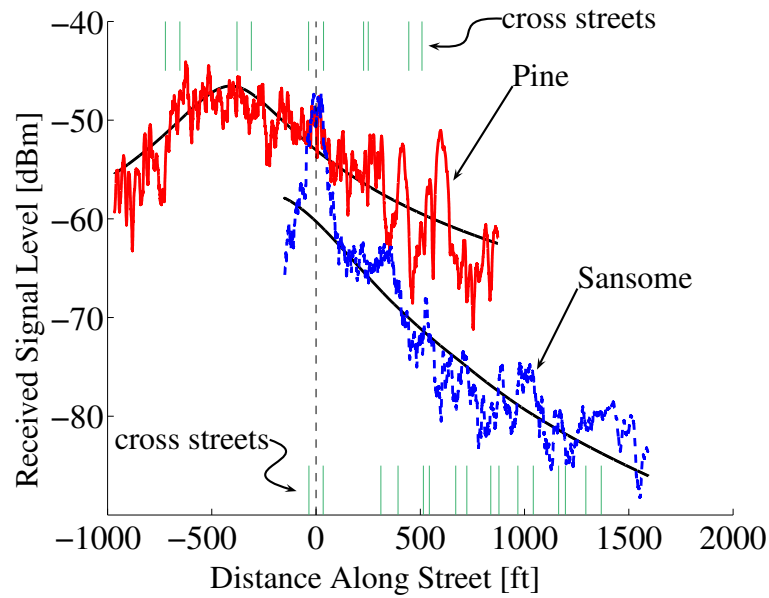
Figure 5.10: Distance-Dependent Trend Offset for Intersecting Streets. These plots overlay the average signal strength measured in two intersecting streets. The smooth, solid lines identify the distance-dependent trends. The markers at the top and bottom of each plot identify the edges of cross streets for each measurement presented. We also note the departure from the distance-dependent trend for measurements along Battery Street. This departure occurs on the street, near the transmitter, and can be attributed to changes in antenna pattern close to the base station.



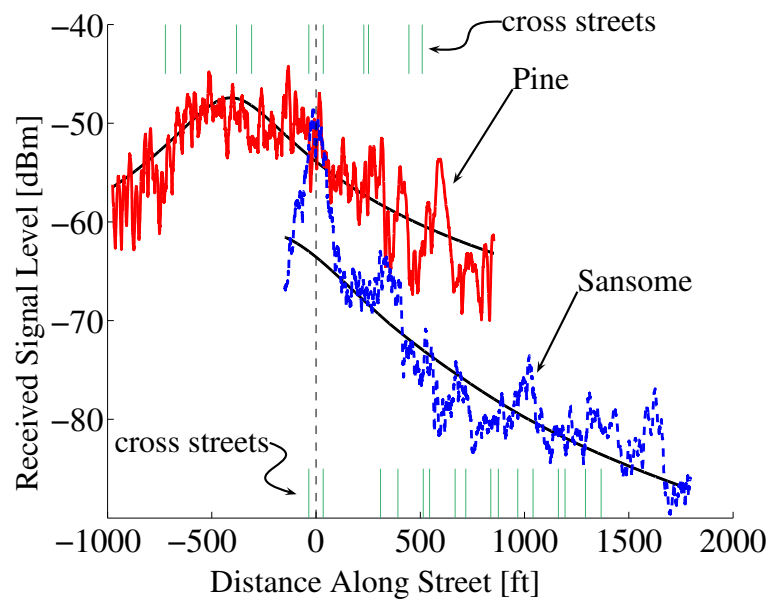
(b) Battery &amp; Pine, 2003

Figure 5.10: Distance-Dependent Trend Offset for Intersecting Streets (*continued*).



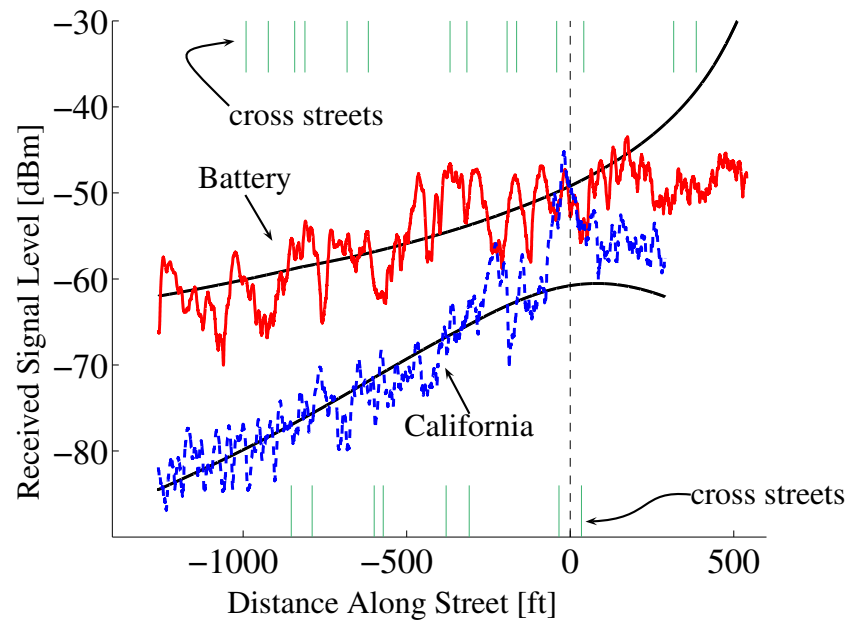


(c) Pine &amp; Sansome, 2002

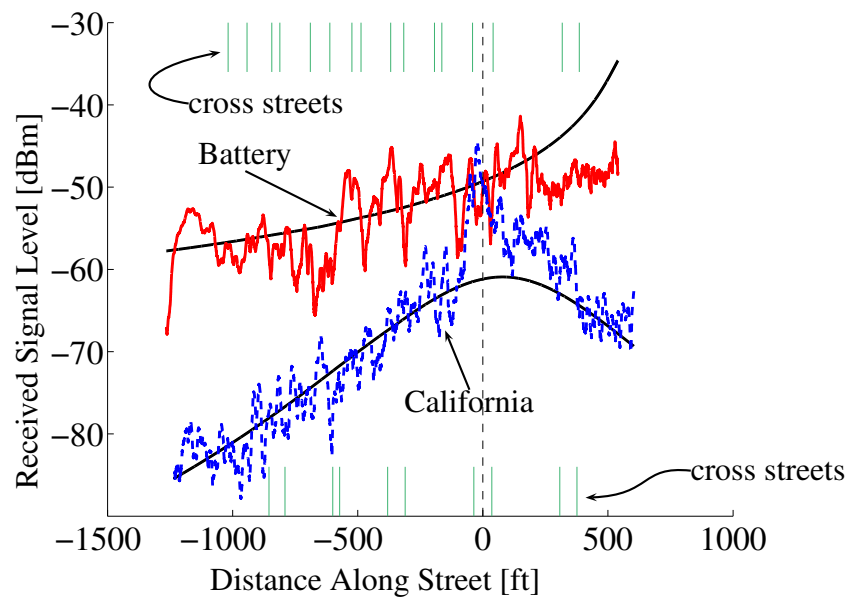


(d) Pine &amp; Sansome, 2003

Figure 5.10: Distance-Dependent Trend Offset for Intersecting Streets (*continued*).

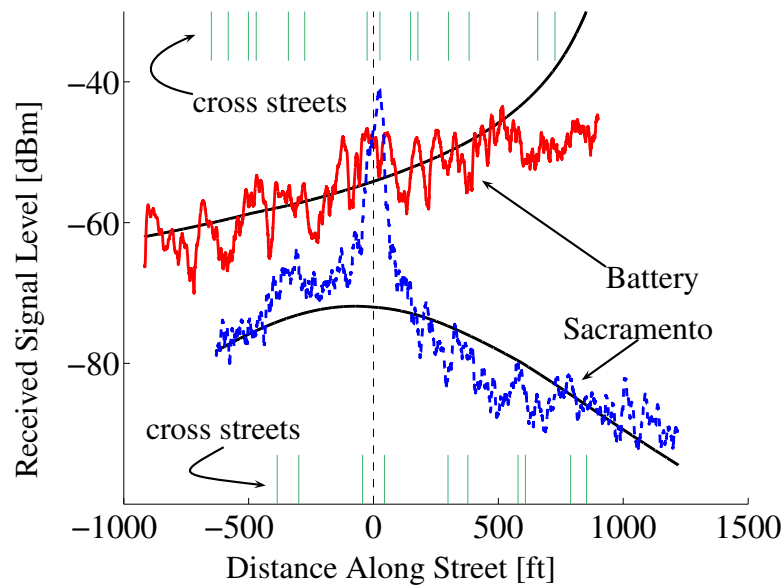


(e) Battery &amp; California, 2002

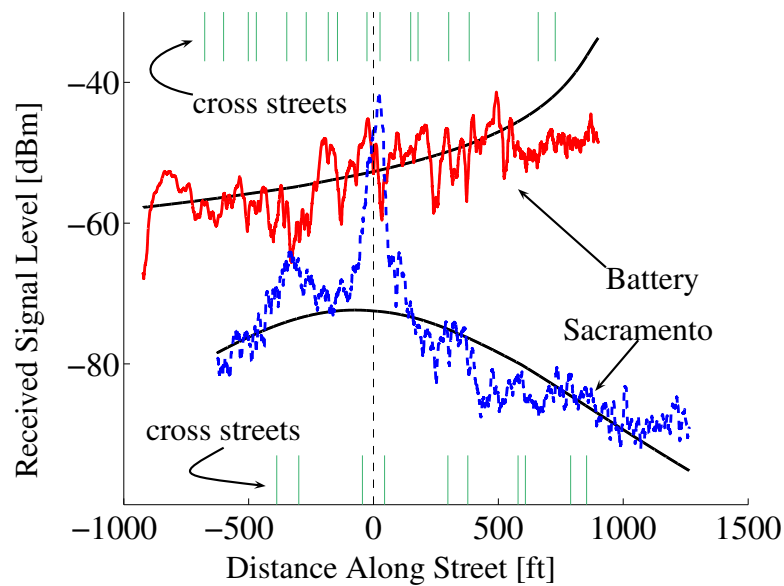


(f) Battery &amp; California, 2003

Figure 5.10: Distance-Dependent Trend Offset for Intersecting Streets (*continued*).

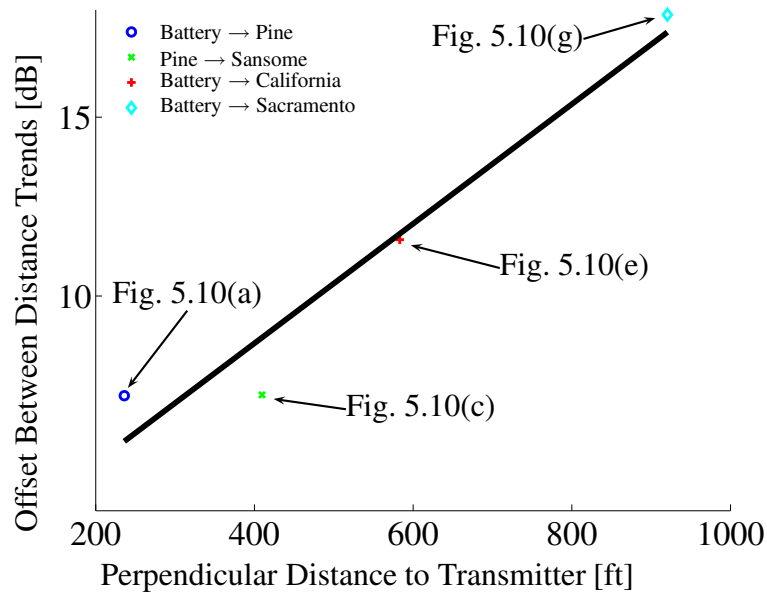


(g) Battery &amp; Sacramento, 2002

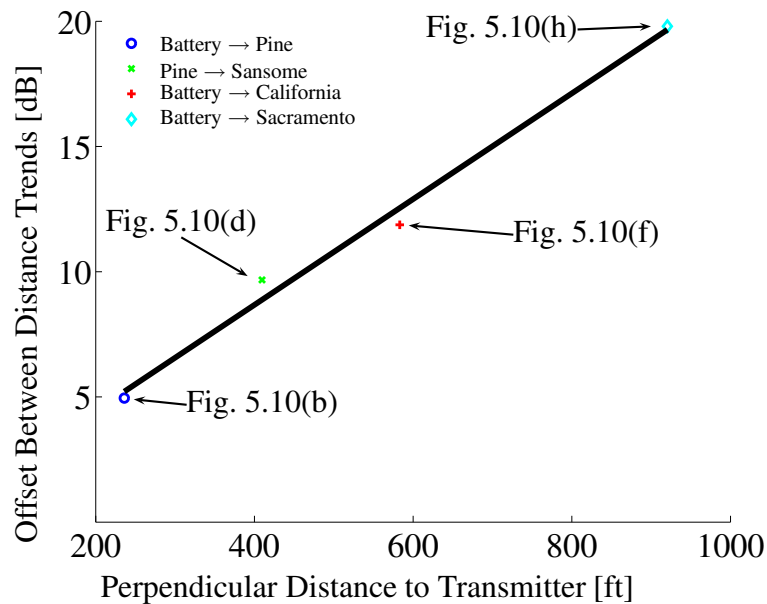


(h) Battery &amp; Sacramento, 2003

Figure 5.10: Distance-Dependent Trend Offset for Intersecting Streets (*continued*).

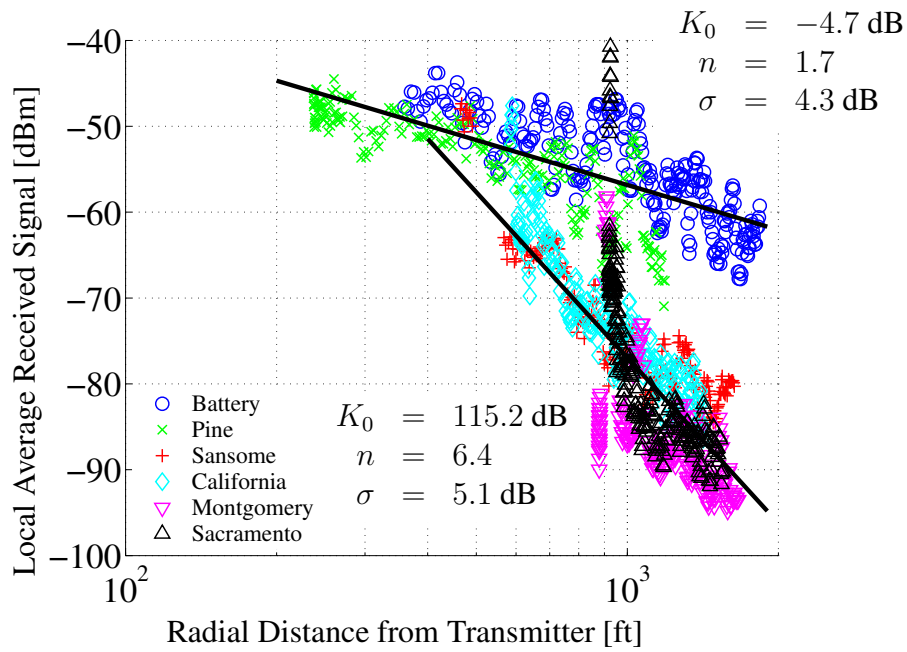


(a) 2002 Measurements

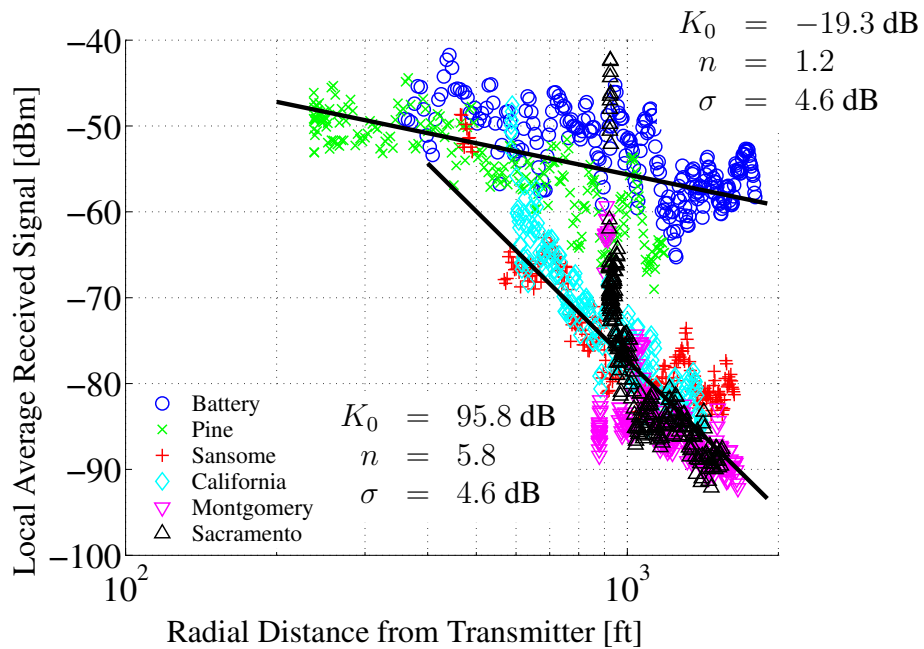


(b) 2003 Measurements

Figure 5.11: Distance Trend Offsets. Summarizing the results in Figs. 5.10(a)–(h), we observe that the offset between distance-dependent trends is greater for cross streets with intersections that are farther from the transmitter.

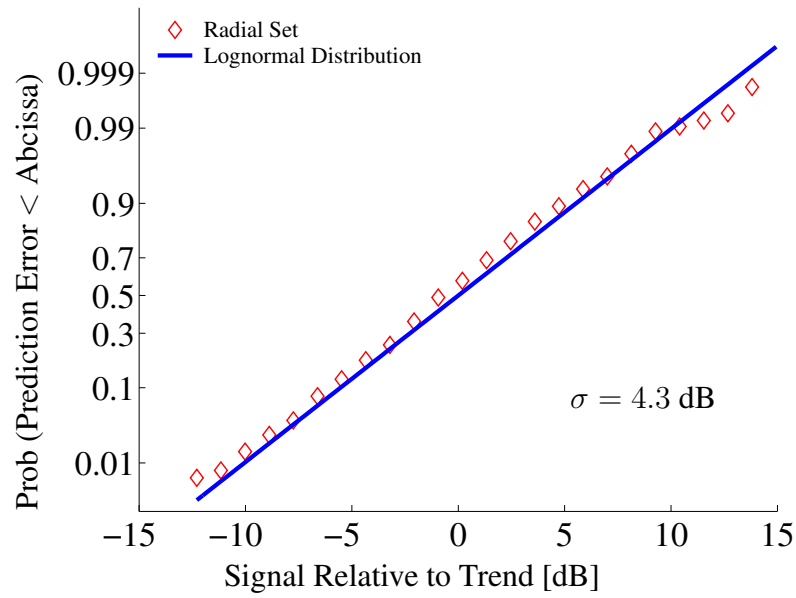


(a) 2002 Measurements

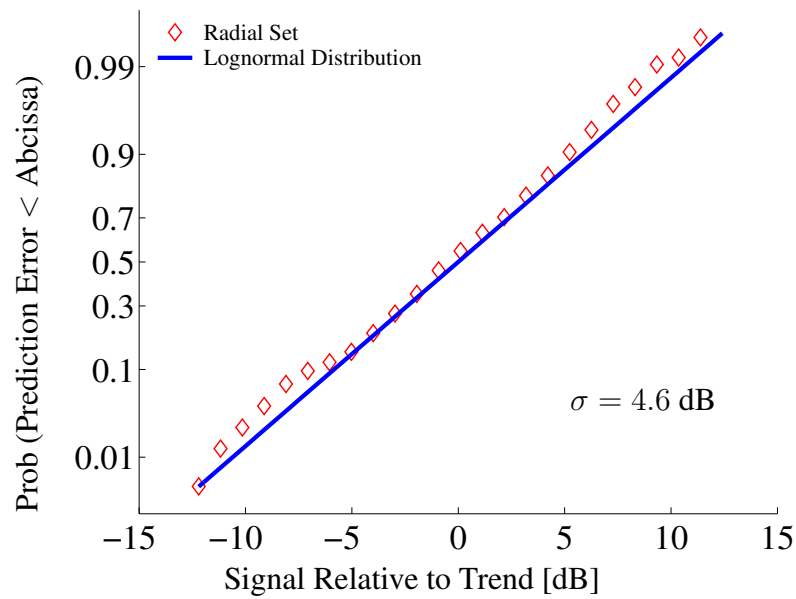


(b) 2003 Measurements

Figure 5.12: Partitioned Fit. By partitioning the streets into radial and cross-street sets, much better path-loss prediction is achieved.

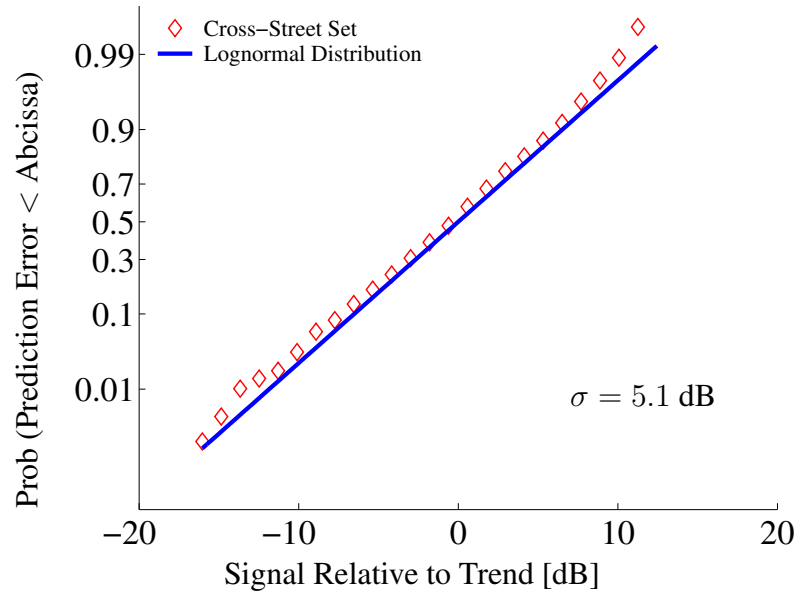


(a) Radial Set, 2002

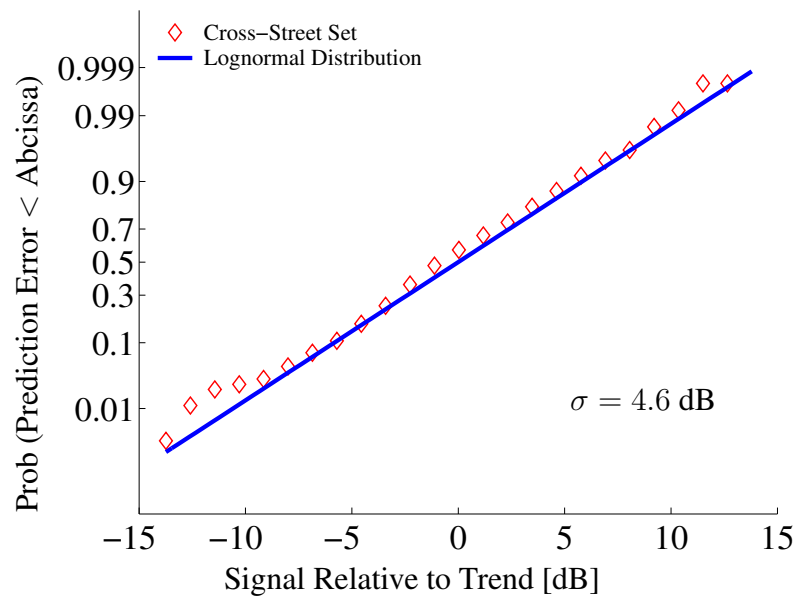


(b) Radial Set, 2003

Figure 5.13: CDF of Estimation Error. The distribution of large-scale averages around the distance-dependent trend is lognormal for both the radial and cross-street sets.



(c) Cross-Street Set, 2002



(d) Cross-Street Set, 2003

Figure 5.13: CDF of Estimation Error (*continued*).

## 5.4 Summary

In this chapter, we introduce some simple tools to augment path-loss modeling in urban environments. Using a map of the coverage area, the wireless engineer can quickly divide the streets of an urban cell into radial and cross-street sets. Each set has its own distance-dependent path-loss trend. The variation of the local averages around each path-loss trend follows a lognormal distribution. This method provides an efficient way to incorporate some structure of the street layout into the propagation model, thereby reducing the standard deviation of the path-loss prediction error by up to 6 dB.

Our method characterizes path loss in the cross streets based on distance from the transmitter, not the distance from the intersection with the radial street as is commonly done. Our method has the advantage of grouping multiple streets together based on a common distance metric. This greatly simplifies the modeling task since it may also be used in cases in which the exact propagation path is unknown.

Even though the transmitter antenna used in these experiments is much higher than those used in the referenced microcell studies, the qualitative behavior is very similar since the antenna is still located below the rooftops of the tall buildings in the vicinity.

The path-loss calculations are performed for both the 2002 and 2003 measurements. Even though the time span between these collections is 15 months, the results are strikingly similar. This similarity is a very general indication that some aspects of the measurements remain the same over time. The next chapter explores the repeatability of these measurements in greater detail.



## Chapter 6

# Repeatability of Large-Scale Signal Variations

The complexity of the wireless propagation environment has led to the use of statistical models to describe the propagation behavior of radio waves from transmitter to receiver. These statistics are used to predict certain measures of system performance, such as bit error rate, outage probability, etc., in various propagation environments. Using statistical models, any degree of determinism can potentially be exploited to enhance certain features of system performance.

In previous chapters, we discuss the various properties of signal propagation in urban environments. The previous discussions provide an adequate framework for describing what happens for a single measurement instance. For systems that exploit repeatability of the parameters of radio wave propagation, however, the previous models lack the description necessary to fully investigate such a system.

This chapter quantifies the repeatability of large-scale signal variations in an urban propagation environment. We propose a model to describe, and use field measurements taken in downtown San Francisco to quantify, how similar received signals appear when a mobile receiver revisits the same general area. The results establish bounds for the variation in repeated measurements taken on different days within a given street in the same and in different traffic lanes.

## 6.1 Motivation

In the past, the focus of propagation modeling was usually on describing the behavior of signal strength as a mobile receiver (or transmitter) operates in a given location relative to a stationary transmitter (or receiver). Given the likelihood that a mobile user may return to a previous location,

or that a different mobile user will enter a location that has previously been occupied, similarities in the received signal may be observed in the two measurements due to the similar surroundings. Exploiting this determinism leads to potential performance gains in the system.

Streets are excellent examples of situations in which repeated measurements are made. By design, vehicles are confined to well-defined lanes as they travel down a street. Any mobile receiver that proceeds down a lane is within a few wavelengths of a position that has at some point in the past been occupied by another receiver.

This occurrence has not been lost on researchers in the field. In particular, Wong and Cox [97–101] pioneered an effort in this area to exploit repeatability in large-scale signal variations to improve handoff performance. Match functions compare large-scale variation estimates against a reference profile of received signal strength to decide if a mobile user is approaching a handoff point. In this case, for multiple trajectories through the same geographical area, the large-scale variation is assumed to be the same on multiple runs, while the small-scale fading is assumed to be independent on each run. Narasimhan and Cox [58, 63] exploit the determinism in received signal strength by using a probabilistic neural network (PNN) to classify large-scale variation patterns to determine when handoffs should occur. After training, the PNN significantly reduces the number of unnecessary handoffs, reducing system overhead, while maintaining the performance of the radio links. Hellebrandt, *et. al.* [35, 36], suggest using databases of signal strength and propagation times from multiple base stations to estimate the position and velocity of mobile users.

The viability of these schemes, however, is contingent upon the reliability of the underlying signal-strength databases in terms of measurement accuracy and the manner in which those measurements change over time. Not only does the repeatability of a signal within a geographic area determine the feasibility of these systems, but the rate at which these patterns change over time determines the interval at which the databases must be updated to optimize and maintain system performance.

One recalls from Chapter 2 that the propagation of high-frequency signals from transmitter to receiver can be characterized by three properties: (1) a distance-dependent trend, (2) large-scale variation over tens of wavelengths, and (3) the small-scale fading indicated by rapid fluctuations in the received signal strength over distances less than a wavelength. The large-scale variation is the result of shadowing by large objects in the propagation environment, such as buildings and hills, while the small-scale fading is caused by phase additions of multiple wavefronts incident on the

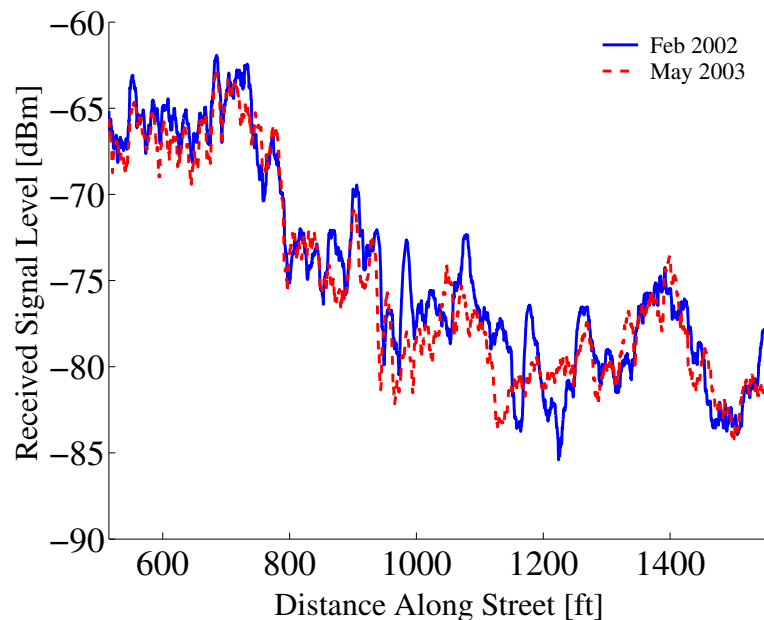


Figure 6.1: Two Drives Down Sansome Street. The signal strength profiles shown in this figure are the result of a  $10\lambda$  sliding window average. Although taken 15 months apart, the profiles are quite similar. At any given point along the street, however, the profiles differ slightly.

receiver.

Since the distance-dependent trend and the large-scale variation are governed by the physics of wave propagation around and through large, stationary objects and are determined primarily by the placement of these objects, one expects these characteristics to be somewhat repeatable at a given location. Since the small-scale variations are due to the phase additions of multiple paths at the receiver, small movements of the receiver or of the reflectors along one of the multiple paths can result in a large change in the signal level received. If one could control the precise locations of the transmitter, receiver, and all the scatterers in the environment from one measurement to the next, then the small-scale signal variations would be the same in both cases. Since the positions of some scatterers change over time, one expects that only the statistics of the small-scale fading remain the same over repeated measurements in the same area.

For example, Fig. 6.1 shows a comparison of two different drives along Sansome Street taken 15 months apart. Each trace shows the signal after it has been averaged over 10 wavelengths to estimate the large-scale variation. While the curves do not lie directly on top of one another, they are quite similar, particularly for the larger-scale variations. We are interested in quantifying this



Figure 6.2: Measurement Area. The repeatability analysis is performed on sections of streets that exhibit an exponential distance-dependent trend. The transitions from intersections with Pine or Battery are not included. Montgomery is not included because of the many transitions from intersections with streets that have higher signal strength.

degree of similarity and determining what factors contribute to the differences.

The measurement area for this analysis is as shown in Fig. 6.2. The measurements are taken in the streets. The measurement locations are indicated by the thick lines in the streets on the map. We analyze the sections of street that best fit an exponential path-loss characteristic. As seen in Chapters 4 and 5, there is a path-loss trend along the street that is different from transition regions near intersections with streets experiencing a stronger signal. Montgomery Street is not included in the analysis of this chapter since it intersects several streets in which the signals are stronger. After the corner transition regions are removed there is not a continuous section longer than a city

block that has a consistent distance trend.

To make direct comparisons of measurements taken in the same street at different times, extra care is used when determining the position corresponding to each measurement sample. This comparison is a primary reason for aligning the distance axes of each measurement run with the corners of buildings along a drive route as described in Chapter 3.

## 6.2 The Repeatability Model

Recalling that the received signal can be characterized by a distance trend and large- and small-scale fading, the received signal level is represented as

$$P(\mathbf{x}) = D(\mathbf{x})L(\mathbf{x})Y(\mathbf{x}) \quad (6.1)$$

where  $P(\mathbf{x})$  is the received power at location  $\mathbf{x}$ ,  $D(\mathbf{x})$  is the distance-dependent trend,  $L(\mathbf{x})$  is the large-scale variation, and  $Y(\mathbf{x})$  is the small-scale variation. Using the transmitter as the origin of the coordinate system,  $\hat{D}(\mathbf{x})$ , when expressed in dB, is a regression fit of  $\langle P(\mathbf{x}) \rangle_W$  to the formula below:

$$\hat{D}_{dB}(\mathbf{x}) = K_0 + 10n \log_{10}(|\mathbf{x}|). \quad (6.2)$$

$K_0$  is a constant that accounts for transmit power, antenna gains, cable losses, etc., and  $n$  is the path-loss exponent.  $\langle \cdot \rangle_W$  denotes the spatial average of the process over  $\mathbf{x}$  in the averaging window  $W$ .

We obtain an estimate of the large-scale variation by removing the distance trend from the spatial average:

$$\hat{L}(\mathbf{x}) = \frac{\langle P(\mathbf{x}) \rangle_W}{\hat{D}(\mathbf{x})}. \quad (6.3)$$

The objective is to average out the rapid fluctuations caused by the small-scale fading process, leaving the remaining variations to be interpreted as the large-scale variation. Examples of this estimation procedure are shown in Appendix A using the San Francisco measurements.

The correlation length of the small-scale fading process is wavelength-dependent, and at cellular frequencies, the small-scale fading process decorrelates at a relative distance much shorter than the correlation length of the large-scale process, which depends on the sizes of large objects,

*e.g.*, buildings and hills, in the environment. One can estimate the large-scale process by averaging over a distance that is several times longer than the correlation distance of the small-scale fading process, which is usually on the order of a wavelength or less. There is, however, a tradeoff in the choice of the averaging interval,  $W$ , in estimating the large-scale variation. Since averaging is performed over a finite interval, not all of the randomness of the small-scale process is averaged out. For smaller values of  $W$ , the estimate  $\hat{L}(\mathbf{x})$  is dominated by variations in the small-scale fading process that are not completely averaged out. On the other hand, as  $W$  becomes larger, the variations in  $L(\mathbf{x})$  are smoothed out as well (see Chapter 4). Austin and Stüber [7] suggest averaging intervals of  $20\text{--}40\lambda$ , where  $\lambda$  is the signal wavelength. For comparing one data set against another, as in Fig. 6.1, we use a slightly smaller window,  $10\lambda$ , the reasons for which become apparent later in this chapter.

We test the hypothesis that the large-scale fading process is repeatable for two different trips down the same street by introducing an additional process,  $\ell(\mathbf{x})$ , that accounts for any differences in the large-scale variation on the second run. To model the difference, we replace the  $L(\mathbf{x})$  term in the first measurement by  $L_r(\mathbf{x})\ell(\mathbf{x})$ , where  $L_r(\mathbf{x})$  is the repeatable part of the large-scale variation that is common to the second measurement. To quantify the repeatability, we bound the variance of the dissimilarity process  $\ell(\mathbf{x})$ .

The distance trend  $D(\mathbf{x})$  describes the distance-dependent behavior of the received signal strength. If the large-scale fading is different on the second run, then  $D(\mathbf{x})$  is different as well. For this analysis, however, we suppose that the distance trend is the same in both cases and that any minor differences in distance trend are absorbed into  $\ell(\mathbf{x})$ .

Next, we divide the length of the data set into finite averaging intervals,  $W_i$ . We then consider the ratio of the smoothed power estimates for different window sizes:

$$\begin{aligned} \frac{S_1(\mathbf{x}_i)}{S_2(\mathbf{x}_i)} &= \frac{\langle P_1(\mathbf{x}) \rangle_{W_i}}{\langle P_2(\mathbf{x}) \rangle_{W_i}} \\ &= \frac{\langle D(\mathbf{x})L_r(\mathbf{x})\ell(\mathbf{x})Y_1(\mathbf{x}) \rangle_{W_i}}{\langle D(\mathbf{x})L_r(\mathbf{x})Y_2(\mathbf{x}) \rangle_{W_i}}. \end{aligned} \tag{6.4}$$

Here,  $i$  is used to index equally spaced locations along the drive route. The averaging operation  $\langle \cdot \rangle_{W_i}$  denotes averaging over interval  $W_i$ , centered on position  $\mathbf{x}_i$ . If the large-scale process is repeatable, *i.e.*,  $\ell(\mathbf{x}) = 1$ , and there are no small-scale variations, *i.e.*,  $Y_1(\mathbf{x}), Y_2(\mathbf{x}) = 1$ , the

ratio (6.4) is always 1. Including the uncertainties  $\ell(\mathbf{x})$ ,  $Y_1(\mathbf{x})$ , and  $Y_2(\mathbf{x})$ , however, yields a distribution of ratios over the data set. By determining the properties of  $\ell(\mathbf{x})$ , we quantify the repeatability of the two measurements. For the data sets analyzed in this chapter, the properties of  $\ell(\mathbf{x})$  are determined indirectly, by observing the statistics of the ratio (6.4) in simulation and adjusting the simulation parameters until the statistics of (6.4) match those of the measured data.

The numerator and denominator in (6.4) are essentially random variables due to the finite averaging window. The extension of the domain of the denominator down to zero raises the concern that the distribution of the ratios might be unbounded. In fact, there are distributions for which the statistics of the ratio are unbounded. In this case, however, for the averaging windows used ( $W_i \geq \lambda$ ), the numerator and denominator exhibit statistics that fit a lognormal distribution for both simulation and measurement data. Furthermore, when expressed in decibels, the ratio becomes the sum of two Gaussian random variables for which the statistics are both bounded and well-defined.

### 6.3 Simulation for Comparison

For comparison to the measurement data, the simulations must generate the random quantities on the right-hand side of equation (6.4). The statistics of the ratio (6.4) taken at locations  $\mathbf{x}_i$  along the route are compared for a number of values of the averaging window length  $W$ . Plotting the ratio (6.4) as a function of the averaging interval  $W$  yields a curve characterizing the tradeoff of the averaging window and displaying the effects of both the large- and small-scale variation.

Since  $D(\mathbf{x})$  varies much more slowly than either the small-scale fading or the large-scale variations in the signal, it is approximately constant over the decorrelation length of any of the simulated random processes. As a result, it is assigned a constant value in all of the simulations.

An overview of the simulation process is shown in Fig. 6.3. The repeatable large-scale variation  $L_r(\mathbf{x})$  is a lognormal sequence that is filtered to give rise to an exponential autocorrelation as observed by Gudmundson [31]. Although the exponential autocorrelation does not always apply well for single streets, as mentioned by Gudmundson, it provides an adequate description of the behavior when the corner transition regions are not included.<sup>1</sup>

We define the decorrelation length as the spatial offset at which the normalized autocorrelation

---

<sup>1</sup>See Appendix A for autocorrelations of the estimated large-scale variation,  $\hat{L}(\mathbf{x})$ , for measurements in the financial district.

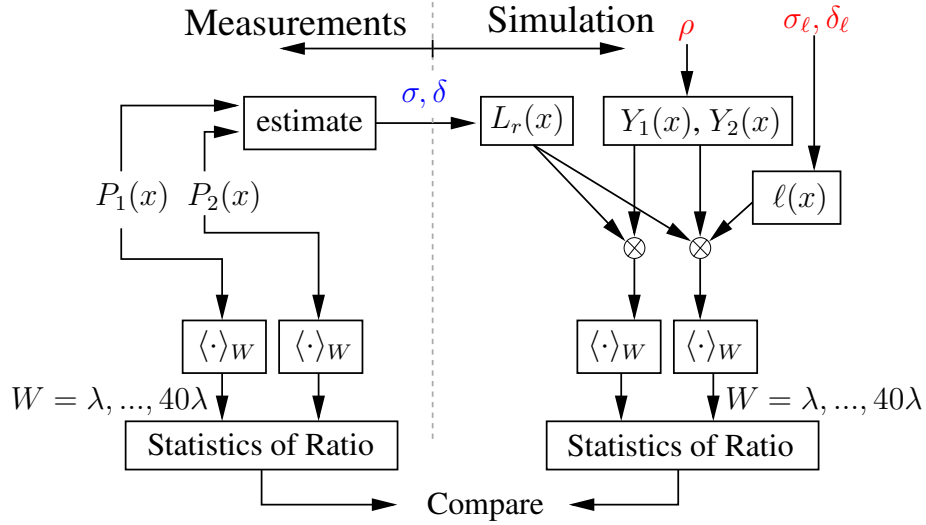


Figure 6.3: Overview of Comparison of Simulation and Measurements. The measurements  $P_1(\mathbf{x}), P_2(\mathbf{x})$  are averaged and the statistics of the ratio (6.4) are computed over a range of averaging intervals to compare with simulation results. The statistics of the large-scale variation are estimated from  $P_1(\mathbf{x}), P_2(\mathbf{x})$  to generate  $L_r(\mathbf{x})$ . The free parameters  $\rho$ ,  $\sigma_\ell$ , and  $\delta_\ell$  are adjusted until the simulation results match those of the measured data.

function reduces to 0.5. The decorrelation length and the standard deviation of  $L_r(\mathbf{x})$  are estimated from the measured data for each street in which the comparison is made. The process  $\ell(\mathbf{x})$  is generated in the same manner as, but independent of,  $L_r(\mathbf{x})$ . By construction, it has a decorrelation length less than or equal to that of the corresponding  $L_r(\mathbf{x})$ .

The small-scale fading processes  $Y_1(\mathbf{x})$  and  $Y_2(\mathbf{x})$  are generated from independent complex Gaussian sequences, constituting the baseband representation  $r_1(\mathbf{x})$  and  $r_2(\mathbf{x})$  of the received signal, as shown in Fig. 6.4. The sequences are filtered to have the Doppler spectrum characteristic of Clarke's two-dimensional isotropic scattering as described in [39, Ch. 1]. The power in the small-scale fading term is computed by multiplying the baseband representation by its complex conjugate:

$$\begin{aligned} Y_1(\mathbf{x}) &= r_1(\mathbf{x})r_1^*(\mathbf{x}) \\ Y_2(\mathbf{x}) &= r_2(\mathbf{x})r_2^*(\mathbf{x}). \end{aligned} \tag{6.5}$$

We account for the repeatability of the small-scale fading term by introducing a parameter to describe the similarity of the small-scale fading processes from one run to the next. The correlation



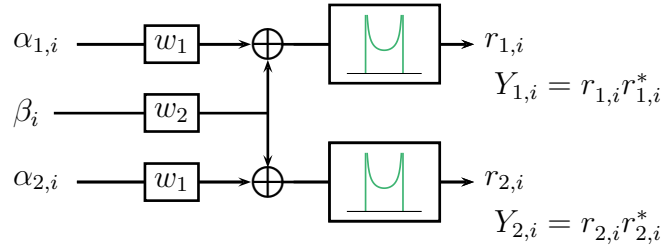


Figure 6.4: Small-Scale Fading Simulation. To generate the correlation properties consistent with Clarke's model, i.i.d. complex Gaussian sequences are filtered. The sequences  $\alpha_1, \alpha_2, \beta$  are complex Gaussians. The weighting factors  $w_1, w_2$  adjust the level of cross-correlation between the simulated small-scale fading terms. Multiplying the generated elements by their complex conjugates yields the power of the small-scale fading term.

coefficient

$$\rho = \frac{\text{COV}(|r_1|, |r_2|)}{\sigma_{|r_1|} \sigma_{|r_2|}} \quad (6.6)$$

describes the normalized cross-correlation of the envelopes of  $r_1(\mathbf{x})$  and  $r_2(\mathbf{x})$  where  $\sigma_{|r_1|}$  and  $\sigma_{|r_2|}$  are the standard deviations of  $|r_1(\mathbf{x})|$  and  $|r_2(\mathbf{x})|$ , respectively.

In some cases these two processes are correlated with each other, and in others, they are uncorrelated. To generate the appropriate cross-correlation, the unfiltered Gaussians are generated with a commonly weighted component as follows:

$$\begin{aligned} z_{1,i} &= w_1 \alpha_{1,i} + w_2 \beta_i \\ z_{2,i} &= w_1 \alpha_{2,i} + w_2 \beta_i. \end{aligned} \quad (6.7)$$

$\alpha_1, \alpha_2$ , and  $\beta$  are independent, complex Gaussian sequences;  $w_1, w_2$  are fractional weighting constants with  $w_1 + w_2 = 1$ ; and  $z_1$  and  $z_2$  are the sequences that are subsequently filtered and multiplied by complex conjugates to generate  $Y_1(\mathbf{x})$  and  $Y_2(\mathbf{x})$ . Figure 6.5 shows the resulting cross-correlation for different values of  $w_2$ .

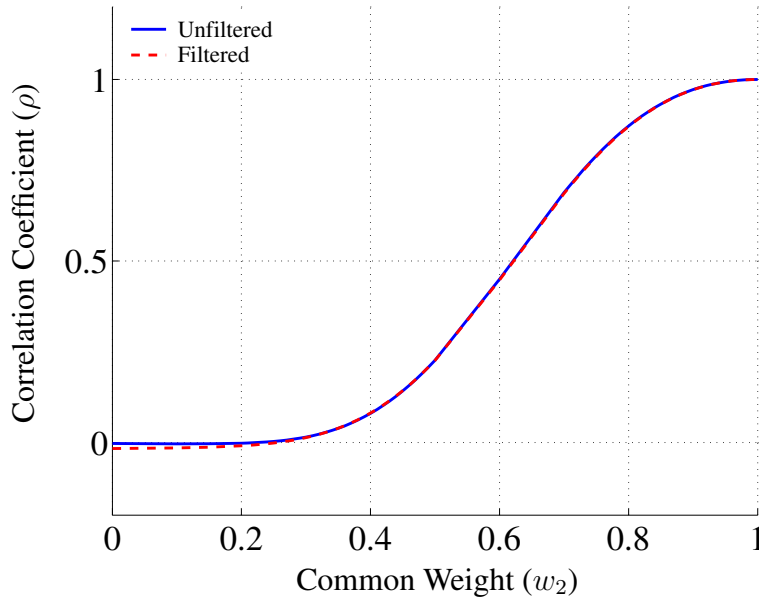


Figure 6.5: Cross-Correlation for Different Weights. With  $w_1, w_2 \geq 0$  and under the constraint  $w_1 + w_2 = 1$ , the envelope cross-correlation generated by weighting factor  $w_1$  is shown in this figure. The spectral shaping is seen to have little effect on the relationship between  $w_1$  and  $\rho$ .

The free parameters in the simulation are the correlation coefficient  $\rho$  of envelope of the small-scale fading terms and the standard deviation  $\sigma_\ell$  and correlation length  $\delta_\ell$  of the dissimilarity process  $\ell(\mathbf{x})$ . These quantities are adjusted until the output of the simulator matches the behavior of the measurements for a particular street. Examples of simulator output are shown in Appendix B, illustrating the qualitative behavior of the large- and small-scale variations for different simulator settings.

## 6.4 Comparing Data Sets

The standard deviation of the ratio (6.4), when the averaging window interval is varied, provides the basis for comparing two different sets of measurements along the same street. The ratio is converted to decibels before the statistics are computed.

The comparison plots for drives along Battery Street are shown in Fig. 6.6(a). Each curve represents a comparison between two measurements made in the same traffic lane along the street. The lower curve represents a comparison between two measurement drives that were taken on

the same night. In this case, the standard deviation of  $\ell(x)$  is zero, meaning that the large-scale variation is completely repeatable. Any differences in the overlay plot in Fig. 6.6(b) are the results of finite averaging. Furthermore, the correlation coefficient  $\rho$  between the small-scale variation processes is 0.45, meaning that the small-scale fading processes are not independent between the two runs. Cross correlation of 100% is not expected since the receiver location is the same only to within several inches between measurement runs, and there is no control over the positions of other scatterers in the environment. The upper curve in Fig. 6.6(a) represents a comparison between two drives made 15 months apart. In this case,  $\rho = 0$ , so the small-scale processes are uncorrelated and  $\sigma_\ell = 3.0$  dB, meaning that the large-scale variations are not identical, and the value of  $\sigma_\ell$  quantifies the degree to which they are dissimilar. For comparison, Fig. 6.6(c) shows the resulting overlay. One can clearly see that the two runs in this case are not as similar as the ones taken on the same night.

The dashed line in Fig. 6.6(a) corresponds to both  $\rho = 0$  and  $\sigma_\ell = 0$  dB. All comparisons in which the curve falls below the dashed line have repeatable large-scale variations, *i.e.*,  $\sigma_\ell = 0$  dB, and small-scale variations that are correlated with each other, *i.e.*,  $\rho \neq 0$ . These curves are characterized by the single parameter  $\rho$ . As  $\rho$  increases, the comparison curve moves downward and flattens out.

Comparisons in which the curve falls above the dashed line have small-scale fading processes that are uncorrelated, *i.e.*,  $\rho = 0$ , and the degree of dissimilarity between large-scale processes is measured by the standard deviation,  $\sigma_\ell$ , and the decorrelation length,  $\delta_\ell$ , of the process  $\ell(\mathbf{x})$ . These curves are characterized by two parameters,  $\sigma_\ell$  and  $\delta_\ell$ . Generally, the value of  $\sigma_\ell$  shifts the curve up or down, and the value of  $\delta_\ell$  determines the slope of the asymptote as the averaging window increases. For smaller values of  $\delta_\ell$ , the asymptote becomes steeper. Figures in Appendix B illustrate the manner in which the comparison curve changes with adjustments to  $\rho$ ,  $\sigma_\ell$ , or  $\delta_\ell$ .

The results for the entire coverage area are summarized in Table 6.1. The ‘Reference’ column calls out Figs. 6.6 through 6.14, referring to the corresponding simulation comparison figure from which the table values are derived. Each comparison figure calls out an overlay plot that shows the similarities qualitatively. The table column labeled ‘Same Night’ shows comparisons between measurements made on May 6, 2003, taken between midnight and 4:00 A.M. with little or no traffic. The column labeled ‘Same Day’ shows comparisons between measurements made on February 15, 2002, taken between 6:00 and 7:30 A.M. under moderate traffic conditions. The comparisons in

the third column, labeled ‘10 Days Apart,’ are for measurements made 10 days apart (Feb. 15–25, 2002). The measurement times are 6:30/9:30 A.M. and 6:00/8:20 A.M., respectively. The fourth column, labeled ‘15 Months Apart,’ compares the data between the 2002 and 2003 measurement campaigns. In this column, the comparisons are made between measurements taken with no traffic (2003) to those made with light to moderate traffic (2002). Because measurements were not made multiple times over the entire coverage area during the 2002 campaign, data are not available for the same comparisons on all streets. The remaining comparisons are summarized in Table 6.1(b), where the columns correspond to the first and last columns of Table 6.1(a).

Street (lane)	Reference	Same Night			Same Day		
		$\rho$	$\sigma_\ell$ [dB]	$D_\ell$ [ $\lambda$ ]	$\rho$	$\sigma_\ell$ [dB]	$D_\ell$ [ $\lambda$ ]
Battery (center)	Fig. 6.8	0.54	0	–	0	0.4	15
California (left)	Fig. 6.9	0.04	0	–	0	2.3	6
Sansome	Fig. 6.7	0.64	0	–	0.36	0	–

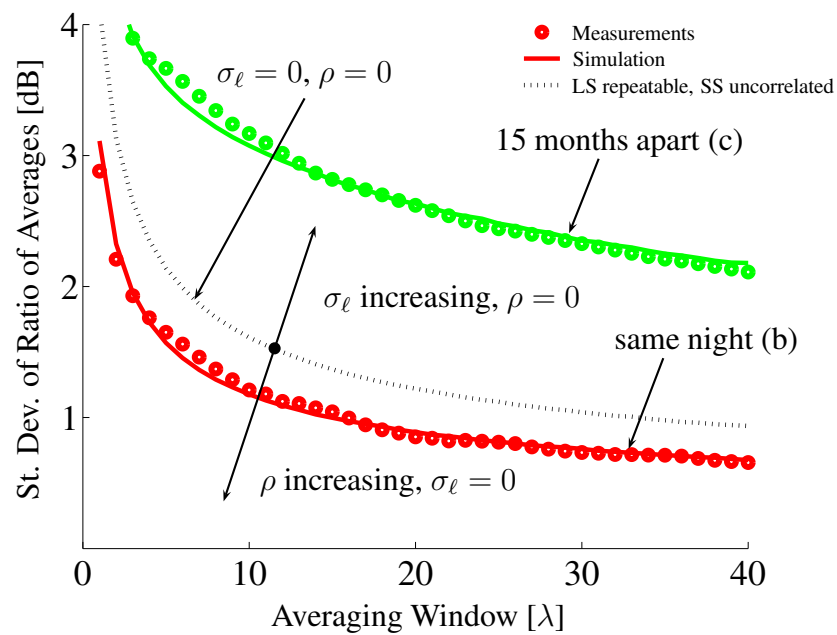
Street (lane)	Reference	10 Days Apart			15 Months Apart		
		$\rho$	$\sigma_\ell$ [dB]	$D_\ell$ [ $\lambda$ ]	$\rho$	$\sigma_\ell$ [dB]	$D_\ell$ [ $\lambda$ ]
Battery (center)	Fig. 6.8	0	2.8	10	0	2.5, 1.8	10
California (left)	Fig. 6.9				0	2.5	10
Sansome	Fig. 6.7	0.13	0	–	0	1.3	16

(a) Repeatability over Time

Street (lane)	Reference	Same Night			15 Months Apart		
		$\rho$	$\sigma_\ell$ [dB]	$D_\ell$ [ $\lambda$ ]	$\rho$	$\sigma_\ell$ [dB]	$D_\ell$ [ $\lambda$ ]
Battery (left)	Fig. 6.6	0.45	0	–	0	3.0	7
Battery (center)	Fig. 6.8	0.54	0	–	0	2.5, 1.8	10
California (left)	Fig. 6.9	0.04	0	–	0	2.5	10
California (right)	Fig. 6.10	0.50	0	–			
Clay	Fig. 6.11	0.17	0	–	0	4.4	30
Sacramento	Fig. 6.12	0	0.6	30	0	1.8	10
Sansome	Fig. 6.7	0.64	0	–	0	1.3	16
Pine (left)	Fig. 6.13	0.29	0	–			
Pine (right)	Fig. 6.14	0.45	0	–	0	0.8	5

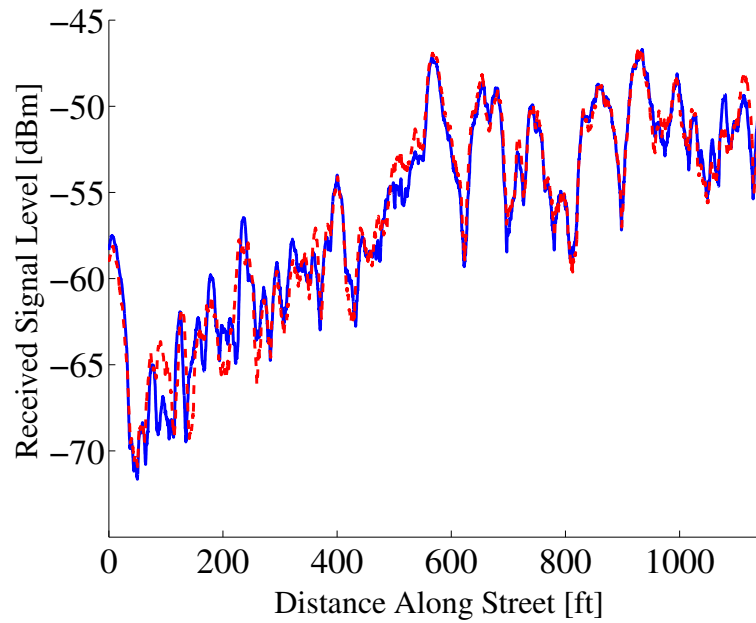
(b) Long-Term Repeatability

Table 6.1: Summary of Same-Lane Repeatability Simulations. This table lists the simulation parameters for which the simulations match the behavior of the measured data when comparing signal strength profiles for measurements in the same lane taken at different times. The ‘reference’ column calls out the comparison curves to which the lines in this table refer. Results for streets in which measurements are available at several different time intervals are shown in (a), and results for streets with measurements on the same night and at 15-month intervals are shown in (b).

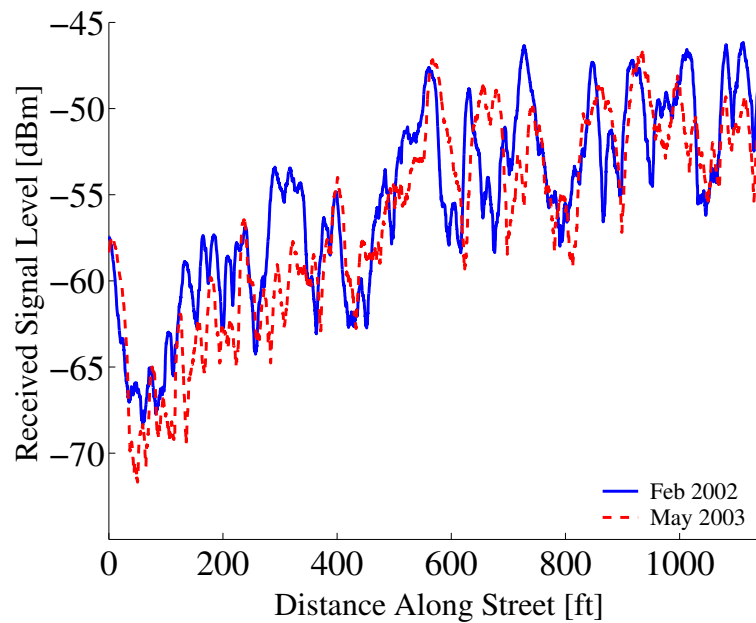


(a) Comparisons Using the Repeatability Model

Figure 6.6: Signal Strength Comparisons for the Left Lane of Battery Street. The measured and simulated results for the repeatability model are shown in (a), and direct overlays of the corresponding signal strength profiles are shown in (b),(c).



(b) Two Measurements Made on the Same Night



(c) Two Measurements Made 15 Months Apart

Figure 6.6: Signal Strength Comparisons for the Left Lane of Battery Street (*continued*).

Figure 6.7(a) shows a progression of the repeatability of the measurements over time. The knees of the comparison curves occur around an averaging window length of  $10\lambda$ , suggesting it is a good choice to use when directly comparing the signal strength values as shown in overlay plots, such as Fig. 6.1. Measurements taken at night when there was little or no traffic provided the highest degree of repeatability ( $\rho = 0.64$  and  $\sigma_\ell = 0\text{dB}$ ). The comparison between two measurements made as the morning commute was beginning shows less cross-correlation between the small-scale processes ( $\rho = 0.36$ ). Proceeding up the chart, the next curve shows even less cross-correlation ( $\rho = 0.13$ ) when compared 10 days apart. Finally, when compared 15 months apart, the dissimilarity process has a standard deviation of  $\sigma_\ell = 1.3\text{ dB}$ .

A similar trend holds for Battery Street (Fig. 6.8), but there are indications that the time of day at which a signal was measured has an impact on its repeatability. Notably, the value of  $\sigma_\ell = 2.8\text{ dB}$  from the 10-day comparison is the result of measurements made during different traffic conditions (6:30/9:30 A.M.). The changing traffic conditions may also account for the two values of  $\sigma_\ell$  in the fourth column. The same 2002 data sets were measured against the 2003 data that were taken when there was very little traffic. The lower value (1.8 dB) corresponds to the 6:30 A.M. comparison, which had lighter traffic than did the comparison with the 9:30 A.M. run.

The differences occurring around 200 ft in Figs. 6.8(d) through 6.8(f) appear to account for the discrepancy in the values for  $\sigma_\ell$ . Since this location is further away from the transmitter, it supports the notion that traffic conditions in the locality cause additional shadowing on the receiver during the Feb. 25, 2002, measurement. Also supporting this interpretation is the 15-month comparison of Sansome Street. In this case, the equivalent early and late comparisons agreed completely as the two sets of measurement data lie on the top simulation curve in Fig. 6.7(a).

Table 6.2 shows the results for comparisons of adjacent lanes in the same street. All of these comparisons come from the 2003 measurement campaign, which took place with little or no traffic in the streets. These conditions are the “most repeatable” according to the previous analysis and provide the best opportunity to isolate the spatial change, *e.g.*, driving in a different lane, from the long-term temporal changes caused by the repositioning of scatterers in the environment.

Each line in the table corresponds to four comparisons made between two runs in each lane. Figures 6.15 through 6.19 show the simulation comparisons for each street and are referenced in the table for the corresponding street. Each comparison agrees well with the other comparisons made using the same lanes and with the simulations using the values shown in the table. The

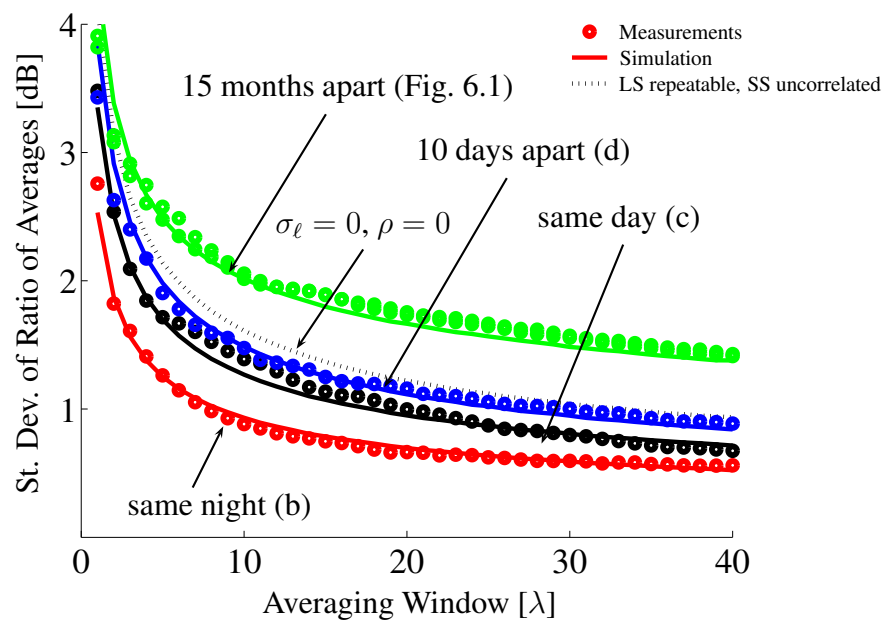


Streets (lanes)	Reference	Parameters	
		$\sigma_\ell$ [dB]	$D_\ell$ [ $\lambda$ ]
Battery (left/center)	Fig. 6.15	4.8	9
Battery (center/right)	Fig. 6.16	4.8	15
Battery (left/right)	Fig. 6.17	4.7	22
California	Fig. 6.18	4.0	5
Pine	Fig. 6.19	4.1	2

Table 6.2: Summary of Adjacent-Lane Repeatability Simulations. This table lists the simulation parameters for which the simulations match the behavior of the measured data when comparing signal strength profiles between adjacent lanes on the same night. The ‘reference’ column calls out the comparison curves to which the lines in this table refer.

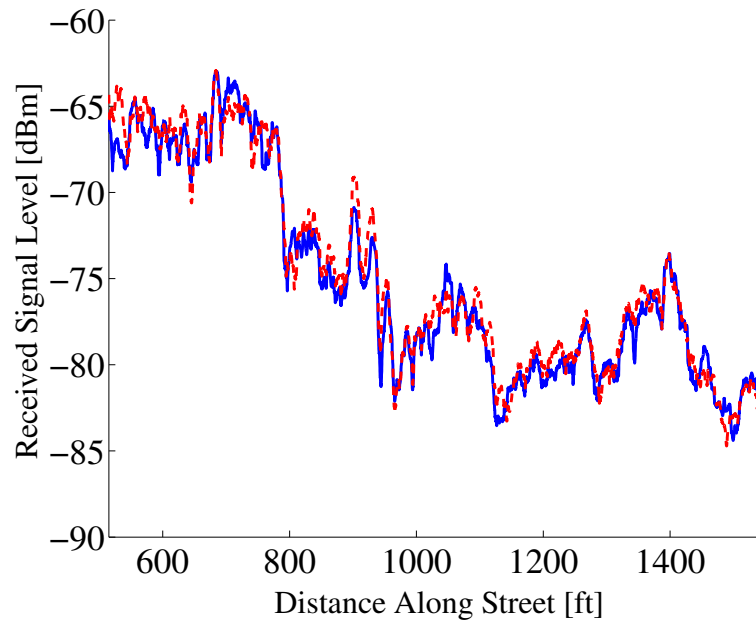
dissimilarity process has a greater magnitude for the adjacent lane comparisons than in almost all of the same-lane comparisons over 15 months, Clay Street being the exception.

Battery Street is the only street in which a comparison is made among three lanes traveling in the same direction. The magnitude,  $\sigma_\ell$ , of the dissimilarity process is the same regardless of whether the comparison is made with measurements in the very next lane or two lanes over. Pine is a one-way street, and both traffic lanes are used for the comparison. California is a wider, two-way street, and only the two eastbound lanes are used for the comparison. Although not explicitly done with the intent of characterizing the repeatability, Ikegami [38] compared the large-scale signal variation from one side of a street to another. The results in this chapter agree with Ikegami, who found that differences between the signals received on either side of a street are greater for streets aligned with the transmitter. Battery is aligned with the transmitter, whereas Pine and California are not.

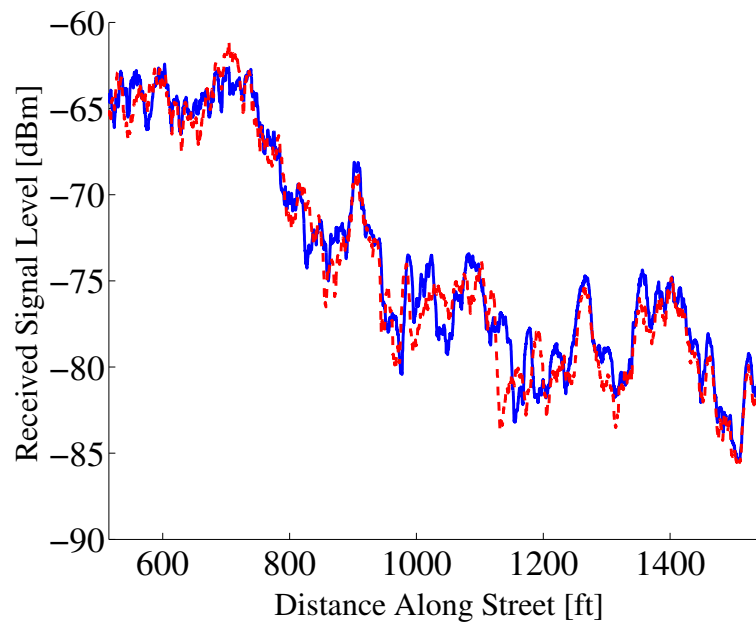


(a) Comparisons Using the Repeatability Model

Figure 6.7: Signal Strength Comparisons for Sansome Street. The measured and simulated results for the repeatability model are shown in (a), and direct overlays of the corresponding signal strength profiles are shown in (b)–(d) and in Fig. 6.1.

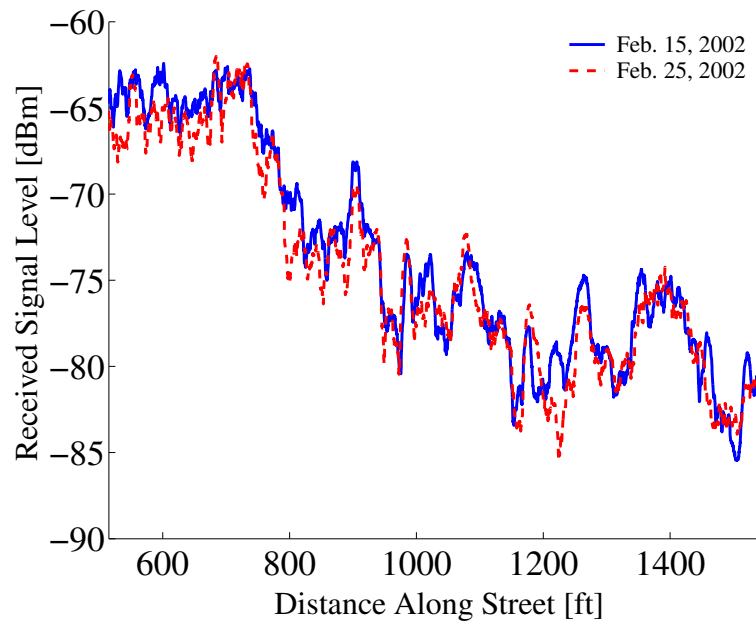


(b) Two Measurements Made on the Same Night



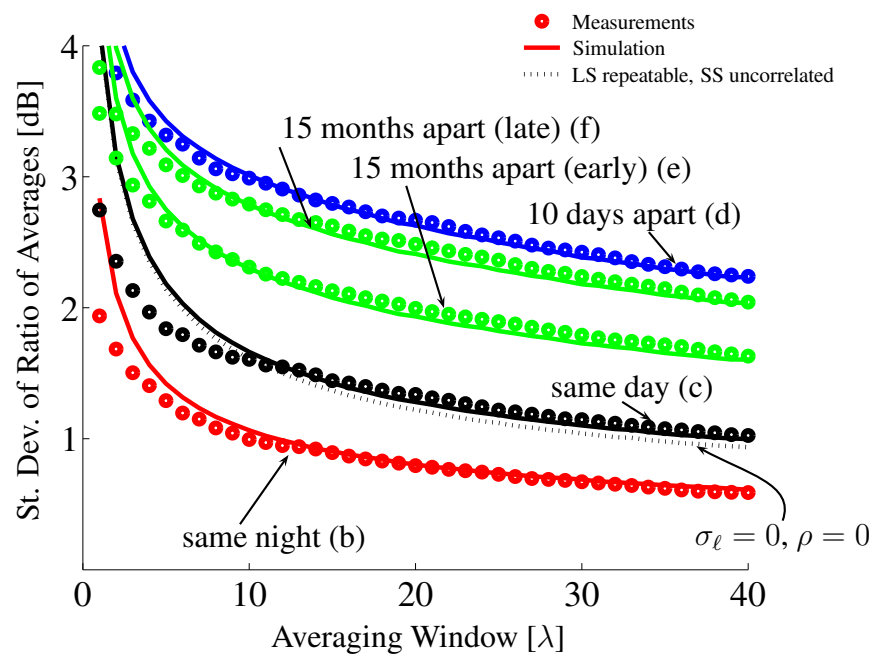
(c) Two Measurements Made on the Same Day

Figure 6.7: Signal Strength Comparisons for Sansome Street (*continued*).



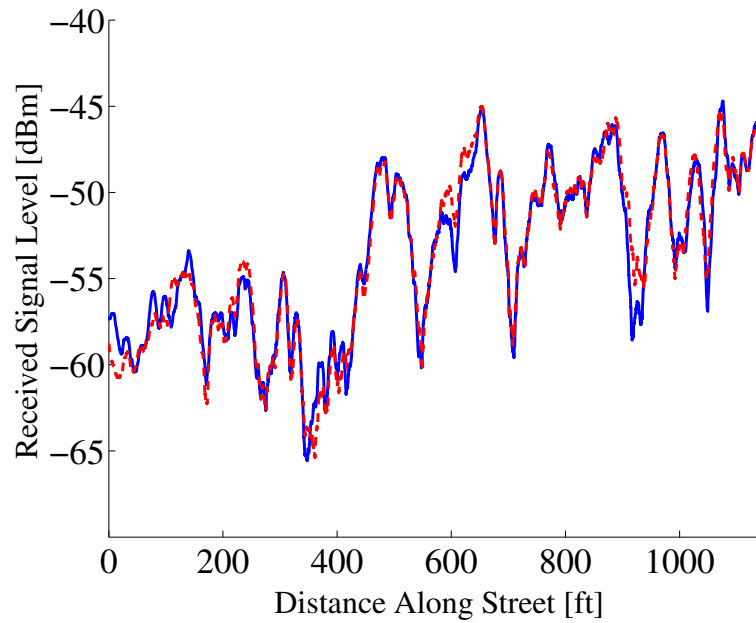
(d) Two Measurements Made 10 Days Apart

Figure 6.7: Signal Strength Comparisons for Sansome Street (*continued*).

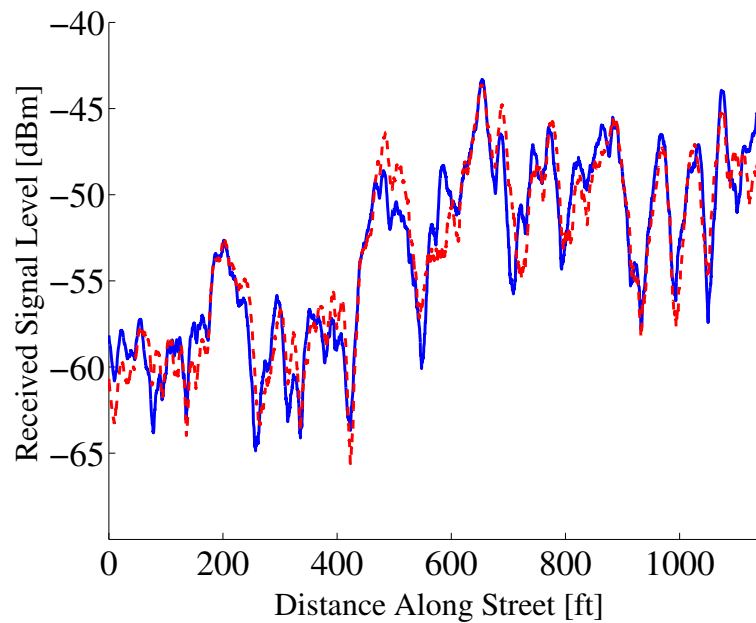


(a) Comparisons Using the Repeatability Model

Figure 6.8: Signal Strength Comparisons for the Center Lane of Battery Street. The measured and simulated results for the repeatability model are shown in (a), and direct overlays of the corresponding signal strength profiles are shown in (b)–(f).

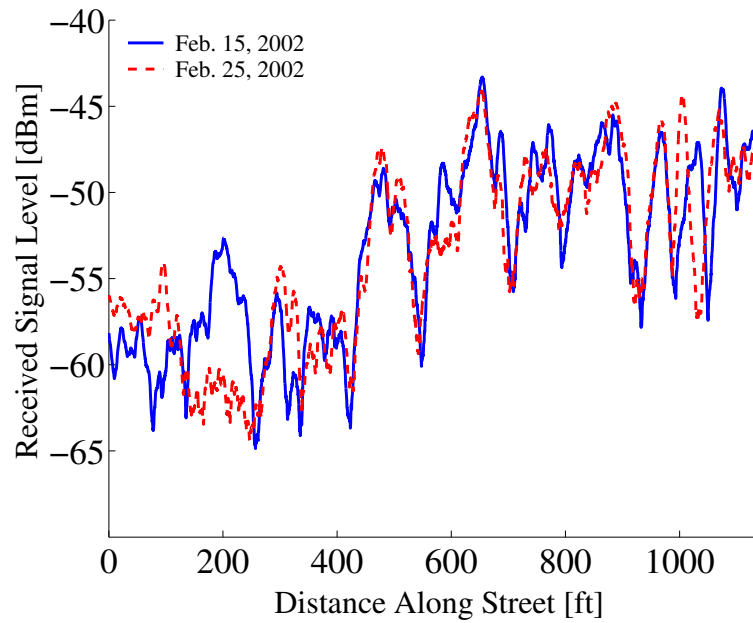


(b) Two Measurements Made on the Same Night

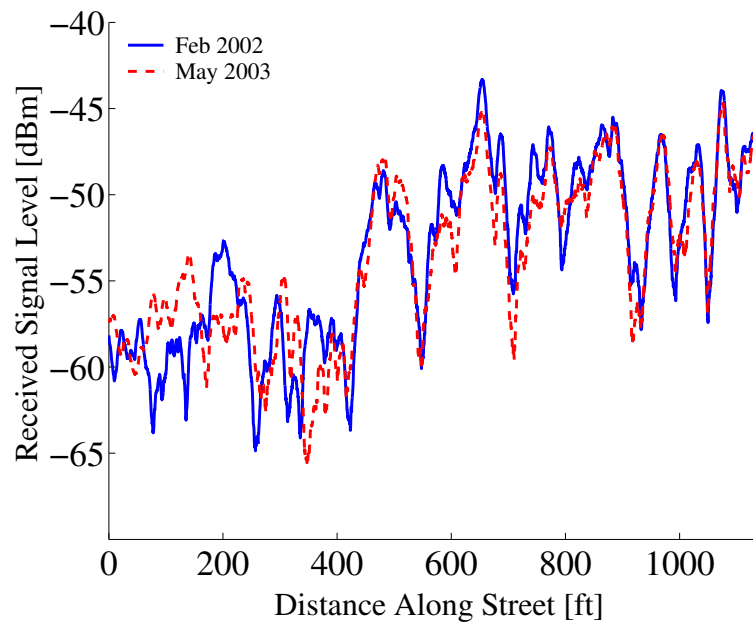


(c) Two Measurements Made on the Same Day

Figure 6.8: Signal Strength Comparisons for the Center Lane of Battery Street (*continued*).

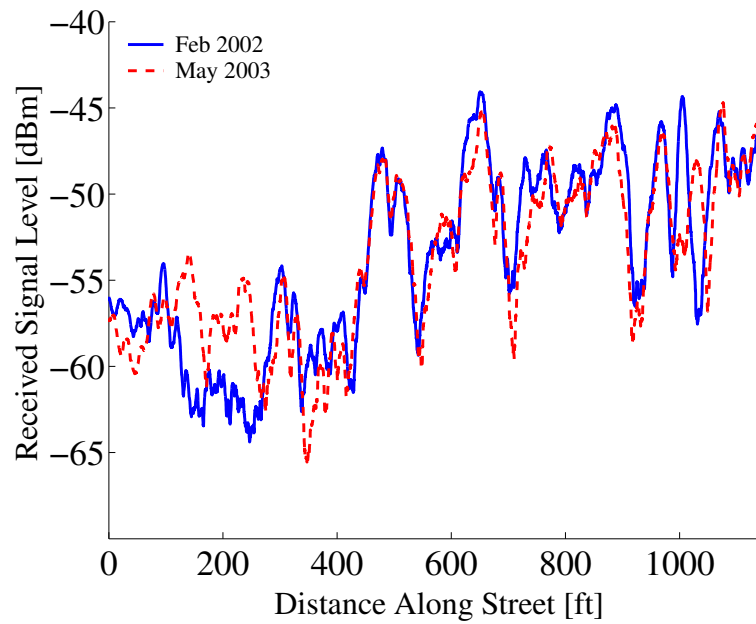


(d) Two Measurements Made 10 Days Apart



(e) Two Measurements Made 15 Months Apart, Early in the Morning

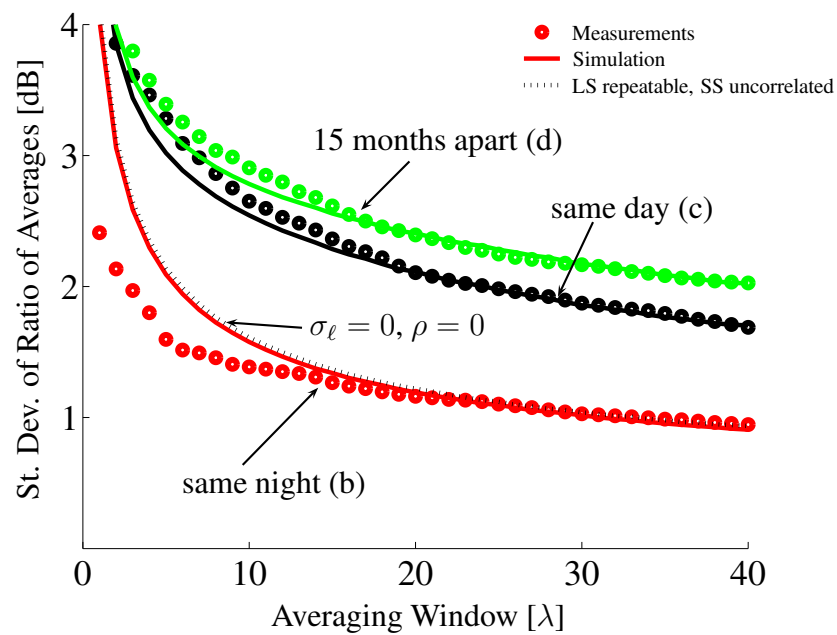
Figure 6.8: Signal Strength Comparisons for the Center Lane of Battery Street (*continued*).



(f) Two Measurements Made 15 Months Apart, Later in the Morning

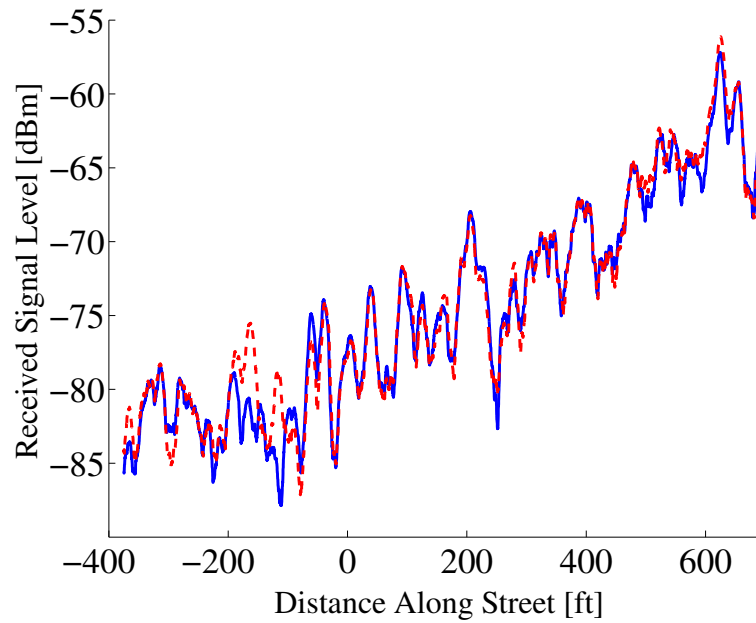
Figure 6.8: Signal Strength Comparisons for the Center Lane of Battery Street (*continued*).



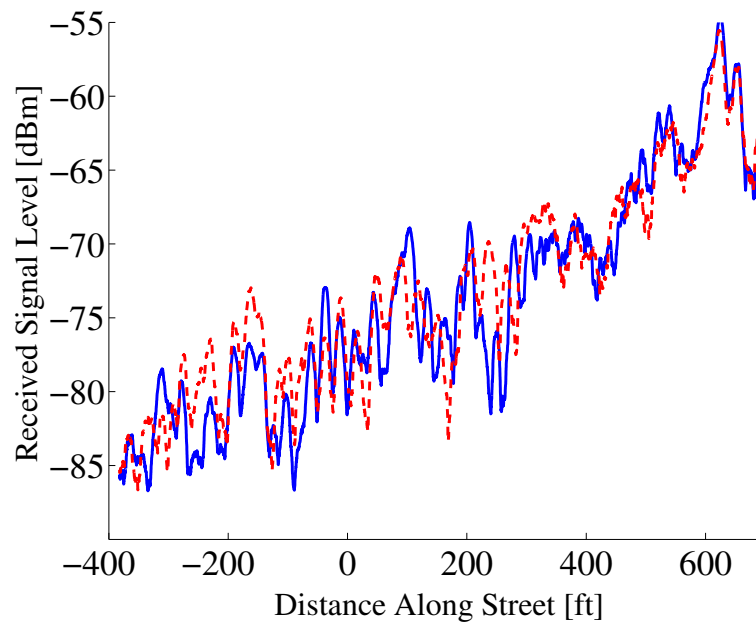


(a) Comparisons Using the Repeatability Model

Figure 6.9: Signal Strength Comparisons for the Left Lane of California Street. The measured and simulated results for the repeatability model are shown in (a), and direct overlays of the corresponding signal strength profiles are shown in (b)–(d).

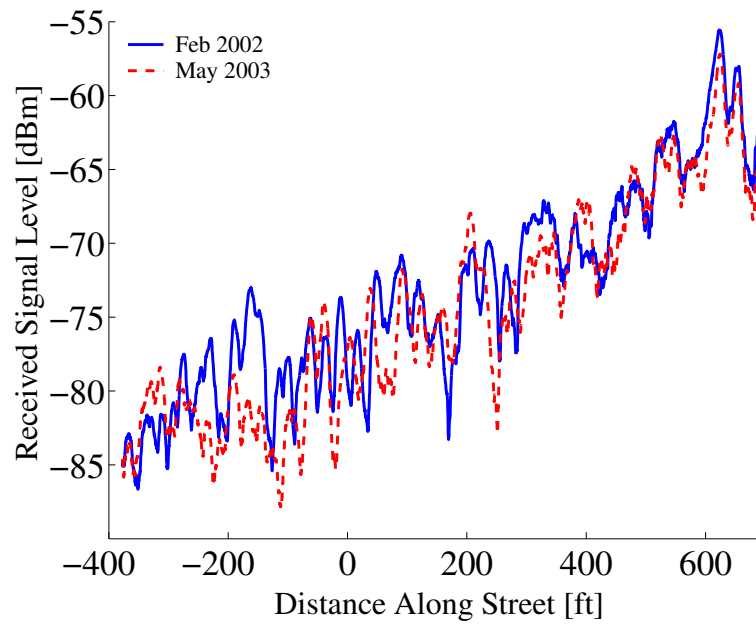


(b) Two Measurements Made on the Same Night



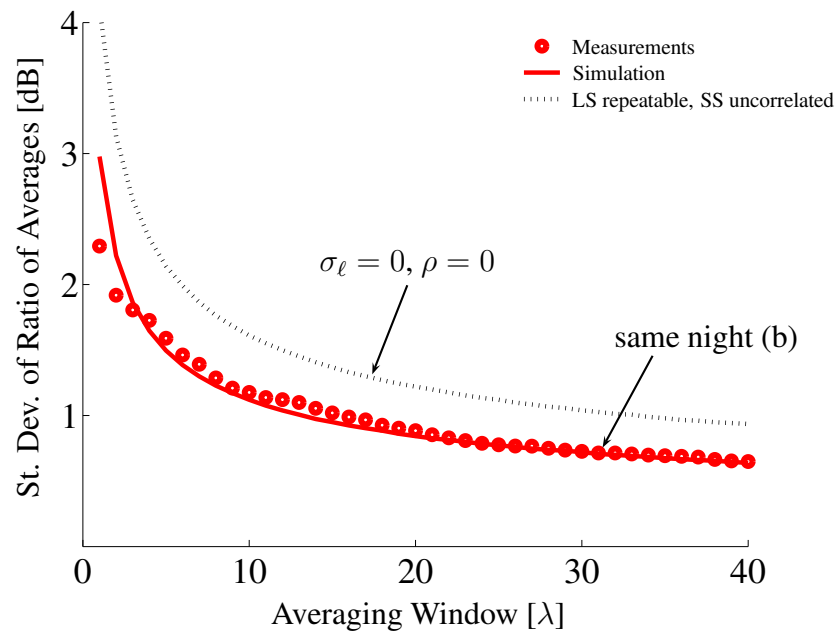
(c) Two Measurements Made on the Same Day

Figure 6.9: Signal Strength Comparisons for the Left Lane of California Street (*continued*).



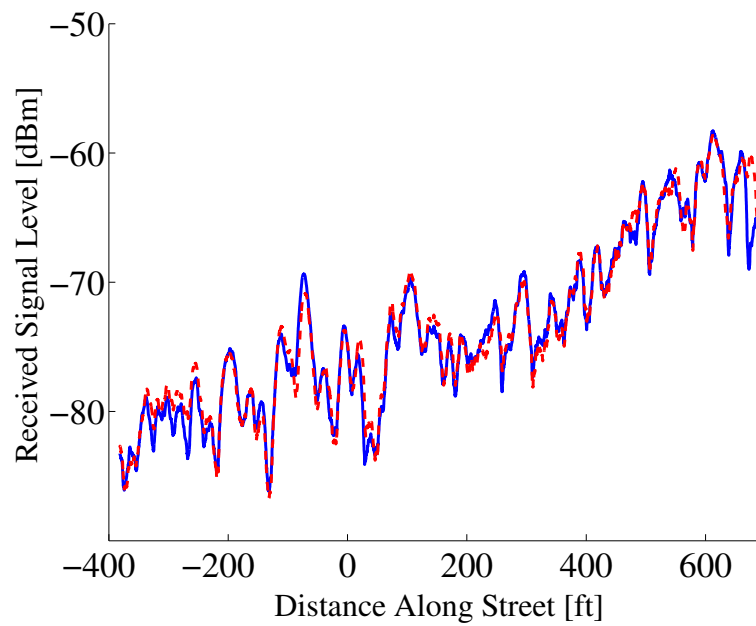
(d) Two Measurements Made 15 Months Apart

Figure 6.9: Signal Strength Comparisons for the Left Lane of California Street (*continued*).



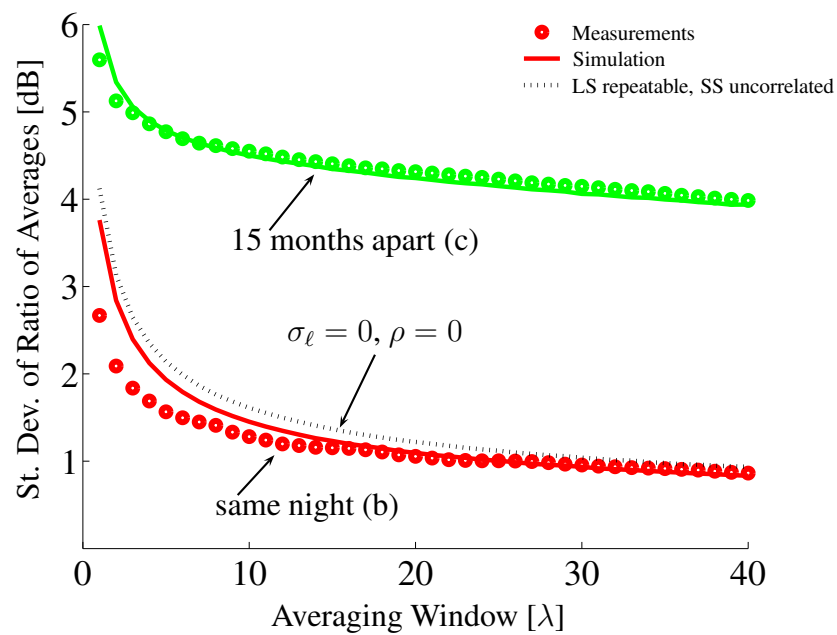
(a) Comparisons Using the Repeatability Model

Figure 6.10: Signal Strength Comparisons for the Right Lane of California Street. The measured and simulated results for the repeatability model are shown in (a), and direct overlays of the corresponding signal strength profiles are shown in (b).



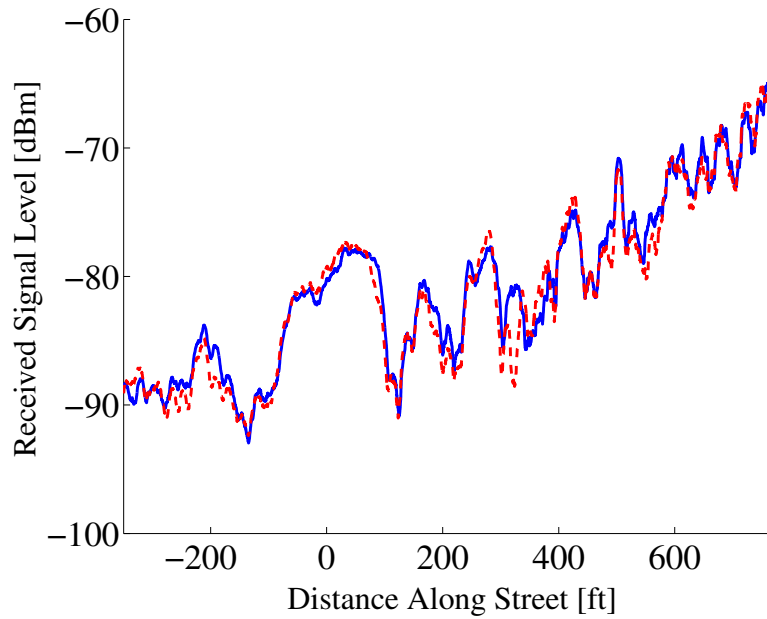
(b) Two Measurements Made on the Same Night

Figure 6.10: Signal Strength Comparisons for the Right Lane of California Street (*continued*).

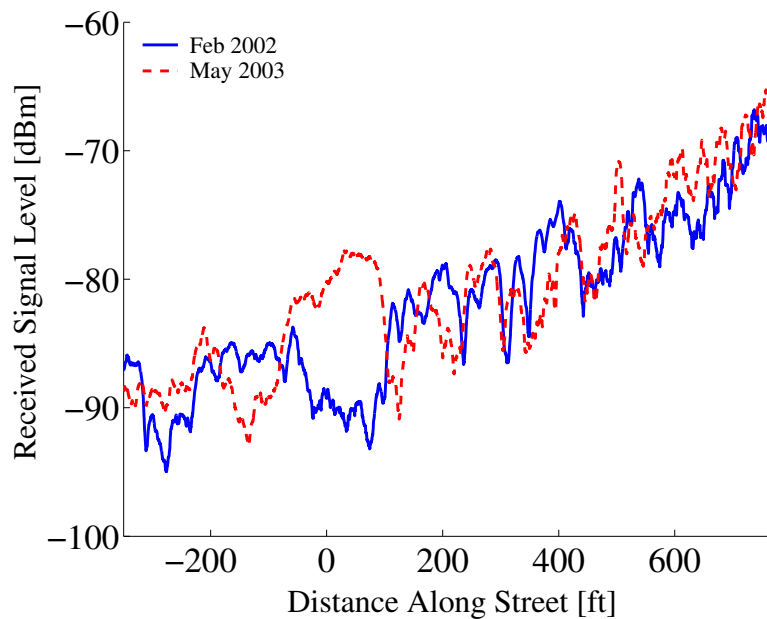


(a) Comparisons Using the Repeatability Model

Figure 6.11: Signal Strength Comparisons for Clay Street. The measured and simulated results for the repeatability model are shown in (a), and direct overlays of the corresponding signal strength profiles are shown in (b)–(c).

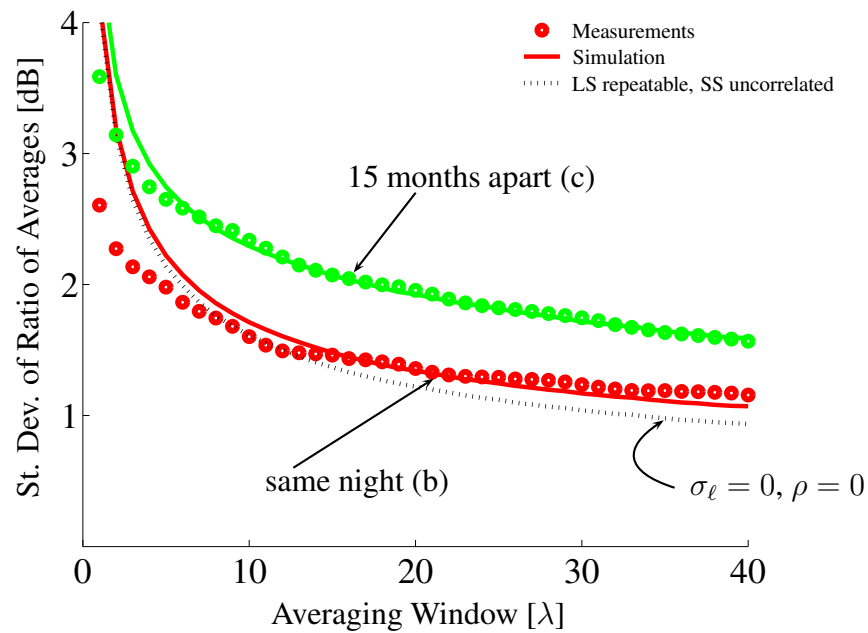


(b) Two Measurements Made on the Same Night



(c) Two Measurements Made 15 Months Apart

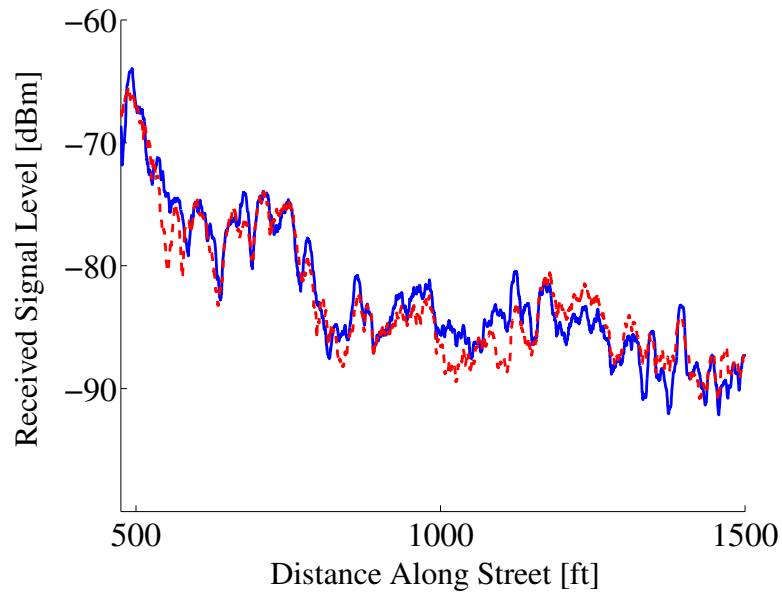
Figure 6.11: Signal Strength Comparisons for Clay Street (*continued*).



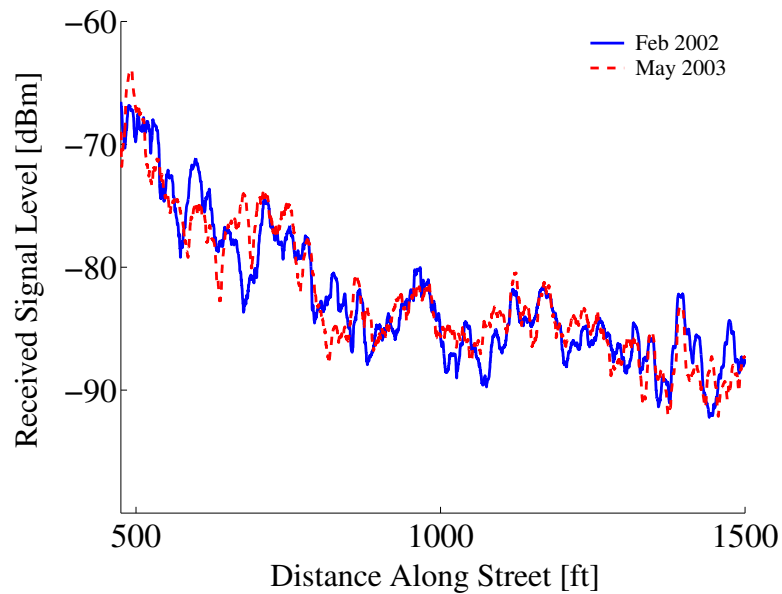
(a) Comparisons Using the Repeatability Model

Figure 6.12: Signal Strength Comparisons for Sacramento Street. The measured and simulated results for the repeatability model are shown in (a), and direct overlays of the corresponding signal strength profiles are shown in (b)–(c).



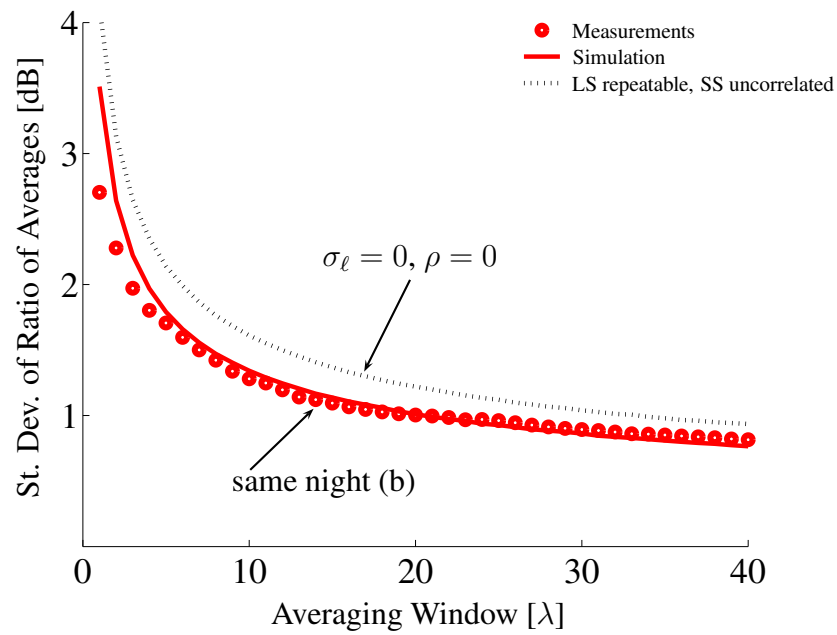


(b) Two Measurements Made on the Same Night



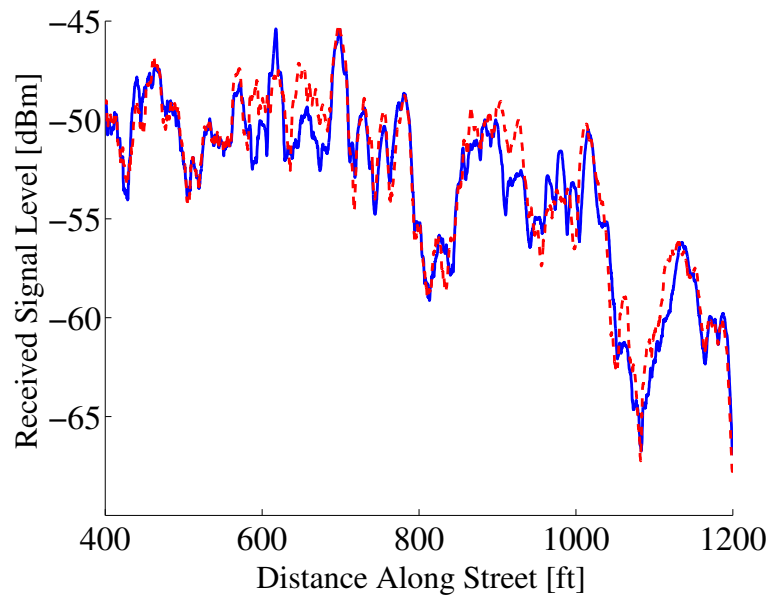
(c) Two Measurements Made 15 Months Apart

Figure 6.12: Signal Strength Comparisons for Sacramento Street (*continued*).



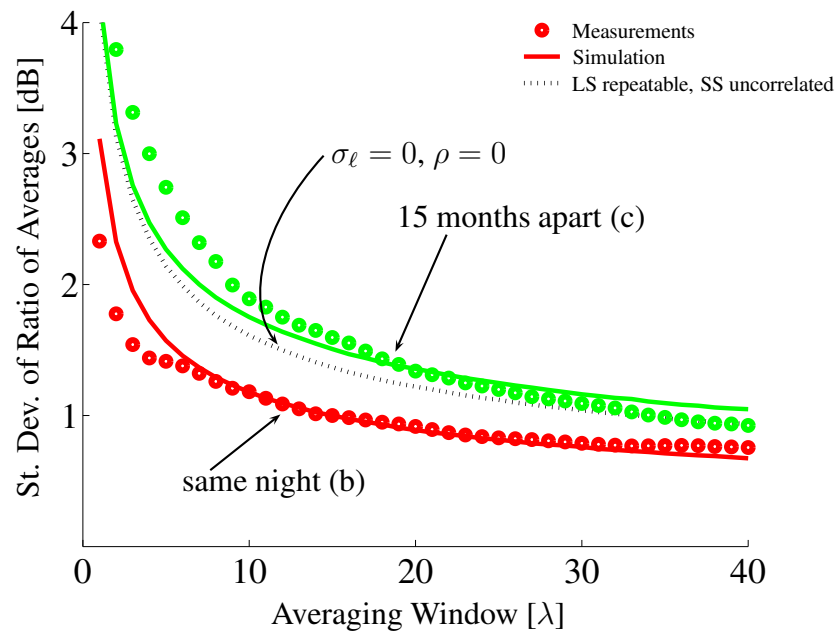
(a) Comparisons Using the Repeatability Model

Figure 6.13: Signal Strength Comparisons for the Left Lane of Pine Street. The measured and simulated results for the repeatability model are shown in (a), and direct overlays of the corresponding signal strength profiles are shown in (b).



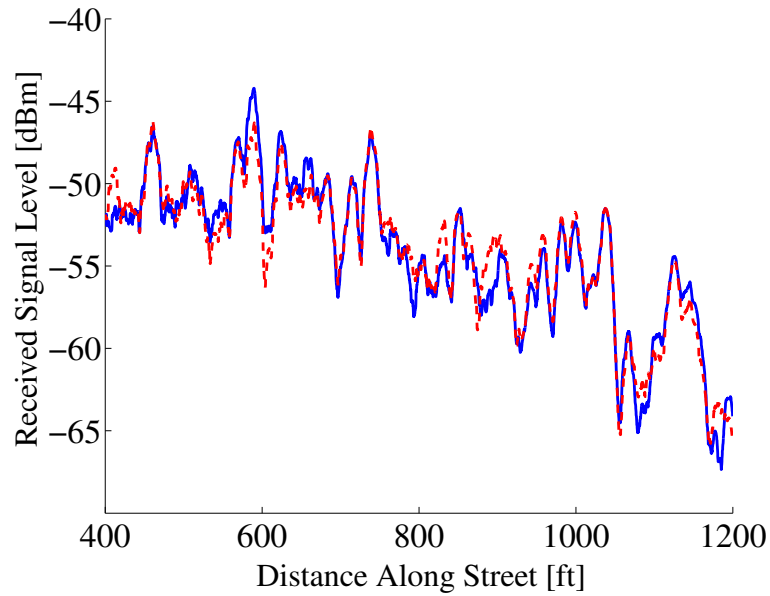
(b) Two Measurements Made on the Same Night

Figure 6.13: Signal Strength Comparisons for the Left Lane of Pine Street (*continued*).

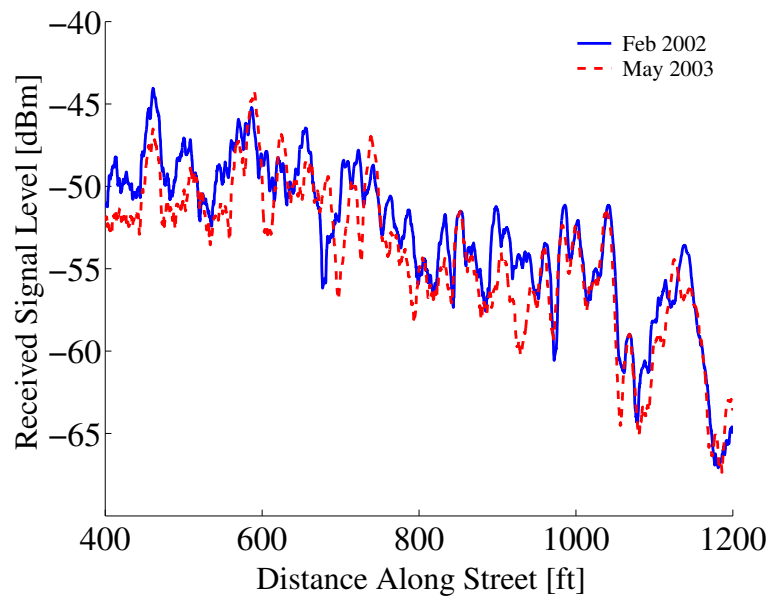


(a) Comparisons Using the Repeatability Model

Figure 6.14: Signal Strength Comparisons for the Right Lane of Pine Street. The measured and simulated results for the repeatability model are shown in (a), and direct overlays of the corresponding signal strength profiles are shown in (b).

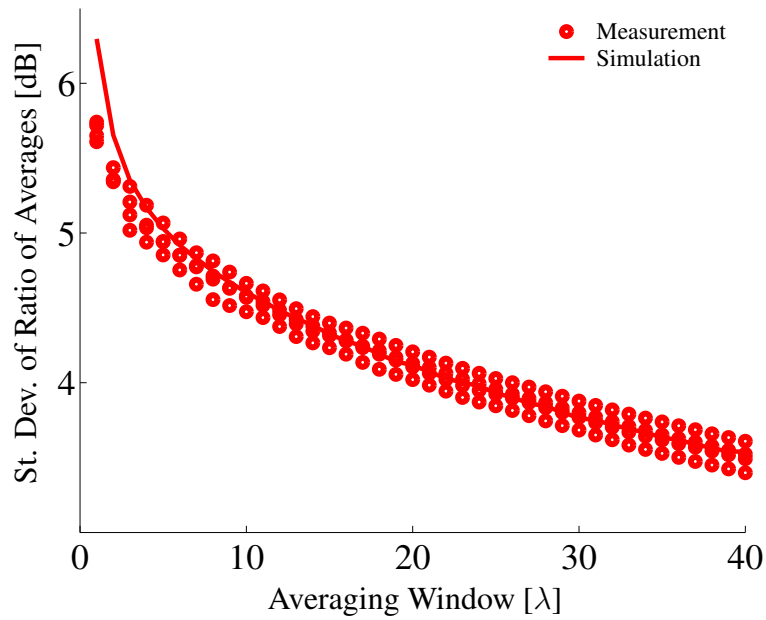


(b) Two Measurements Made on the Same Night

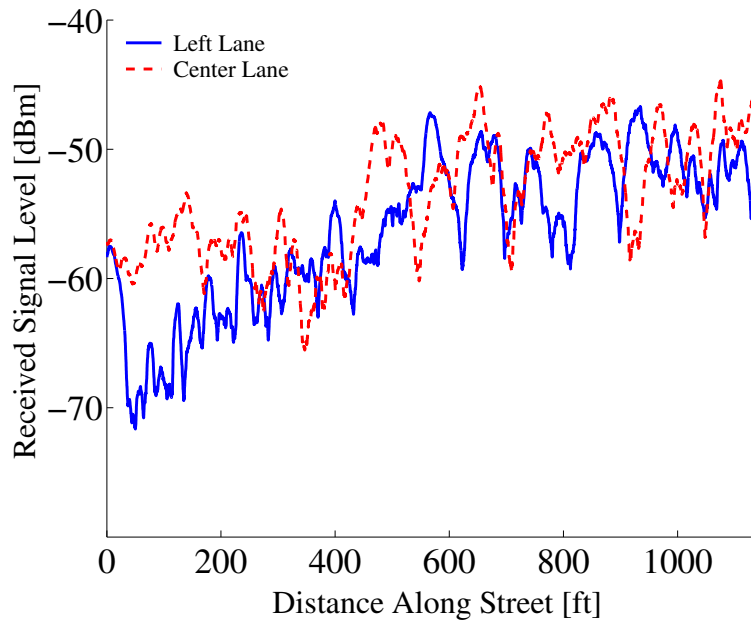


(c) Two Measurements Made 15 Months Apart

Figure 6.14: Signal Strength Comparisons for the Right Lane of Pine Street (*continued*).

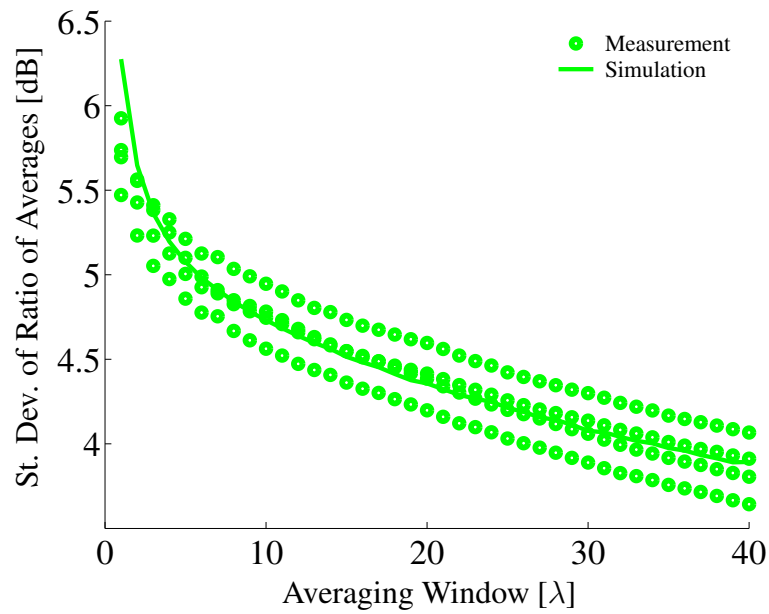


(a) Comparisons Using the Repeatability Model

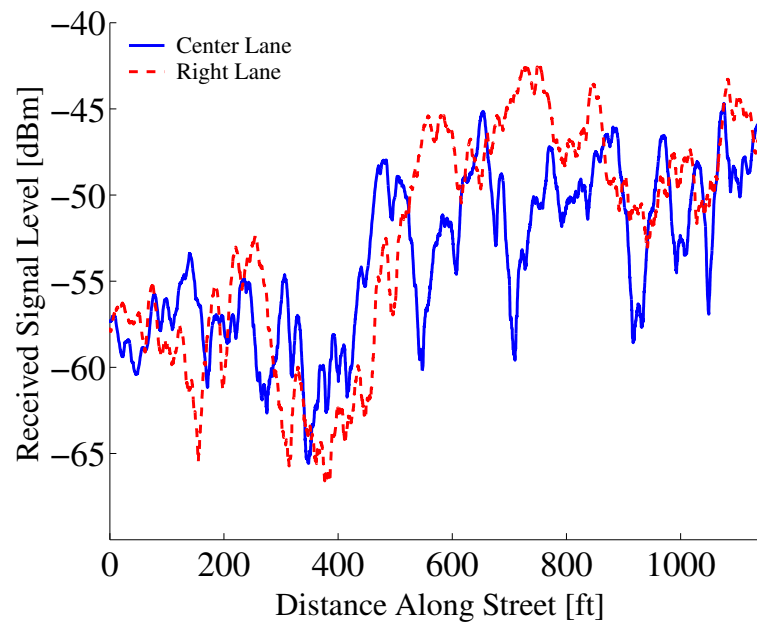


(b) Drive Path Signal Strength Profiles

Figure 6.15: Signal Strength Comparisons for the Left and Center Lanes of Battery Street. Four comparisons between two measurements taken in the left and center lanes are shown in (a). Representative measurements of the two lanes are shown in the overlay plot in (b).

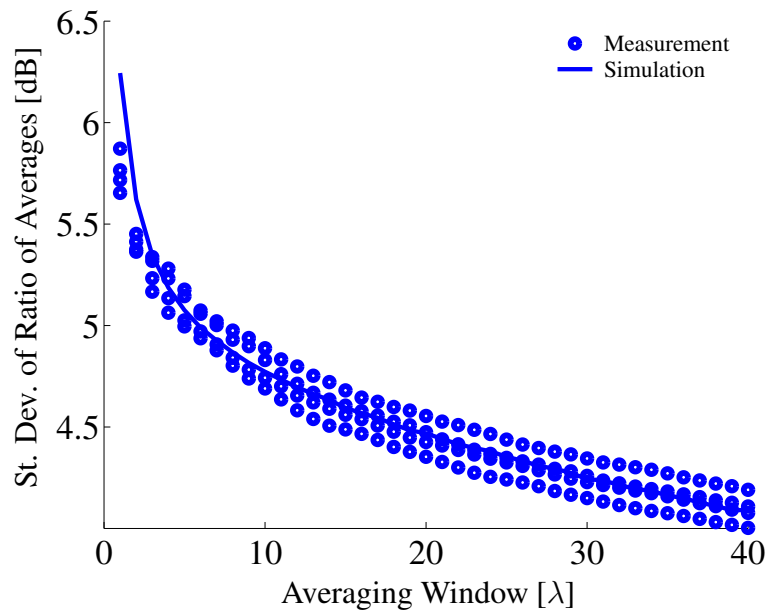


(a) Comparisons Using the Repeatability Model

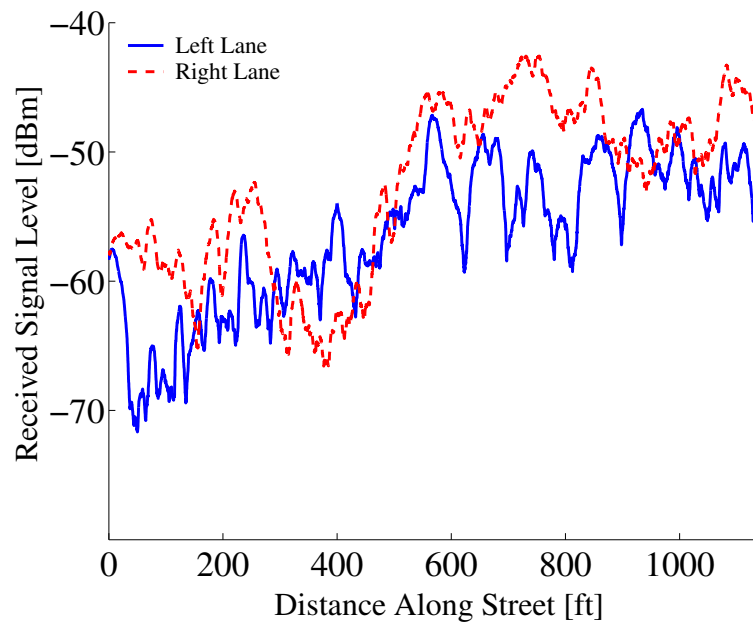


(b) Drive Path Signal Strength Profiles

Figure 6.16: Signal Strength Comparisons for the Center and Right Lanes of Battery Street. Four comparisons between two measurements taken in the center and right lanes are shown in (a). Representative measurements of the two lanes are shown in the overlay plot in (b).



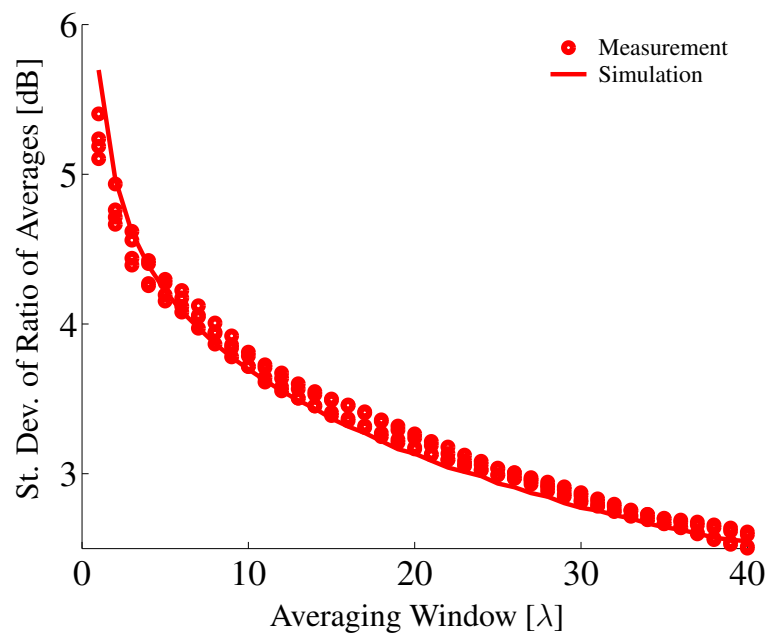
(a) Comparisons Using the Repeatability Model



(b) Drive Path Signal Strength Profiles

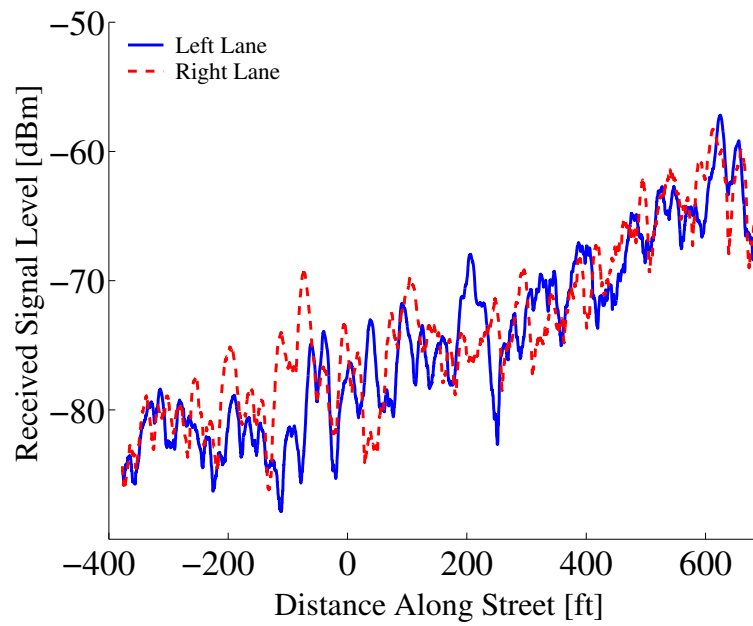
Figure 6.17: Signal Strength Comparisons for the Left and Right Lanes of Battery Street. Four comparisons between two measurements taken in the left and right lanes are shown in (a). Representative measurements of the two lanes are shown in the overlay plot in (b).





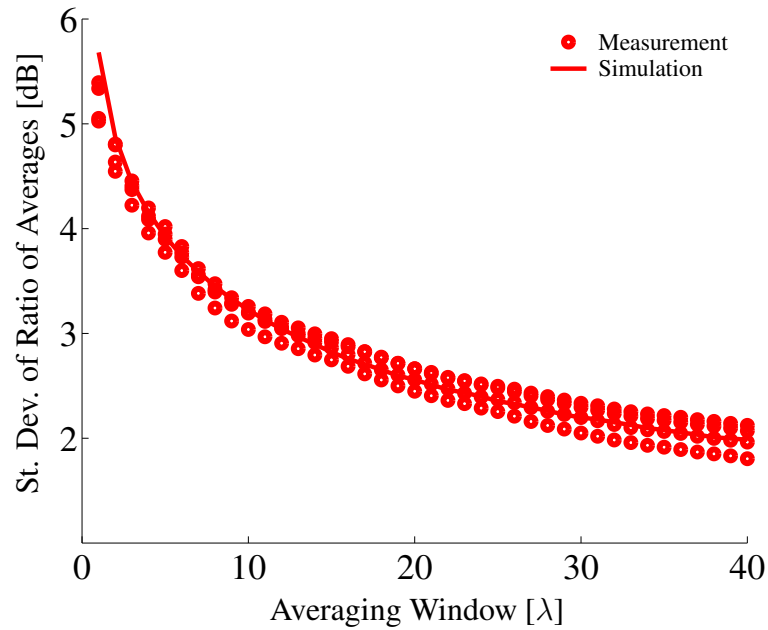
(a) Comparisons Using the Repeatability Model

Figure 6.18: Signal Strength Comparisons for the Left and Right Lanes of California Street. Four comparisons between two measurements taken in the left and right lanes are shown in (a). Representative measurements of the two lanes are shown in the overlay plot in (b).

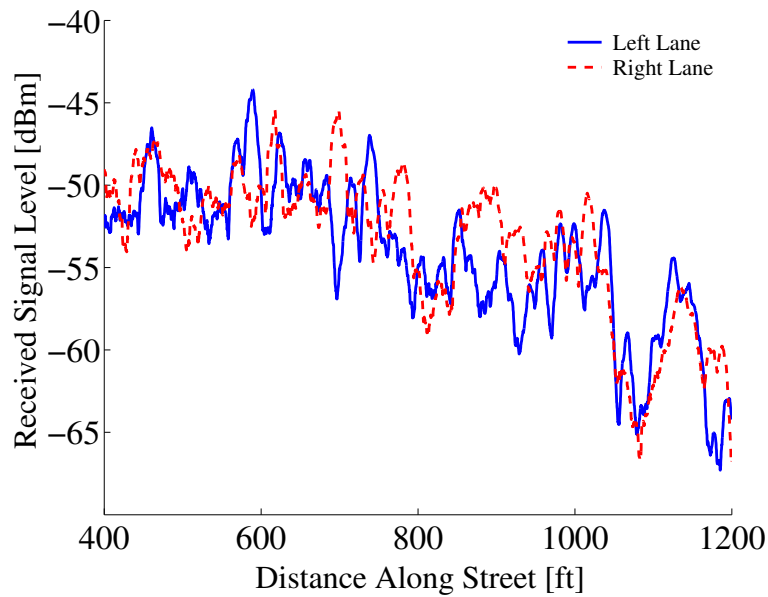


(b) Drive Path Signal Strength Profiles

Figure 6.18: Signal Strength Comparisons for the Left and Right Lanes of California Street (*continued*).



(a) Comparisons Using the Repeatability Model



(b) Drive Path Signal Strength Profiles

Figure 6.19: Signal Strength Comparisons for the Left and Right Lanes of Pine Street. Four comparisons between two measurements taken in the left and right lanes are shown in (a). Representative measurements of the two lanes are shown in the overlay plot in (b).

## 6.5 Summary

In this chapter, we introduce a model that quantifies the repeatability of signal strength measurements in the streets of a built-up urban area. This model includes a lognormal dissimilarity process that accounts for the changes, if any, in the large-scale variation between measurement sets. The measurements yield a range in the magnitude of the dissimilarity process over time and over distance between the measurements. The measurements are the most repeatable when the two data sets are taken in the same lane with little time between measurement runs with little or no traffic. Under these conditions we find that not only is the large-scale variation repeatable, but the small-scale fading is correlated between the two runs. As traffic increases, the small-scale fading tends to decorrelate between the two runs, and in many cases there are small changes in the large-scale variation. Over long periods of time, the repositioning of scatterers in the environment causes minor changes to the large-scale variation. Measurements in the same lane, however, generally show better agreement after 15 months than similar comparisons of adjacent lanes on the same night, indicating that the repositioning of a receiver to a different lane has more of an effect than the long-term temporal change caused by the repositioning of reflectors in the environment.

# Chapter 7

## Conclusion

### 7.1 Report Summary

Urban areas continue to be lucrative markets for wireless service providers. As subscribership continues to increase, network operators need to find ways to service the increasing demand. Additional demand may be met by installing more base stations. A less costly approach, however, is desired. Employing more efficient resource allocation methods is one way to extend system capacity while leveraging existing infrastructure. Since signal strength is the primary parameter affecting resource allocation decisions, propagation models play a pivotal role in evaluating alternative resource allocation methods through simulation.

In this report we study signal strength measurements made in the San Francisco financial district to draw new conclusions about signal strength prediction, transient behavior near street intersections, and the repeatability of signal strength measurements. Improved signal strength prediction is useful in analyzing interference and link-level performance of a communication system throughout a coverage area. The transient behavior of signal strength near corners determines how quickly a system must respond to such changes. Characteristics of the repeatability of signal strength measurements are important in evaluating methods that infer position from signal strength measurement properties.

Chapters 2 and 3 provide the requisite background material for the remainder of the report. Chapter 2 provides information on propagation models in various environments. Starting with free-space models and gradually adding more obstacles to the environment, we see the increasing

complexity of the so-called deterministic propagation models. When details of the environment are unavailable or the computation of the fields using deterministic models is too expensive, statistical models are used. These models are simpler and required only broad classifications of the propagation environment. Statistical models form the basis of our studies in this report.

Chapter 3 identifies how the measurements are taken. The data set collected for these studies is unique in the accuracy of the position estimate for the mobile receiver. The use of a video camera, synchronized to the measurements, allows each measurement run to be aligned with the buildings along the drive route. The fidelity of the position estimate makes possible the repeatability studies and provides a way to study signal changes and where they occur relative to street corners.

Chapter 4 covers the corner effect. The corner effect refers to the sudden change in signal strength experienced by a mobile user after turning a corner. The fixed-length averaging interval typically used to estimate local received signal power smooths out the abruptness of signal change at street corners. We introduce an adaptive averaging method that captures the transient nature of the signal strength changes at corners by using shorter averaging windows in these regions. Away from the edges of the intersections,  $20\text{--}40\lambda$  window lengths are used, while window lengths of  $1\text{--}5\lambda$  are used to identify the abrupt changes at the edges of the intersections.

The results of the adaptive averaging method are piecewise linear segments<sup>1</sup> of signal strength in and adjacent to street intersections. We find that the corner effect is more pronounced when turning from a radial street—one that extends directly from the transmitter—to a cross street.

We also characterize the rate and the extent of the signal change at these corners. We find that the corners have typically one or two segments at the edge of the intersection where the signal falls off before it meets the distance-dependent trend for the cross street. In some cases, the trend adjacent to the intersections falls off very rapidly—up to 6 dB/ft. For these segments, the extent of the signal change is usually 5–10 dB, regardless of the rate. For the more gradual transitions, the extent of the signal change has an empirical relationship to the rate of signal strength change:  $\text{extent} = m \times \text{rate}$ , with  $m = 77$  ft.

In Chapter 5, we augment statistical models for improved path-loss prediction in urban environments. Statistical models are used to predict path loss in areas where detailed information about the dimensions and material properties of the buildings are either unavailable or too expensive to obtain and use. Statistical models, however, generally assume a homogeneous environment, *i.e.*,

---

<sup>1</sup>when the distance is expressed in linear units and the signal strength in decibels

one that has the same statistical properties regardless of the direction from the transmitter. The grid-like structure of the streets, and the directional coupling of the wave propagation by buildings causes this homogeneity assumption to break down. As a result, statistical models subsume the deterministic effects of the street layout.

Our augmentation of the statistical model incorporates the layout of the streets into the model by partitioning streets according to their orientation relative to the transmitter. By partitioning streets into two groups—radial streets and cross streets—we improve the prediction error by up to 6 dB. The partitioning increases the complexity of the model only slightly for this significant improvement in prediction error.

In Chapter 6 we quantify the repeatability of signal measurements in urban areas. By inserting a term for the dissimilarity between two measurements of the large-scale fading, we are able to test the canonical hypothesis that the large-scale fading is completely repeatable and the small-scale fading is not.

From our measurements and from simulations using our augmented model, we quantify the repeatability. We find that when measurements are taken under the best conditions, *i.e.*, little traffic and not much time between measurements, the large-scale fading is repeatable and there is a high degree of cross correlation between the small-scale fading terms for measurements made in the same lane. With more time between measurements, allowing more changes in the environment to occur, the high degree of repeatability degrades over time. In fact, after 15 months, the dissimilarity between large-scale fading is as high as 4 dB between measurements.

Changing position, however, seems to have more of an effect on repeatability. We find that measurements for adjacent lanes, even when taken on the same night, are more dissimilar than measurements taken in the same lane over a period of 15 months. The implication is that algorithms relying on signal strength databases to determine mobile user position may require a different database for each lane in the same street. Changes in the signal measurements in the same lane indicate that updates to a signal database must be performed more than once per year.

## 7.2 Contributions

The research conducted for this report makes the following contributions to the study of radio wave propagation:

1. To characterize abrupt changes in signal strength at intersections in urban environments, averaging windows with lengths of  $1\text{--}5\lambda$  should be used rather than the averaging windows of more than  $20\lambda$  used elsewhere.
2. For abrupt changes in signal strength, *i.e.*, changes greater than 0.3 dB/ft, adjacent to the edges of street intersections, the extent of the change in signal strength is typically 5–13 dB.
3. For gradual changes in signal strength, *i.e.*, changes less than 0.3 dB/ft, adjacent to the edges of street intersections, the extent of the change in signal strength is related to the rate as:  $\text{extent} = m \times \text{rate}$ , with  $m = 77$  ft.
4. The corner effect is not exhibited as strongly at intersections that are near a  $45^\circ$  line drawn from the transmitter, bisecting the quadrant between radial streets.
5. For intersections with abrupt changes at the edges, the average signal strength profile changes by less than 2.5 dB within the intersection.
6. Partitioning streets in statistical models according to their orientation—radial or cross streets—can reduce path-loss prediction error by up to 6 dB. The average received signal power is lognormally distributed about distance-dependent trends for the radial and the cross-street partitions.
7. To quantify the similarity of two signal strength profiles measured in the same street, a dissimilarity process is introduced to account for changes in the large-scale signal variation between measurement runs. The similarity between the small-scale fading processes is quantified by the envelope cross correlation.
8. The most repeatable conditions exist when two signal strength profiles are measured in the same lane with little time between measurements. In this case, the repeatability is modeled by a dissimilarity process with 0 dB standard deviation, *i.e.*,  $\sigma_\ell = 0$  dB, and the cross correlation of the envelope of the small-scale fading between runs is as high as 0.6, *i.e.*,  $\rho \leq 0.6$ .
9. Measurements made in the same lane over a period of 15 months are modeled by a dissimilarity process with standard deviation as high as 4 dB, *i.e.*,  $\sigma_\ell \leq 4$  dB.



10. Measurements made in adjacent lanes on the same night are modeled by a dissimilarity process with magnitude greater than 4 dB, *i.e.*,  $\sigma_\ell \geq 4$  dB, and small-scale fading that is independent from one run to the next, *i.e.*,  $\rho = 0$ .

### 7.3 Future Work

The results reported in this report open new avenues for further research using the augmented models presented here. Straightforward extensions of this work involve plugging the new models into previous simulation studies that relied on the previous, unaugmented models.

Previous pattern recognition algorithms relied on the assumptions that the large-scale variations were repeatable and the small-scale fading was different between measurement runs [58, 63, 101]. These algorithms could be evaluated with new repeatability model outlined in Chapter 6 to see how the performance changes when the repeatability is either better or worse than previously assumed. This performance evaluation would also help determine how frequently to update the signal strength databases.

In addition to studying handoff performance, the new properties of the corner model of Chapter 4 could be used to evaluate corner detection techniques such as those reported in [62, 63]. The underlying propagation mechanisms that give rise to the piecewise linear model could be explored. Recognizing that wave propagation is a local phenomenon, it would be useful to determine if the propagation through an intersection could be determined by the information local to that intersection, namely the angular distribution or the mode composition of the incident signal, the street dimensions, and the building types.

The economic feasibility of any signal strength database-driven resource allocation algorithm depends on the capability to populate and update the databases in a distributed manner. Presumably the large-scale signal variation is the quantity that should be stored in the database. In addition to a potential dissimilarity of large-scale signal variations between measurement runs, each large-scale fading estimate is contaminated by the finite-window effects of the small scale fading. Considering these uncertainties, one could determine how many measurements would be required to get a “valid” database entry for a particular position. Keeping in mind that the repeatability degrades as a function of both time and position, one could potentially use rate-distortion theory to determine the storage requirements for such a database.

# **Appendix A**

## **Experiment Details**

Chapter 3 provides details of the experiment that are required to understand the analysis of the measurements in this report. This appendix provides additional, low-level details explaining the interaction between components used in the experiment.

### **A.1 Hardware Design and Configuration**

The hardware is designed to coordinate the measurements from the different sensors so that the data from each sensor may be pieced together during offline data reduction. All the data collection activities are tied to the same time source, namely the system clock, on the laptop computer (see Fig. A.1). Each measurement is stored, along with periodic timestamps, in data files to be processed offline. The list of equipment used for the experiment is in Table A.1. The remainder of this section outlines how the hardware components are connected together to meet the objectives of the experiment.

#### **A.1.1 Distance Measurement**

To understand how the distance measurement is derived from the Anti-lock Braking System (ABS), a brief description of the system is useful. A sensor, like the one shown in Fig. A.2, is located on each wheel. Each wheel has a separate cylinder through which pressure is applied to the calipers or brake drums to slow down the vehicle. When the brakes are applied, the ABS module monitors the rotation of each wheel. If any wheel stops rotating prematurely, the system commands the cylinder

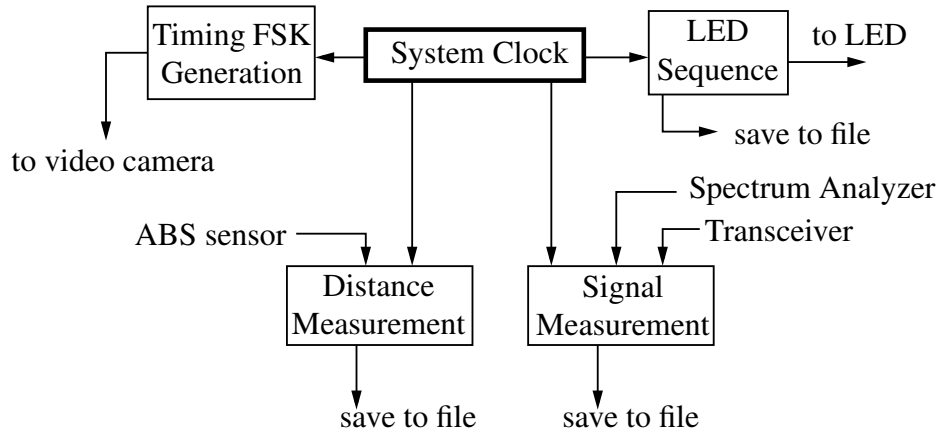


Figure A.1: Synchronization Overview. Separate device drivers are responsible for the interaction of the laptop computer with the video camera, spectrum analyzer, ABS sensor, base station transceiver, and the synchronizing LED. Timestamps from the same system clock, with “near microsecond resolution” [79], are used by each driver to tag each data stream with time markers to be used in offline processing.

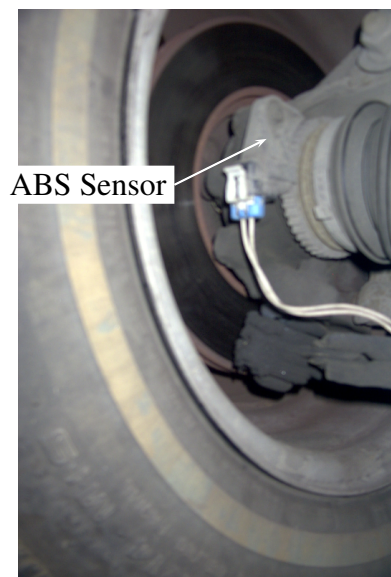


Figure A.2: Anti-Lock Braking System (ABS) Sensor. The ABS sensor attached to the front, passenger-side wheel is rewired to the soundcard of the laptop computer for the drive path distance measurement.

Component	Manufacturer/Model
Spectrum Analyzer	HP 8595E
Preamplifier	Mini-Circuits ZFL-1000LN
Laptop Computer	Toshiba Satellite 1605CDS
A/D Card	Measurement Computing PC-CARD DAS16/12
GPIB Interface Card	Measurement Computing PCM-GPIB
Splitter	Mini-Circuits ZX10-2-12
Magnetic Mount Antenna	Antenna Specialists ASP-1890T
Base Station Transceiver	Kokusai Electric Transmitter/Receiver Subassembly for the APX-100 Cellular System
Vehicle	1992 Chevrolet Cavalier
Power Inverter	Kingson Mobile Power 300 W
Video Camera	Panasonic AG-188
Video Cassette Recorder	Panasonic PV-V4022
Video Monitor	Guangzhou Jiahe Electronic MTR-5
Custom-Built Interface Boxes	
Additional Items Used for Signal Strength Calibration	
RF Signal Generator	HP 8664A
Power Meter	HP E4418A
Video Digitization	
Apple PowerMac G4 with iMovie	

Table A.1: Equipment List. The first section of this table lists components used during data collection. The middle and last sections list equipment used for signal strength calibration and initial data reduction.

for that wheel to release the pressure to keep it from locking up. For this to work, the ABS sensor for each wheel must provide a fine-scale reading of wheel rotation.

This fine-scale measurement of wheel rotation is very useful for measuring distances as well. Throughout all of the measurements for this experiment, the voltage from the ABS sensor is sampled and stored in its raw format so that the distance may be calibrated offline. The distance calibration is performed by driving next to two different landmarks that have been measured manually with a tape measure. The vehicle, on separate measurement runs, is driven next to a building and next to light poles in a parking lot which serve as calibration markers. The curb next to the building and the parking lot markings are used to help keep the vehicle moving in a straight line and parallel to the markers. The video camera marks the passing of the markers and is used to pinpoint their locations so that the number of ABS pulses may be counted between them. The calibration is performed on the day of the experiment, both before and after the trip to San Francisco, minimizing the impact of tire pressure changes on the distance measurement. An average of all the calibrations for a particular day is used to analyze the measurement data.

The video camera provides a transcript of each measurement run. The audio track is used to record a timing signal generated by the computer and is referenced to the system clock for synchronization to the other measurements. The camera is mounted perpendicular to the direction of travel to identify the locations of building corners along the route. The video is digitized for offline processing. A flashing LED is used at the beginning and at the end of each run to calibrate any delays in the video circuitry and the digitization process. The parallel port on the computer powers the LED, and the timestamp of each time the LED turns on or off is logged in a file and stored on the computer. A sequence of 10 flashes is used to align the video stream with the system clock. The LED intensity and the timing in the digitized video are compared to the on/off times of the LED to calculate the delay. By timing the 10 flashes to occur over nine video frames, the delay can be calculated to within less than a video frame. Because of timing problems in the laptop generating the flashing sequence, however, the delay was calibrated only to within one video frame.

### **A.1.2 Base Station Identification**

Because we are monitoring active cellular base stations, there remains a remote possibility that the signal strength reported by the spectrum analyzer comes from a nearby base station that uses the

same carrier frequency. To rule out this possibility, or at least to determine where it occurs, the base station control channel is decoded to learn the base station's identity.

The AT&T base stations in the financial district adhere to the TIA/EIA-136 (TDMA Cellular PCS) standard [91]. Part of this standard requires backward compatibility to the Advanced Mobile Phone System (AMPS) which was the initial analog cellular standard used in the U. S. As the standards evolved, an interim standard, IS-54, called for the use of a digitally modulated control channel for analog calls. This channel is called the Forward Analog Control Channel (FOCC). This channel broadcasts various information regarding the system status and features to mobiles in the coverage area. The two pieces of information in which we are most interested are the system identifier (SID) and the digital color code (DCC). The SID is an identifier that is assigned by the FCC and is unique to each service provider. The DCC is a two-bit identifier to distinguish between the two closest base stations that use the same control channel frequency. The service provider, then, must ensure that two base stations that are within range of each other and use the same control channel frequency have different DCCs.

Since many service providers are upgrading their older equipment to handle the newer digital formats, many of the old assets are being auctioned off to surplus warehouses. As a result, we were able to obtain, rather inexpensively, two AMPS base station transceivers. These transceivers are rather useful since they are relatively easy to reconfigure to receive the control channel signal.

The most daunting challenge in reconfiguring the transceivers is that they were originally configured to be used in a base station and to receive on the uplink frequencies (825.030–844.980 MHz) and transmit on the downlink frequencies (870.030–889.980 MHz). We, however, needed to receive on the downlink frequencies. Figure A.3 shows a transceiver in its original configuration. On the left side of the picture are two receivers that are connected to two separate antennas for receive diversity. In the center of the case is the channel selection board. This board divides an external frequency reference down to a 15 kHz reference signal used by the phase-lock loop (PLL). The channel selection board also shifts the appropriate counter value into the PLL so that the voltage-controlled oscillator (VCO) tunes to the appropriate downconversion frequency. The counter value is derived from a channel setting read from DIP switches or set externally by the system bus. Finally, on the right are modulation and power amplification circuitry for the transmit functions.

At the input to the two receivers are large rectangular cavity filters that are centered on the

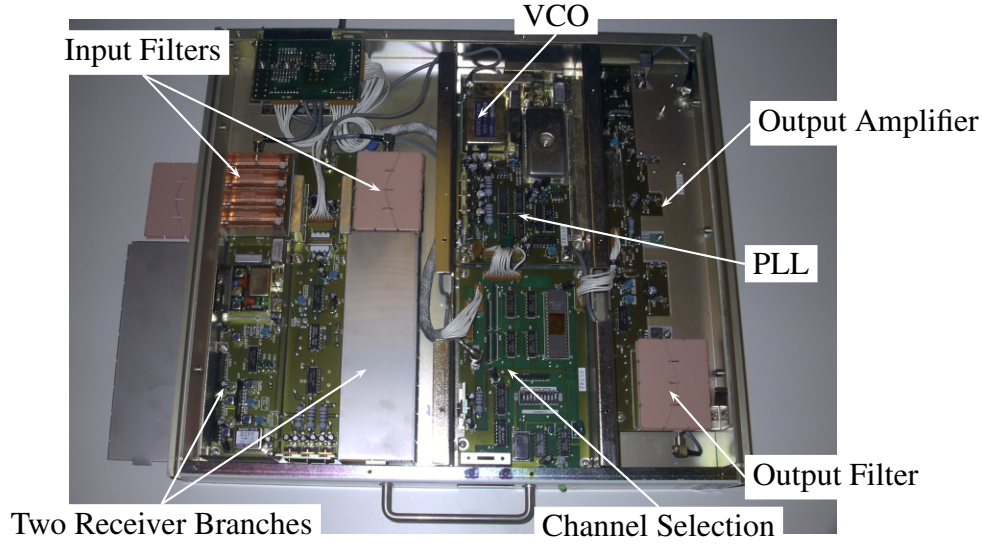


Figure A.3: AMPS Base Station Transceiver. This image shows the base station transceiver in its original configuration. The filter cover and RF shield are removed from one of the receiver branches to show the circuit detail.

uplink frequency band and serve as both image rejection and channel isolation filters to isolate the uplink from the downlink frequencies. Similarly, the output circuit has a filter that is centered on the downlink frequency band. Fortunately, the filters have the same footprint. The output filter is removed to replace the input filter on the receiver branch to be used in this experiment.

For the modified receiver branch to receive the downlink signal, the VCO must provide the proper downconversion frequency. The first intermediate frequency (IF) in the receiver is at 45 MHz, so the VCO must be tuned 45 MHz below the desired receive frequency. To receive the downlink frequencies around 879 MHz, the VCO must tune around 834 MHz. As seen in Fig. A.4, the VCO, in its original configuration, tunes to a frequency band that is lower than what is needed for this experiment.

To alter the VCO's characteristics, one must look inside the case as shown in Fig. A.5. The VCO is a Colpitts oscillator that uses a strip-line resonator as part of the tank circuit. Since the resonant frequency is proportional to  $1/\sqrt{LC}$  where  $L$  and  $C$  are the inductance and capacitance, respectively, of the tank circuit, one must either reduce  $L$  or  $C$  in order to achieve a higher resonant frequency. For this circuit, the easiest method is to remove some capacitors from the tank circuit. The removal of a 14.8 pF capacitor pushes the resonant frequency higher, as shown in Fig. A.4.

The PLL, however, requires a precise and stable reference frequency in order to hold the VCO

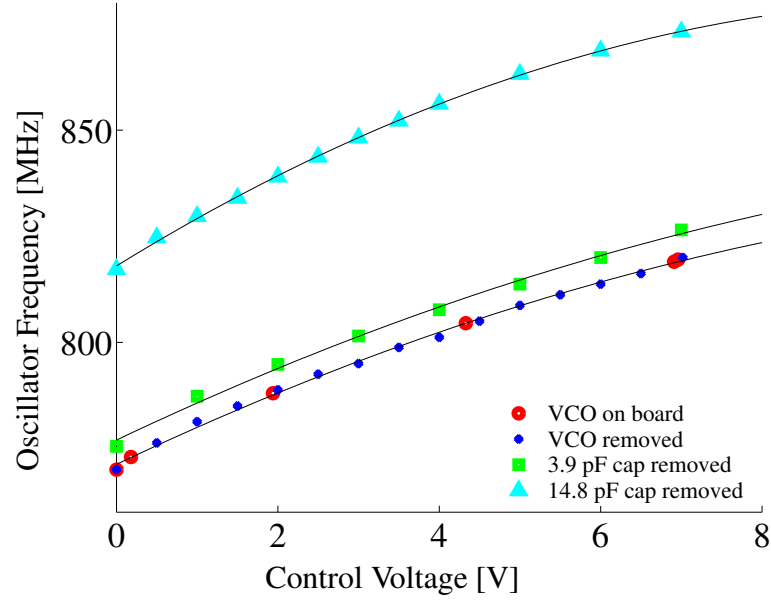


Figure A.4: VCO Tuning Characteristics. After removing the 14.8 pF capacitor from the tank circuit, the VCO is tunable throughout the desired 834 MHz tuning range.

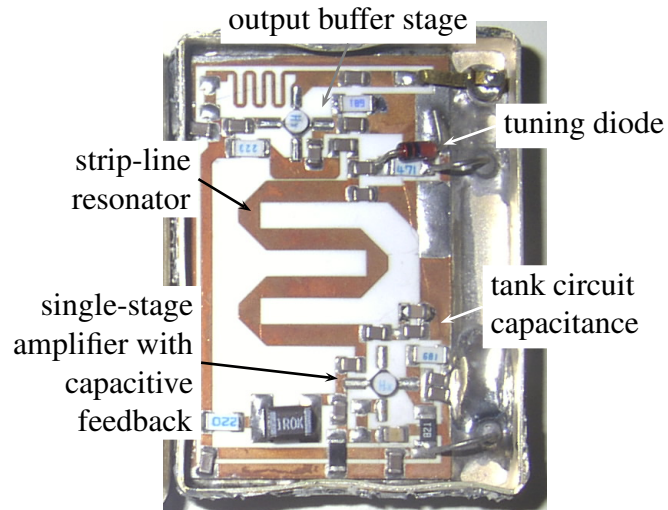


Figure A.5: VCO Circuit. With the lid removed, one can see the Colpitts configuration of the VCO. The tank circuit capacitance is reduced to shift the VCO tuning range higher.



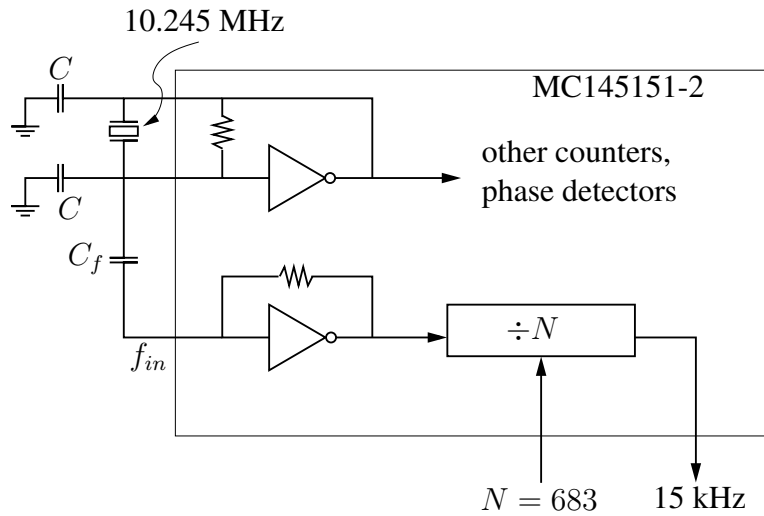


Figure A.6: Frequency Reference Circuit. The MC145151-2 is used in a non-standard configuration to divide the frequency of a 10.245 MHz reference oscillator down to the desired 15 kHz reference frequency. The oscillator load capacitors,  $C$ , are adjusted so that the final VCO frequency is within 100 Hz of the downlink carrier frequency.

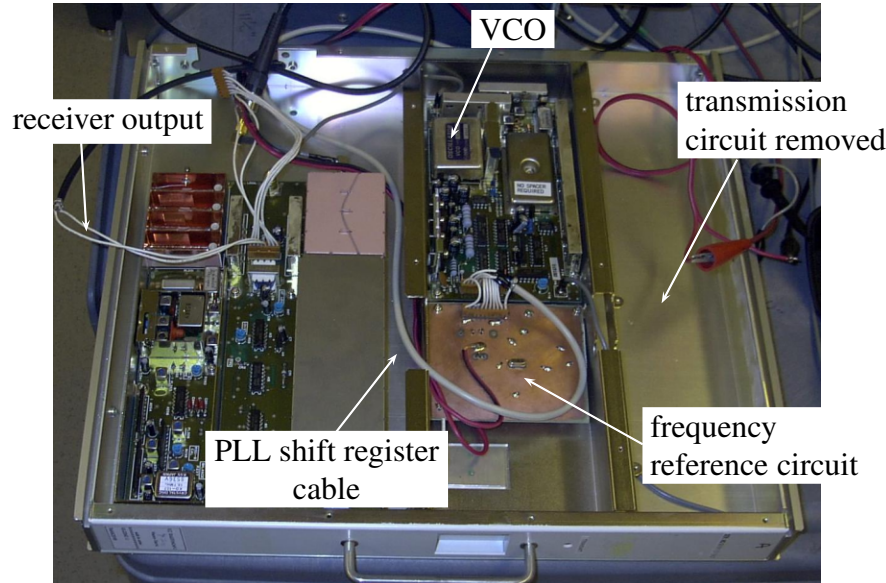


Figure A.7: Modified Base Station Transceiver. After the modifications, the transceiver uses one receiver branch with the input filter replaced. With the modified VCO and the new frequency reference circuit in place, the appropriate counter value for the PLL is shifted in from the laptop computer. The transmitter circuit is removed to conserve power and eliminate unwanted interference.

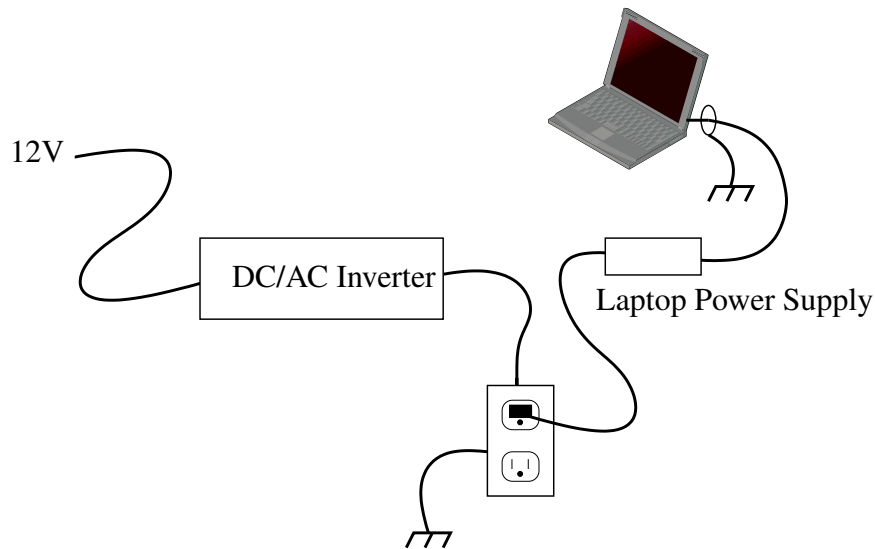


Figure A.8: Power Supply Grounding Scheme. Transients from the power inverter and the laptop power supply are eliminated by grounding the power supply cable at the laptop and the ground prong at the inverter.

steady and at the right frequency for the receiver to work. When this transceiver was used in a base station, a stable oscillator, external to the transceiver, provided the reference frequency. The reference frequency for this experiment, however, is provided by the circuit represented by Fig. A.6. The MC145151-2 is normally used in a PLL, and the input frequency,  $f_{in}$ , usually comes from a VCO and not from the crystal oscillator itself. In this case, however, a simple frequency division is all that is needed, so only the frequency division and the oscillator feedback portions of the chip are used. The load and coupling capacitances  $C$  and  $C_f$  are adjusted so that the resulting VCO frequencies are stable and within 100 Hz of the desired local oscillator frequency. Since the original channel selection board is replaced (see Fig. A.7) and since the DIP switches do not provide the PLL with the right counter values for the new, higher frequencies, the PLL counter value is shifted in from the digital I/O board used in the laptop computer.

### A.1.3 Power Supplies

A clean power supply is required for high-fidelity signal measurements. For example, the A/D converters in the laptop computer used in this experiment are sensitive to power supply fluctuations,

especially when reading the ABS sensor, which is referred to the vehicle chassis ground. Extra steps are therefore taken to eliminate unwanted ground currents.

A 300 W power inverter is used to power the instrumentation for this experiment. This power supply was not designed as an instrumentation power supply and is most often used for camping. Additionally, the laptop power supply does not use a three-pronged plug and therefore has no solid ground reference to the vehicle chassis, which is required for reading the ABS sensor. To provide a common ground reference for both the laptop and the spectrum analyzer, the ground terminal of an external utility outlet is grounded to the vehicle chassis. The outer conductor on the plug to the laptop is the negative lead of a DC power supply. This lead is also grounded to the vehicle chassis. The final grounding scheme is shown in Fig. A.8.

## A.2 Software Design and Configuration

As seen in Fig. A.1, there are a number of separate data streams that must be synchronized by a single computer. Each data stream must time-share the CPU. This section outlines the software required to provide the appropriate timing indicators to each data stream and how the separate data streams are put back together during offline processing.

### A.2.1 Device Drivers

The laptop computer runs the Linux operating system. This is a multi-tasking operating system. A device driver is a software module that enables the operating system to communicate to a particular hardware device. In this case, a separate device driver is provided for each of the following hardware devices: the GPIB card, the parallel port, the sound card, and the data acquisition card.

The GPIB device driver has no strict synchronization requirements in terms of the measurement setup. Its only task during the experiment is to command the spectrum analyzer to enter zero-span mode, to tune to the proper frequency, and to set the bandwidth of the resolution filter. This device driver is largely adapted from the device drivers written for the Windows operating system and provided by the manufacturer of the card.

The parallel port driver is the simplest device driver used in this configuration. Its only task is to toggle the output pin that turns the LED on and off while recording the system time of each

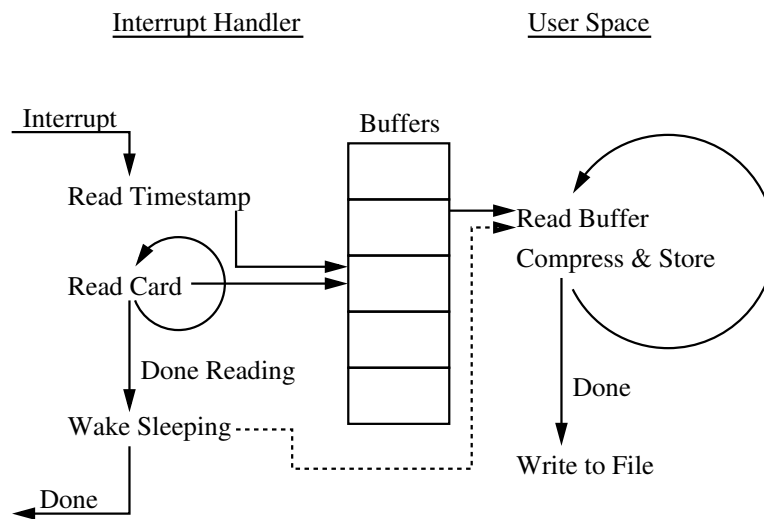
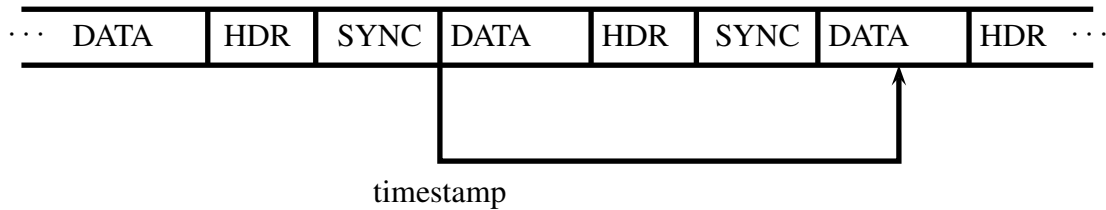


Figure A.9: A/D Control Flow. When its input buffer is full, the A/D card signals the device driver with a hardware interrupt. The device driver services the interrupt by immediately taking a timestamp and storing it along with the new samples into a circular buffer. Finally, the device driver signals, through the operating system, the user-space program waiting on the data. The user-space program then reads the buffer from the device driver.

event. The timestamps are then made available to the data collection program.

The analog input operation of the data acquisition card and the reading of the sound card both perform an analog-to-digital conversion. Although they require separate device drivers, the functional description of each operation is very similar and is shown in Fig. A.9. An interrupt occurs whenever the card has filled its input buffer. Since the sound card has direct memory access, the input buffer is merely the assigned buffer in the driver's buffer pool. The interrupt marks the time of the last sample and is stored in the buffer along with the data samples. The data acquisition card, on the other hand, does not have direct memory access, so the CPU must move each sample to its buffer at interrupt time. The time-tagging of the samples, however, is identical to what is done with the sound card. Whenever the driver's buffer is ready to be delivered to the data collection program, the driver notifies the operating system that the user program may read the buffer if it is waiting on new data.

In addition to reading the ABS sensor, the sound card must also generate the timing signal to be recorded on the audio track of the video camera. The format of the data stream is shown in



HDR  $\Rightarrow$  10101010101010101010 (20 bits)

SYNC  $\Rightarrow$  1111111111 (10 bits)

DATA  $\Rightarrow$  timestamp of previous frame + checksum (90 bits)

Figure A.10: Video Camera Timing Frame Format. The continuous timing data stream is broken into frames consisting of header and sync blocks for frame synchronization and a data portion that holds the timestamp of the previous SYNC/DATA boundary along with a timestamp. The bitstream is modulated onto the sound card output using frequency-shift keying.

Fig. A.10. The data modulation used is frequency-shift keying (FSK) where a logic “0” corresponds to a 4 kHz tone and a logic “1” corresponds to an 8 kHz tone. Frame synchronization is provided by the header (HDR) and synchronization (SYNC) blocks with the bit patterns as identified in the figure. The data portion consists of the system time (8 bytes) followed by a 1-byte checksum. Each data byte starts with a start bit (logic “0”) and ends with a stop bit (logic “1”).

The flow of the device driver operation is outlined in Fig. A.11. The driver pre-computes each timing frame and uses double-buffering to provide a continuous stream of output samples. Each buffer is allocated to hold enough samples for a complete frame. At interrupt time, the driver immediately records the timestamp and commands the previously computed buffer to play on the sound card output by adjusting the sound card’s direct memory access (DMA) pointers. The subsequent buffer is then computed using the current timestamp. The pre-computation goes through the last bit of the SYNC block. Therefore, the timestamp that is stored in the following frame is synchronized to the “1” to “0” bit transition of the SYNC block and the start bit of the data block.

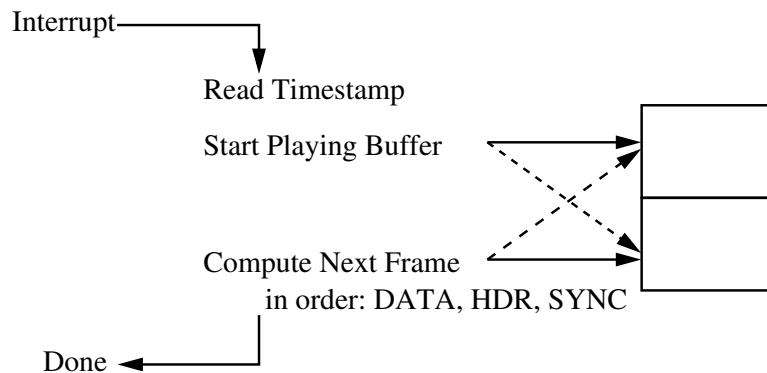


Figure A.11: Sound Card Interrupt Service Routine. Double-buffering is used to generate a continuous output stream on the sound card. When the previous output buffer is finished, the sound card generates an interrupt. Within the interrupt handler, the sound card is directed to start playing immediately the next buffer, which was pre-computed. Then, the subsequent buffer is computed before the interrupt handler exits.

### A.2.2 Software Tools

After the measurements are collected, there are some tasks that must be done before the data can be interpreted. First, the identity of the base station must be verified by decoding the FOCC.

The FOCC consists of a Manchester-encoded FSK signal keyed at 10 kbps. The frame format is shown in Fig. A.12. The dotting and word sync bits provide for frame synchronization. Five repetitions of two 40-bit words (A and B) follow the word sync bits. A mobile listens to either the A word or the B word, depending on the parity of its mobile identification number. Interspersed throughout the frame are busy/idle (B/I) bits that indicate which time slots on the reverse analog control channel are in use. The B/I bits are inserted before the dotting sequence, before the word sync, and every 10 bits throughout the remainder of the frame.

Every system word has a type field (TY) and a parity field. The parity field holds the results of the cyclic redundancy check (CRC) that is performed on the word. The type field is a 2-bit indicator of how the remainder of the word is to be interpreted. When this field is 11, then the word is treated as a system overhead word, and the 3-bit overhead field (OHD) determines the overhead word type. We are specifically interested in the System Parameter Word 1 (OHD = 110) since it contains the digital color code (DCC) and the first 14 bits of the system identifier (SID1), which together uniquely identify the base station in the local area.

The modified base station transceiver receives the control channel signal and demodulates it.

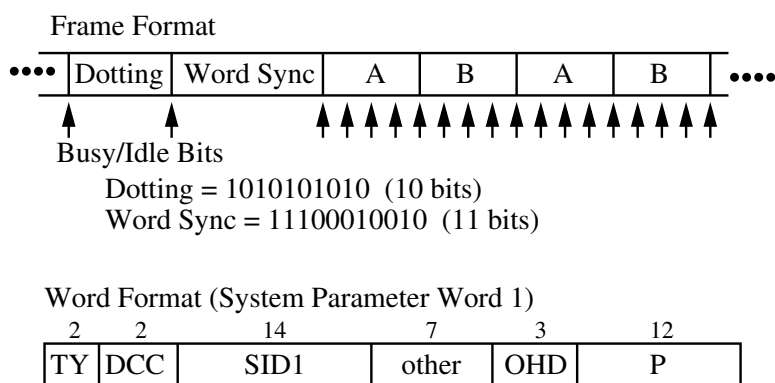


Figure A.12: TIA/EIA-136 Control Channel Format. The control channel frame synchronization is established by finding the dotting and word sync bit patterns. The busy/idle bits are removed before the A and B system words are decoded. Word sequences are parsed across different frames to find System Parameter Word 1, which holds the base station identification.

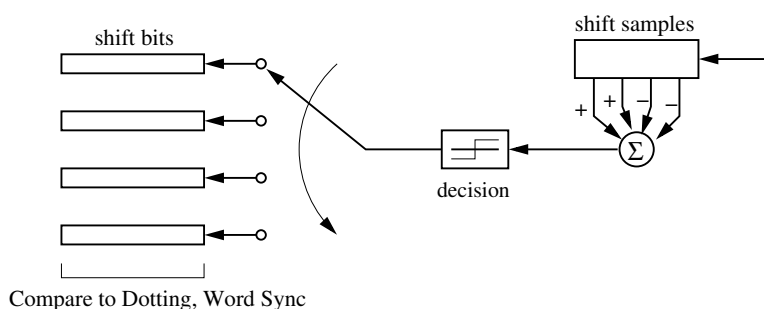


Figure A.13: Base Station Decoder. Analog samples are shifted into a decision unit that decodes a single bit. Each bit is shifted into one of four candidate bit streams. When the dotting and word sync sequences are found in one of the candidate bit streams, frame synchronization is flagged, and the remainder of the frame is decoded.

The transceiver itself simply acts as an FM demodulator, so the bitstream must also be decoded. Since the raw data samples are stored in a file, the decoding process may be done offline. The outline of the decoder is shown in Fig. A.13.

The signal is sampled at 40 kHz, providing four samples per symbol. The Manchester decoding is done by a simple addition and subtraction of the four most recent samples. The polarity of the sum determines the logic level which is shifted into one of four candidate bitstreams until the correct synchronization is found. Each of the candidate bitstreams is searched for the dotting and word sync bits. Once they are found, the bit and frame synchronization are set for the entire frame. After a complete frame is received, the busy/idle bits are removed, and a CRC is performed using a table-assisted computation that takes in 8 bits at a time and can be done in five steps. An error vector table is used to correct up to two bit errors in case of a nonzero CRC. The decoding program searches successive frames, eventually finding System Parameter Word 1 and noting the base station's identity.

Another important post-processing task is feature identification in the video transcript. Features in the video are identified for the distance calibration, for corner identification, and for the LED sequence calibration. A screenshot of the tool is shown in Fig. A.14.

The video alignment tool decodes the timing stream stored on the audio track. Each video frame is tagged with a time that refers back to the computer's system clock. Additionally, the user can view the video frame by frame, manually entering points of interest that are stored in Matlab data files to be used for further processing. Because many of the measurements are taken at night, the tool also has an edge detector built in to aid in feature identification when there is very little contrast due to the darkness of the image.

### **A.3 Transmitter Location**

The location of the transmitting antenna relative to the surrounding tall buildings provides insight to the mechanisms that govern the propagation of signals throughout the coverage area. The location of the transmit antenna used for the measurements in this report is shown in Fig. A.15. The building heights are from maps maintained by the San Francisco Planning Department. The orientation parameters of the antenna are provided by AT&T Wireless and are given in Table A.2.

The antenna is mounted on a medium-sized building at 22 Battery Street. The antenna is lower





Figure A.14: Video Alignment Tool. A custom video processing tool is used to annotate features manually in the digitized video stream during offline processing. The timing signal is decoded from the audio track to correlate the video frames with the measurement data. Edge detection is used to identify building features in low-light conditions.

Address	22 Battery Street
Azimuth	20°
Height	178 ft
Tilt	10°

Table A.2: Transmit Antenna Location and Orientation. The values in this table are provided by the cellular service provider, AT&T Wireless.

than the rooftops of the surrounding tall buildings. As a result, the propagation of radio waves down the streets in the financial district is expected to come primarily from waves diffracted around the corners of and guided by the tall buildings in the area.

## A.4 Summary of Measurements

The statistical propagation model used throughout this report is

$$P(\mathbf{x}) = D(\mathbf{x})L(\mathbf{x})Y(\mathbf{x}), \quad (\text{A.1})$$

where  $P(\mathbf{x})$  is the received signal power at position  $\mathbf{x}$ ,  $D(\mathbf{x})$  is a distance-dependent trend,  $L(\mathbf{x})$  is the large-scale signal variation, and  $Y(\mathbf{x})$  is the small-scale fading. The position  $\mathbf{x}$  is a two-dimensional vector lying in the plane of the streets and indicating the position of the mobile receiver, with the base of the transmitter as the origin of the coordinate system.

In this section, we present the parameters of the distance-dependent trend and the statistics of the large- and small-scale fading for streets in the financial district. Chapter 5 presents the large-scale fading statistics for the entire area, including the effects of the corner transitions (see Fig. 5.3). The large-scale fading statistics of the entire measurement area are consistent with macrocell measurements [14,66,75], while the statistics of the individual streets are consistent with the microcell measurements reported by Berg, *et. al.* [10]. The statistics for the individual streets presented in this appendix use the same street segments—with the corner transitions removed—as was done in Chapter 6 (see Fig. 6.2).

Since parameters change slightly from one measurement to the next, the values presented in this section are slightly different from some of the values reported in Chapter 5. The most significant disagreement between the results presented in this appendix and those in Chapter 5 is for

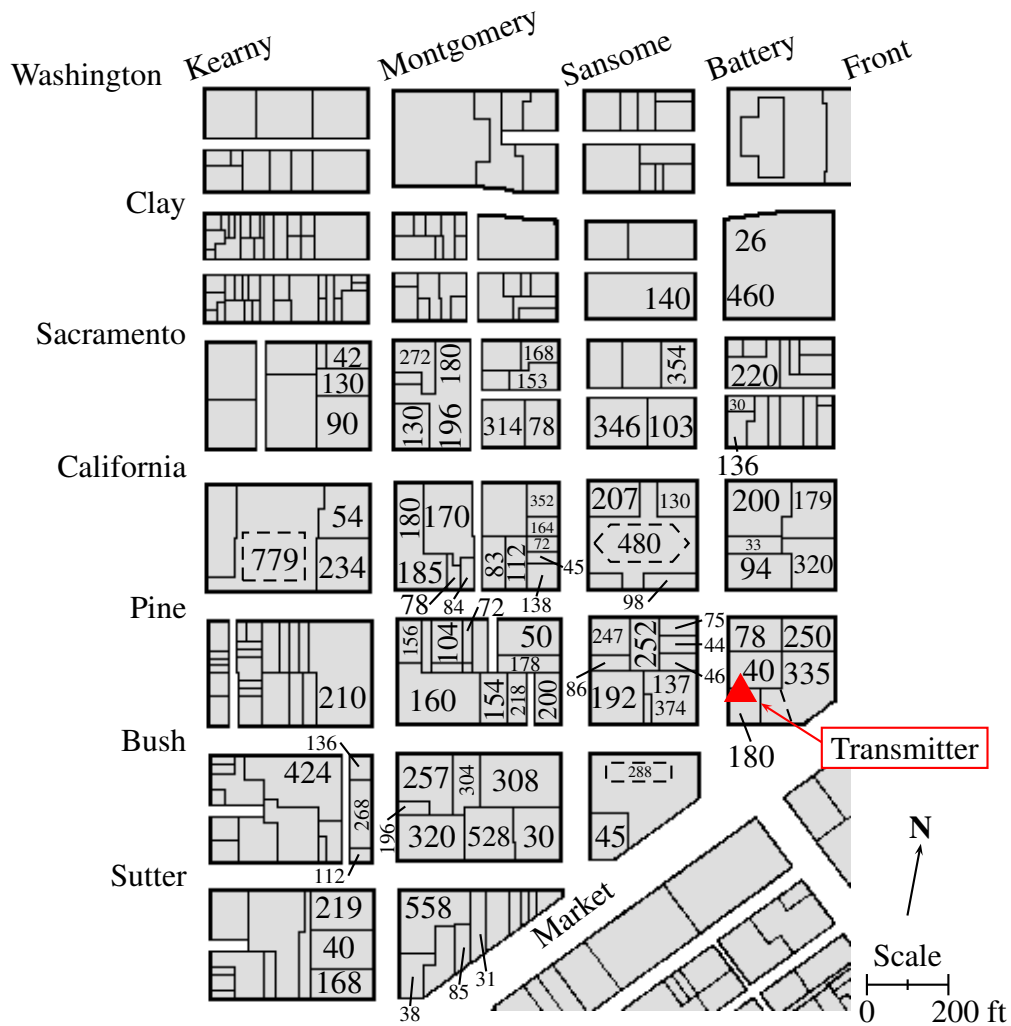


Figure A.15: Heights of Buildings in the Vicinity of the Transmitter. The numbers on this map indicate building heights, given in feet. The solid lines represent property boundaries. The dashed lines represent footprints of buildings, if available and if they deviate significantly from the property lines.

Sacramento Street. Identifying where the distance-dependent trend is different from the transition at the edge of an intersection is somewhat arbitrary. The cutoff point used in this appendix is the same as that used in Chapter 6, accounting for the disagreement with the Sacramento Street results in Chapter 5.

For the remainder of this section, the following notation is used: For measurements on a given street, there is a finite number of samples,  $N$ . The sample locations are indexed by a subscript of the position variable,  $\mathbf{x}$ , and are equally spaced along the drive path such that  $\|x_{i+1} - x_i\| = \Delta d$ . Some quantities are computed using linear units, while others use decibels. For convenience, the subscript ‘dB’ is affixed to any quantity for which the units are decibels.

### A.4.1 Large-Scale Properties

The large-scale fading is the deviation of the average received signal power from a distance-dependent trend from the transmitter. The large-scale variation for measurements made in the financial district follows a lognormal distribution as seen in Fig. A.16. The autocorrelation of the large-scale fading is shown in Fig. A.17 and is compared to the exponential model proposed by Gudmundson [31].

To identify the large-scale variation of the received signal strength, the effects of the small-scale fading are averaged out. The received signal power  $P(\mathbf{x})$  is smoothed using spatial averaging:

$$S(\mathbf{x}) = \langle P(\mathbf{x}) \rangle_W. \quad (\text{A.2})$$

The  $\langle \cdot \rangle_W$  operation denotes the spatial average with window  $W$  taken along the drive path of the vehicle. In addition to the large-scale variation, the smoothed estimate  $S(\mathbf{x})$  also includes the distance-dependent trend

$$D_{\text{dB}}(\mathbf{x}) = K_0 - 10 n \log_{10} \|\mathbf{x}\| \quad (\text{A.3})$$

where  $K_0$  is a constant accounting for gains and losses, and  $n$  is the path-loss exponent. The parameters  $K_0$  and  $n$  for the distance-dependent trend are computed from samples of the smoothed

power profile using least squares:

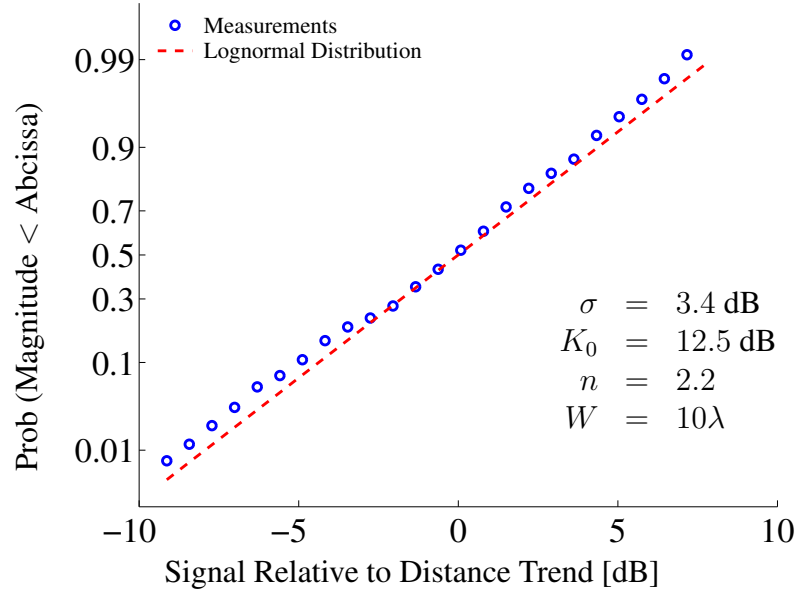
$$\begin{bmatrix} K_0 \\ n \end{bmatrix} = \begin{bmatrix} 1 & -10 \log_{10} ||\mathbf{x}_1|| \\ \vdots & \vdots \\ 1 & -10 \log_{10} ||\mathbf{x}_N|| \end{bmatrix} \setminus \begin{bmatrix} S_{\text{dB}}(\mathbf{x}_1) \\ \vdots \\ S_{\text{dB}}(\mathbf{x}_N) \end{bmatrix}. \quad (\text{A.4})$$

The estimated large-scale variation is then computed by removing the distance-dependent trend from the smoothed estimate:

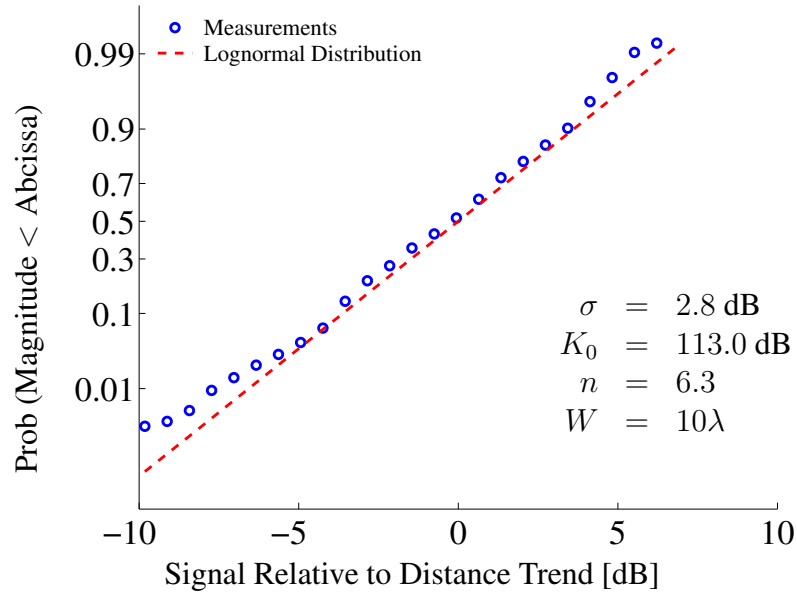
$$\begin{aligned} \hat{L}_{\text{dB}}(\mathbf{x}) &= S_{\text{dB}}(\mathbf{x}) - D_{\text{dB}}(\mathbf{x}) \\ &= S_{\text{dB}} - (K_0 - 10 n \log_{10} |\mathbf{x}|). \end{aligned} \quad (\text{A.5})$$

The autocorrelation of the large-scale variation is computed as

$$R_{\hat{L}}(k\Delta d) = \frac{1}{N-k} \sum_{i=1}^{N-k} \hat{L}_{\text{dB}}(\mathbf{x}_{i+k}) \hat{L}_{\text{dB}}(\mathbf{x}_i). \quad (\text{A.6})$$

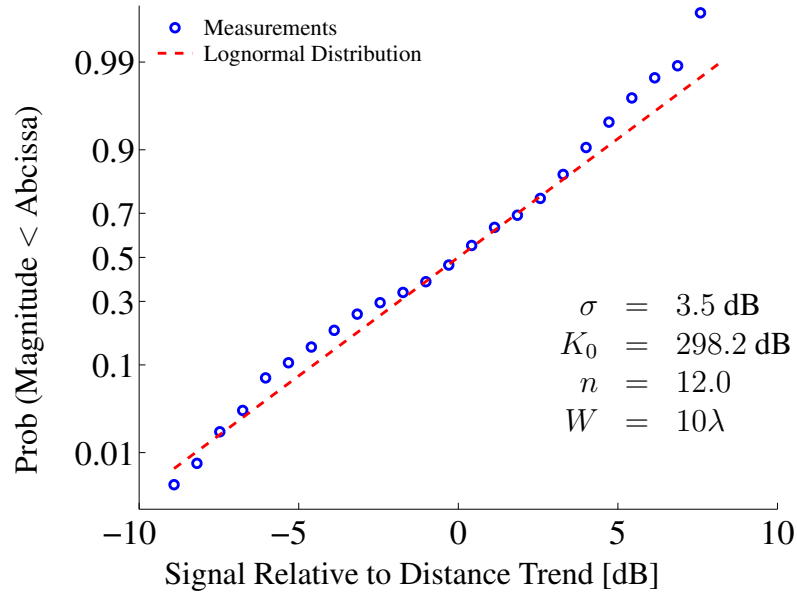


(a) Battery Street

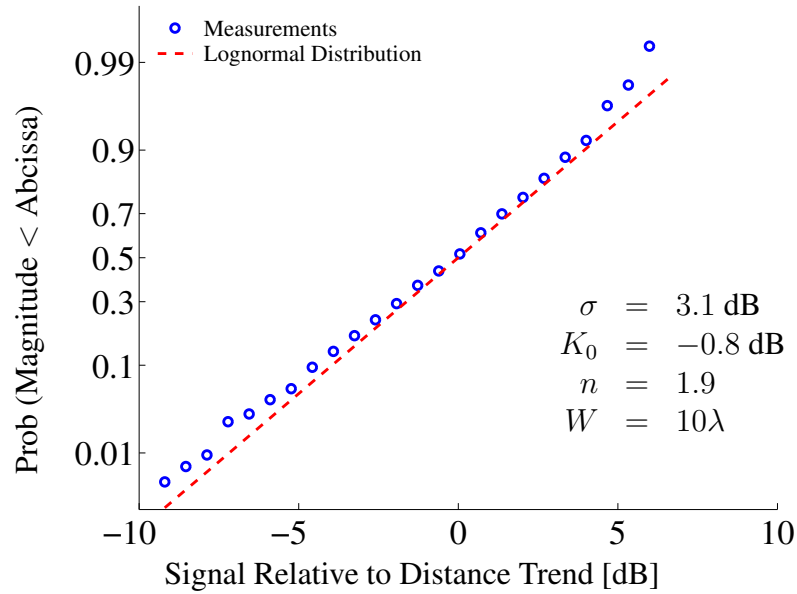


(b) California Street

Figure A.16: Large-Scale Signal Distributions. After the distance-dependent trend is removed, the distribution of the large-scale variation for each street agrees well with lognormal distributions.

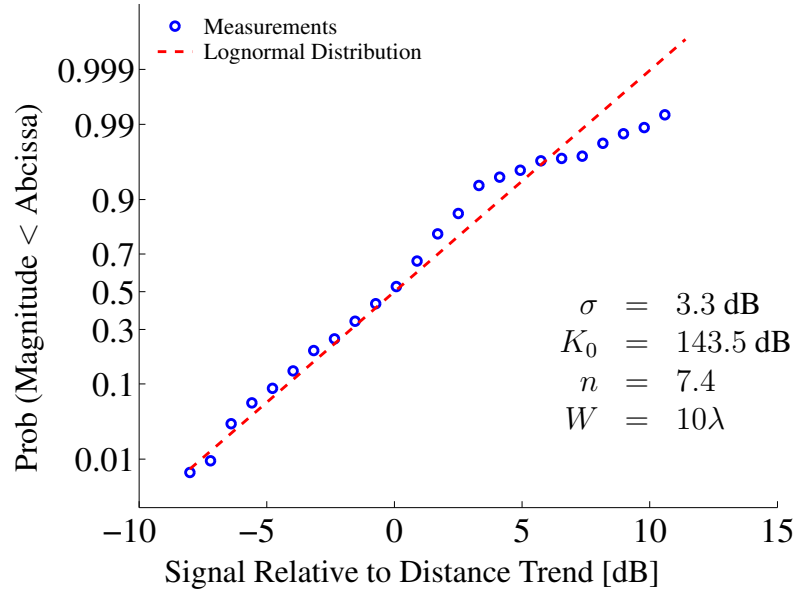


(c) Clay Street

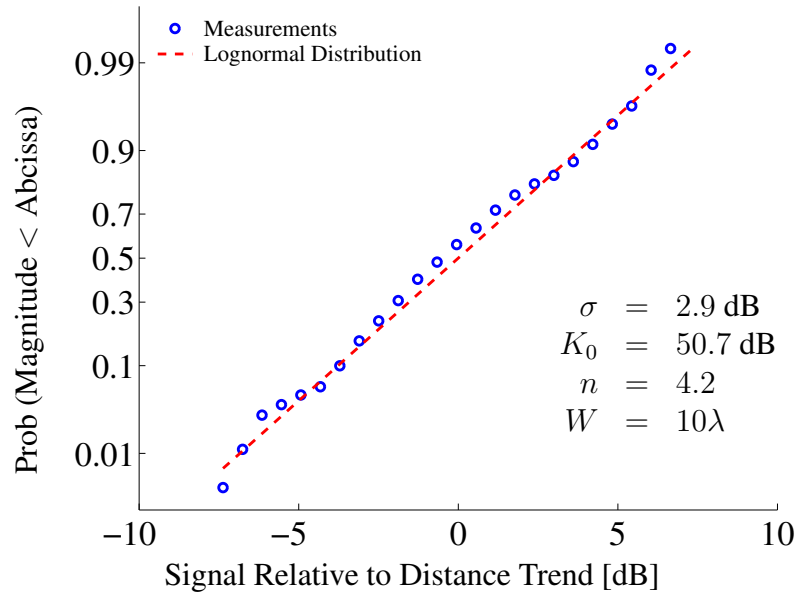


(d) Pine Street

Figure A.16: Large-Scale Signal Distributions (*continued*).



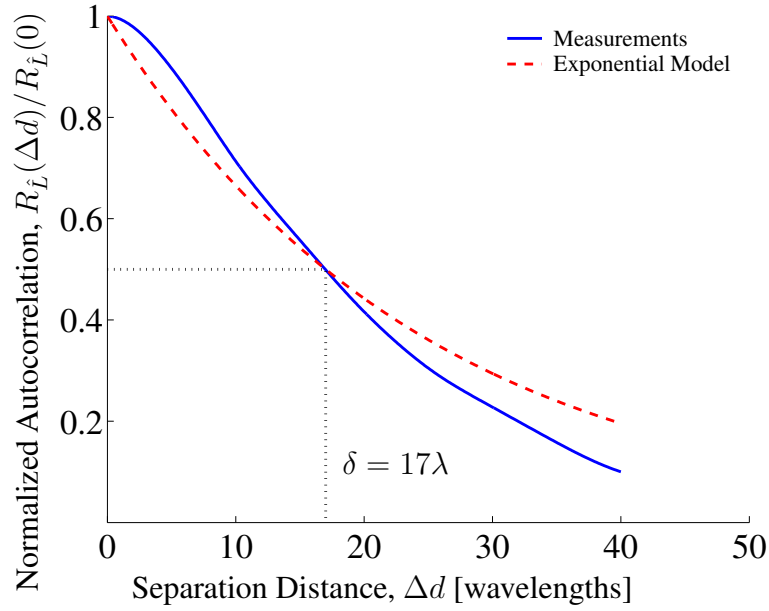
(e) Sacramento Street



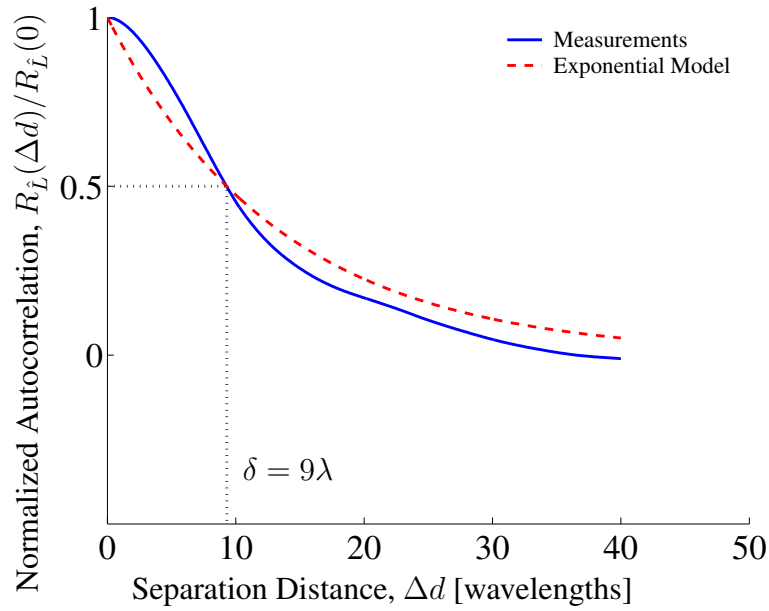
(f) Sansome Street

Figure A.16: Large-Scale Signal Distributions (*continued*).



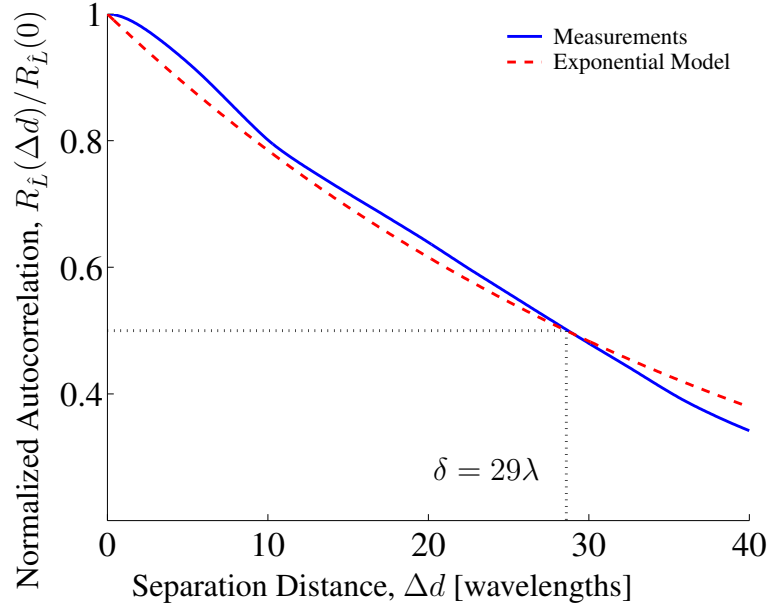


(a) Battery Street

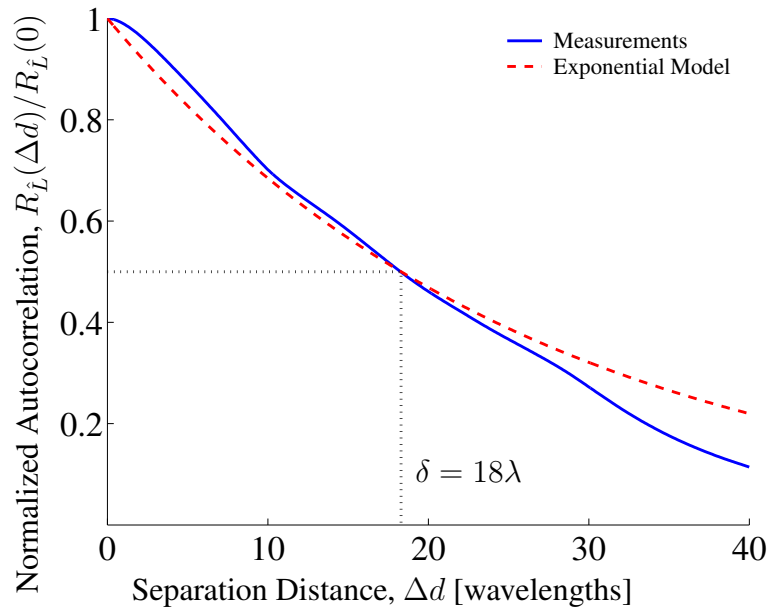


(b) California Street

Figure A.17: Large-Scale Autocorrelations. The autocorrelations of the estimated large-scale fading for each street are compared to the exponential autocorrelation model. The decorrelation distance  $\delta$  is given in each subplot.

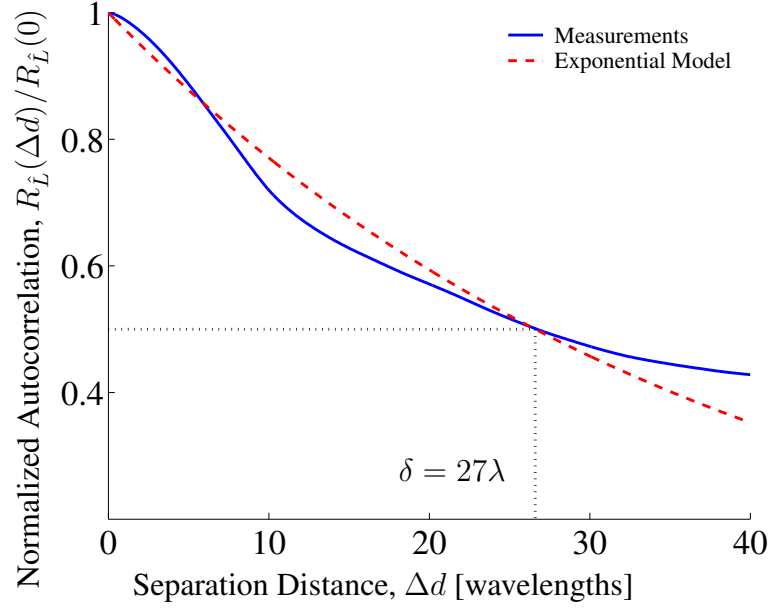


(c) Clay Street

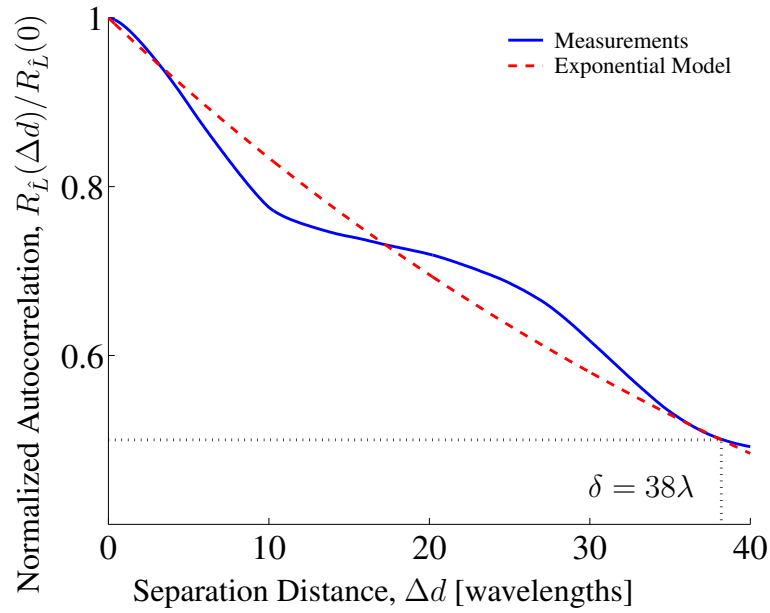


(d) Pine Street

Figure A.17: Large-Scale Autocorrelations (*continued*).



(e) Sacramento Street



(f) Sansome Street

Figure A.17: Large-Scale Autocorrelations (*continued*).

### A.4.2 Small-Scale Properties

Figure A.18 shows the small-scale fading distributions for streets in the financial district. The measured distributions are compared to Rayleigh and Ricean distributions representing ideal multipath models.<sup>1</sup> The autocovariances of the small-scale fading are shown in Fig. A.19 and are compared to the autocovariance of the small-scale fading in the Clarke isotropic scattering model.

The estimated small-scale fading is computed by removing the smoothed estimate, computed using (A.2), from the received signal power measurement:

$$\hat{Y}_{\text{dB}}(\mathbf{x}) = P_{\text{dB}}(\mathbf{x}) - S_{\text{dB}}(\mathbf{x}). \quad (\text{A.7})$$

The statistical distribution and autocovariance are computed from  $\hat{Y}(\mathbf{x})$ , given in linear units. The autocovariance is computed as:

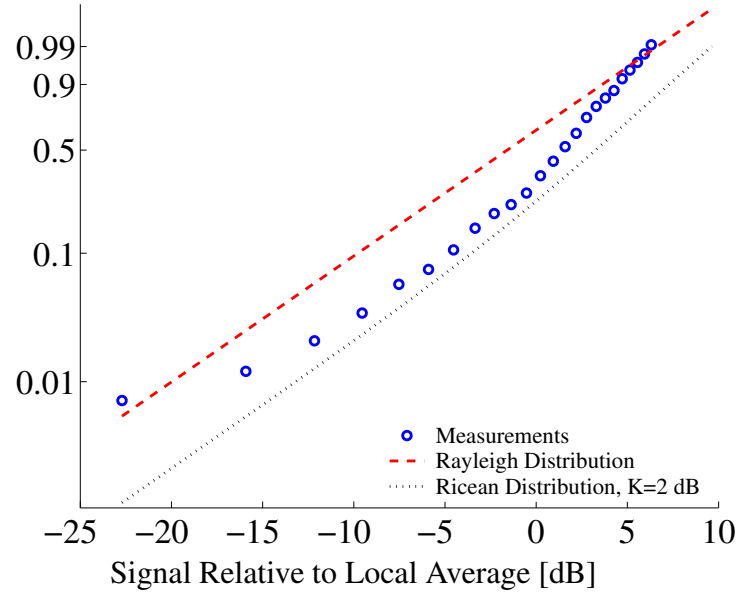
$$R_{\hat{Y}}(k\Delta d) = \frac{1}{N-k} \sum_{i=1}^{N-k} (\hat{Y}(\mathbf{x}_{i+k}) - \overline{\hat{Y}})(\hat{Y}(\mathbf{x}_i) - \overline{\hat{Y}}). \quad (\text{A.8})$$

The quantity  $\overline{\hat{Y}}$  is the average of the small-scale fading over the length of the measurement run and is computed using linear units as well:

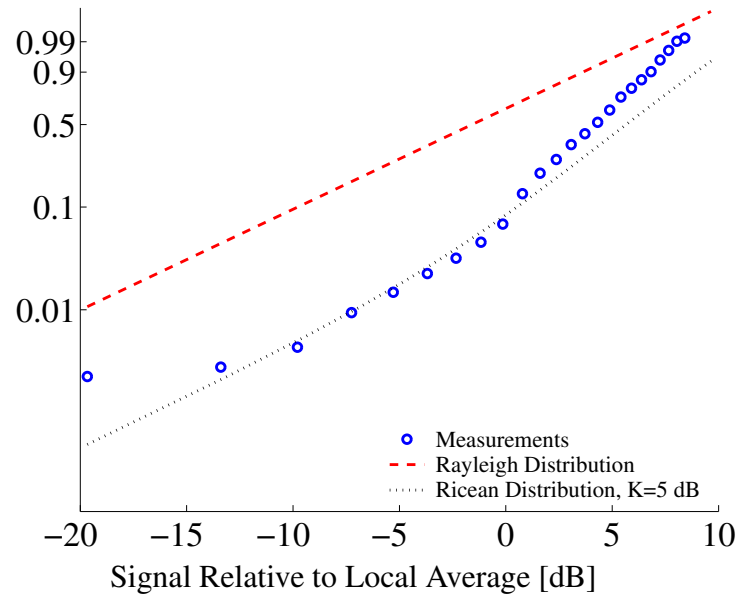
$$\overline{\hat{Y}} = \frac{1}{N} \sum_{i=1}^N \hat{Y}(\mathbf{x}_i). \quad (\text{A.9})$$

---

<sup>1</sup>Note that the vertical axis is “warped” so that a straight line represents a Rayleigh distribution.

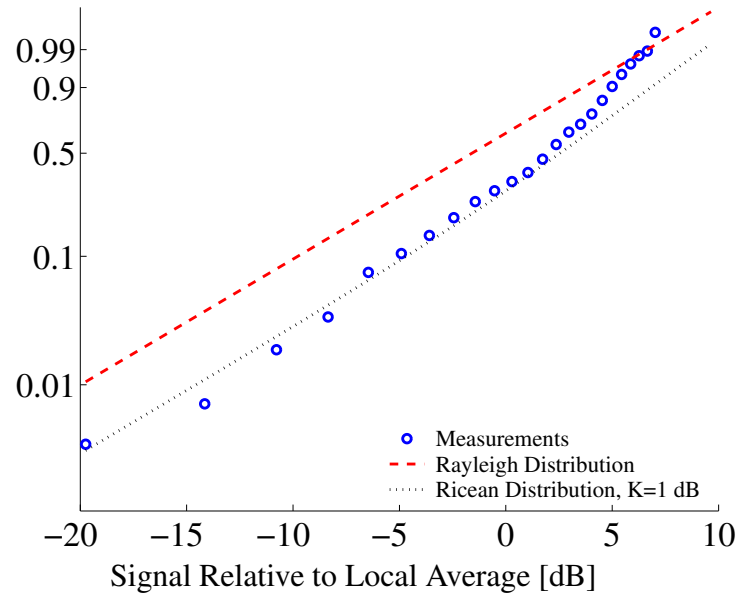


(a) Battery Street

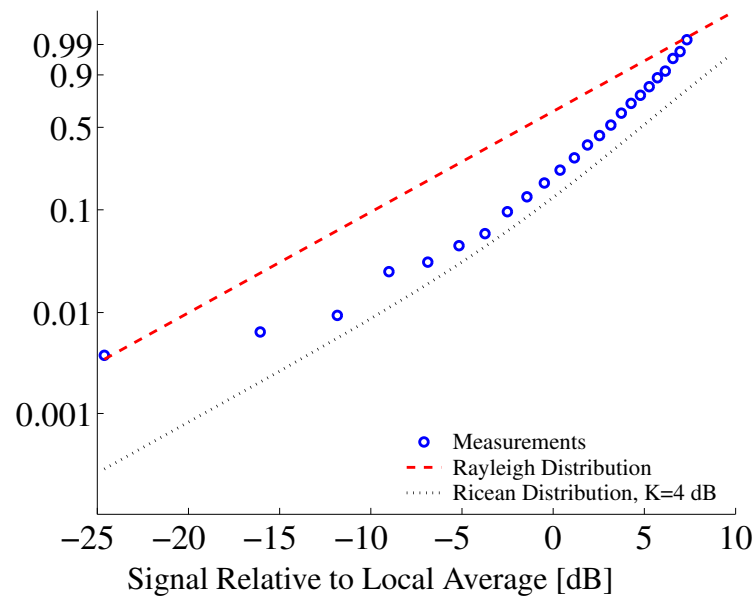


(b) California Street

Figure A.18: Small-Scale Signal Distributions. After the distance-dependent trend and the estimated large-scale fading are removed, the statistics of the small-scale fading are computed. The actual distribution of the small-scale fading for each street is bounded by Rayleigh and Ricean distributions.

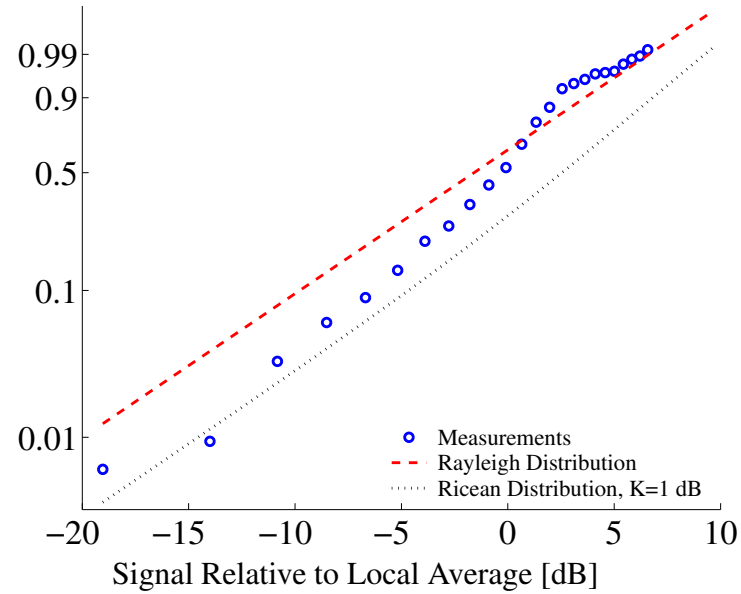


(c) Clay Street

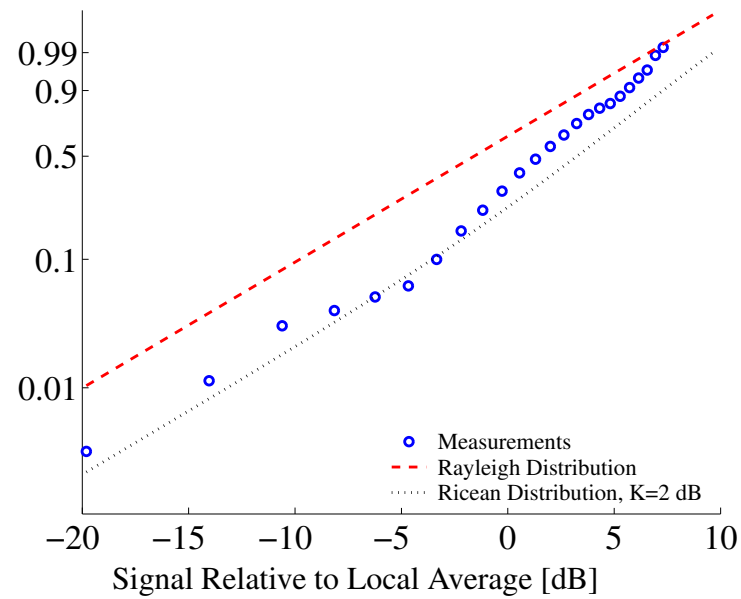


(d) Pine Street

Figure A.18: Small-Scale Signal Distributions (*continued*).

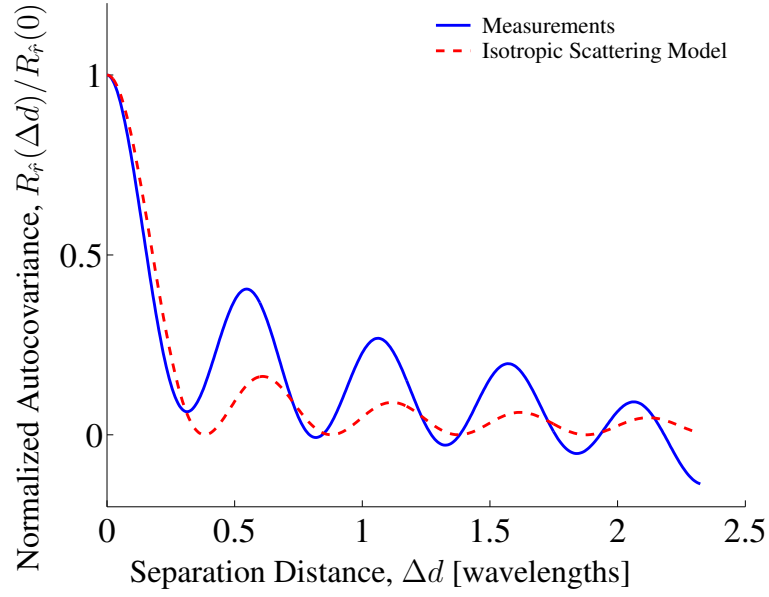


(e) Sacramento Street

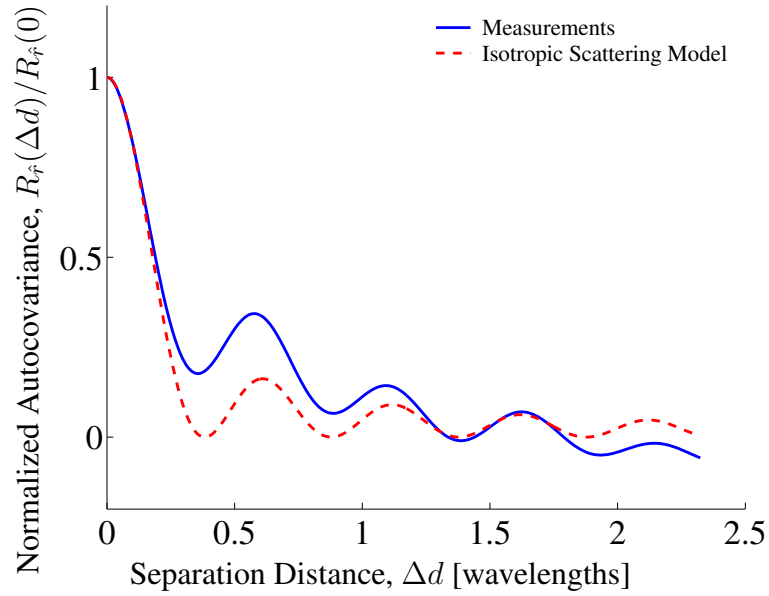


(f) Sansome Street

Figure A.18: Small-Scale Signal Distributions (*continued*).



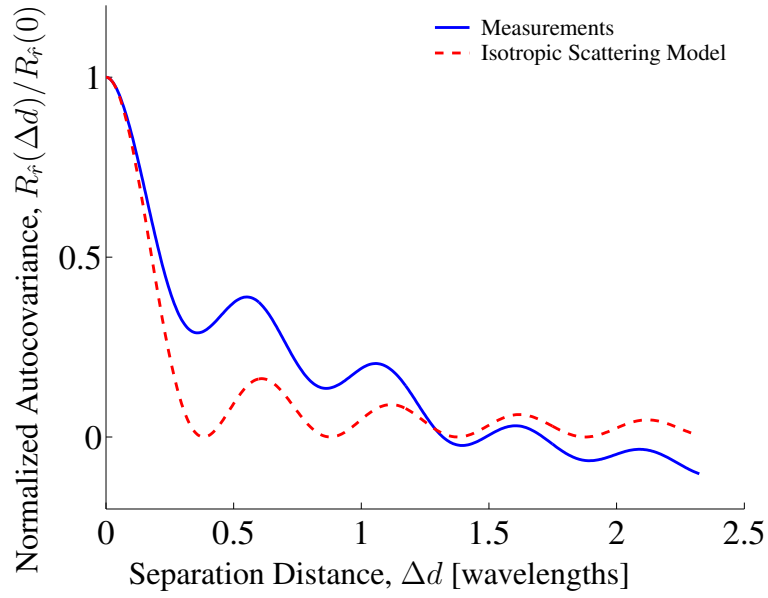
(a) Battery Street



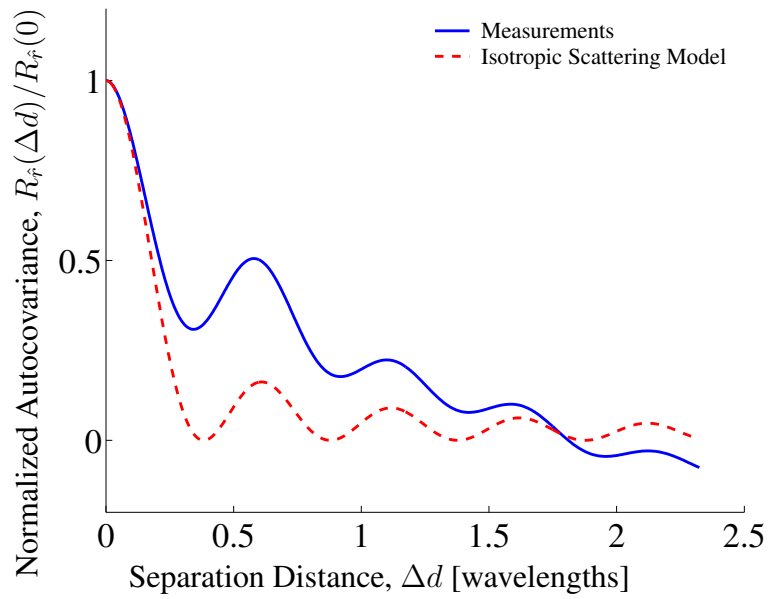
(b) California Street

Figure A.19: Small-Scale Autocorrelations. The autocovariance for the estimated small-scale fading for each street is compared to the autocovariance for ideal, 2-D isotropic scattering.



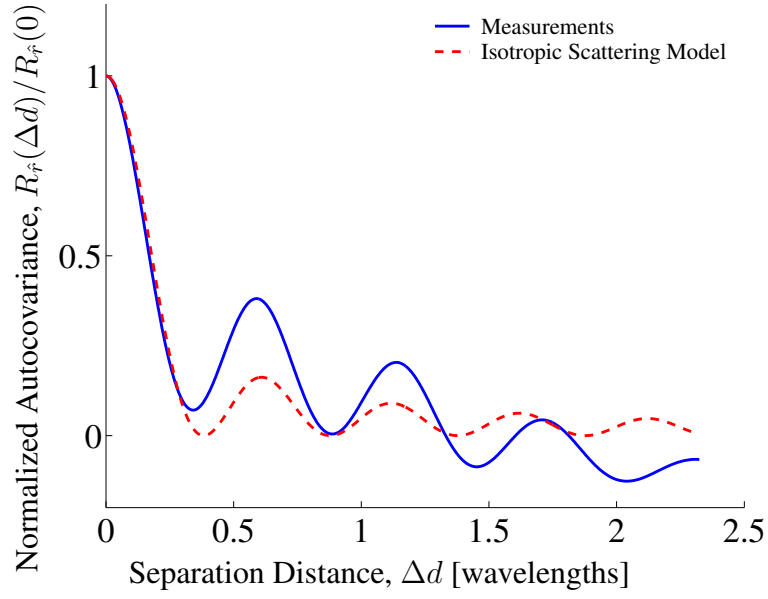


(c) Clay Street

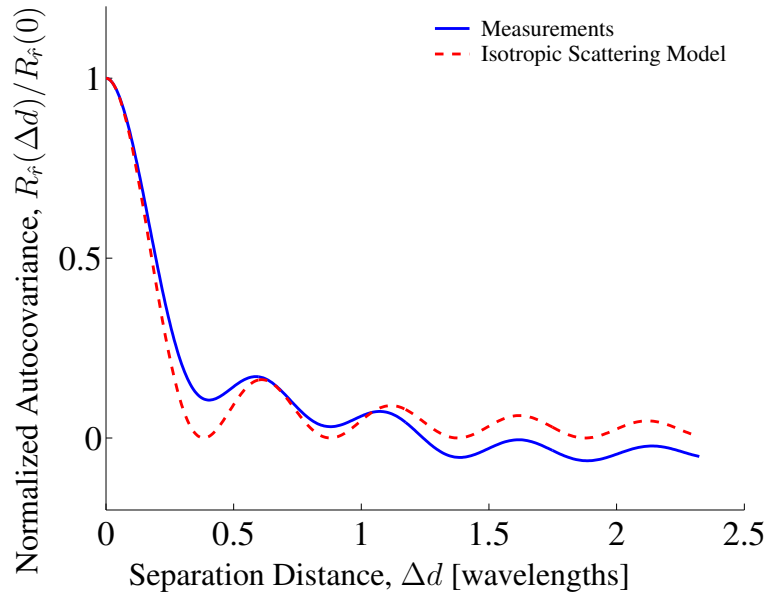


(d) Pine Street

Figure A.19: Small-Scale Autocorrelations (*continued*).



(e) Sacramento Street



(f) Sansome Street

Figure A.19: Small-Scale Autocorrelations (*continued*).

## Appendix B

### Simulation Examples

The computer simulations in Chapter 6 provide a method for indirectly estimating the parameters of the repeatability model from measurements. The examples in this appendix illustrate the relevance of the computer simulations to estimate these parameters. For the simulation to be effective, it must reflect the behavior of the actual signal strength measurements while adhering to a theoretical model.

The construction of the simulation model is given in Section 6.3. The parameters of the model are summarized in Table B.1. The simulated length of the measurement run is chosen to be sufficiently large to ensure that enough variations in the large-scale fading are included.

An example of the simulated signal strength, consisting of both large- and small-scale fading, is shown in Fig. B.1. A 1000-ft section of the run length is displayed in Fig. B.1(a), which is approximately the run length of measurements presented in Chapter 6. The standard deviation and correlation length of the large-scale variation used to generate this figure are 2.8 dB and  $15\lambda$ , respectively, and are the same as those estimated for the left lane of California Street. The distribution and the autocovariance of the small-scale fading envelope are given in Figs. B.2 and B.3. The distribution and the autocorrelation of the large-scale variation are given in Figs. B.4 and B.5. The statistics of the large- and small-scale variation in Figs. B.2 through B.5 are comparable to the equivalent computations on the measurements as given in Section A.4.

Figure B.6 overlays two simulated profiles generated with the same parameters and averaged using a sliding window of  $10\lambda$ . The subfigures illustrate a range of quantified repeatability, and the signal strength profiles are generated to match the statistical parameters of various examples in Chapter 6.

$\mathbf{x}$	two-dimension position vector
$D(\mathbf{x})$	distance-dependent path-loss trend
$L_r(\mathbf{x})$	repeatable large-scale variation
$\ell(\mathbf{x})$	large-scale variation dissimilarity
$Y(\mathbf{x})$	small-scale fading power
$r(\mathbf{x})$	baseband representation of small-scale fading
$\rho$	cross-correlation of small-scale fading envelope $ r(\mathbf{x}) $
$\sigma$	standard deviation of large-scale variation
$\delta$	correlation length of large-scale variation
$\sigma_\ell$	standard deviation of dissimilarity process
$\delta_\ell$	correlation length of dissimilarity process

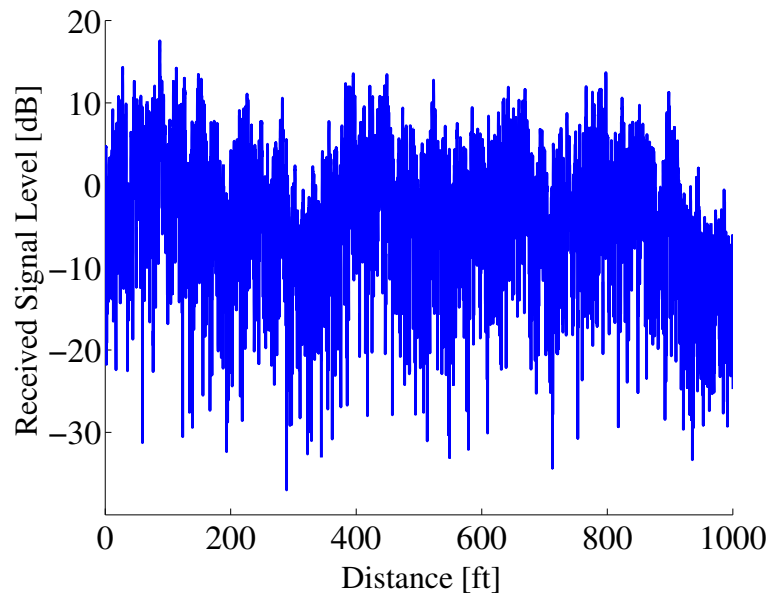
(a)

$F$	sampling frequency	$16/\lambda$
$f_c$	carrier frequency	880 MHz
$M$	length of simulated measurement run	$65.5 \times 10^4 \lambda$

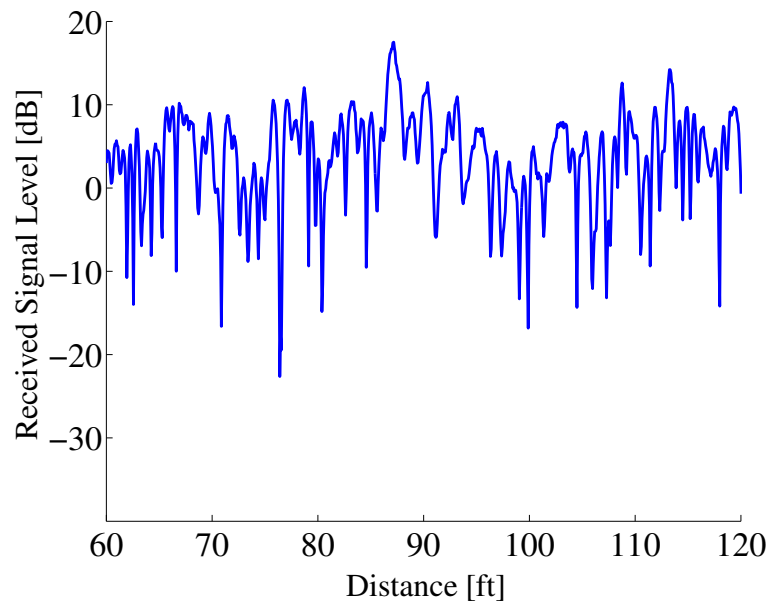
(b)

Table B.1: Simulation Parameters. (a) gives descriptions of terms used in the repeatability model. (b) gives the values of fixed parameters used in the simulation model.

Figure B.7 demonstrates how the comparison curves change with adjustments each of the free simulation parameters  $\rho$ ,  $\sigma_\ell$ , and  $\delta_\ell$ . The trends in Fig. B.7 are used to adjust the parameters so that the simulation matches the measurements. Below the boundary  $\sigma_\ell = 0, \rho = 0$ , increasing the value of  $\rho$  causes the comparison curve to shift down and flatten out. Above the  $\sigma_\ell$ - $\rho$  boundary, increasing  $\sigma_\ell$  shifts the curve up, and decreasing  $\delta_\ell$  makes the comparison curve asymptote steeper.



(a)



(b)

Figure B.1: Composite Signal Strength. The simulated composite signal strength, consisting of large- and small-scale fading, is shown in (a). (b) zooms in on a portion of the distance axis to show the detail of the small-scale fading.

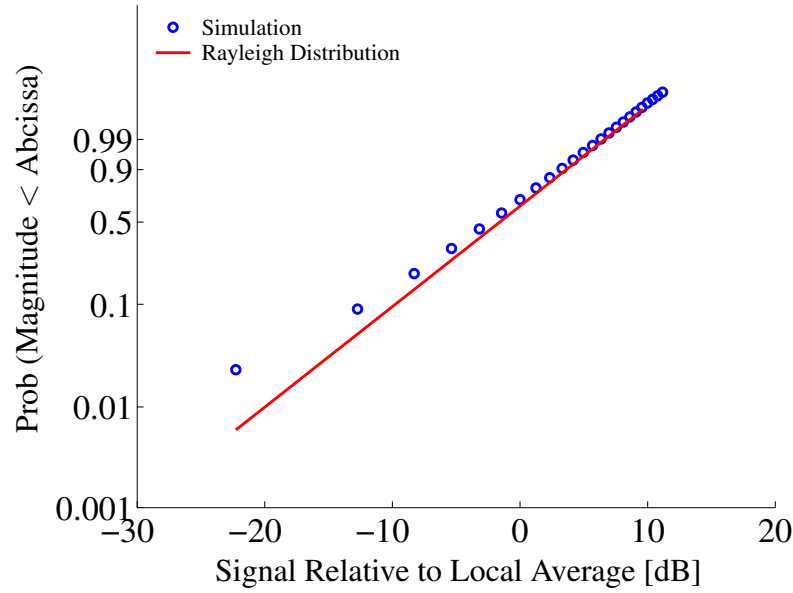


Figure B.2: Small-Scale Fading Envelope Distribution. This figure compares the distribution of the simulated small-scale fading envelope  $|r(\mathbf{x})|$  against a Rayleigh distribution, which is characteristic of Clarke's two-dimensional isotropic scattering model.

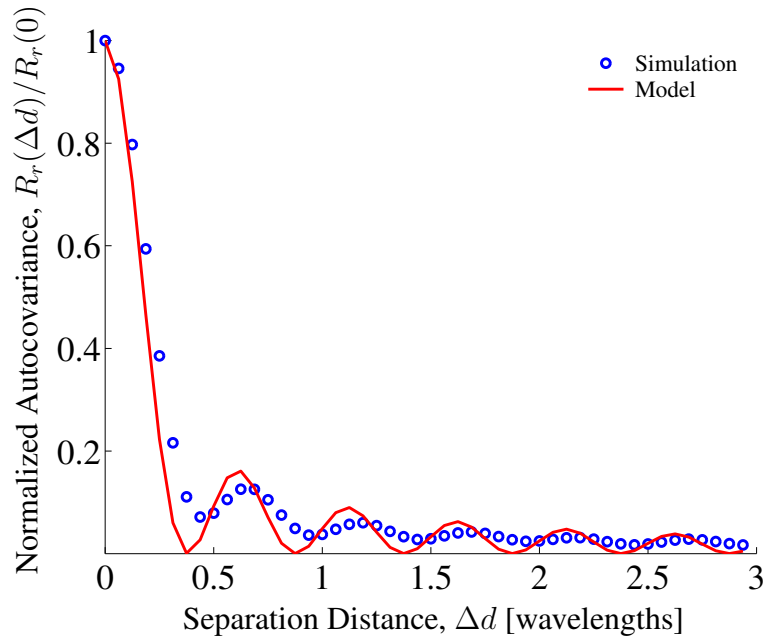


Figure B.3: Autocovariance of the Small-Scale Fading Envelope. This plot compares the autocovariance of the small-scale fading term generated in simulation to that of the small-scale fading predicted by Clarke's isotropic scattering model.

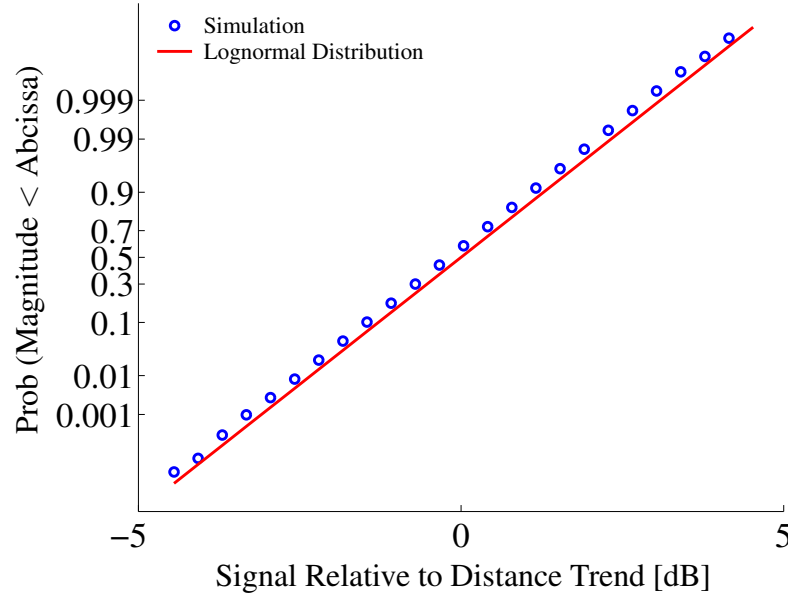


Figure B.4: Large-Scale Fading Distribution. This figure compares the distribution of the large-scale variation term  $L_r(\mathbf{x})$  generated by the simulator using the lognormal fading model.

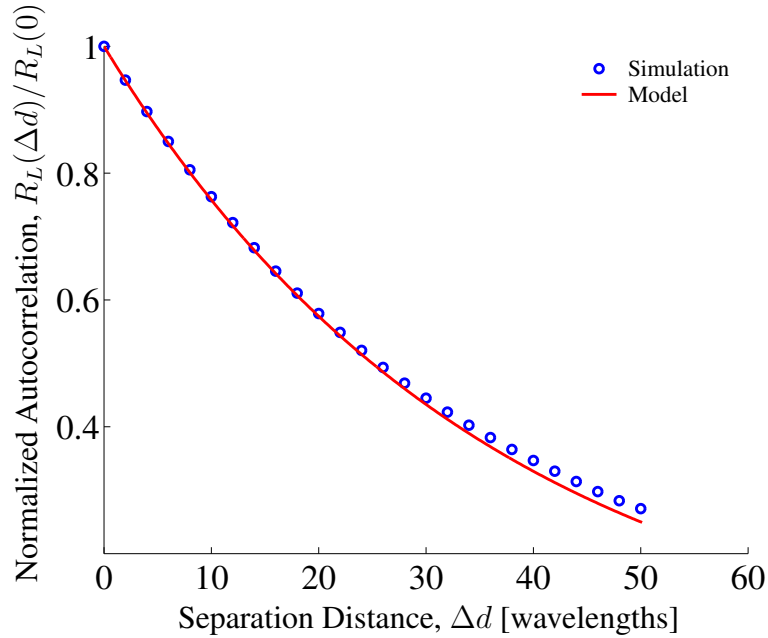
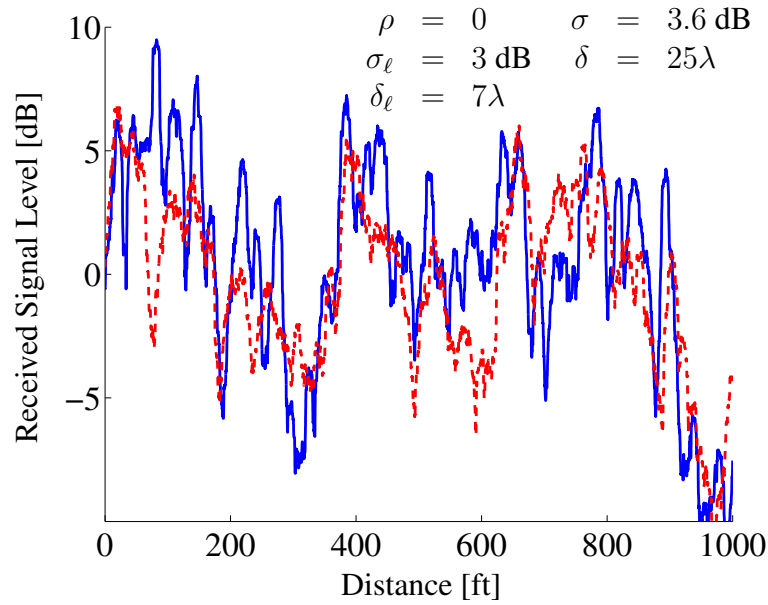


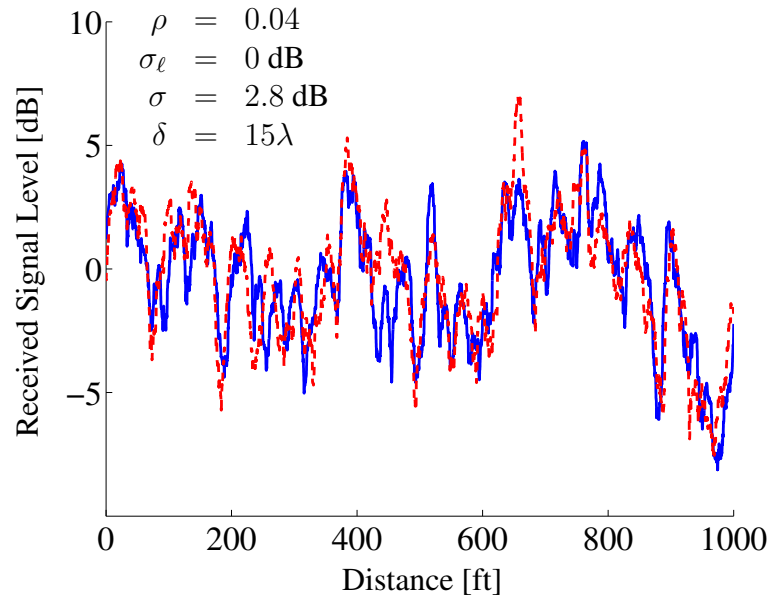
Figure B.5: Autocorrelation of the Large-Scale Fading Power. This plot compares the autocorrelation of the large-scale fading term generated in simulation to the exponential autocorrelation model.



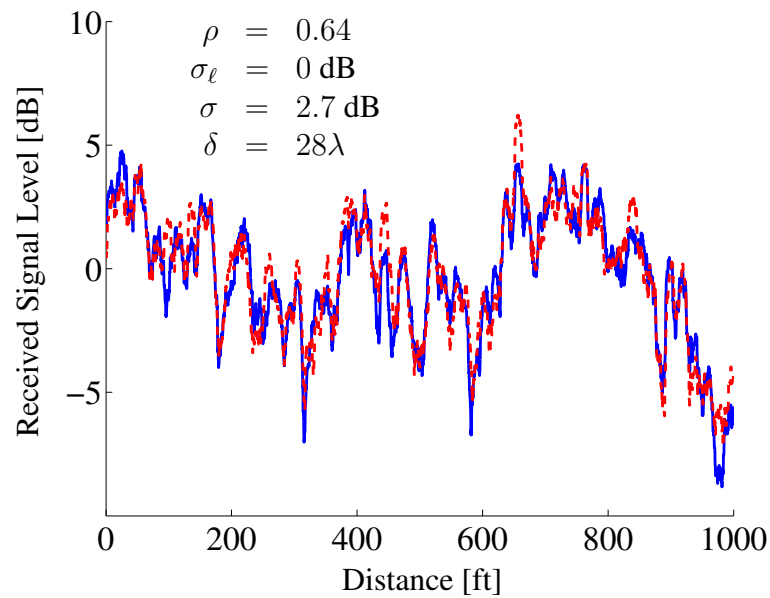
(a)

Figure B.6: Simulated Repeatability Overlay Comparisons. This figure shows three examples of simulated repeatability comparisons over a range of simulation parameters. For qualitative comparisons, the parameters are chosen to match measured data results in Chapter 6: simulation parameters for (a) match for Sansome Street in Fig. 6.6(c); parameters for (b) match those for the left lane of California in Fig. 6.9(b); parameters for (c) match those for the left lane of Battery in Fig. 6.7(b). The magnitude of the large-scale fading is determined by  $\sigma$ , and the degree of repeatability is determined by  $\rho$  and  $\sigma_\ell$ .





(b)



(c)

Figure B.6: Simulated Repeatability Overlay Comparisons (*continued*).

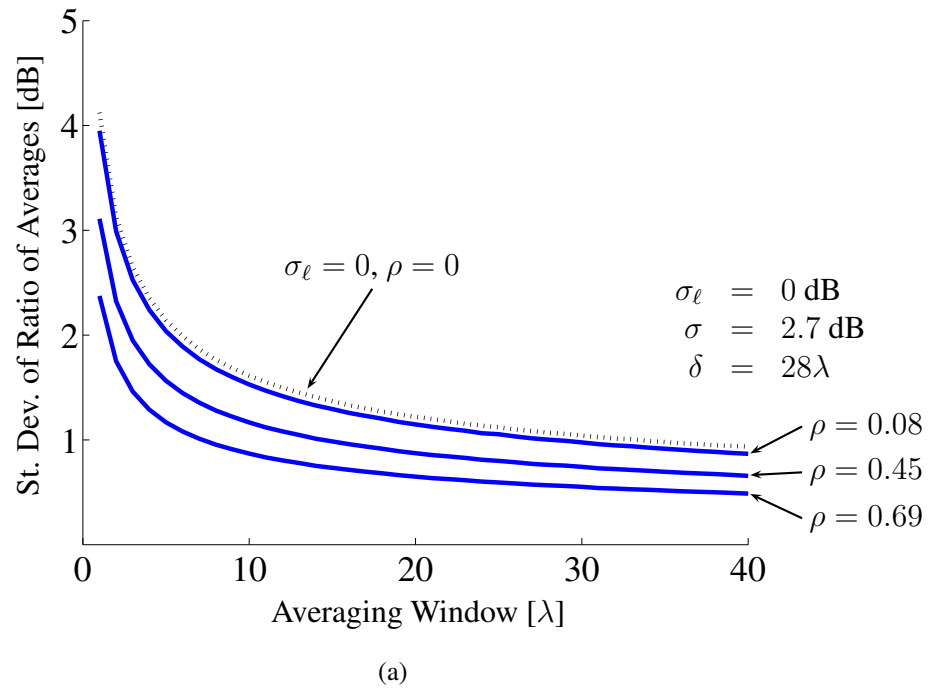
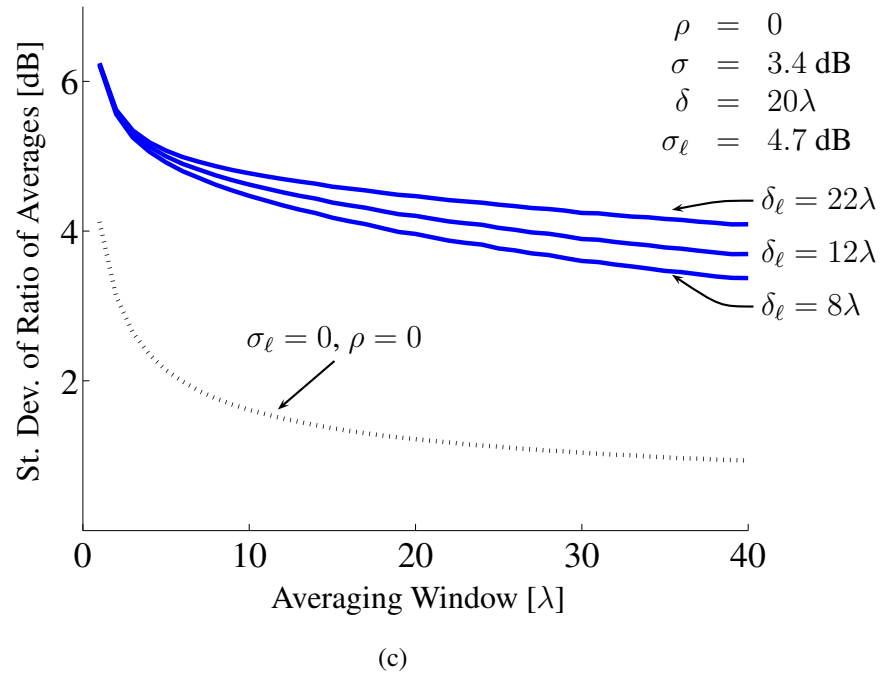
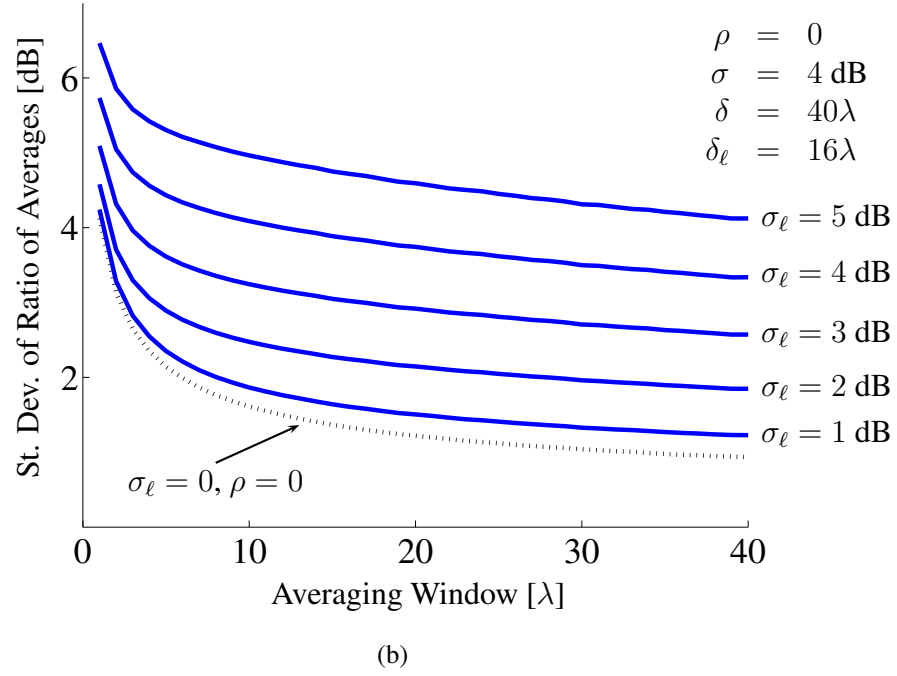


Figure B.7: Simulated Comparison Curves. This figure illustrates how the comparison curves change when the simulation's free parameters,  $\rho$ ,  $\sigma_\ell$ , and  $\delta_\ell$ , are adjusted. (a) As  $\rho$  increases, the comparison curve shifts down and flattens out. (b) Increasing  $\sigma_\ell$  shifts the comparison curve up. (c) Decreasing  $\delta_\ell$  makes the asymptote steeper.

Figure B.7: Simulated Comparison Curves (*continued*).

## **Appendix C**

# **Mobile-User Velocity Estimation in Multipath Environments**

Electromagnetic propagation through scattering environments yields site-specific signal strengths that vary as a function of position of the receiver. Processing data to obtain the propagation characteristics requires computations referenced to the spatial domain. Since communication equipment does not typically contain sensors that accurately determine physical location of the user, and since signal processing typically takes place in the time domain, some method must be used to provide a map from the temporal domain to the spatial domain. Velocity estimation has generated considerable research activity in recent years as a way of mapping spatial domain characteristics into the time domain [4–7, 22, 36, 37, 41, 59, 62, 82, 88, 95]. The mobile-user velocity can also be useful in certain resource allocation problems.

This chapter presents an overview of mobile-user velocity estimation techniques. A closed-loop Doppler measurement is introduced to provide precise frequency references required by some velocity estimation techniques. This measurement can also be used to provide a lower bound on mobile-user velocity.

## **C.1 Motivation**

In large-scale wireless systems, where signal propagation is hindered by reflections or obstructions by buildings, trees, hills, and other natural terrain or artifacts, network control tasks must be performed with significant margin in the network resources so that the performance for the individual

user will not suffer. The corner effect<sup>1</sup> is an example in which a network resource, *i.e.*, link quality, may suddenly be degraded after turning a corner, resulting in a dropped call if insufficient link margin is built into the system and no other channels are available. As more users are added to the system, network resources become more scarce. New resource allocation techniques exploit user position and velocity to improve the performance of these network control tasks. In particular, dynamic channel allocation techniques show improved network performance when either the speed or the velocity (with a directional component) is known. By partitioning mobile users into groups according to their speeds, unnecessary handoffs may be reduced by placing faster-moving mobile users into larger, overlaid “umbrella” cells [88]. By tracking the direction of motion, in addition to the speed, of mobile users, channel sets migrate through a network by following groups with similar speed and direction, thereby simultaneously reducing the rate of forced call termination and increasing the overall system capacity [65].

The speed of the mobile user is also useful for determining the length of the temporal averaging interval to use for estimating the local received signal power. Proposed handoff algorithms often have requirements on the spatial sampling that must take place [58,97,98,100]. In order to average out the effects of the small-scale fading, averages must take place over a spatial interval that is long enough to reduce the variance of the estimate to an acceptable level. On the other hand, the interval must be short enough to track abrupt changes in the received power level.<sup>2</sup> The spatial interval between samples is also important because taking samples too far apart can increase the error in the estimate of the average received signal power [7].

Current radiolocation techniques are not viable solutions because they suffer from deviations of several hundred meters from the true mobile location when several multipath components exist [32,36,81].<sup>3</sup> Not only is this accuracy too imprecise to be used by the high-level handoff algorithms, such as the pattern recognition techniques proposed by Wong and Narasimhan [58,101], but the deviation in position is still much too large for determining an appropriate spatial averaging window. An alternative to these spatial location techniques is to map the mobile user’s position from a time reference and an estimated velocity. Using oscillators that have approximately 1 ppm

---

<sup>1</sup>The corner effect is addressed in Chapter 4 by driving through intersections.

<sup>2</sup>The sudden changes in signal strength at corners is discussed more thoroughly in Chapter 4.

<sup>3</sup>Caffery [17] reports errors of less than 100 m, but his work considered only urban microcells with few multipath components.

accuracy, the fidelity of the relative spatial distance traveled<sup>4</sup> is limited by the accuracy of the velocity estimate.

The velocity of a mobile station can be estimated by exploiting some of the well-known characteristics of the propagation environment that are known to vary as the mobile user's speed changes. The problem with many of these techniques, as will be seen later, is that the best estimates rely heavily on specific knowledge of the scattering environment, which may not actually be known in any specific implementation. This leads to an interesting problem: The best velocity estimators are subject to great variation when the scattering environment deviates from the assumed model. This chapter presents the various velocity estimation methods currently found in the technical literature and discusses the strengths and limitations of each. Additionally, a method for estimating a round-trip Doppler frequency shift is introduced. This round-trip estimate can be used to provide an upper bound for the mobile-user velocity.

## C.2 The General Problem of Velocity Estimation

As with any multifaceted problem, a few initial assumptions are often necessary to make progress. Implementation of a robust velocity estimator, however, requires that the number of assumptions about the scattering environment be kept to a minimum. Identified below are some of the most common assumptions that make most velocity estimation methods impractical for implementation in cellular systems. These assumptions and their challenges will be referenced throughout this chapter when discussing the merits of each velocity estimation technique.

*Challenge #1. Perfect knowledge of the scattering characteristics is assumed.* Perhaps the most common assumption—and possibly the most difficult to avoid—is the assumption of the scattering characteristics of the channel to be analyzed. For example, ideal isotropic scattering is assumed in the derivation for the estimators by [50, 59]. Although an assumed scattering model is often a necessary step before any channel parameters may be estimated, it is often the deviation from the assumed channel model that introduces the most significant bias into an estimate [7]. In a sense, all of the challenges are in some way, either directly or indirectly, related to the scattering model assumption. These are identified separately here because they are barriers to implementation.

---

<sup>4</sup>This method does not give absolute position, but it can give an indication of how far the mobile user has traveled in a specified time interval, which is sufficient to get a local average of the received signal power.

*Challenge #2. Some parameter of the estimator must be adjusted based on the current velocity of the mobile user.* Because the approximations made in the derivation of an estimator may be valid only under certain conditions, *e.g.*, a certain range of velocities, the accuracy of the estimator may change if the speed itself changes. This may not be a problem if the parameter can be set to accommodate the maximum range of velocities expected in the system and still yield acceptable performance. It becomes a problem, however, when the parameter, such as the averaging time or the bandwidth of a filter, must be adapted to the speed of the mobile user, as the performance of such an estimator depends on *a priori* knowledge of the parameter being estimated.

*Challenge #2.5. The local average received power is assumed to be known.* This is really a special case of Challenge #2 since the time interval over which an average is taken depends on the velocity. Quite often, the average received signal power is a required input parameter to the velocity estimator. At first glance, this may not seem to be a problem. After further review, however, it becomes evident that in order to get a “good” estimate of the average power, the average must be taken over a minimum spatial distance. As an example, some researchers consider  $20\lambda$  to be an appropriate distance [7, 47]. The local average received power is determined through a spatial average. In communication systems, however, time sampling is used. To determine if the averaging is sufficient, one must know the parameter to be estimated, *e.g.*, the velocity. This issue is so often overlooked that it merits being pointed out separately here.

*Challenge #3. Smoothing the estimate leads to a tradeoff between response time and a reduction in the variance of the estimate.* Stationarity of the received signal power over small distances is, in many cases, a necessary assumption for analysis. In reality, abrupt changes in received signal power can be experienced, most notably when a mobile station with line of sight to the base station suddenly goes behind a building—see Chapter 4, the “Corner Effect.”. Responsiveness to these changes drives the averaging interval to be as short as possible. More accurate estimates require longer averaging intervals, however.

*Challenge #4. The precise transmitted carrier frequency is not known at the receiver.* This, too, is often overlooked. If a precise reference of the transmit carrier frequency were available at the receiver, measuring the relative offset of the received carrier frequency would yield a simple method of estimating the velocity, as long as the arrival angle relative to the direction of travel is also known<sup>5</sup>, assuming that there is line of sight to the transmitter. This would require oscillators

---

<sup>5</sup>Knowing the arrival angle is encompassed in Challenge #1—knowing the properties of the scattering environment.

with very tight frequency tolerance. Since the carrier frequencies are on the order of  $10^9$  and Doppler shifts are on the order of  $10^2$  in mobile wireless systems, one would want an oscillator accuracy to within about 10 Hz for this type of measurement to work. The required accuracy of the oscillator would then be 10 parts per billion, which is a few orders of magnitude more precise than the oscillators used in low-cost handheld devices.

Instead, the mobile user's receiver synchronizes to an average frequency determined by the bandwidth of the loop filter in the carrier recovery circuit phase-lock loop. The average frequency experiences a shift as a result of the user motion. To make an estimate of this shift, the carrier frequency of the return channel must be derived from the received carrier frequency. This could be done by deriving an intermediate frequency from the downlink carrier. The return channel would then transmit at a multiple of this intermediate frequency. The base station would then have both frequencies available and would be able to compute a round-trip Doppler shift. This method is outlined in more detail in Section C.6.

*Challenge #5. A significant bias in the estimate may appear when additive noise is considered.* Since the estimators are usually designed for a specific scattering environment, the noise is left out of the derivation. When noise is actually considered, the terms that include noise power are often non-negligible and have a severe impact on the estimate. Some researchers suggest using a separate, narrower filter for use in the estimator [7, 37]. Inter-symbol interference (ISI) can cause similar biasing effects if not considered in the original derivation of the estimator.

## C.3 Time Methods

### C.3.1 Estimation Based on Envelope Variations

Holtzman and Sampath [37] also observe that in order to average out the effects of the small-scale fading, an averaging interval must be adapted to balance the accuracy of a local power estimate against the responsiveness of the estimator; this addresses challenge #3. They consider the deviation of the signal envelope in order to estimate the maximum Doppler frequency from which a velocity estimate may be derived. The velocity estimate is then used to adjust the averaging interval in their handoff algorithm.

To get an estimate of the speed of the mobile user, the variation in adjacent samples of the



envelope of the received signal is observed. Qualitatively, one would expect that as the speed of the user increases, the adjacent samples of the received signal envelope would become less correlated, assuming the samples are taken at constant time intervals, causing the deviation between them to grow.<sup>6</sup>

When an isotropic scattering environment is considered, the variance of the logarithm of the signal envelopes may be used to avoid computing estimates of local means. This variance is computed as

$$V = \frac{1}{N} \sum_{i=0}^{N-1} (y_{i+1} - y_i)^2 \quad (\text{C.1})$$

where  $y_i = 20 \log_{10} x_i$  and  $x_i$  is the received signal envelope.<sup>7</sup> For  $N$  sufficiently large, and by assuming ergodicity, (C.1) can be equated to the ensemble average

$$E[(y_{i+1} - y_i)^2] = 2(\text{Var}(y_i) - \text{Cov}(y_{i+1}, y_i)) \quad (\text{C.2})$$

Since the logarithm of the envelope is used,  $\text{Var}(y_i)$  becomes independent of the signal amplitude. The covariance term is simplified by taking an upper bound, which is  $\text{Cov}(y_{i+1}, y_i) = 5.57^2 J_0^2(2\pi f_D \tau)$ , where  $\tau$  is sampling interval of  $y_i$  [37]. At this point, the Doppler shift  $f_D$  is the only unknown in the equation. Assuming  $2\pi f_D \tau \ll 1$ , the function  $J_0^2(\cdot)$  can be approximated by its zeroth and second-order terms to get an estimate of the Doppler shift. The approximation is

$$J_0^2(x) \approx 1 - \frac{1}{2}x^2 \quad (\text{C.3})$$

and is shown in Fig. C.1. The approximation will introduce a bias in the estimate at higher speeds because the higher-order terms of  $2\pi f_D \tau$  will contribute more to the covariance term. A second-order biasing effect results from the fact that an upper bound on the covariance term was used in the derivation rather than the covariance itself.

By using the logarithm in the derivation of this estimator, the dependence upon a known average

---

<sup>6</sup>The autocovariance of the squared envelope is [87]  $\mu_{z^2 z^2} = 4|\phi_{rr}(\tau)|^2$ , where the subscript  $z^2$  indicates that the covariance is taken over the squared envelope, and  $\phi_{rr}$  is the autocorrelation of the complex baseband received signal. In an ideal, isotropic scattering environment this autocovariance becomes [87]  $4\sigma^2 J_0^2(2\pi f_D \tau)$ . By squaring  $J_0(\cdot)$  in the plot in Fig. 2.4, one can get a qualitative feel for how the channel decorrelates as the time samples grow further apart in distance.

<sup>7</sup>The units of  $y_i$  are decibels, and the reference level is arbitrary here.

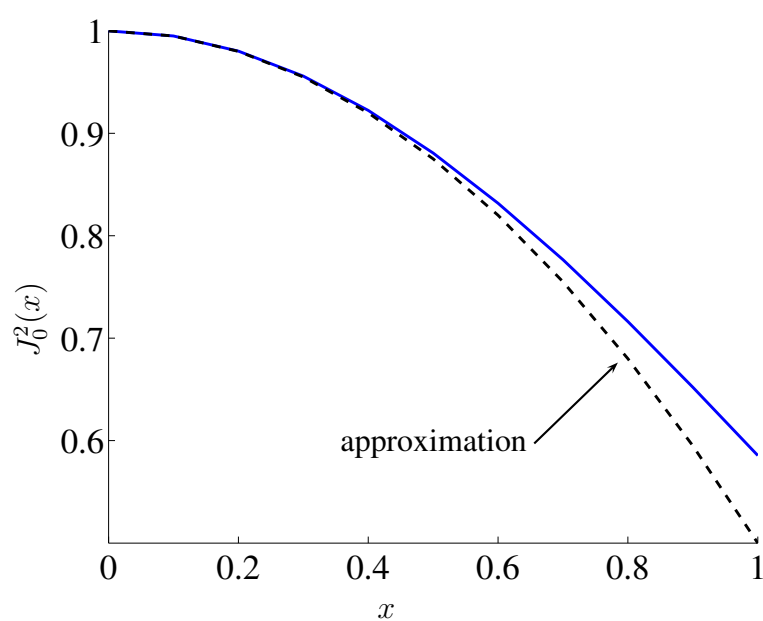


Figure C.1: Squared Bessel Function and Approximation. The covariance estimator derived by Holtzman and Sampath [37] relies on a quadratic approximation of  $J_0^2(x)$ . The solid line is  $J_0^2(x)$ , and the dashed line is the approximation using the zeroth and second order terms of the series expansion of  $J_0^2(x)$ .

received signal power is avoided (Challenge #3). However, this comes at a cost of being more dependent upon the assumed fading model (Challenge #1). As will be discussed in the following paragraphs, deviation from this assumed model indirectly requires an estimate of the received signal power.

When a LOS component is also present, the derivation of the velocity estimator using the logarithm becomes too complex for the previous analysis, in which case the variation of the signal envelope itself is considered. Following a similar derivation as before, but after substituting the square of the received envelope ( $x_i^2$ ) in for  $y_i$  in (C.1), a different estimator is derived. This time, however, the estimate of a local mean is no longer avoided. In fact, the metric  $V$  must be normalized by the variance of the square of the received envelope ( $\text{Var}(x_i^2)$ ) before an estimate of  $f_D$  can be made. Since this variance for a Ricean fading environment is given as  $\text{Var}(x_i^2) = 4\sigma^4(1+2K)$  [37], this is equivalent to having knowledge of the power both in the scattered components and in the LOS component (Challenge #3).

Additionally, the size of the estimation error is heavily dependent upon the angle of arrival, as defined in Fig. C.2, of the LOS component. At arrival angles of  $\pm \frac{\pi}{4}$  and  $\pm \frac{3\pi}{4}$  the error is zero. On the other hand, when the arrival angles are  $0$ ,  $\pm \frac{\pi}{2}$ , or  $\pi$ , the error can be 20% or more depending on the Rice factor  $K$ .

The ideal performance analysis considers only the case without additive noise. Since the estimators were derived for the noiseless case, the inclusion of additive white Gaussian noise (AWGN) at the receiver introduces a significant bias into the estimate of the maximum Doppler frequency (Challenge #5). This bias is bounded only by the noise power that is passed through the receiver filters. For this reason, it is suggested by [37] that a separate, narrower filter be used for the Doppler estimator in the carrier recovery loop. This allows the bias to be reduced by further limiting the noise power that enters the Doppler estimator. This filter may have a bandwidth much lower than the signal bandwidth, but it must be wide enough to accommodate the maximum Doppler shift.

### C.3.2 Estimation Based on Level Crossing

The level crossing rate (LCR) is defined as the rate at which the received signal strength crosses a fixed signal strength threshold over a period of time. The signal level threshold is a design parameter of the estimator. The LCR is a function of both the scattering environment and the chosen

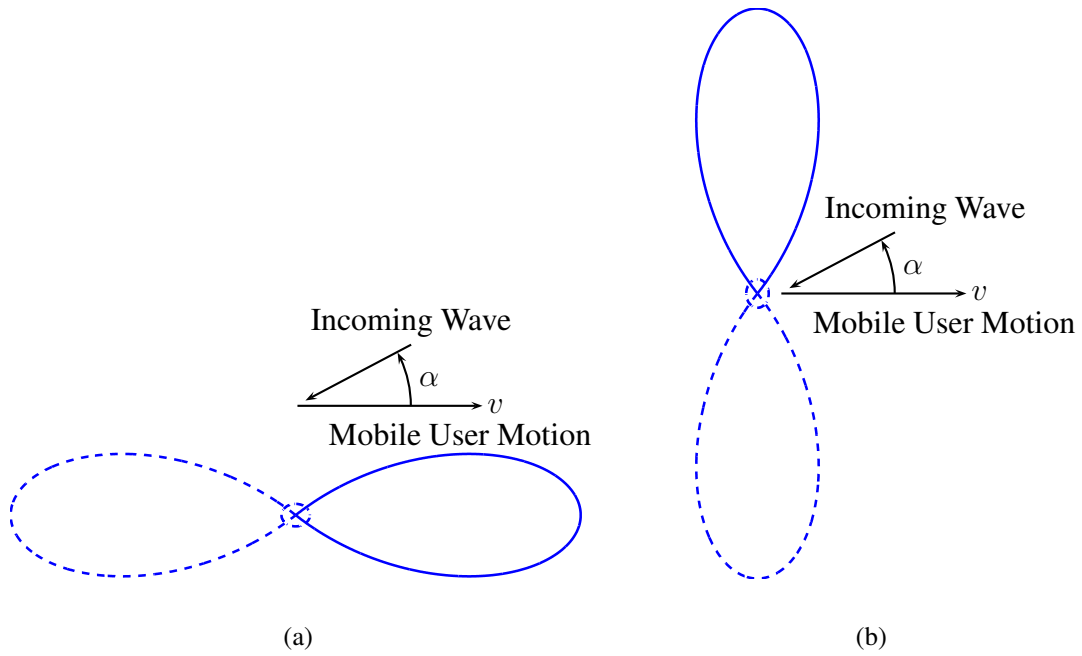


Figure C.2: Angle-of-Arrival Distributions Relative to User Motion. This figure illustrates the cases considered by Austin and Stüber [7]. The arrival angle  $\alpha$  of an incoming wave is the angle between the mobile user's velocity vector and the propagation direction of the incoming wave. The figure-eights represent the angle-of-arrival distribution of received signal energy in the two-dimensional horizontal plane. In some cases, both lobes are considered, and in other cases, only one lobe is used. In (a), the received signal energy arrives mostly parallel to the direction of travel, as would be the case in which mobile user and transmitter are located in the same street. In (b), the signal energy arrives perpendicular to the direction of travel, as would be the case in which the mobile user drives through an intersection with a street in which the transmitter is located.

threshold. From the work of Rice [76] it is well known that the level crossing rate can be determined if both the scattering environment and the mobile speed are well-defined. In general, the LCR depends on the angle-of-arrival distribution that defines the scattering environment. Under specific assumptions about the scattering environment, some have proposed the use of the measured level crossing rate to estimate mobile velocity. Austin and Stüber [7] characterize these types of level crossing estimators as well as the covariance estimator derived by Holtzman and Sampath [37] for different Ricean fading environments. They also consider environments in which the power is distributed non-uniformly in the two-dimensional horizontal plane, which is a modification to the isotropic scattering model described in Chapter 2.

In the context of handoff algorithm performance, Austin and Stüber note that a fixed temporal averaging window optimizes their handoff algorithm for a specific velocity [7]. As discussed in Chapter 2, an “acceptable” spatial averaging window is determined to be at least  $20\lambda$  with sampling intervals of less than  $0.5\lambda$ . Austin and Stüber explore the possibility of using level crossing or covariance techniques to estimate the mobile-user velocity.

Three LCR estimators are discussed by [7]. The first LCR estimator considers the zero crossing rate of  $X(t) - \bar{x}$  where  $X(t)$  is either the in-phase or the quadrature component of the received signal, and  $\bar{x}$  is the average of that component. A Ricean fading environment can be constructed by adding a LOS component to an isotropic scattering model. Since the mean is subtracted, the LOS component in this Ricean fading environment is effectively removed so that the zero crossing rate is just that of the ideal isotropic scattering environment, yielding a simple proportional relationship to the estimated user velocity,  $v$ . Although this method removes dependence on the LOS component, it also assumes the mean,  $\bar{x}$ , is stationary and an accurate value of this average is available to the estimator (Challenge #2.5).

The second LCR estimator treated by [7] is the same as the first, except that the mean of the chosen component is not subtracted. Naturally, this estimator has a strong dependence on both the strength and the arrival angle of the LOS component relative to the mobile’s direction of travel. In fact, when the estimator is designed assuming a Rayleigh fading channel, which lacks a LOS component, and a LOS component actually exists, the estimator error varies as a function of the scattering environment. Even for environments with a Rice factor as small as  $K = \frac{1}{2}$ , the estimation error varies greatly with the angle of arrival of the LOS component relative to the direction of travel. When the LOS component makes a  $45^\circ$  or  $135^\circ$  angle with respect to the

direction of travel, the estimation error approaches zero. When traveling directly towards, away, or perpendicular to the arrival of the LOS component, however, the error approaches 20%. These errors become more extreme as the LOS component becomes stronger. Errors of +40% or -80% are experienced in an environment with Rice factor  $K = 10$ .

The final LCR estimator considered by [7] is the level crossing rate of the envelope of the received signal. The level crossing rate is less sensitive to the strength of a LOS component when the level chosen is the root mean square value of the envelope. The sensitivity analysis shows only the results for the case in which the mobile user is heading directly into the LOS component ( $\alpha = 0$ ). Once again, an average must be available in order for the estimator to work. The performance for other angles of arrival ( $\alpha \neq 0$ ) is not reported. Of course, these results are for ideal channel models, and the true performance depends on the actual angle-of-arrival distribution experienced in the field.

The covariance estimator of Holtzman [37] is also considered by [7]. This estimator also depends on the distribution of power arriving in the horizontal plane. This dependence is outlined by [7]. The accuracy in a Ricean fading environment depends on the Rice factor ( $K$ ) and the arrival angle ( $\alpha$ ) of the LOS component. These performance characteristics are discussed by [37] and are outlined in the previous section.

The non-isotropic environments that are considered by [7] are those represented in Figs. C.2(a) and C.2(b), which may be typical of urban street microcells. The first environment considered is represented by the solid line pattern in Fig. C.2(a). This pattern is like that of an antenna gain, but here it represents the probability distribution of the power arriving in the two-dimensional horizontal plane.<sup>8</sup> In this case, a receiver travels towards the transmitter, with several reflections from buildings also arriving at the receiver. The second environment considers both the solid and dashed patterns in Fig. C.2(a) as the distribution of received power. The third and fourth environments considered are similar to environments 1 and 2 with the exception that the signal arrives primarily perpendicular to the motion of travel (as shown in Fig. C.2(b)). These correspond to traveling through an intersection that crosses the streets described in environments 1 and 2. Examples of these scenarios are seen in Chapter 5. Because the transmitter antennas are lined up with Battery Street, Fig. C.2(a) is similar to what should be experienced along Battery. Figure C.2(b) represents

---

<sup>8</sup>In the analysis, the treatment of this pattern as an antenna gain pattern or the distribution of power are equivalent to within a scale factor.

what might happen as a mobile user crosses Battery at California (Fig. 5.10(e)) or Sacramento (Fig. 5.10(g)).

The covariance and LCR velocity estimators mentioned previously are designed for isotropic scattering. All of the estimators experience some bias when placed into non-isotropic environments. Under consideration are non-isotropic scattering environments with power distribution in the 2-D horizontal plane given by [7]

$$p(\alpha) = \begin{cases} \frac{\pi}{4|\alpha_m|} \cos\left(\frac{\pi}{2} \cdot \frac{\alpha}{\alpha_m}\right) & |\alpha| \leq |\alpha_m| \leq \frac{\pi}{2} \\ 0 & \text{otherwise.} \end{cases} \quad (\text{C.4})$$

The parameter  $\alpha_m$  is the beam angle.

To characterize their robustness, each estimator is modified and designed specifically for these non-isotropic scattering environments with a fixed beam angle of  $\frac{\pi}{2}$ . Naturally, the estimators perform best when the design parameters precisely match the environment parameters.

In general, for perpendicularly arriving components, as in Fig. C.2(b), all estimators are significantly biased, and most estimators report velocities below that of the true velocity. Qualitatively, taking only the perpendicularly arriving components cuts out the regions near the peaks of the Doppler spectrum shown in Fig. 2.5, leaving only the center portion. This truncated spectrum resembles a Doppler spectrum with a lower maximum Doppler shift,  $f_D$ , and it makes sense that this spectrum would yield lower velocity estimates. This qualitative behavior is not true in all cases for the envelope LCR estimator and the covariance estimator since each of these depend on the envelope, *i.e.*, both the in-phase and quadrature components, whereas the first and second LCR estimators of [7] are based on either the in-phase or quadrature component, but not both.

When considering only the components arriving primarily parallel to the direction of travel, as in Fig. C.2(a), only the portion of the spectrum near the peaks remain, and the components near the carrier frequency are cut out. Unfortunately, this spectrum does not lead to a simple, qualitative explanation, but it is clear from the results of [7] that there is a heavy dependence on the scattering environment for these estimators.

In general, when the arriving components received are confined to a smaller range of arrival angles, the received signal is more coherent and experiences less variation. The reduced channel variation in all of the estimators makes each of them unusable, yielding estimates that are well

below the true velocity, when the angular power distribution approaches that of a single LOS component.

Of all of the estimators, only the first zero crossing rate (ZCR) estimator of [7], which subtracted out the mean of either the in-phase or quadrature component, achieves errors of approximately 10% over a range of environments with directivity angles ( $\alpha_m$ ) greater than  $10^\circ$ . These errors occur only after the subsequent redesign of the estimator for a directive environment with  $\alpha_m = 90^\circ$ . All of the other estimators have errors greater than the first ZCR estimator. The trade-off, however, is that this estimator does not work as well under isotropic scattering. When placed back into an isotropic scattering environment, errors greater than 15% can occur [7].

The envelope LCR estimator, when designed for isotropic scattering, does not work well in non-isotropic scattering environments. In fact, errors of more than 70% are reported for this estimator when  $\alpha_m = 90^\circ$ . These errors grow to more than 90% when the signal is confined to a narrower range of arrival angles, *e.g.*,  $\alpha_m = 10^\circ$ . The covariance methods of [37] work well over a range of directivity only when a LOS component exists. Without a LOS component, errors approach more than 90% when confined to narrower angles of arrival ( $\alpha_m = 10^\circ$ ).

The analysis of the estimators described so far has considered only the effects of the scattering environment. It is also reported by [7] that additive noise can introduce a significant bias into the estimated velocity, particularly at lower speeds (Challenge #5). Even with signal-to-noise ratios of greater than 20 dB, the estimate may be off by a factor of 10 or more, depending on the speed, scattering environment, and estimation method used. For all of the estimators, however, the biasing problem due to noise becomes less of a problem at higher speeds.

Considered by both [7] and [37], the effects of additive noise are shown to depend on the Rice factor ( $K$ ), the arrival angle of the LOS component, the mobile-user velocity, the signal-to-noise ratio, and the signal bandwidth. One parameter that can be tightened is the bandwidth of an additional noise removal filter. Since the channel characteristics are observed after the modulation is removed, *e.g.*, in a carrier recovery loop, a filter with a bandwidth narrower than the bandwidth of the signal may be used to filter out excess noise to reduce its biasing effects. In fact, the bandwidth must only be wide enough to accommodate the highest expected Doppler frequency. It is even suggested by [7] that this filter bandwidth be adaptively adjusted according to the mobile user's speed. This adaptation is unrealistic in practice since the velocity estimate from which the bandwidth would be adjusted fluctuates wildly at best. Adapting a filter bandwidth to this



inaccurate velocity estimate in order to improve its accuracy would likely lead to instabilities of the estimate itself.

### C.3.3 Methods Almost Independent of Small-Scale Fading

Hellebrandt, *et. al.* [36], propose a method to estimate velocity using measurements taken by handsets operating under the GSM standard. They propose that throughout a coverage area, a database of stored signal strength and propagation delay measurements from base stations be generated. This database is used to determine both the mobile user's position as well as the velocity. The method introduced by [36] uses only the average signal strength measurements. In this scenario, the mobile handset continually monitors the GSM broadcast control channel (BCCH) from multiple base stations and makes power measurements. This measurement, which is specified to have six-bit precision, is used to make a least-squares best fit of the received signal power to the known signal levels in the vicinity of the mobile user. Newton's method is used to iteratively converge to a local minimum of the mean squared error (MSE) of the measured signal power against the values in the database. The estimated position is the point that minimizes the MSE. Averaging is required to refine this noisy estimate.

The position is differentiated to determine the mobile user's velocity. Since there is a potentially large error in the position estimate, the differentiated position will have a large error that will require even more averaging. The choice of averaging interval leads to a familiar tradeoff: A longer average is required to get closer to the actual user speed, but at the same time, this leads to a sluggish response if the speed changes quickly (Challenge #3).

On the surface, this approach appears to be independent of the specific small-scale fading environment. One realizes, however, that the minimization is being performed on local averages of the received power. To get these averages, one must average over a sufficient spatial distance, requiring some knowledge of the scattering environment as well as the distance traversed by the mobile user in a fixed amount of time (Challenge #2.5).

Some further implementation difficulties are as follows: First, extensive knowledge of average signal strength is required over a large geographical area. Extensive measurements must be made to ensure accurate performance. These measurements must be repeated unless an update algorithm is employed to track the changes that are known to occur over time (see Chapter 6). Furthermore,

the minimization finds a local, not global, minimum of the least squared error of position. For mobile users at higher speeds, a larger search area is required, necessitating more computational power and *a priori* knowledge of the speed to find the global minimum (Challenge #2). Although the technique is based on measurements readily available, unless the database and computation are located at the mobile station, which is unlikely, a method must be provided to feed the information back to a base station with more computational power and storage capacity.

The simulations of [36] use constant mobile-user speeds of 27.8 m/s (approximately 10 km/hr). After a regression is made to refine the estimate for position, which initially has deviations of up to 95 m, the smoothed velocity estimate still has deviations of up to 30 m/s. With additional averaging, the deviations are reduced to 10 m/s, which is still a large fraction of the original speed.

Lee and Chung [45] propose an extension to this method that is supposed to have improved the accuracy of the estimates. It is unclear to this author, however, that any improvement is made. First of all, neither [36] nor [45] give the parameters of the respective simulations. Furthermore, Hellebrandt simulates a rural, hilly environment with a mobile-user speed of 27.8 m/s, whereas Lee simulates an urban (Manhattan) environment with a mobile-user speed of 5 m/s. Without a relative performance comparison of any differences in the techniques, it seems that any reduction in absolute variance can be directly attributed to differences in the propagation environment and the lower velocity used in the simulations of [45].

### C.3.4 Speed Estimation Using Wavelets

One of the challenges of using level crossing rates for velocity estimation in an isotropic scattering environment is the selection of the crossing threshold. Looking at the sample Rayleigh-distributed envelope in Fig. 2.6, one can see that the number of level crossings depends on the threshold selected. The threshold setting is important and must take into account the changes in the average received power, which effectively shifts the entire plot in Fig. 2.6 up or down if the mobile user travels over distances of more than a few wavelengths.

Narasimhan and Cox [59] observe that the positive slope zero crossings of the first derivative of the received signal envelope do not depend on the local average received power. These points refer to the local minima of each undulation in Fig. 2.6. Exploiting this property is attractive since it avoids the use of an average power estimate (Challenge #2.5). Exploiting its properties of

singularity detection, the continuous wavelet transform (CWT) is used to detect the local minima in the received signal envelope. The logarithm of the received envelope is used since the minima become more pronounced, making them easier to detect.

The expected distance between nulls is derived by [59] and is found to be proportional to the carrier wavelength,  $\lambda$ . Since this average distance is known for a given frequency and the assumed isotropic scattering model (Challenge #1), a measured time average of the interval between minima can be used to derive an estimate of velocity in real-time.

One must choose a time observation window over which the CWT is computed. The number of local minima counted in this window is used to compute the average temporal spacing of the minima from which the velocity estimate is derived. Since at lower velocities there may be no minima to count in an individual window, the observation window must be made long enough to accommodate a minimum velocity that the system is able to detect. All velocities below this minimum value are regarded as zero. Because of this minimum detectable velocity, the normalized MSE is increased slightly for users at low speeds since there are fewer inter-arrival times of minima over which to compute an average.

Determination of the observation window indicates how frequently the velocity estimates are made available. Although the velocity estimates are smoothed over the length of an observation window ( $T_{\text{obs}}$ ) using a moving average, these values are available only when the entire window has been received and the CWT has been performed. The velocity estimates therefore come in increments of  $T_{\text{obs}}$ .

When taking the CWT of the received signal envelope, there are some implementation issues to consider. First of all, the observation window must be lengthened to reduce the edge effects of the CWT on the data samples. This lengthened part of the observation window is overlapped with adjacent observation windows, and the data points in these overlapping regions are not used in the current observation. Because the window must be lengthened, an additional delay in the reporting of the estimate is incurred.

Second, there are parameters of the CWT, *i.e.*, a scale factor and a significance threshold, which must be determined so that the CWT estimates the correct number of minima. Although these values are determined empirically and they depend on the assumed scattering model and observation time, they do not depend on velocity, and thus, they need not be adaptively adjusted (Challenge #2).

Another important feature of this estimation method is that stationarity is required only over a single observation window. In addition to the fact that detecting nulls allows the average power to fluctuate, the relaxed stationarity requirement allows a variable velocity profile to be tracked over a wide area. This can be done without adjusting any of the fixed parameters of the estimator.

As stated previously, for lower velocities, the normalized MSE is slightly increased since fewer minima are available to average in a single observation window. At higher velocities, more samples are available to average, so the normalized MSE converges towards zero. Although the normalized MSE may be very small, the absolute MSE scales with the square of the velocity. The performance with additive noise is unknown at present since [59] considers only the noiseless case (Challenge #5).

This wavelet method requires *a priori* knowledge of the scattering environment (Challenge #1) since the average null spacing is derived from the ideal 2-D isotropic scattering model. The analysis of [59] considers only a uniform angle-of-arrival distribution.

## C.4 Phase and Frequency Methods

### C.4.1 Estimation of the Doppler Shift Using the Phase Drift in DPSK Signals

In the absence of scattered components and of noise, the phase drift during each symbol period in a differentially coherent<sup>9</sup> continuous-phase modulated (CPM) signal is linearly proportional to the Doppler shift experienced at the receiver. If line of sight exists between transmitter and receiver, the Doppler shift can be estimated in the presence of additive noise by averaging the phase drift over several symbol periods. This method can be used to estimate the mobile-user velocity only if the signal angle of arrival with respect to the user motion is also known.

Biglieri [13] presents three estimators that estimate the Doppler shift for differentially coherent CPM signals. Using post-detection decisions, the phase modulation of each symbol is removed from the complex baseband received signal. One point of the autocorrelation of this modified

---

<sup>9</sup>Here, *differentially coherent* refers to the assumptions that symbol synchronization is perfect and that the Doppler shift, additive noise, and the transmitted data sequence completely account for the phase disturbances in the received signal.

baseband signal is computed for adjacent symbols. The phase of this autocorrelation is the phase drift between adjacent symbols, assuming the oscillator is precisely tuned to the carrier frequency as mentioned in Challenge #4.

In general, the use of M-ary differential phase shift keying (DPSK) implies that a maximum Doppler shift may be tolerated before phase ambiguities occur. Specifically,

$$2\pi |f_D| T_s < \frac{\pi}{M} \quad (\text{C.5})$$

must hold [13]. The constraint (C.5) limits the maximum Doppler shift detectable by this estimator based on the symbol period ( $T_s$ ) and the constellation size ( $M$ ). Furthermore, samples in the time average that are heavily affected by fading should be weighted less in the overall average [13].

Austin and Stüber [6] expand on this technique to show that by using the autocorrelation across multiple symbols, in addition to the autocorrelation between adjacent symbols, as done by [13], the variance of the estimate from the true mean may be reduced, even in a Ricean fading environment, *i.e.*, isotropic scattering plus a specular component. In a sliding window of  $L$  symbols,  $P + 1$  autocorrelations of the complex baseband received signal are computed after the modulation is removed. The index of the autocorrelation  $R(\cdot)$  refers to the time offset in symbols. Since the autocorrelation is taken across a maximum offset of  $P$  symbols, the phase ambiguity constraint (C.5) becomes [6]

$$2\pi |f_D| T_s < \frac{\pi}{MP} \quad (\text{C.6})$$

To use the simple, constant weighting suggested by Biglieri [13], the window over which the autocorrelations are taken must consist of symbols that are not affected by fading. To meet this fading constraint, the autocorrelation interval is constrained to one-tenth of the channel coherence time. Since the time elapsed in the transmission of  $P$  symbols is  $PT_s$ , the fading interval constraint becomes [6]

$$PT_s v < 0.1\lambda \quad (\text{C.7})$$

where  $v$  is the mobile-user velocity and  $\lambda$  is the carrier wavelength. One immediately notes that user velocity limits the number of autocorrelations which may be used in an estimate (Challenge #2).

To take full advantage of the fact that multiple autocorrelations,  $R(k)$ , of different time lags

$k$ , are used over the same time interval of  $L$  samples, the number of autocorrelations should be  $P > 7$  [6]. This choice of  $P$  is the point of diminishing returns; increasing  $P$  beyond this point yields smaller reductions in the mean square estimation error. The choice of  $P$  and the constraint in (C.7) limit the maximum allowable velocity for this technique to work. The phase ambiguity constraint in (C.6) limits the maximum velocity to

$$v < \frac{c}{2MPf_cT_s} \quad (\text{C.8})$$

For example, a system operating at 900 MHz, using an autocorrelation across 7 symbols ( $P = 7$ ), using a constellation of 4 points ( $M = 4$ ), and using a symbol rate of 2400 Hz, the maximum allowable velocity from (C.7) is 41.1 km/hr. Under these same conditions, the phase ambiguity constraint (C.6) limits the velocity to 51.4 km/hr.

Unless the parameter  $P$  is adaptively adjusted with the instantaneous velocity, it must be set to a maximum allowable value based on the assumed maximum speed in the system (Challenge #2). This setting would limit the use of this technique to high data rate applications when high frequencies are used and mobile users move at vehicular speeds.

The accuracy of the estimate improves when more autocorrelations are used. As a result of constraint (C.7), the achievable accuracy deteriorates at lower symbol rates and at higher mobile-user velocities. The exact performance also depends on the scattering assumption [6] (Challenge #1).

Austin considers a Ricean fading environment in which the power of the LOS component is 10 times stronger than the sum of the power of all components received as a result of the isotropic scatter, *i.e.*, the Rice factor is  $K = 10$ . Additionally, the model assumed by [6] has the mobile user traveling directly into the oncoming LOS wave, making it not only the strongest component but also the strongest contributor to the Doppler shift. Essentially this technique estimates the shift of the LOS component in lieu of the perturbations caused by the scattering components.

In the derivation of the estimator, Austin shows that the autocorrelation of the complex base-band received signal resulting from a DPSK signal, after the phase modulation is removed, has the same mathematical form as a complex exponential plus additive Gaussian noise [6]. Various eigen-based spectral estimation techniques, which are known to pick out the dominant frequency component of a complex Gaussian in the presence of additive noise, are applied using the autocorrelations described above.

The results presented by [6] are a limiting best case since the LOS component also happens to be the dominant contributor at the Doppler frequency. Since the problem is cast in the form of a complex Gaussian for mathematical convenience, and since the autocorrelations are taken over such a short time interval, it seems that the spectrum estimation is not estimating the spectrum of the received signal. It is unclear without further analysis whether these methods will estimate the maximum Doppler shift, the frequency shift of the LOS component, or some combination of each. Certainly without such a dominant component at  $f_D$ , the estimation of the maximum Doppler shift of the isotropic scattering alone would be much more difficult.

The simulations are reported for mobile-user speeds of 3 km/hr. Since (C.7) stipulates that fewer samples may be used at higher speeds, the achievable performance of the estimator will degrade as mobile users at vehicular speeds are considered with all other parameters unchanged (Challenge #2).

Hidden in the analysis of this technique is the assumption that the carrier frequency is known precisely at the receiver (Challenge #4), requiring highly accurate clocks at both transmitter and receiver to enable the estimation of the phase drift. In practice, the mismatch in oscillators also contribute to the phase drift in adjacent symbols. Because of this mismatch, the resulting estimate would then be skewed.

### C.4.2 Parametric Estimation of the Doppler Shift

Lin and Proakis [50] consider parametric estimation of the maximum Doppler shift in an ideal, isotropic scattering channel. In this case, a wide-sense stationary channel with uncorrelated scattering (WSSUS) is modeled. The Clarke model assumptions (see Chapter 2) are made so that the autocorrelation and power spectral density are precisely known by (2.30) and (2.31) with the only unknown being the Doppler shift,  $f_D$ .

The receiver architecture considered by [50] consists of a Viterbi sequence detector, a channel estimator, and the Doppler estimator being discussed in the paper. Although details of the channel estimator are not discussed by [50], it is clear that the output of the channel estimator is the complex baseband received signal once the modulation has been removed. It should be noted that both the detected sequence and the estimated Doppler shift are used to remove the modulation effects.

The mention of a channel estimator by [50] would lead one to believe that a wideband channel,

*i.e.*, the delay spread is greater than the symbol period, is being considered here. The channel estimate would correspond to the channel impulse response averaged over a data frame. A single channel estimate would be derived for the local spatial region traversed during each frame. The autocorrelation relationship (2.30) could be computed for an isotropic scattering environment by computing the autocorrelation of the baseband channel estimate at a fixed excess delay across multiple frames. The autocorrelation could then be normalized and averaged over different excess delays.

This wideband channel model, however, is not used by [50]. Instead, the autocorrelation is computed at adjacent symbol times in the same data frame. This computation indicates that either narrowband scattering is assumed so that all multipath components are averaged during a single symbol period, or that paths at different excess delays are uncorrelated but have precisely the same spatial autocorrelation as in (2.30) when  $f_D\tau$  is replaced by  $d/\lambda$ . This latter assumption is made by [50].

Since an ideal, isotropic scattering channel is assumed for each uncorrelated, delayed fading path, the autocorrelation of the baseband received signal should closely match (2.30). In fact, the Doppler estimator performs a least-squares approximation of a polynomial representation of (2.30) to the autocorrelation of the baseband received signal. Once the autocorrelation of the baseband received signal is computed across a range of time differences of interest, the minimization is left in the form of a polynomial equation. Newton's method is used iteratively to find the Doppler shift that minimizes the mean square error using the polynomial approximation.

Since the channel estimator depends on the Doppler estimate, the Doppler estimator depends on the channel estimate, and both depend on the isotropic scattering assumption, this estimator is doubly dependent upon the assumptions regarding the scattering environment (Challenge #1).

Since the estimate is derived via a polynomial approximation to (2.30), its accuracy depends on the proper choice of the polynomial degree as well. The polynomial degree depends on the expected range of the argument of  $J_0(\cdot)$  in (2.30) since the higher order terms contribute more to the evaluation as the velocity—and thus, the quantity  $2\pi f_D\tau$ —increases. Therefore, the number of terms to include is dependent upon the parameter being estimated (Challenge #2).

Also worth noting is that implicit in the estimation is the knowledge of the average received power. The autocorrelation of the baseband received signal is matched in a least-squares sense to  $\sigma^2 J_0(2\pi f_D\tau)$ , which implies that the average received signal power ( $\sigma^2$ ) of the in-phase or



quadrature component must be known (Challenge #2.5).

The estimator discussed here is targeted for use in a TDMA system, and as such, it makes an estimate of  $f_D$  during each data frame. Averaging of this estimate to reduce its variance must take place over several frames, leading to the responsiveness tradeoff outlined in Challenge #3.

### C.4.3 Best Basis Method

Narasimhan and Cox [62] propose a velocity estimation technique that is robust to changes in the scattering environment and to changes in the mobile user's speed. This technique uses best basis methods of statistical analysis to obtain spectral estimates of the time-varying fading process. These estimates do not depend on the local average received power, freeing this method of parameters that need to be adjusted as the user's speed changes. Additionally, the dependence on a specific angular distribution of incident power is eliminated through the use of a two- or three-element antenna array at the receiver.

The best basis technique consists of a two-step process: The first step is to select a basis of smooth, windowed cosine functions—or complex exponentials if a baseband representation is used—that approximately diagonalizes the covariance matrix of the small-scale fading process. The best basis is the one that maximizes the energy in the diagonal covariance coefficients.

To reduce the complexity of the basis search, a time window<sup>10</sup> is recursively partitioned into dyadic, *i.e.*, powers of two, subintervals. Each partitioning corresponds to a basis selection that is used to diagonalize the covariance matrix of the fading process. An algorithm analogous to tree pruning is performed to determine the best basis. Once this basis is determined, the corresponding time partitioning results in subintervals of varying lengths. In each of these subintervals, the fading process is approximately stationary. A spectral estimate is then taken over each of these quasi-stationary time intervals.

The resulting frequency spectra are used to determine the maximum Doppler shift. Since the maximum Doppler shift corresponds to signals arriving along the direction of travel, this metric alone does not yield an unbiased estimate in environments where there is no significant power received directly in front of or directly behind the mobile user. To generalize this method for environments with different angular distributions of incident power, an antenna array is used.

---

<sup>10</sup>There is an inherent tradeoff in the choice of time window length and the delay in obtaining the velocity estimate.

For a two-element array oriented along the direction of travel, the phase difference between the signals at each frequency received at each antenna is used to determine the arrival angle of each multipath component. These arrival angles are used to jointly estimate the velocity of the mobile user. A three-element antenna array is used when the orientation along the axis of motion cannot be guaranteed. Because the frequency estimates are sensitive to variations in the carrier frequency, a precise frequency reference is required at the receiver (Challenge #4).

## C.5 Indirect Methods

### C.5.1 Cell Dwell Time

Because of the difficulty in getting an estimate of the average received power (Challenge #2.5), some researchers have resorted to monitoring other system parameters to infer some notion of mobile-user velocity. Sung and Wong use the dwell time of a mobile user in a cell between handoffs as a rough estimate of velocity in order to assist in handoff decisions in a hierarchical network [88].<sup>11</sup> Different strategies include considering only the dwell time in the current cell and considering a history of previous dwell times. The following assumptions are made: The traffic arrival follows a Poisson distribution. When a call arrives, it is uniformly distributed over the area of the cell. All users have constant speed once a call is initiated.

The goal of this strategy is to minimize the expected number of handoffs. Considering only this criteria leads to an overload in the highest tier of the system since the larger cells have fewer handoffs. To keep from overloading the highest tier, an additional constraint requiring a constant blocking probability at each tier is imposed.

When a handoff is required, the time since the mobile user entered the current cell is considered. If this dwell time is shorter than a predetermined threshold, then the user is assumed to be traveling at a “high” velocity and the call is handed up to a higher-tier overlay cell. Similarly, a different threshold can be considered, and if the dwell time is greater than this threshold, then the call is handed to a lower-tier microcell. If the dwell time falls between these two thresholds, the call is handed over to a neighboring cell in the same tier as the current cell. If a record of these cell

---

<sup>11</sup>Here, a *hierarchical network* refers to one in which larger umbrella macrocells are overlaid upon a collection of smaller microcells in the same geographical area. Specifically, Sung and Wong [88] consider a network with three such layers of hierarchical cells.

dwelling times is considered, then a minimum mean square error (MMSE) estimator or a maximum likelihood (ML) estimator can be used to estimate the speed. This estimate assumes that the speed will remain constant over a large area, *e.g.*, the size of the cells. The estimated speed is compared to predetermined velocity thresholds that are used to partition the mobile users into sets much the same way as the dwell time thresholds do.

This analysis shows that even a crude estimate of velocity *may* be useful in handoff algorithms. There are, however, serious limitations to its utility.

The method presented by [88] is almost independent of the specific scattering environment. Handoff decisions in this system model are based strictly on the distance from the base station, not on the characteristics of the fading signal. In reality, the handoff decision will be based on an estimate of the local signal power, which implicitly depends on the scattering environment (Challenge #1) and the averaging interval for the specified scattering environment (Challenge #2.5).

Additionally, the technique presented by [88] evaluates only the velocity of the mobile user when a handoff is required, making it unsuitable for applications that require more accurate and more frequent velocity estimates. Furthermore, since the method is designed for a handoff application, the deviation of the velocity from its true value when either the fading environment or the velocity itself changes is not of great concern since the decision thresholds can be adjusted based on empirical data to achieve the desired performance in the handoff algorithm. A further limitation of the use of this technique is that when the system load increases, the reduction in the number of handoffs approaches zero.

### C.5.2 Velocity Estimation Using Diversity

Kawabata, *et al.* [41], attempt to derive an estimator that is independent of the average received signal power. They consider a two-branch selection diversity receiver and derive a relationship between the number of branch switches per second and the maximum Doppler frequency. There are some flaws, however, in their derivation which make their method impractical for implementation.

The first assumption in the derivation is that the two receive antennas must be spaced far enough apart to experience independent fading. This assumption is acceptable, but it may be difficult to implement in a small handheld receiver where the size of the unit itself may be smaller than the necessary antenna separation distance. The minimum antenna spacing also includes an implicit

assumption about the scattering environment (Challenge #1). The scattering assumed by [41] is that of an isotropic scattering channel.

The second, and perhaps more disturbing, assumption is that diversity selection takes place only after intervals where the fading has become perfectly uncorrelated, *i.e.*, only at or near points where  $J_0(\cdot)$  in (2.30) is zero. Not only does this heavily depend on the scattering assumption (Challenge #1), but it also assumes *a priori* knowledge of the maximum Doppler frequency (Challenge #2).

Not surprisingly, the results of [41] show that the signal correlation between selection decision times must be low in order for this method to work. Furthermore, branches that have different average received power show a downward bias in the estimate of the maximum Doppler frequency since the branch with the highest average will be preferred, resulting in fewer branch switches.

Doumi and Gardiner [22] recast the problem as an envelope level crossing rate problem with a random level to characterize the dependence of this method on both the environment and on received signal power, a dependence originally avoided by [41]. Using Rice's derivation [76] of the envelope level crossing rate, the expectation of the number of branch switches per second is taken over the distribution of a random crossing threshold. In this case, it is also shown that the relationship also depends on the Doppler spectrum.

When the average received power on each branch is equal, the number of branch switches per second is found to be [22]

$$N = \frac{1}{4} \sqrt{\frac{b_2}{b_0}} \quad (\text{C.9})$$

where

$$b_i = (2\pi)^i \int_0^\infty S(f) f^i df. \quad (\text{C.10})$$

From these relationships, one can see that the average received power is actually necessary (Challenge #2.5) for the calculation of  $b_0$ . The specific scattering environment must also be known (Challenge #1) for this estimator to work since through the Doppler spectrum and the value of  $b_2$  the characteristics of the spatial correlation affects the number of branch switches.

### C.5.3 Other Methods

In wideband channels, *i.e.*, where the channel delay spread is greater than the symbol period, the combination of multipath components can make it increasingly difficult to characterize the small-scale fading characteristics of the channel.

Wang, *et. al.* [95], also consider velocity estimation in such a wideband channel. The work focuses on characterizing the deviation characteristics of the samples in the frames of a TDMA network. Under consideration are two of the power delay profiles specified in the GSM standard. The first profile is the rural area (RA) channel, in which ISI is not much of a problem since there are few multipath components. The second profile is the typically urban (TU) channel, which exhibits more ISI since there are more multipath components.

Although the results reported by [95] seem impressive at first, further analysis of their methods calls into question not only the viability of their techniques, but also the validity of their results. First, the channel model used for the analysis may not take into account all of the necessary features of a scattering environment in which one user is mobile. The only distorting feature of the channel mentioned is the inter-symbol interference caused by the delayed multipath components. There is no mention of the correlation between spatially separated samples which gives rise to the Doppler spectrum. The correlation would certainly have an effect on the accuracy of the channel estimator used in the proposed receiver architecture. Although not specifically stated by [95], it is entirely possible that the same channel characterization used for the simulation is also used as a perfect reconstruction in the channel estimator for the purposes of analysis. The second problem with accepting the results from this paper is that there is no specific rationale given as to why this method should work. This leaves one to wonder whether the results are simply empirically derived, making it much more difficult to determine the limitations of the techniques.

Two algorithms are presented by [95]. Both algorithms attempt to characterize the variations of the signal envelope in the two different multipath environments mentioned earlier. The first algorithm, dubbed “T-mean,” is proposed for use in channels inducing little inter-symbol interference. In this algorithm, the following metric is used:

$$D = \frac{1}{N} \sum_{i=1}^N (\bar{y}_1(i) - \bar{y}_2(i))^2. \quad (\text{C.11})$$

$\bar{y}_1(i)$  is the average of the signal envelope taken over the first half of frame  $i$ , and  $\bar{y}_2(i)$  is the average taken over the second half of the frame.  $N$  is the number of frames over which this metric is taken.

Qualitatively, this method is similar to the Holtzman covariance method of [37] in that the value of  $D$  should increase as the speed of the mobile user increases since the samples become less correlated as they are spaced further apart in distance. The difference between this method and Holtzman's is that the "deviation" is between half-frames rather than between adjacent samples.

One problem with this method is that the averaging interval is fixed in time, not in space. As the speed varies, the spatial distance between samples that are equally spaced in time vary also (Challenge #2). Similar to the sampling analysis by [7], the variance of the estimate is a non-monotonic function of the distance between spatial samples. It is unclear whether the deviations measured by [95] are indicative of the channel characteristics, a fundamental change in the way the process is sampled, or some combination of both.

Another problem with this first algorithm is that when ISI is introduced, the estimator becomes biased since the deviations are a result of ISI in addition to that of the channel (Challenge #5). This effect is observed by [95] and gives rise to their second algorithm called "Pattern-mean."

In this second algorithm, a channel estimator is used to determine what the received waveform would be in the absence of additive noise, *i.e.*, when corrupted only by the combination of multipath components. A "pattern" algorithm then picks out features, such as voltage peaks, of the predicted waveform that match sequences of data symbols. When these sequences of data symbols appear throughout the frame, the values of the previously mentioned features are averaged together over a half-frame. These average values are subtracted and squared as in (C.11) to get a deviation metric.

One implementation problem of this second algorithm is that the "patterns" in the received signal waveform will change every time the multipath intensity profile changes, making frequent generation of the recognizable patterns necessary. Furthermore, the accuracy of the channel estimate becomes extremely important. Not only will the channel estimate need to converge quickly in a rapidly changing environment, but it must accurately track the changes as well.

The performance of these estimators is compared to stored theoretical values of [95]. Since the underlying characteristics of the channel giving rise to the observed behavior are not discussed, it is unclear what the theoretical values represent, *e.g.*, they may be empirically derived values from

previous simulation runs under more ideal conditions.

## C.6 Closed-Loop Doppler Estimate for Velocity Estimation

One significant but often overlooked challenge in velocity estimation is that of frequency reference at the receiver. Velocity estimators, such as those by [6, 13, 62], require a precise frequency reference at the receiver to detect small changes in frequency or phase shift that are caused by the motion of the user. To further complicate matters, the oscillators used in communication equipment typically have tolerances in the same range as the expected Doppler shifts. For example, in the EIA/TIA-136 standard, base stations and mobile stations using digital channels require oscillators with frequency tolerances of  $\pm 0.25$  ppm.<sup>12</sup> Base station or mobile user transmission frequencies may be offset from the true carrier frequency by as much as 220 Hz. For comparison, a user traveling at 60 miles per hour would have a maximum Doppler shift of 78 Hz at the frequencies around 880 MHz used by this standard.

Without a precise frequency reference at the receiver, the carrier recovery loop tracks the received carrier frequency which may have been subjected to a frequency shift. In the most general case, the scattering environment is also unknown. In fact, the Doppler spectrum may not be symmetric. To resolve these problems of precision and ambiguity in the Doppler spectrum, a closed-loop measurement between transmitter and receiver must be performed. This section introduces a closed-loop Doppler measurement that has application to velocity estimation in mobile wireless systems.

To propose a closed-loop measurement that is applicable to current systems, a few assumptions about the application environment must be made: (1) The uplink and downlink frequencies are close enough that the Doppler spectrum on the uplink is essentially the same as that on the downlink. (2) The modulation can be removed from the received signal, yielding a signal that shows only the effects of the channel. (3) The signals transmitted and received are not continuous and have a well-defined time gating. These assumptions are consistent with TDMA system standards [27, 91] and impact the design of the closed-loop measurement.

To make a closed-loop frequency measurement between transmitter and receiver, the transmit

---

<sup>12</sup>Base stations using analog channels require  $\pm 1.5$  ppm tolerances whereas mobile stations require  $\pm 2.5$  ppm tolerances for analog channels.

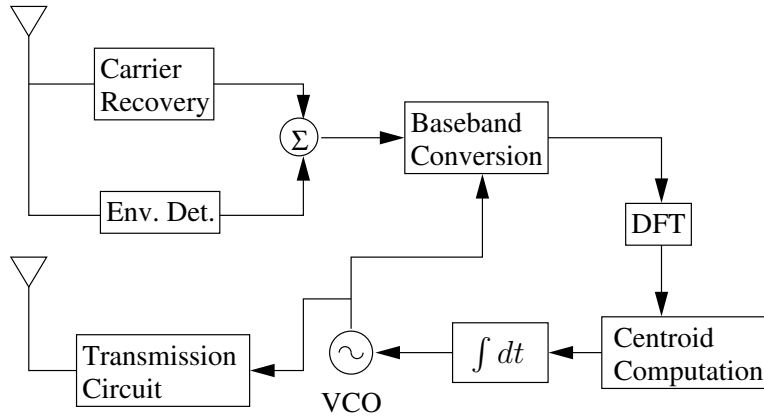


Figure C.3: Overview of Mobile Terminal Frequency Tracking. The mobile unit derives the uplink frequency from the downlink frequency.

frequency must be derived from the receive frequency at either the mobile unit or the base station. The transceiver that does not perform this frequency loopback will have immediate access to the round-trip measurement. In a cellular system, this immediate access is most useful at the base station since that is where the decision infrastructure exists. The mobile unit, therefore, performs the frequency loopback. The base station oscillator, which may be more expensive and more precise than those in mobile units, acts as the primary reference oscillator for the round-trip measurement. An overview of this loopback operation is shown in Fig. C.3.

After carrier recovery is performed, the recovered carrier signal is converted to baseband. Since the modulating signal has been removed, the baseband signal shows only the effect of the channel. The Doppler spectrum is computed by performing a discrete Fourier transform (DFT) of the baseband signal. The centroid of the Doppler spectrum is computed and forces the local reference oscillator to track the center of the received Doppler spectrum. Since the uplink frequency is derived from this reference oscillator, it is linked to the downlink frequency, which may have experienced a shift. At the base station, a similar carrier recovery operation is performed, followed by a centroid computation. If the Doppler spectrum is symmetric, then the centroid will be zero at both the base station and the mobile terminal, and no shifting of the computed Doppler spectrum takes place. If the Doppler spectrum is not symmetric, however, the base station centroid value indicates how far to shift the computed Doppler spectrum.

Figure C.4 shows the frequency loopback operation in more detail. The examples in Figs. C.4



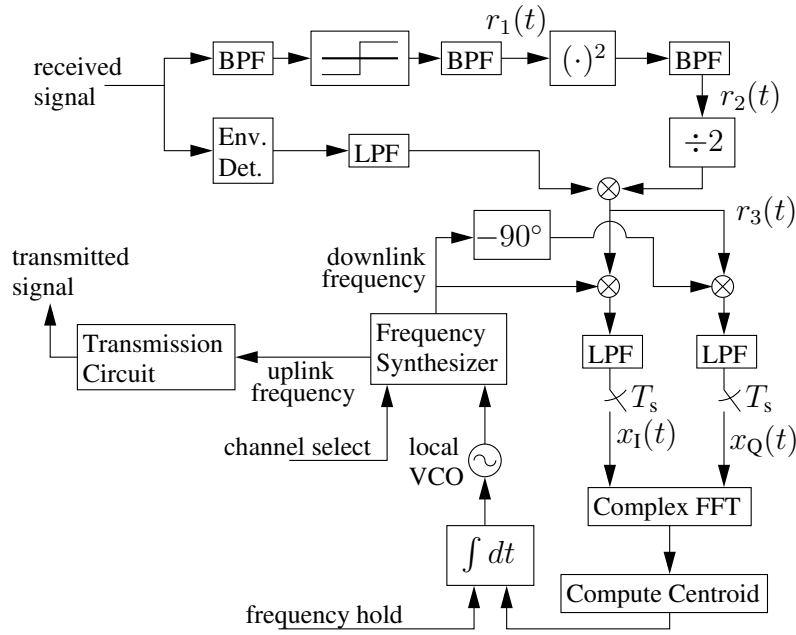


Figure C.4: Mobile Unit Doppler Computation. The BPSK modulation is removed from the received signal. The centroid of the frequency spectrum controls the uplink frequency.

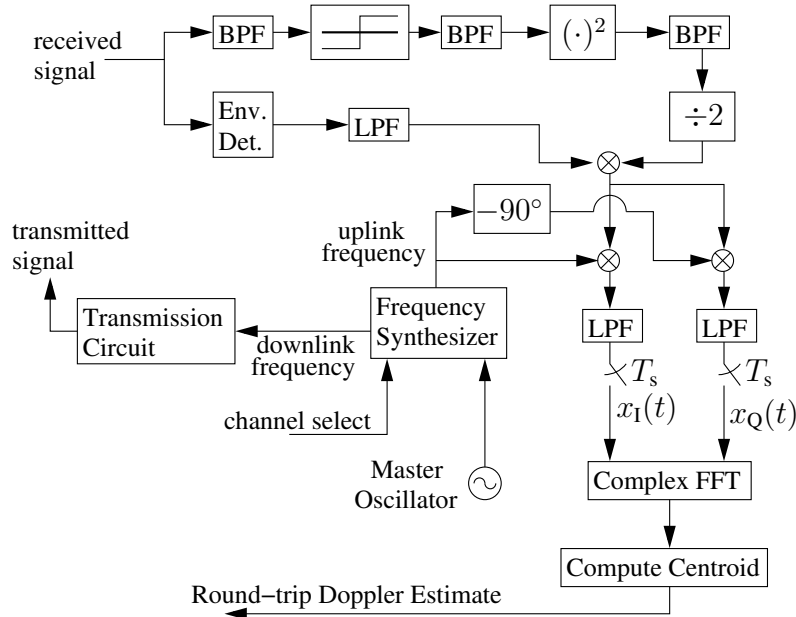


Figure C.5: Base Station Doppler Computation. The centroid of the baseband frequency spectrum gives an estimate of the round-trip Doppler shift.

and C.5 assume that binary phase shift keying (BPSK) is used for the data modulation. The transmitted signal is

$$x(t) = \cos(2\pi f_c t + \phi(t)) \quad (\text{C.12})$$

where  $f_c$  is the carrier frequency, and  $\phi(t)$  takes on values of  $(0, \pi)$  to represent the data symbols transmitted. The received signal is

$$r(t) = A_c(t) \cos(2\pi f_c t + \phi_c(t) + \phi(t)) \quad (\text{C.13})$$

where  $A_c(t)$  and  $\phi_c(t)$  account for the signal impairments caused by the propagation channel. In the carrier recovery loop (Fig. C.4), the output of the envelope detector is  $A(t)$ . After the limiter and bandpass filter in the other branch of the carrier recovery circuit, the signal is

$$r_1(t) = \cos(2\pi f_c t + \phi_c(t) + \phi(t)). \quad (\text{C.14})$$

After the squaring circuit, the signal becomes

$$r_2(t) = \cos(4\pi f_c t + 2\phi_c(t) + 2\phi(t)) \quad (\text{C.15})$$

where the  $2\phi(t)$  term drops out due to phase wrapping, *i.e.*,  $2\pi$  is indistinguishable from 0. After the frequency divider and mixing with the output of the envelope detector, the signal becomes

$$r_3(t) = A_c(t) \cos(2\pi f_c t + \phi_c(t)) \quad (\text{C.16})$$

which contains only the terms accounting for the channel impairments. This signal is then converted to baseband, after which the frequency spectrum is computed. Since the mobile unit may monitor other channels between frames, there is a “frequency hold” option that holds the last value of the control voltage on the reference oscillator.

An overview of the base station’s role in the measurement is shown in Fig. C.5. The primary difference between Figs. C.4 and C.5 is that the centroid value does not close the loop in the base station. Instead, the base station oscillator acts as a reference oscillator for the measurement. The base station centroid value is used as an estimate of the closed-loop Doppler shift.

The frequency synthesizer is shown in Fig. C.6. The synthesizer uses the reference oscillator

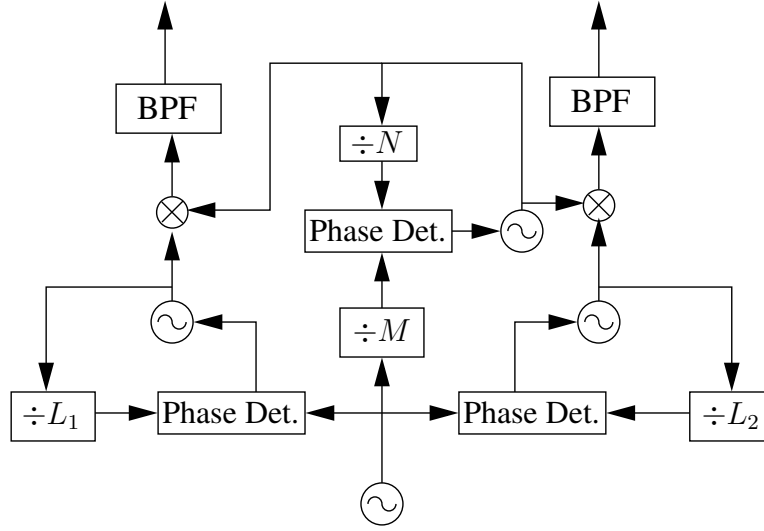


Figure C.6: Frequency Synthesis.  $M$  and  $N$  select the frequency band while  $L_1$  and  $L_2$  select the individual uplink and downlink channels within that band.

to derive the conversion frequency for both the downlink and the uplink. The uplink and downlink frequencies are  $f_{\text{ref}}(\frac{M}{N} \pm L_1)$  and  $f_{\text{ref}}(\frac{M}{N} \pm L_2)$ . An example in which transmitter and receiver have line of sight illustrates how the entire process works.

If the base station reference oscillator operates at frequency  $f_r$ , then the downlink center frequency is  $f_r(\frac{N}{M} + L_1)$ . At the mobile terminal, the received frequency is  $f_r(\frac{N}{M} + L_1) + f_\Delta$  where  $f_\Delta$  is the frequency shift caused by the motion of the mobile user. The mobile terminal's reference oscillator tracks to

$$\begin{aligned} f_r' &= \frac{f_r \left( \frac{N}{M} + L_1 \right) + f_\Delta}{\left( \frac{N}{M} + L_1 \right)} \\ &= f_r + \frac{f_\Delta}{\left( \frac{N}{M} + L_1 \right)}. \end{aligned} \tag{C.17}$$

The uplink frequency is  $f_r'(\frac{N}{M} + L_2)$ , and the base station experiences an equivalent frequency shift

of  $f_\Delta$ . At the base station, the centroid value would drive an equivalent reference oscillator to

$$\begin{aligned} f_r'' &= f_r' + \frac{f_\Delta}{\left(\frac{N}{M} + L_2\right)} \\ &= f_r + \frac{f_\Delta}{\left(\frac{N}{M} + L_1\right)} + \frac{f_\Delta}{\left(\frac{N}{M} + L_2\right)}. \end{aligned} \quad (\text{C.18})$$

The base station centroid value is proportional to

$$f_r - f_r'' \approx \frac{2Mf_\Delta}{N} \quad (\text{C.19})$$

where the approximation can be made if the channel spacing is much less than the multiplication factor ( $L_1, L_2 \ll M/N$ ).

For the LOS case, the Doppler shift is

$$f_D = \frac{1}{2}(f_r - f_r''). \quad (\text{C.20})$$

The Doppler frequency is related to the mobile-user velocity as follows:

$$f_D = \frac{v}{c} f_c \cos \alpha \quad (\text{C.21})$$

where  $v$  is the mobile-user speed,  $c$  is the speed of light, and  $\alpha$  is the angle between the velocity vector and the arrival direction of the signal. The velocity is

$$\begin{aligned} v &= \frac{cf_D}{f_c \cos \alpha} \\ &\geq \frac{cf_D}{f_c} \end{aligned} \quad (\text{C.22})$$

where the inequality holds since  $\cos \alpha \leq 1$ . Since the arrival angle is unknown, only a lower bound on the mobile-user velocity can be determined. If an antenna array is used, however, the arrival angle may be estimated as done by [62] to give a better estimate of the mobile-user velocity.

The sampling rate used in the closed-loop Doppler measurement is limited by the frame rate of the system standard since the Doppler spectrum is sampled once per frame. Table C.1 shows the

<b>Standard</b>	<b>Carrier Frequency [MHz]</b>	<b>Frame Period</b>	<b>Maximum Detectable Velocity</b>
IS-136	824–849 / 869–894	20 ms	30.2 km/hr
JDC	940–956 / 810–826	20 ms	28.2 km/hr
JDC	1429–1441 / 1477–1489	20 ms	18.1 km/hr
IS-95	824–849 / 869–894	20 ms	30.2 km/hr
PACS	1850–1910 / 1930–1990	2.5 ms	108.5 km/hr
PHS	1895–1918	5 ms	56.3 km/hr
DECT	1800–1900	10 ms	28.4 km/hr
GSM	930–960 / 890–915	4.62 ms	121.8 km/hr
CT-2	864–868 / 944–948	2 ms	284.8 km/hr

Table C.1: Frame Rate Restrictions. Using the closed-loop Doppler measurement with frame-rate sampling, the maximum detectable velocity is limited by the carrier frequency and the frame rate.

frame rates for several standards and the maximum velocity that the closed-loop Doppler measurement can detect based on the frequency and the sampling rate constraint. Furthermore, since the initial frequency offset between transmitter and receiver oscillators may be greater than the maximum expected Doppler shift, an initialization procedure must be used to ensure that the receiver does not lock to an aliased version of the Doppler shift. During initialization, the receiver locks to a broadcast channel which transmits continuously and may be sampled at a higher rate. The mobile unit's local oscillator is then brought to within one maximum Doppler shift of the master oscillator. Finally, frame-rate sampling is used to keep the mobile unit's local oscillator from drifting to an aliased version of the Doppler spectrum.

## C.7 Summary

Traditional approaches to mobile-user velocity estimation assume a scattering model for a specific environment and derive an estimator that exploits specific features of the assumed model. Unfortunately, this approach leads to estimators that must be revised whenever the scattering characteristics of the propagation environment are changed, making them impractical for general-purpose use.

The assumption of the small-scale scattering environment is the largest obstacle to surmount since it provides most of the insight into the behavior of the channel. For this reason, most analyses do not even consider what might happen if the scattering environment changes. The ones that

consider even simple modifications to the underlying assumptions find that the best estimators do not perform well in environments other than the ones for which they are specifically designed [7, 37].

Some techniques, such as the multidimensional scaling technique used by Hellebrandt [36] and the cell dwell time technique used by Sung and Wong [88], appear to avoid this dilemma by assuming that an average power will be known. Determining the average power leads to the question of how long to average, *i.e.*, how many time samples, in order to get an accurate power estimate. The answer to this question depends both on the scattering environment and the distance traversed in a specified period of time. The handoff criteria used by [88] is further complicated by the fact that a simple path-loss distance measurement might not be appropriate in all cases.

The averaging interval and reporting time are also problems that many estimators encounter. The cell dwell time estimator of [88] is not useful for applications that require frequent velocity estimates since the velocity is updated only when handoffs are required. The triple averaging—once for the average power, again for the position measurement, and once more for the velocity estimate—required for the multidimensional scaling of Hellebrandt [36] would levy heavy computation and storage requirements on the system in addition to delaying the velocity estimate. Furthermore, when the averaging requirements are specified in distance, as done by [6, 7, 36, 37], and the samples are taken in time, a circular logic exists in that velocity—through the distance and time relationships—must be known in order to estimate the velocity.

Even trying to compute the Doppler shift of a LOS component, either alone or with other scattered components, can be treacherous. These simple measurements cannot be done in practice since they require knowledge of the precise transmit frequency at the receiver. Since the receiver simply synchronizes to the received frequency, the precise transmit frequency may be unknown, making even this simple measurement impossible to perform.

In addition to the challenges presented previously, the following observations are also made:

*Observation #1. The mean square error scales with velocity.* Unfortunately, most of the estimators in the literature are not characterized for different velocities. It is, however, noted that due to the constraint (C.7) on the number of autocorrelations which may be used in Austin's eigen-space method, the accuracy deteriorates at higher speeds due to the number of autocorrelations which may be used. The wavelet estimator of [59] experiences an absolute mean square error which scales with the square of the velocity (the normalized MSE, however, remains constant).

The noise biasing problem is primarily a problem at slow speeds [7]. At higher speeds and in the noiseless cases, most velocity estimators have a reduced accuracy when the speed of the mobile user is increased. This could be due in part to the fact that the samples of the channel are still spaced equally in time, and at higher speeds the channel is simply undersampled.

*Observation #2. Components arriving perpendicular to the direction of travel provide little information about the velocity.* The Doppler shift of a perpendicularly arriving component is zero. At the receiver, waves arriving perpendicular to the direction of user motion are difficult to distinguish from signals arriving at any angle when the receiver is stationary. Second, we observe the frequency of a component arriving at angle  $\alpha$  with respect to the direction of travel:  $f = f_D \cos \alpha + f_c$ , where  $f_D$  is the maximum Doppler shift at the given velocity and  $f_c$  is the carrier frequency. Since  $\frac{f-f_c}{f_D} = \cos \alpha$ , the graph in Fig. 2.5 could have been written in terms of  $\cos \alpha$ , i.e.,  $S_r(f') = S_r(\cos \alpha)$  where  $f' = \frac{f-f_c}{f_D}$ . One recalls that the assumptions for Clarke's scattering model include power arriving uniformly distributed in the 2-D horizontal plane. We consider the distribution of this received power in terms of the arrival angle  $\alpha$  to be a function  $S_\alpha(\alpha)$  which is constant over the interval  $0 \leq \alpha \leq 2\pi$ . For the following discussion, we consider both  $S_\alpha(\cdot)$  and  $S_r(\cdot)$  to be probability distribution functions. In reality, they will be scaled by a constant that depends on the signal power incident upon the receiver.

To convert the uniform probability distribution function to one that depends on frequency ( $f'$  in this case), we can use the following transformation [48, Ch. 3]:

$$S_r(f') = \frac{S_\alpha(\alpha)}{\left| \frac{d}{d\alpha} \cos \alpha \right|} + \frac{S_\alpha(-\alpha)}{\left| \frac{d}{d\alpha} \cos(-\alpha) \right|} \quad (\text{C.23})$$

Equation (C.23) reduces to the form in (2.31). Observing the equation as written in (C.23), one can see how the “peaks” in Fig. 2.5 arise. Since the derivative of the cosine function approaches zero at angles near 0 and  $\pi$ , these are the locations where the terms in (C.23) approach infinity. When power is uniformly distributed over some portion of the 2-D horizontal plane, the components arriving more parallel to the direction of travel (Fig. C.2(a)) are emphasized more than those arriving more perpendicular to the direction of travel (Fig. C.2(b)).

*Observation #3. Usually only constant velocities are considered.* Implicit in the design of many velocity estimators is the stationarity of the velocity itself. Since characteristics such as the Doppler spectrum arise due to the spatial variation of the signal strength, a constant velocity and equally

spaced time samples are required to give the equally spaced spatial samples which are commonly used in analysis. Over short time intervals, *e.g.*, the duration of a bit period or the duration of a data frame, this constant velocity assumption is usually valid. When the estimate must be averaged over a longer period of time, *e.g.*, several frames in a TDMA system, the assumption may break down, leading to a larger-than-expected variance. The choice of averaging interval relative to the stationarity of the mobile-user velocity is a consequence of the “responsiveness” tradeoff outlined in Challenge #3.

Narasimhan introduces two estimators that overcome two significant challenges in mobile-user velocity estimation. First, the wavelet-based estimator introduced by [59] overcomes the need to adjust parameters based on the speed of the mobile user. The wavelet-based estimator bypasses the requirement for a local average power estimate by detecting the spacing of the nulls in the received signal. The null spacings are a function of the carrier frequency and the scattering environment, however, limiting the robustness of this technique to changes in scattering conditions.

Narasimhan’s second estimator [62] uses a best-basis technique to estimate the time-varying Doppler spectrum for regions in which the statistics of the small-scale fading are stationary. This estimator determines the average power without adjusting an averaging parameter that depends on the mobile user’s speed. Furthermore, this method is robust to changes in the scattering environment. Using an antenna array to determine arrival direction, the velocity is estimated from the arrival angle and the frequency shift. This method, however, also requires a precise frequency reference at the receiver.

The closed-loop Doppler measurement introduced in this chapter solves the frequency reference problem by making a closed-loop frequency measurement between transmitter and receiver. This round-trip measurement can be combined with any method that requires a precise frequency reference to make a more robust velocity estimator. However, the maximum Doppler shift that can be accommodated is limited by the sampling rate, which depends on the framing used by the mobile communication standard. Thus the range of speeds that can be accommodated is constrained by a wireless standard rather than the physics of the problem.



## Bibliography

- [1] H. G. J. Aitken, *Syntony and Spark—The Origins of Radio*. New York: Wiley, 1976.
- [2] ———, *The Continuous Wave: Technology and American Radio, 1900–1932*. Princeton, New Jersey: Princeton U.P., 1985.
- [3] N. Amitay, “Modeling and computer simulation of wave propagation in lineal line-of-sight microcells,” *IEEE Transactions on Vehicular Technology*, vol. 41, no. 4, pp. 337 – 342, 1992.
- [4] K. D. Anim-Appiah, “On generalized covariance-based velocity estimation,” *IEEE Transactions on Vehicular Technology*, vol. 48, no. 5, pp. 1546 – 1557, 1999.
- [5] M. D. Austin and G. L. Stüber, “Velocity adaptive handoff algorithms for microcellular systems,” in , *2nd International Conference on Universal Personal Communications, 1993*, vol. 2, 1993, pp. 793 – 797.
- [6] ———, “Eigen-based Doppler estimation for differentially coherent CPM,” *IEEE Transactions on Vehicular Technology*, vol. 43, no. 3, pp. 781 – 785, 1994.
- [7] ———, “Velocity adaptive handoff algorithms for microcellular systems,” *IEEE Transactions on Vehicular Technology*, vol. 43, no. 3, pp. 549 – 561, 1994.
- [8] W. T. Barnett, “Multipath propagation at 4, 6, and 11 GHz,” *Bell System Technical Journal*, vol. 51, pp. 321 – 361, 1972.
- [9] Bell Telephone Laboratories Technical Staff, *Transmission Systems for Communications*, 5th ed. Bell Telephone Laboratories, 1982.

- [10] J.-E. Berg, R. Bownds, and F. Lotse, "Path loss and fading models for microcells at 900 MHz," in *Proceedings of the 42nd IEEE Vehicular Technology Conference*, 1992, pp. 666 – 671.
- [11] H. L. Bertoni, P. Pongsilamanee, C. Cheon, and G. Liang, "Sources and statistics of multipath arrival at elevated base station antenna," in *Proceedings of the 49th IEEE Vehicular Technology Conference*, vol. 1, 1999, pp. 581 – 585.
- [12] H. L. Bertoni, *Radio Propagation for Modern Wireless Systems*. Upper Saddle River, New Jersey: Prentice Hall PTR, 2000.
- [13] E. Biglieri, F. Abrishamkar, and Y.-C. Jou, "Doppler frequency shift estimation for differentially coherent CPM," *IEEE Transactions on Communications*, vol. 38, no. 10, pp. 1659 – 1663, 1990.
- [14] D. M. Black and D. O. Reudink, "Some characteristics of mobile radio propagation at 836 MHz in the Philadelphia area," *IEEE Transactions on Vehicular Technology*, vol. VT-21, no. 2, pp. 45 – 51, 1972.
- [15] H. Borjeson, C. Bergljung, and L. G. Olsson, "Fading characteristics in outdoor microcell at 1700 MHz," in , *Third IEEE International Symposium on Personal, Indoor and Mobile Radio Communications*, 1992, 1992, pp. 88 – 91.
- [16] —, "Outdoor microcell measurements at 1700 MHz," in *Proceedings of the 42nd IEEE Vehicular Technology Conference*, 1992, pp. 927 – 931.
- [17] J. J. Caffery and G. L. Stüber, "Radio location in urban CDMA microcells," in , *Sixth IEEE International Symposium on Personal, Indoor and Mobile Radio Communications*, 1995, vol. 2, 1995, pp. 858 – 862.
- [18] K. F. Casey, "Modal propagation in a circular waveguide with a rough wall," in *2003 IEEE Society International Conference on Antennas and Propagation*, Columbus, Ohio, 2003.
- [19] E. Damosso and L. M. Correia, Eds., *Urban Transmission Loss Models for Mobile Radio in the 900 and 1800 MHz Bands*. The Hague: European Cooperation in the Field of Scientific and Technical Research EURO-COST 231, 1991.

- [20] C. Demetrescu, C. C. Constantinou, and M. J. Mehler, "Corner and rooftop diffraction in radiowave propagation prediction tools: a review," in *48th IEEE Vehicular Technology Conference, 1998*, vol. 1, 1998, pp. 515 – 519.
- [21] U. Dersch and E. Zollinger, "Propagation mechanisms in microcell and indoor environments," *IEEE Transactions on Vehicular Technology*, vol. 43, no. 4, pp. 1058 – 1066, 1994.
- [22] T. L. Doumi and J. G. Gardiner, "Use of base station antenna diversity for mobile speed estimation," *Electronics Letters*, vol. 30, no. 22, pp. 1835 – 1836, 1994.
- [23] H. M. El-Sallabi, G. Liang, H. L. Bertoni, I. T. Rekanos, and P. Vainikainen, "Influence of diffraction coefficient and corner shape on ray prediction of power and delay spread in urban microcells," *IEEE Transactions on Antennas and Propagation*, vol. 50, no. 5, pp. 703 – 712, 2002.
- [24] V. Erceg, S. J. Fortune, J. Ling, A. J. Rustako, and R. A. Valenzuela, "Comparisons of a computer-based propagation prediction tool with experimental data collected in urban microcellular environments," *IEEE Journal on Selected Areas in Communications*, vol. 15, no. 4, pp. 677 – 684, 1997.
- [25] V. Erceg, S. Ghassemzadeh, M. Taylor, D. Li, and D. L. Schilling, "Urban/suburban out-of-sight propagation modeling," *IEEE Communications Magazine*, vol. 30, no. 6, pp. 56 – 61, 1992.
- [26] V. Erceg, A. J. Rustako, and R. S. Roman, "Diffraction around corners and its effects on the microcell coverage area in urban and suburban environments at 900 MHz, 2 GHz, and 4 GHz," *IEEE Transactions on Vehicular Technology*, vol. 43, no. 3, pp. 762 – 766, 1994.
- [27] European Telecommunications Standards Institute, "GSM technical specification," Nov. 1998.
- [28] M. J. Feuerstein, K. L. Blackard, T. S. Rappaport, S. Y. Seidel, and H. H. Xia, "Path loss, delay spread, and outage models as functions of antenna height for microcellular system design," *IEEE Transactions on Vehicular Technology*, vol. 43, no. 3, pp. 487 – 498, 1994.

- [29] H. T. Friis, "A note on a simple transmission formula," *Proceedings of the I.R.E. Waves and Electrons*, vol. 34, pp. 254 – 256, 1946.
- [30] A. J. Goldsmith and L. J. Greenstein, "A measurement-based model for predicting coverage areas of urban microcells," *IEEE Journal on Selected Areas in Communications*, vol. 11, no. 7, pp. 1013 – 1023, 1993.
- [31] M. Gudmundson, "Correlation model for shadow fading in mobile radio systems," *Electronics Letters*, vol. 27, no. 23, pp. 2145 – 2146, 1991.
- [32] H. Hashemi, "Pulse ranging radiolocation technique and its application to channel assignment in digital cellular radio," in '*Gateway to the Future Technology in Motion*', *41st IEEE Vehicular Technology Conference, 1991*, 1991, pp. 675 – 680.
- [33] S. Hassanzadeh and H. Hashemi, "A propagation model for microcellular mobile and personal radio communications," in , *Sixth IEEE International Symposium on Personal, Indoor and Mobile Radio Communications, 1995*, vol. 2, 1995, pp. 392 – 396.
- [34] M. Hata, "Empirical formula for propagation loss in land mobile radio services," *IEEE Transactions on Vehicular Technology*, vol. 29, no. 3, pp. 317 – 325, 1980.
- [35] M. Hellebrandt and R. Mathar, "Location tracking of mobiles in cellular radio networks," *IEEE Transactions on Vehicular Technology*, vol. 48, no. 5, pp. 1558 – 1562, 1999.
- [36] M. Hellebrandt, R. Mathar, and M. Scheibenbogen, "Estimating position and velocity of mobiles in a cellular radio network," *IEEE Transactions on Vehicular Technology*, vol. 46, no. 1, pp. 65 – 71, 1997.
- [37] J. M. Holtzman and A. Sampath, "Adaptive averaging methodology for handoffs in cellular systems," *IEEE Transactions on Vehicular Technology*, vol. 44, no. 1, pp. 59 – 66, 1995.
- [38] F. Ikegami, S. Yoshida, T. Takeuchi, and M. Umehira, "Propagation factors controlling mean field strength on urban streets," *IEEE Transactions on Antennas and Propagation*, vol. 32, no. 8, 1984.
- [39] W. C. Jakes, Ed., *Microwave Mobile Communications*. IEEE Press, 1994.

- [40] A. G. Kanatas, I. D. Kountouris, G. B. Kostaras, and P. Constantinou, "A UTD propagation model in urban microcellular environments," *IEEE Transactions on Vehicular Technology*, vol. 46, no. 1, pp. 185 – 193, 1997.
- [41] K. Kawabata, T. Nakamura, and E. Fukuda, "Estimating velocity using diversity reception," in *1994 IEEE 44th Vehicular Technology Conference*, 1994, pp. 371 – 374.
- [42] S.-C. Kim, B. J. Guarino, T. M. Willis, V. Erceg, S. J. Fortune, R. A. Valenzuela, L. W. Thomas, J. Ling, and J. D. Moore, "Radio propagation measurements and prediction using three-dimensional ray tracing in urban environments at 908 MHz and 1.9 GHz," *IEEE Transactions on Vehicular Technology*, vol. 48, no. 3, pp. 931 – 946, 1999.
- [43] T. Kurner, D. J. Cichon, and W. Wiesbeck, "Concepts and results for 3D digital terrain-based wave propagation models: an overview," *IEEE Journal on Selected Areas in Communications*, vol. 11, no. 7, pp. 1002 – 1012, 1993.
- [44] J. Lee and H. L. Bertoni, "Coupling at L, T and cross junctions in tunnels and urban street canyons," in *Proceedings of the 53rd Vehicular Technology Conference*, vol. 1, 2001, pp. 274 – 278.
- [45] S. Lee and W. Chung, "Estimation of position and velocity for a mobile station," in *Proceedings of the Third International Symposium on Multi-Dimensional Mobile Communications*, 1998, pp. 256 – 260.
- [46] T. H. Lee, *The Design of CMOS Radio-Frequency Integrated Circuits*. Cambridge: Cambridge U.P., 1998.
- [47] W. C.-Y. Lee, "Estimate of local average power of a mobile radio signal," *IEEE Transactions on Vehicular Technology*, vol. VT-34, no. 1, pp. 22 – 27, 1985.
- [48] A. Leon-Garcia, *Probability and Random Processes for Electrical Engineering*. New York: Addison-Wesley, 1989.
- [49] G. Liang and H. L. Bertoni, "A new approach to 3-D ray tracing for propagation prediction in cities," *IEEE Transactions on Antennas and Propagation*, vol. 46, no. 6, pp. 853 – 863, 1998.

- [50] J. Lin and J. G. Proakis, "A parametric method for Doppler spectrum estimation in mobile radio channels," in *Proceedings of the 27th Annual Conference on Information Sciences and Systems*, The Johns Hopkins University, 1993, pp. 875 – 880.
- [51] F. Lotse and A. Wejke, "Propagation measurements for microcells in central Stockholm," in *1990 IEEE 40th Vehicular Technology Conference*, 1990, pp. 539 – 541.
- [52] A. Lozano, "Integrated dynamic channel assignment and power control in mobile wireless communication systems," Ph.D. dissertation, Stanford University, 1998.
- [53] L. R. Maciel and H. L. Bertoni, "Cell shape for microcellular systems in residential and commercial environments," *IEEE Transactions on Vehicular Technology*, vol. 43, no. 2, pp. 270 – 278, 1994.
- [54] K. Mahbobi, "Radio wave propagation in urban microcellular environment," in *Proceedings of the 42nd IEEE Vehicular Technology Conference*, 1992, pp. 951 – 955.
- [55] J. C. Maxwell, "A dynamical theory of the electromagnetic field," *Philosophical Transactions of the Royal Society of London*, vol. 155, pp. 459 – 512, 1865.
- [56] H. Mokhtari and P. Lazaridis, "Comparative study of lateral profile knife-edge diffraction and ray tracing technique using gtD in urban environment," *IEEE Transactions on Vehicular Technology*, vol. 48, no. 1, pp. 255 – 261, 1999.
- [57] Y. Nagata, Y. Furuya, E. Moriyama, M. Mizuno, I. Kamiya, and S. Hattori, "Measurement and modeling of 2ghz-band out-of-sight radio propagation characteristics under microcellular environments," in , *IEEE International Symposium on Personal, Indoor and Mobile Radio Communications*, 1991, pp. 341 – 346.
- [58] R. Narasimhan and D. C. Cox, "A handoff algorithm for wireless systems using pattern recognition," in *The Ninth IEEE International Symposium on Personal, Indoor and Mobile Radio Communications*, 1998, vol. 1, 1998, pp. 335 – 339.
- [59] —, "Speed estimation in wireless systems using wavelets," in *1999 IEEE International Conference on Communications*, 1999, vol. 3, 1999, pp. 1773 – 1778.

- [60] —, “Wavelet-based estimation of the nonstationary mean signal in wireless systems,” *IEEE Journal on Selected Areas in Communications*, vol. 18, no. 11, pp. 2220 – 2226, 2000.
- [61] —, “Estimation of mobile speed and average received power in wireless systems using best basis methods,” *IEEE Transactions on Communications*, vol. 49, no. 12, pp. 2172 – 2183, 2001.
- [62] —, “Estimation of mobile speed and average received power in wireless systems using best basis methods,” *IEEE Transactions on Communications*, vol. 49, no. 12, pp. 2172 – 2183, 2001.
- [63] R. Narasimhan, “Estimation of mobile speed and average received power with application to corner detection and handoff,” Ph.D. dissertation, Stanford University, 1999.
- [64] F. Niu and H. L. Bertoni, “Path loss and cell coverage of urban microcells in high-rise building environments,” in *Proceedings of the IEEE Global Telecommunications Conference*, 1993, pp. 266 – 270.
- [65] K. Okada and F. Kubota, “A proposal of a dynamic channel assignment strategy with information of moving direction in micro cellular systems,” *IEICE Transaction Fundamentals*, vol. E75-A, 1992.
- [66] Y. Okumura, E. Ohmori, T. Kawano, and K. Fukuda, “Field strength and its variability in vHF and UHF land-mobile radio service,” *Review of the Electrical Communication Laboratory*, vol. 16, no. 9–10, pp. 825 – 873, 1968.
- [67] J. D. Parsons, *The Mobile Radio Propagation Channel*. New York: Wiley, 2000.
- [68] L. Piazzzi and H. L. Bertoni, “Achievable accuracy of site-specific path-loss predictions in residential environments,” *IEEE Transactions on Vehicular Technology*, vol. 48, no. 3, pp. 922 – 930, 1999.
- [69] D. Porrat, “Radio propagation in hallways and streets for UHF communications,” Ph.D. dissertation, Stanford University, 2002.

- [70] D. Porrat and D. C. Cox, "UHF propagation in indoor hallways," *IEEE Transactions on Wireless Communications*, accepted for publication.
- [71] —, "A waveguide model for UHF propagation in streets," in *The 11th Virginia Tech/MPRG Symposium on Wireless Personal Communications*, Blacksburg, Virginia, 2001.
- [72] D. M. Pozar, *Microwave Engineering*, 2nd ed. New York: Wiley, 1998.
- [73] S. Ramo, J. R. Whinnery, and T. Van Duzer, *Fields and Waves in Communication Electronics*, 3rd ed. New York: Wiley, 1994.
- [74] A. Ranade, "Local access radio interference due to building reflections," *IEEE Transactions on Communications*, vol. 37, no. 1, pp. 70 – 74, 1989.
- [75] T. S. Rappaport, *Wireless Communications: Principles and Practice*. Upper Saddle River, New Jersey: Prentice Hall, 1996.
- [76] S. O. Rice, "Statistical properties of a sine wave plus random noise," *Bell Systems Technical Journal*, vol. 27, pp. 109 – 157, 1948.
- [77] K. Rizk, J.-F. Wagen, and F. Gardiol, "Two-dimensional ray-tracing modeling for propagation prediction in microcellular environments," *IEEE Transactions on Vehicular Technology*, vol. 46, no. 2, pp. 508 – 518, 1997.
- [78] —, "Influence of database accuracy on two-dimensional ray-tracing-based predictions in urban microcells," *IEEE Transactions on Vehicular Technology*, vol. 49, no. 2, pp. 631 – 642, 2000.
- [79] A. Rubini, *Linux Device Drivers*. Cambridge: O'Reilly, 1998.
- [80] A. J. Rustako, N. Amitay, G. J. Owens, and R. S. Roman, "Radio propagation at microwave frequencies for line-of-sight microcellular mobile and personal communications," *IEEE Transactions on Vehicular Technology*, vol. 40, no. 1, pp. 203 – 210, 1991.
- [81] S. Sakagami, S. Aoyama, K. Kuboi, S. Shirota, and A. Akeyama, "Vehicle position estimates by multibeam antennas in multipath environments," *IEEE Transactions on Vehicular Technology*, vol. 41, no. 1, pp. 63 – 68, 1992.



- [82] A. Sampath and J. M. Holtzman, "Estimation of maximum Doppler frequency for handoff decisions," in *Proceedings of the 43rd IEEE Vehicular Technology Conference*, 1993, pp. 859 – 862.
- [83] S. R. Saunders and F. R. Bonar, "Building diffraction modelling for area coverage predictions in mobile radio propagation," *IEE Colloquium on Diffraction Propagation Modelling Techniques Embracing Surface Feature Data*, pp. 4/1 – 4/3, 1990.
- [84] S. A. Schelkunoff and H. T. Friis, *Antennas: Theory and Practice*. New York: Wiley, 1952.
- [85] W. M. Smith and D. C. Cox, "Urban cell partitioning for improved statistical propagation modeling," in *2003 IEEE Society International Conference on Antennas and Propagation*, vol. 4, 2003.
- [86] H.-W. Son and N.-H. Myung, "A deterministic ray tube method for microcellular wave propagation prediction model," *IEEE Transactions on Antennas and Propagation*, vol. 47, no. 8, pp. 1344 – 1350, 1999.
- [87] G. L. Stüber, *Principles of Mobile Communications*. Kluwer Academic Publishers, 1996.
- [88] C. W. Sung and W. S. Wong, "User speed estimation and dynamic channel allocation in hierarchical cellular system," in *1994 IEEE 44th Vehicular Technology Conference*, 1994, pp. 91 – 95.
- [89] S. Y. Tan and H. S. Tan, "UTD propagation model in an urban street scene for microcellular communications," *IEEE Transactions on Electromagnetic Compatibility*, vol. 35, no. 4, pp. 423 – 428, 1993.
- [90] ———, "A theory for propagation path-loss characteristics in a city-street grid," *IEEE Transactions on Electromagnetic Compatibility*, vol. 37, no. 3, pp. 333 – 342, 1995.
- [91] Telecommunications Industry Association and Electronics Industries Alliance, "TIA/EIA-136 TDMA Cellular PCS," Mar. 1999.
- [92] A. Vigants, "Space diversity engineering," *Bell System Technical Journal*, vol. 54, pp. 103 – 142, 1975.

- [93] J.-F. Wagen, "Signal strength measurements at 1881 MHz for urban microcells in downtown Tampa," in *Featuring a Mini-Theme on: Personal Communications Services Global Telecommunications Conference, 1991*, 1991, pp. 1313 – 1317.
- [94] J. Walfisch and H. L. Bertoni, "A theoretical model of UHF propagation in urban environments," *IEEE Transactions on Antennas and Propagation*, vol. 36, no. 12, pp. 1788 – 1796, 1988.
- [95] L. Wang, M. Silventoinen, and Z. Honkasalo, "A new algorithm for estimating mobile speed at the TDMA-based cellular system," in *Proceedings of the 46th IEEE Vehicular Technology Conference*, vol. 2, 1996, pp. 1145 – 1149.
- [96] J. H. Whitteker, "Measurements of path loss at 910 MHz for proposed microcell urban mobile systems," *IEEE Transactions on Vehicular Technology*, vol. 37, no. 3, pp. 125 – 129, 1988.
- [97] D. Wong and D. Cox, "A handoff algorithm using pattern recognition," in *IEEE 1998 International Conference on Universal Personal Communications, 1998*, vol. 1, 1998, pp. 759 – 763.
- [98] —, "Multi-state pattern recognition handoff algorithms," in *IEEE Global Telecommunications Conference, 1998*, vol. 3, 1998, pp. 1420 – 1425.
- [99] K. D. Wong and D. C. Cox, "A pattern recognition system for handoff algorithms," *IEEE Journal on Selected Areas in Communications*, vol. 18, no. 7, pp. 1301 – 1312, 2000.
- [100] —, "Two-state pattern-recognition handoffs for corner-turning situations," *IEEE Transactions on Vehicular Technology*, vol. 50, no. 2, pp. 354 – 363, 2001.
- [101] K.-S. D. Wong, "Handoff algorithms using pattern recognition," Ph.D. dissertation, Stanford University, 1998.
- [102] H. Zhang, T. Yoshina, S. Ito, and Y. Nagasawa, "A UTD-based approach to predicting diffraction by buildings for cellular mobile communication," in *1998 IEEE-APS Conference on Antennas and Propagation for Wireless Communications, 1998*, 1998, pp. 13 – 16.